



Università degli Studi di Cagliari



Consorzio AUSI

DOTTORATO DI RICERCA

Scienze e Tecnologie Chimiche

Ciclo XXVII

Mesostructured metal oxide-based nanocomposites as sorbents for H₂S removal from syngas coal gasification

Settori scientifici disciplinari di afferenza

CHIM/02 - CHIM/03 - CHIM/04

Presentata da:

Mauro Mureddu

Coordinatore Dottorato:

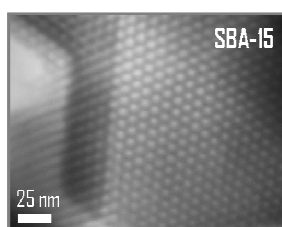
Prof. Mariano Casu

Tutor/Relatore:

Prof.ssa Anna Musinu
Prof.ssa Carla Cannas

Esame finale anno accademico 2013 – 2014

Mesostructured metal oxide-based nanocomposites as sorbents for H₂S removal from syngas coal gasification



A dissertation submitted to Cagliari University for the degree of

Doctor of Philosophy in Chemical Sciences

presented by

Mauro Mureddu (XXVII cycle)

Supervisor: **Prof. Anna Musinu**

Project Coordinator: **Prof. Carla Cannas**

PhD Coordinator: **Prof. Mariano Casu**



Department of Chemical and Geological Sciences

Cagliari University – Italy



Consorzio AUSI

Consorzio Promozione Attività

Universitarie Sulcis-Iglesiente

DECEMBER 2014

*To my beloved parents, teachers
...and to my sweet girlfriend*

Acknowledgements

There are many people I would like to thank for their support, encouragement, and comments over the duration of this project. First, my supervisors, Prof. Anna Musinu and Prof. Carla Cannas, deserve a great deal of credit for my academic formation, who showed great confidence in me, and provided me with a great deal of support. With their creativity, new ideas, advices, and continued guidance throughout this investigation, greatly improved the final product.

My sincere thanks also go to my advisors, Prof. Italo Ferino, Dr. Elisabetta Rombi, Dr. Maria Giorgia Cutrufello for their proper guidance, suggestions, scientific support, and superb competence in the field of "industrial chemistry". I express my gratitude to all the members of "Industrial Chemistry" group, Prof. Roberto Monaci, Dr. Franca Sini and Dr. Daniela Meloni.

Prof. Antonella Rossi and Dr. Marzia Fantauzzi are acknowledged for kindly providing me with the XPS analyses.

I am extremely happy to express my deep sense of gratitude to my lovable labmates Andrea Ardu, Federica Orrù, Giuseppe Muscas, Valentina Mameli, Claudio Cara, Roberto Piras for their help and support. It has been a pleasure sharing happy moments. Their moral support and lending a hand whenever needed were instrumental in the completion of my dissertation.

A very special thank goes to my "second" supervisors, with whom I worked and learned a lot during my six months of internship in the Elcogas IGCC power plant of Puertollano: Eng. Francisco Garcia Peña and Eng. Pedro Casero Cabezon. Without their patience and help, it would have been impossible to reach the prefixed goal of this important and profitable experience. My sincere thanks to my dear colleagues and friends of Elcogas, Miguel, Manuel, Guillermo, Carlos, Eduardo, Mariola, Laura, Maria, Sonia and Natalia (*mi familia*). You are wonderful people, thanks for your love and care; you made my life much more enjoyable

and unforgettable during my stay in Spain. I extend my thanks to all the staffs of the Department of Engineering, R&D group of Elcogas for their help and courteousness.

Consorzio AUSI (Consorzio per la Promozione delle Attività Universitarie del Sulcis-Iglesiente) is gratefully acknowledged for the grant financing. This work was also supported by ENEA (Italian National Agency for New Technologies, Energy and Sustainable Economic Development).

This acknowledgments would be incomplete without mentioning my family for their adoration, support, and their understanding during the whole period of my doctorate. Thanks to my lovelable girlfriend for always being by my side, encouraging me, and comforting me.

Mauro Mureddu

December 2014

Foreword

Desulphurization of gas phase sulphur compounds has been receiving dramatic attention since hazardous, corrosive, and toxic gases that cause environmental damages (especially acid rain) and industrial challenges (*i.e.*, corrosion of equipment and deactivation of catalysts).

This dissertation presents results of R&D efforts to develop efficient $\text{MeO}_x/\text{SBA-15}$ -based sorbents for H_2S removal in view of possible applications in hydrogen purification, air pollution control, and deep desulphurization of fossil fuels. It is precisely in the latter topic that the research project was born. The production of power, fuels and chemicals in most countries is predominantly based on oil and, to a minor extent, on natural gas. It is well-known that the reserves of both of these fuels are limited to a range of 40, 60 years. On the contrary, coal is a widely available fossil fuel, and it is expected to last for about 230 years. The imminent oil production limitations and the longer availability of coal, the wish to improve the security of the energy supply, and the possibility to reduce greenhouse gas emissions by means of carbon capture and sequestration (CCS) are sufficient motivations to increase the use of this resource. *Integrated Gasification Combined Cycle* (IGCC) process is a high efficiency power generation technology which gasifies coal to generate the fuel (syngas) for a high efficiency gas turbine. A key challenge for producing clean power or hydrogen via gasification is cost effective purification of the sour syngas. There are many commercial treatment techniques that are used to remove H_2S , but their disadvantage is that hot coal gas must be cooled down near to ambient temperature for desulphurization. The cooling equipment required, and the need to reheat the clean syngas before its use in a gas turbine result in economic and thermodynamic penalties that decrease the efficiency of a gasification plant. It is for this reason that hot gas desulphurization technique has attracted more and more attention due to the fact that it can reduce H_2S down to 100 ppm level and avoid heat loss. Mid-temperature desulphurization is achieved by the use of solid sorbents such as oxides of those metals that form stable sulphides, based on the non-catalytic reaction between a metal oxide and hydrogen sulphide. The optimum desulphurization temperature has been recommended in the range of 300 to 450 °C, also in according to the more

favourable thermodynamic equilibrium of sulphur compounds removal. To accomplish this task, Zinc oxide- and Iron oxide-based materials have been successfully employed for decades in different domains of the chemical industry. The pure metal oxides used as sorbents, however, suffer from evaporation, loss in the surface area and porosity due to sintering and mechanical disintegration that affect their performance and life time adversely. With the purpose of overcoming this problem and to improve their performance, metal oxides can be confined into a support, where under such conditions the materials are stable. The main properties required for support materials are inertness, high surface area, large pores and good mechanical strength.

The thesis reports some simple and versatile routes which can be proposed to prepare a great variety of $\text{MeO}_x/\text{SBA-15}$ composites where the mesostructured SBA-15 silica, a high-surface area (up to $1000 \text{ m}^2/\text{g}$) material, with 6–7 nm-wide regular channels and thick (3–4 nm) pore walls has been used as efficient and stable support. MeO_x active phase, formed inside the mesochannels, can reach the maximum size of 6–7 nm physically imposed by the pore diameter. Such a structure provides an ideal reactor where the mesopores act as channels for the transport of reactant. As a consequence, enhancement of the active phase reactivity might be expected. The proposed “Two-solvents” incipient impregnation method is easily reproducible and easy to scale up. Furthermore, this method should provide, at least in principle, ideal systems to be compared, and therefore to understand how the active phase nature influence their performance.

For the first time, a careful comparative study on the effect of the different nature of the nanostructured MeO_x ($\text{Me} = \text{Zn}, \text{Fe}$) dispersed into a mesostructured silica matrix (SBA-15) on the H_2S removal performance is carried out.

The behaviour of the $\text{MeO}_x/\text{SBA-15}$ composites in the removal of H_2S is investigated in a fixed-bed reactor and compared with that of an unsupported ZnO commercial sorbent. The morphological, structural, and textural features of fresh, sulphided, and regenerated sorbents have been assessed by a multi-technique approach, including the study of the possible interactions between the guest oxide and the host silica support. Furthermore, the sorption-desorption behaviour, which is commonly justified only

on the basis of the different nature of the active phase and of the textural features (surface area and pore volume), is discussed also considering the morphology and the crystallinity of the active phase.

In the literature, to our best knowledge, no one have reported similar correlations. For this reason this work can give an important contribution to improve the basic knowledge in the field of sorbents for gas-removal.

All the measurements, synthesis, and materials testing, have been carried out both at the Department of Chemical and Geological Sciences of the University of Cagliari, and at Consorzio AUSI (Consorzio per la promozione delle Attività Universitarie del Sulcis-Iglesiente).

Thesis outline

This thesis consists of eight chapters, organized as follows:

- ✚ **Chapter 1** introduces the present work, its motivation, research objectives, and provide an energy outlook and theoretical background.
- ✚ **Chapter 2** provides the necessary background on sorbent materials and also gives the description of the Hot Gas Desulphurization technology, determining the criteria for selecting sulphur sorption materials and focusing on the best and promising sorbents. Also analyses the best support materials, especially the mesoporous ones. The last section of this chapter is devoted on the ways for confining the metal oxides in the pores of the support.
- ✚ **Chapter 3** provides the descriptions of experimental details including the synthesis methods of the SBA-15 support, sorption-regeneration test equipment set-up, operational procedures and characterization methods.
- ✚ **Chapter 4** presents the experimental results and discussion for ZnO/SBA-15 sorbents. The composites, differing as to the ZnO loading and the calcination treatment, are characterised by

X-ray diffraction, transmission electron microscopy (also in the high resolution mode) and N_2 physisorption, in both fresh, sulphided, and regenerated state.

- ✚ **Chapter 5** presents the experimental results and discussion for H_2S multi-cycle on iron oxide/SBA-15 composites compared with both a zinc oxide/SBA-15 sorbent and unsupported ZnO commercial product. In this chapter, the different sorption behaviours are discussed in terms of the nature of the nanocomposites.
- ✚ **Chapter 6** presents the experimental results and discussion for H_2S multi-cycle on zinc ferrite/SBA-15 composites compared with the unsupported ZnO commercial product. The effects of an innovative impregnation-sol-gel autocombustion combined strategy, compared with the “two-solvents impregnation”, in terms of sorption and regenerative behaviour, are described.
- ✚ **Chapter 7** introduces to the Elcogas Power plant experience in the “Assessment of mid-temperature sorbent desulphurization technology in Puertollano IGCC process. It analyzes the possible integration alternatives of a unit based on the sorbent technology in the current IGCC process in place of the conventional “MDEA-solvent” technology used in the desulphurization unit. The objective of the work is to conceive how conceptually incorporate the solid sorbents technology in the pre-existing plant, detailing the technical specifications, understanding how this influence the different IGCC system and establish the criteria for comparison of different alternatives.
- ✚ **Chapter 8** covers an important part of the work carried out in Puertollano IGCC plant, examining in more detail the layout configurations proposed in the chapter 7. Aim of this chapter is to performs the mass and energy balance in the sorbent desulphurization unit proposed, and to evaluate the effect in the combined cycle of the plant in terms of thermal and gross efficiency compared with the MDEA-solvent technology. The Thermo-economic Diagnosis System “TDG” software, has been used in order to perform the simulations.

Table of contents

Acknowledgements	II
Foreword	IV
Thesis outline	VI
Chapter 1 Introduction, Energy outlook and Theoretical background	1
1 Introduction	1
1.1 Energy outlook & Motivations	1
1.2 Focus of the research	4
1.3 Literature review & Theoretical background	5
1.3.1 Integrated Gasification Combined Cycle Systems (IGCC)	5
1.3.2 Hydrogen sulphide properties	7
1.3.3 Current Acid Gas Removal (AGR)	8
1.3.4 Mid-temperature gas desulphurization	9
1.4 General basic principles of "sorbent technology"	10
References	11
Chapter 2 Sorbent materials	13
2.1 Sorbent materials	13
2.1.1 General characteristics of sorbent materials	14
2.1.2 New developments in sorbent materials and applications	15
2.2 Description of the New Hot Gas Desulphurization technology	16
2.3 Reaction mechanism	17
2.3.1 Non-catalytic gas-solid reaction models	19
2.3.2 Unreacted shrinking core reaction model	19

2.3.3 Grain model	21
2.4 Criteria for selecting sulphur sorption materials	22
2.4.1 Zinc-oxide based sorbent	25
2.4.2 Iron-oxide based sorbent	27
2.5 Sorbent support	28
2.6 Introduction to porous materials	29
2.6.1 Periodic Mesoporous Silica	30
2.6.2 Structural classification	31
2.6.3 Mesoporous SBA-15	32
2.6.4 Mechanism of formation of SBA-15	34
2.7 Metal Oxides in the SBA-15 Pores	37
2.7.1 Synthesis details using impregnation	40
2.7.2 New impregnation technique: The "Two-Solvents" strategy	42
References	44
Chapter 3 Materials, methods, and experimental setup	49
3.1 Experimental Methods	49
3.2 Synthesis of mesoporous SBA-15	49
3.3 Determination of the sulphur loading and the breakthrough curve	51
3.3.1 Desulphurization setup	54
3.3.2 Multicycle Tests and Sorbent Regeneration	56
3.4 Characterization of the sorbents	57
References	60
Chapter 4 Zinc oxide/SBA-15 sorbents	61

4.1	Preparation of ZnO/SBA-15 nanocomposite sorbents	61
4.2	Low- and wide-angle X-ray diffraction characterization	63
4.3	N ₂ physisorption measurements: textural properties	66
4.4	TEM images: morphological characterization	70
4.5	Desulphurization behaviour and post-sorption characterization of the ZnO/SBA-15 sorbents...	72
4.5.1	Desulphurization runs	72
4.5.2	Effect of the synthesis method	73
4.5.3	Effect of the zinc oxide loading	74
4.5.4	Effect of the calcination treatment	75
4.6	Characterization of the sulphided sorbents	78
4.7	Sorbents regeneration and desulphurization-regeneration cycles	80
4.7.1	Temperature-programmed oxidation of the sulphided sorbents	80
4.7.2	Sorption features of the regenerated samples	82
4.8	Conclusions	89
Chapter 5	Iron oxide/SBA-15 sorbents	92
5	Introduction	92
5.1	Preparation of iron oxide/SBA-15 nanocomposite sorbents	93
5.2	Desulphurization activity of fresh sorbents	94
5.3	Characterization of the fresh sorbents	96
5.3.1	Low- and wide-angle X-ray diffraction characterization	96
5.3.2	N ₂ physisorption measurements: textural properties	98
5.3.3	TEM images: morphological characterization	100
5.3.4	FT-IR and XPS characterization	103
5.4	Characterization of the sulphided sorbents	105
5.5	Sorbents regeneration and desulphurization-regeneration cycles	114

5.5.1	Temperature-programmed oxidation of the sulphided sorbents	114
5.5.2	Sorption features of the regenerated samples	118
5.6	Insight of the sulphidation-regeneration mechanism	123
5.7	Conclusions	124
References	126
Chapter 6	Zinc ferrite/SBA-15 sorbents	128
6	Introduction	128
6.1	Preparation of Zinc ferrite/SBA-15 nanocomposite sorbents	128
6.2	Desulphurization activity of fresh sorbents	132
6.3	Characterization of the fresh sorbents	134
6.3.1	Low- and wide-angle X-ray diffraction characterization	134
6.3.2	N ₂ physisorption measurements: textural properties	136
6.3.3	TEM images: morphological characterization	139
6.3.4	FT-IR characterization	141
6.4	Characterization of the sulphided sorbents	142
6.5	Sorbents regeneration and desulphurization-regeneration cycles	148
6.5.1	Temperature-programmed oxidation of the sulphided sorbents	148
6.5.2	Sorption features of the regenerated samples	152
6.6	Insight of the sulphidation-regeneration mechanism	159
6.7	Conclusions	160
References	162
Chapter 7	Assessment of mid-temperature sorbent desulphurization technology in Puertollano IGCC process	164

7	Introduction	164
7.1	ELCOGAS: Puertollano IGCC power plant	165
7.2	Overall description of the Puertollano IGCC Plant	166
7.2.1	IGCC power plant with CGD system	166
7.3	Basis of design of a sorbent desulphurization unit in Puertollano IGCC Plant	172
7.4	IGCC power plant with HGD system	174
7.4.1	Possible <i>HGD&R</i> unit configurations	174
7.5	Different integration alternatives of a unit based on solid sorbents technology in IGCC Puertollano process	175
7.6	Discussion	178
7.7	Impact on the different IGCC systems	179
7.7.1	Advantages and disadvantages with the use of different alternatives	179
	References	183

Chapter 8 Mass and Energy balance with the mid-temperature H₂S removal in Puertollano IGCC power plant

8	Introduction	184
8.1	Hot Gas Desulphurization and Regeneration "HGD&R" unit proposed	184
8.1.1	Fluidized Desulphurizer	185
8.1.2	Flow diagram for the proposed HGD&R unit	187
8.2	Specifications of the gas streams used in the mass and energy balance	189
8.3	Material Balance Calculation	190
8.3.1	Mass balance in the Desulphurizer	192
8.3.2	Mass balance in the Regenerator	194
8.4	Energy balance calculations	197

8.4.1	Energy balance in the Desulphurizer	199
8.4.2	Energy balance in the Regenerator	199
8.4.3	Global final heat required or necessary in the Desulphurizer and Regenerator reactors.....	200
8.4.4	Recoverable or provided energy in the heat exchangers of the HGD&R unit	201
8.5	Cold and hot gas efficiency (CGE and HGE)	204
8.6	Thermal Efficiency comparison with the conventional "MDEA-Solvent" method	204
8.6.1	Thermal efficiency in the Solvent-MDEA desulphurization	206
8.6.2	Thermal efficiency in the ZnO-Sorbent desulphurization	207
8.7	General impact of the use of oxygen, air and steam on the different plant sections	209
8.7.1	Impact of the use of oxygen, air and steam on the Claus unit	210
8.8	Impact of ZnO-Sorbent technology in the Puertollano IGCC efficiency	211
8.8.1	Different impacts of the ZnO-Sorbent technology on the Combined Cycle efficiency	212
8.8.2	Impact of the clean syngas in the outlet of the Desulphurizer	212
8.8.3	Impact of the new oxygen amount required in the Regenerator	214
8.8.4	Impact originated from the steam balance in the <i>HGD&R</i> unit	215
8.9	Simulation tests with the Thermo-economic DiaGnosis System "TDG" software	216
8.9.1	Low pressure Steam turbine Power determination	220
8.10	Comparison with the Siemens MC15.100 reference data	221
8.11	Conclusions and future R&D overview	223
	References	227
	Overall Summary and Conclusions	228
	Recommendations and future works	231
	Nomenclature	232
	List of publications	234

List of Figures

Chapter 1

Figure 1. World market energy consumption from different fuel sources (quadrillion Btu per year)	1
Figure 2. Ultimate recoverable fossil fuel reserves in the world	2
Figure 3. Integrated Gasification Combined Cycle system	6

Chapter 2

Figure 1. Important factors for regenerative high temperature desulphurization with solid sorbents	17
Figure 2. Mechanism of surface reaction of H_2S with metal oxide (Me)	18
Figure 3. Schematic diagram for unreacted shrinking core model	20
Figure 4. Schematic diagram for a grain model (dark parts of the grains represent the product layer) ...	21
Figure 5. Desulphurization potential of candidate solids	22
Figure 6. Stable solid phases of candidate solids	23
Figure 7. Equilibrium H_2S concentration (ppmv) using HSC software	26
Figure 8. Background on commercial ZnO sorbent based on literature search	26
Figure 9. Equilibrium H_2S concentration (ppmv) using HSC software	27
Figure 10. Examples of structural geometries of mesoporous silica structures: MCM-41 (a) , MCM-48 (b) and MCM-50 (c)	32
Figure 11. TEM images of mesostructured SBA-15	33
Figure 12. Proposed silanol groups at the silica surface: (a) isolated silanols, (b) geminal silanols, and (c) hydrogen-bonded silanols	33
Figure 13. Formation process of the mesoporous materials by the true liquid crystalline template mechanism (a) and the cooperative liquid crystalline template mechanism (b)	35
Figure 14. Schematic drawing of a micelle formed by Pluronic block copolymers	36
Figure 15. Schematic representation of the impregnation technique	40

Chapter 3

Figure 1. Equipment setup of SBA-15 preparation	50
Figure 2. Evolution of the SBA-15 preparation before (left), during (centre), and after (right) the addition of tetra ethyl ortho silicate	51
Figure 3. Profile of gas phase H ₂ S concentration in the adsorbent bed from the breakthrough point, t _b , to the complete saturation point t _s	52
Figure 4. Profile of gas phase H ₂ S concentration in the adsorbent bed: development and progression of a transition zone along the bed: transition zones at different times t ₁ , t ₂ , and t ₃	52
Figure 5. Scale-laboratory pilot plant for the desulphurization tests	55
Figure 6. Schematic diagram of experimental setup: 1) Helium tank; 2) Air tank; 3) H ₂ S tank; 4) mass flow controllers; 5) gases mixer; 6) furnace; 7) thermocouple; 8) temperature controller; 9) fixed-bed reactor	55

Chapter 4

Figure 1. Graphical representation of the Incipient Wetness Impregnation technique	62
Figure 2. Graphical representation of the Two-solvents technique	63
Figure 3. Fresh ZnO/SBA-15 sorbent	63
Figure 4. XRD patterns of bare SBA-15 and ZnO/SBA-15 fresh sorbents treated at 500 °C at low angle (a) and wide angle (b)	64
Figure 5. Scheme of hexagonal packed channels with relationship between diffraction planes (blue lines) with associate distance (d) and centre-to-centre distance (a)	65
Figure 6. Nitrogen adsorption-desorption isotherms (a) and pore size distribution (b) of the bare SBA-15 and IWI_T500 fresh sorbents (empty circles bare SBA-15, empty triangles IWI_10, full triangles IWI_30, full rhombs IWI_60)	67

Figure 7. Nitrogen adsorption-desorption isotherms (a) and pore size distribution (b) of the bare SBA-15 and TS_T500 fresh sorbents (empty circles bare SBA-15, empty squares TS_10, full squares TS_30)	67
Figure 8. Surface area and pore volume (inset) versus ZnO loading for the IWI- and TS-sorbents treated at 500 °C (a) and at 500 °C + 600 °C (b) (full triangles IWI-series, full squares TS-series)	69
Figure 9. TEM images of mesostructured SBA-15 (a,b) and ZnO/SBA-15 sorbents prepared via conventional Incipient Wetness Impregnation (c,d,e) and Two-Solvents routes (f,g,h)	71
Figure 10. H ₂ S breakthrough curves of ZnO/SBA-15 sorbents at 10 wt.% (a) and 30 wt.% (b) prepared through IWI and TS methods	73
Figure 11. H ₂ S breakthrough curves of ZnO/SBA-15 sorbents at 10, 30 and 60 wt.% prepared through IWI (a) and TS (b) methods	74
Figure 12. H ₂ S breakthrough curves of ZnO/SBA-15 nanocomposites at temperature of 500 and 600 °C prepared through IWI (a) and TS (b) methods	75
Figure 13. Sulphur retention capacity of the ZnO/SBA-15 sorbents versus S _{BET} surface area (a) and V _p pore volume (b)	77
Figure 14. Low-angle XRD patterns of IWI_T500 (a) and TS_T500 (b) samples series before (F) and after sulphidation (S)	78
Figure 15. Wide-angle XRD patterns of fresh (F) and sulphided (S) ZnO/SBA-15 samples, IWI-series (a) and TS-series (b). The data refer to the sorbents originated by the one-step calcination at 500 °C	79
Figure 16. HRTEM images of the sulphided IWI_30_T500 sorbent	80
Figure 17. TPO profile of the IWI_30_T500 regenerated at 700 °C for 3 hours (a, solid line), 500 °C for 4 hours (a, dotted line) and regenerated through a two step (500 and 700 °C) treatment (b)	81
Figure 18. TPO profiles of the Katalco _{JM} 32-5 _{JM} commercial sorbent at 500 and 700 °C	82
Figure 19. H ₂ S breakthrough curves upon three sorption-regeneration cycles for IWI_30_T500 (a) and TS_30_T500 (b)	83
Figure 20. Low-angle XRD patterns of fresh (F), sulphided (S), regenerated (R) IWI_30_T500 (a) and TS_30_T500 (b) sorbents	86

Figure 21. Nitrogen adsorption-desorption isotherms (a,b) and pore size distribution (inset) of: (a) IWI_30_T500 sorbents (full triangles IWI_30 F, empty triangles IWI_30 R) and (b) TS_30_T500 sorbents (full squares TS_30 F, empty squares TS_30 R)	87
Figure 22. Schematic representation of the sulphurization and regeneration process for ZnO/SBA-15 sorbents	88
Figure 23. Dark Field TEM images of fresh (a), sulphided (b) and regenerated (c) IWI_30_T500 sorbent	89

Chapter 5

Figure 1. Fresh $\text{Fe}_2\text{O}_3/\text{SBA-15}$ sorbent	94
Figure 2. H_2S breakthrough curves of the ZnO commercial sorbent (Katalco _{JM} _F), Zn_F and Fe_F supported sorbent at the first sulphidation run	95
Figure 3. XRD patterns of bare SBA-15, zinc oxide- and iron oxide-based fresh sorbents at low-angle (a) and wide-angle (b). The main reflection planes are marked	97
Figure 4. Nitrogen adsorption-desorption isotherms (a) and pore size distribution (b) of bare SBA-15, zinc oxide- and iron oxide-based sorbents in the fresh state (full circles bare SBA-15, empty circles Zn_F, full squares Fe_F)	98
Figure 5. Representative TEM images of: bare SBA-15 viewed along (a) and perpendicular (b) to the axis of the hexagonal arranged mesopores; Zn_F (c and d); Fe_F (e and f)	101
Figure 6. FTIR spectra of bare SBA-15, zinc oxide- and iron oxide-based fresh sorbents	105
Figure 7. $\text{Zn}2p_{3/2}$ (a) and $\text{Fe}2p_{3/2}$ (b) XPS spectra of fresh and sulphided sorbents	105
Figure 8. XRD patterns of bare SBA-15, zinc oxide- and iron oxide-based sorbents in the fresh and sulphided state at low-angle (a) and wide-angle (b). The main reflection planes are marked	106
Figure 9. Nitrogen adsorption-desorption isotherms (a) and pore size distribution (b) of zinc oxide- and iron oxide-based sorbents in the sulphided state (empty circles Zn_S, full squares Fe_S)	107
Figure 10. Representative TEM images of the sulphided Zn_S sorbent	109
Figure 11. Representative TEM images of the sulphided Fe_S sorbent	110

Figure 12. FTIR spectra of bare SBA-15, zinc oxide- and iron oxide-based sorbents in the fresh (F) and sulphided state (S)	111
Figure 13. Zn _{2p_{3/2}} (a) and Fe _{2p_{3/2}} (b) XPS spectra of fresh and sulphided sorbents. (c) S _{2p} XPS signals of Fe_S and Zn_S sorbents	112
Figure 14. Graphical representation of the reaction process in the zinc oxide/SBA-15 nanosorbent	113
Figure 15. Graphical representation of the reaction process in the iron oxide/SBA-15 nanosorbent	114
Figure 16. TCD profiles of the Fe_S (a), Zn_S (b), and Katalco _{JM} _S (c) sulphided sorbents, regenerated through a two-step (500 and 700 °C) treatment	115
Figure 17. TPO profile and SO ₂ and O ₂ quadrupole mass spectrometer (QMS) signals of the Fe_S sulphided sorbent regenerated at 500 °C	117
Figure 18. TPO profile and SO ₂ and O ₂ quadrupole mass spectrometer (QMS) signals of the Zn_S sulphided sorbent regenerated at 500 °C	118
Figure 19. H ₂ S breakthrough curves upon three sorption-regeneration cycles (S1, S2, S3) for the zinc oxide-based sorbent (a) and iron oxide-based sorbent (b)	119
Figure 20. Wide-angle XRD patterns of the zinc oxide- and iron oxide-based sorbents in the regenerated (R) state compared with the fresh (F) and sulphided (S) ones. The main reflection planes are marked ...	121
Figure 21. FTIR spectra of the zinc oxide- and iron oxide-based sorbents in the regenerated (R) state compared with the fresh (F) and sulphided (S) ones	122
Figure 22. XRD patterns of the fresh (γ-Fe_F), sulphided (γ-Fe_S) and regenerated (γ-Fe_R) pure nanostructured maghemite sample (γ-Fe ₂ O ₃ , Aldrich commercial product)	124

Chapter 6

Figure 1. Fresh ZnFe ₂ O ₄ /SBA-15 sorbents through two-solvents- (top) and self-combustion-impregnation (bottom)	131
Figure 2. Graphical representation of the innovative impregnation via “Self-Combustion” approach	132

Figure 3. H ₂ S breakthrough curves of the ZnO commercial sorbent (Katalco _{JM} _F), ZF_TS_F and ZF_SC_F supported sorbent at the first sulphidation run	133
Figure 4. XRD patterns of bare SBA-15, ZF_TS_F and ZF_SC_F zinc ferrite sorbents synthesized through the two-solvents and self-combustion route at low-angle (a) and wide-angle (b). The main reflection planes are marked	135
Figure 5. Nitrogen adsorption-desorption isotherms (a) and pore size distribution (b) of bare SBA-15 and zinc ferrite-based sorbents in the fresh state (full circles bare SBA-15, empty triangles ZF_TS_F, empty squares ZF_SC_F)	137
Figure 6. Representative TEM images of ZF_TS_F (a and b) and ZF_SC_F (c and d)	140
Figure 7. FTIR spectra of bare SBA-15, zinc ferrite-based sorbents in the fresh state (ZF_TS_F and ZF_SC_F)	142
Figure 8. XRD patterns of bare SBA-15, ZF_TS and ZF_SC sorbents before (F) and after sulphidation (S) at low-angle (a) and wide-angle (b). The main reflection planes are marked	143
Figure 9. Nitrogen adsorption-desorption isotherms (a) and pore size distribution (b) of zinc ferrite-based sorbents in the sulphided state (empty triangles ZF_TS_S, empty squares ZF_SC_S)	144
Figure 10. Representative TEM images of ZF_TS_S (a and b) and ZF_SC_S (c and d)	147
Figure 11. FTIR spectra of bare SBA-15, ZF_TS and ZF_SC in the fresh (F) and sulphided state (S)	148
Figure 12. TCD profiles of the ZF_TS_S (a), ZF_SC_S (b) sulphided sorbents regenerated at 500 °C, and Katalco _{JM} _S (c) sulphided sorbents, regenerated through a two-step (500 and 700 °C) treatment	150
Figure 13. TPD profile and SO ₂ and O ₂ quadrupole mass spectrometer (QMS) signals of the ZF_TS_S (a) and ZF_SC_S (b) sulphided sorbent regenerated at 500 °C	151
Figure 14. H ₂ S breakthrough curves upon four sorption-regeneration cycles (S1, S2, S3, S4) for the zinc ferrite-based sorbents, ZF_TS (a) and ZF_SC (b)	152
Figure 15. Nitrogen adsorption-desorption isotherms (a) and pore size distribution (b) of zinc ferrite-based sorbents in the regenerated state (empty triangles ZF_TS_R, empty squares ZF_SC_R)	155

Figure 16. XRD patterns of bare SBA-15, ZF_TS and ZF_SC sorbents before (F), after sulphidation (S), and after regeneration (R) at low-angle (a) and wide-angle (b). The main reflection planes are marked	157
Figure 17. FTIR spectra of the ZF_TS and ZF_SC sorbents in the regenerated (R) state compared with the fresh (F) and sulphided (S) ones	158
Figure 18. XRD pattern of the sulphided pure nanostructured zinc ferrite sample	159

Chapter 7

Figure 1. Elcogas IGCC power plant	166
Figure 2. General diagram of the gasification and CGD gas cleaning system	167
Figure 3. Simplified layout of the hot gas desulphurization and regeneration process in a fixed-bed reactor configuration	175
Figure 4. Schematic layout of the HGD&R solid sorbents unit at mid temperature (Layout 1)	177
Figure 5. Schematic layout of the HGD&R solid sorbents unit at mid temperature (Layout 2)	178

Chapter 8

Figure 1. Coupled circulating fluidized bed reactors	187
Figure 2. Simplified flow diagram of the HGD&R process	188
Figure 3. Simplified box for mass balance	190
Figure 4. Gas and solid streams flow diagram	193
Figure 5. Flow diagram of the HGD&R unit with heat exchangers identification	202
Figure 6. Schematic block diagram of the MDEA-Solvent considered in the thermal efficiency calculation	205
Figure 7. Schematic block diagram of the ZnO-Sorbent considered in the thermal efficiency calculation	205
Figure 8. Example of gas turbine TDG performance results in the case of ZnO-Sorbent technology	217
Figure 9. Example of steam turbine TDG performance results in the case of ZnO-Sorbent technology	218

List of Tables

Chapter 4

Table 1. d-spacing and unit cell parameter of the fresh nanocomposite sorbents	65
Table 2. Breakthrough time (B_t) and H_2S Sulphur Retention Capacity of the IWI- and TS- sorbents series resulting from one-step (500 °C) and two-step (500 °C + 600 °C) calcination for sorption runs at 300 °C. Data obtained on the commercial Katalco _{JM} 32-5 sorbent are also reported for comparison	76
Table 3. Breakthrough time (B_t) and Sulphur Retention Capacity of the fresh and regenerated IWI_30_T500 and TS_30_T500 sorbents during sorption-regeneration cycles. Data for the commercial Katalco _{JM} 32-5 sorbent are also reported for comparison	84

Chapter 5

Table 1. Breakthrough time (B_t) and Sulphur Retention Capacity (SRC) of fresh zinc oxide- and iron oxide-based sorbents. Data for the ZnO commercial sorbent (Katalco _{JM} 32-5) are also reported for comparison	96
Table 2. N_2 physisorption data of fresh zinc oxide- and iron oxide-based sorbents compared with the bare SBA-15 and the ZnO commercial sorbent (Katalco _{JM} 32-5). The thickness of the pore walls (T_w) is also reported	99
Table 3. N_2 physisorption data of fresh, sulphided and regenerated zinc oxide- and iron oxide-based sorbents compared with the bare SBA-15 and the ZnO commercial sorbent (Katalco _{JM} 32-5). The thickness of the pore walls (T_w) is also reported	108
Table 4. Breakthrough time (B_t) and Sulphur Retention Capacity (SRC) of fresh and regenerated zinc oxide- and iron oxide-based sorbents during sorption-regeneration cycles. Data for the commercial Katalco _{JM} 32-5 sorbent are also reported for comparison	120

Chapter 6

Table 1. Breakthrough time (B_t) and Sulphur Retention Capacity (SRC) of fresh zinc ferrite-based sorbents. Data for the ZnO commercial sorbent (Katalco _{JM} 32-5) are also reported for comparison	133
Table 2. N ₂ physisorption data of fresh ZF_TS_F and ZF_SC_F zinc ferrite sorbents compared with the bare SBA-15 and the ZnO commercial sorbent (Katalco _{JM} 32-5). The thickness of the pore walls (T_w) is also reported	138
Table 3. N ₂ physisorption data of fresh, sulphided and regenerated zinc ferrite-based sorbents (ZF_TS and ZF_SC) compared with the bare SBA-15 and the ZnO commercial sorbent (Katalco _{JM} 32-5). The thickness of the pore walls (T_w) is also reported	145
Table 4. Breakthrough time (B_t) and Sulphur Retention Capacity (SRC) of fresh and regenerated zinc ferrite-based sorbents during sorption-regeneration cycles. Data for the commercial Katalco _{JM} 32-5 sorbent are also reported for comparison	154

Chapter 7

Table 1. Raw coal and petroleum coke analyses	169
Table 2. Gasifier design data	170
Table 3. Design data for the CGD unit	170
Table 4. Resulting properties of the clean gas sent to the Combined Cycle	171
Table 5. Properties of clean syngas upon entering the Gas Turbine	171

Chapter 8

Table 1. Characteristics of the raw gas after the wet scrubbing system	189
Table 2. Composition and mass balance in the desulphurizer of selected streams of Figure 4	194
Table 3. Composition and mass balance in the regenerator of selected streams of Figure 4	197
Table 4. Total energy balance in different regeneration conditions	200

Table 5. Energy required to heat up the raw gas and the different oxidation gases at the working temperature	201
Table 6. Mass flow of HP and LP steam in the heat exchangers of the HGDR unit	203
Table 7. Energy streams data in the HGDR unit	203
Table 8. Cold and hot gas efficiency in MDEA-Solvent and ZnO-Sorbent technology	204
Table 9. Comparison data between MDEA-Solvent and ZnO-Sorbent technology	207
Table 10. Different off-gas in outlet from the regenerator	210
Table 11. Characteristics of the clean gas after the HGDR unit in comparison with the reference data (MC15.100)	213
Table 12. Impact of the new oxygen demand in the combined cycle and ASU unit	215
Table 13. Mass flow of HP-, IP-, LP-steam streams	215
Table 14. Different parameters introduced in the TDG software for the simulation (2.5% Water)	219
Table 15. Performance results in different sections of the plant (2.5% Water)	220
Table 16. Performance results comparison between ZnO-Sorbents and MC15.100 Reference Case	220

1 Introduction

1.1 Energy outlook & Motivations

Primary energy demand in the world continues to increase with the increase in population and economic development. In the Annual Energy Outlook 2014 prepared by U.S. Energy Information Administration, total energy consumption will increase by ~60% by the end of 2040 (98 to 162 quadrillion Btu)^[1]. Liquid, primarily fossil, fuels remain the world's largest source of energy (>30%, Figure 1). However, due to limited fossil resources but increasing fuel demand, oil prices will continue to grow, and renewable energy must eventually be exploited to replace traditional fossil fuels. Moreover, nowadays strict environmental regulations are driving forces to seek efficient and "zero-emission" energy production.

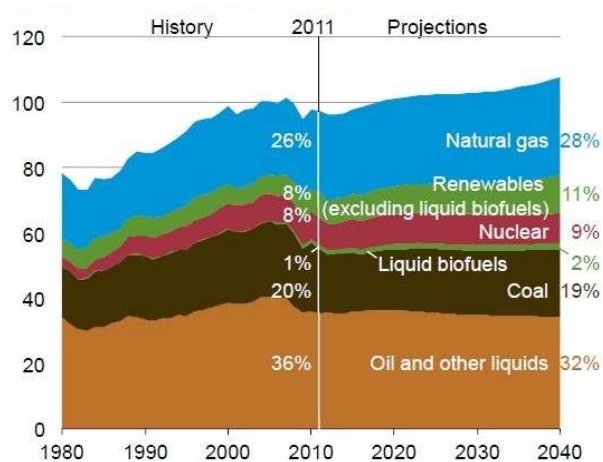


Figure 1. World market energy consumption from different fuel sources (quadrillion Btu per year)^[1].

Presently, only about 15 % of the world energy use is from renewable sources. Producing energy in a clean and responsible manner can be accomplished in a number of ways. The use of non-fossil fuel energy sources such as solar, wind, and nuclear power will eventually replace fossil fuels. However, many of these technologies will require many years before they are able to provide the amount of energy needed. In the immediate future, fossil fuel-based energy production will continue, and new technologies need to be developed in order to produce clean fuels to supply power our societies.

The non-renewable energy sources include all potentially recoverable coal, conventional oil and natural gas, unconventional oil resources (*e.g.*, oil shale, tar sands and heavy crude) and unconventional natural gas resources (*e.g.*, gas in pressurized aquifers and coal seams). Among the non-renewable energy sources, as seen in [Figure 2](#), coal reserves have the highest share in recoverable fossil fuel reserves ^[2]. Thus, coal seems to have the highest potential as an energy source within the next decades.

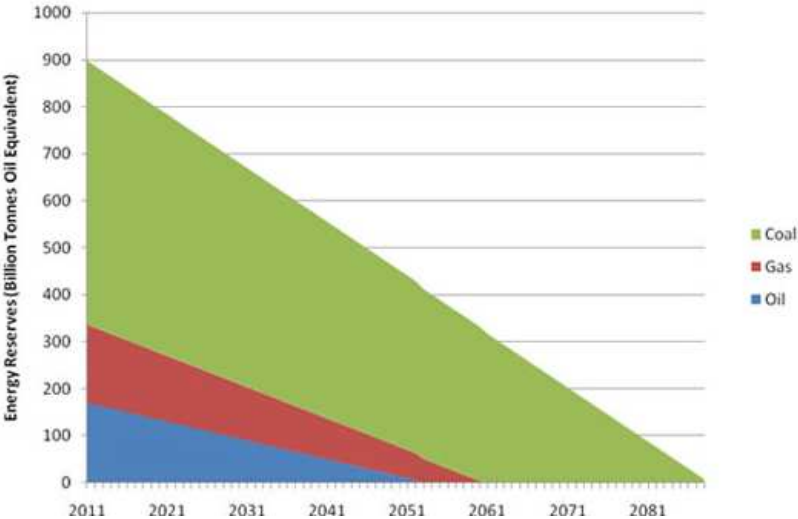


Figure 2. *Ultimate recoverable fossil fuel reserves in the world.*

Currently, the need to release energy production from the use of oil and natural gas as primary energy sources and, in general, to diversify such sources in order to assure the supplying, is making coal more interesting. This fuel, widely available in the world and distributed more uniformly compared to the other non-fossil fuels, allows a great price stability and represents a secure source from a strategic point of view ^[3]. Furthermore, the increasing interest in environmental problems has recently led to the development of *clean coal technologies*, designed to enhance both the efficiency and environmental acceptability of coal extraction, preparation and use, in particular for power generation. The recently released DOE Vision 21 program anticipates much more stringent control of hazardous material in coal-derived synthesis gas. Therefore, utility companies world-wide must adopt new plans for the future associated with those new regulations. As milestones for preparing new technology, "efficiency", "environmentally sound", and "low cost" are rising as new parameters. Improved technologies may provide cost-effective ways to reduce emissions from coal-fired power plants. Even a one percent improvement in the thermal efficiency of a coal-fired power plant is significant. Therefore, research and demonstration of advanced coal-fired electric power generation systems are being funded all over the world.

Among clean coal technologies, gasification is particularly interesting since it allows both power generation (in Integrated Gasification Combined Cycles power plants, IGCC) and environmental-friendly fuel production, with a particular reference to hydrogen ^[4]. All over the world, gasification processes, due to the low flexibility of synthesis gas (syngas) production, are, so far, mainly used in large-scale IGCC power plants in order to supply base energy load. But in a short-term future, the possibility to use syngas to produce hydrogen could make gasification technologies very interesting for medium- and small-scale industrial application. When coal is gasified, the reaction environment is reducing, as opposed to the oxidizing environment in coal combustion. Consequently, sulphur in coal (in form of organic sulphur compounds and inorganic pyrites) is converted primarily to hydrogen sulphide (H₂S) gas, with low quantities of carbonyl sulphide (COS). Usually, these sulphur compounds need to be removed from the syngas.

1.2 Focus of the research

The thesis discusses the removal of H_2S from the syngas derived from coal gasification, but more extensively from other industrial feed stocks which is a very important task. The goal of this research is focused on the development of efficient $MeO_x/SBA-15$ -based sorbents ($Me = Zn, Fe$) for H_2S removal in view of possible applications in hydrogen purification, deep desulphurization of fossil fuels for fuel cells, and air pollution control.

The following tasks were considered to achieve the research objectives:

- ✚ Study of a simple and versatile route which can be proposed to prepare a great variety of $MeO_x/SBA-15$ nanocomposites where the active phase, MeO_x , formed inside the mesochannels, can reach the maximum size of 6-7 nm physically imposed by the pore diameter. The proposed impregnation method is easily reproducible and easy to scale up.
- ✚ Study of the enhanced desulphurization performance compared with the commercial sorbent.
- ✚ Understanding how the active phase nature influence their performance.
- ✚ Study of the different interactions between the Me^{n+} and the silanols groups at the surface of the SBA-15.
- ✚ Evaluating the regeneration of the synthesized nanocomposites.
- ✚ Understanding of the sorption-desorption behaviour, which is commonly justified only on the basis of the different nature of the active phase and of the textural features.
- ✚ Assessment of mid-temperature sorbent desulphurization technology in the existing IGCC power plant of Puertollano (**ELCOGAS S.A.**) with the proposal of different layout plant configurations and the conceptual integration of a unit based on this technology in the Puertollano IGCC process.

In the literature, to our best knowledge, no one have reported similar correlations between sorption-desorption behaviour and microstructure of the sorbent. For this reason we believe that this research can give an important contribution to improve the basic knowledge in the field of sorbents for gas-removal. Moreover, only in very few cases, a similar scale up assessment study of this kind of technology has been carried out (the most important example is in the Polk IGCC plant, Tampa Electric).

1.3 Literature review & Theoretical background

1.3.1 Integrated Gasification Combined Cycle Systems (IGCC)

In IGCC systems, coal or other fossil fuel is fed to a gasifier at elevated pressure, where it reacts with oxygen or air and steam, to produce a raw fuel gas (generally named *synthesis gas* or *syngas*). This raw gas is cleaned to remove particulate materials and other gaseous pollutants before being fired in a gas turbine (GT). Hot gas from the gas turbine exhaust is passed through a waste heat recovery system and the steam produced is used to drive a conventional steam turbine (ST). Hence, electricity is produced from both the gas and steam turbines ^[5]. A typical IGCC block diagram is shown in [Figure 3](#). During gasification, coal containing carbon, hydrogen, oxygen, as well as impurities such as sulphur, nitrogen, ash and trace metals, reacts with steam and either air or oxygen to produce a fuel gas. The fuel gas consists of mainly CO, CO₂, H₂, CH₄, N₂ and H₂S. This mixture of CO, CH₄ and H₂ produced through gasification is burned after a gas clean up unit and the clean syngas is routed through a GT to generate electricity.

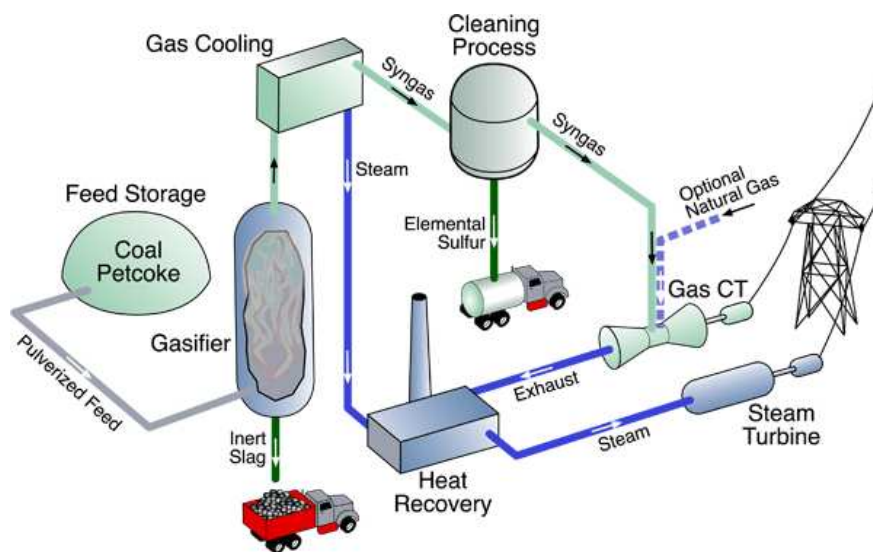


Figure 3. *Integrated Gasification Combined Cycle system.*

(http://thefraserdomain.typepad.com/energy/images/igcc_flow_diagram.gif)

Afterwards, the residual heat in the exhaust gas is used to boil water for a conventional steam turbine generator via a heat recovery steam generator thus producing more electricity. In a coal gasifier, unlike coal combustion processes, the sulphur in the coal is released in the form of hydrogen sulphide, H_2S , rather than sulphur dioxide, SO_2 . The IGCC process should employ hot gas clean up techniques to remove sulphur and other impurities in the syngas stream, principally to meet the stringent governmental regulations for sulphur emission and also to protect turbine components and in general plant equipments, from the corrosive action of H_2S . Typical gasifier exhaust contains about 5000 – 15000 ppmv H_2S whereas a sulphur concentration limitations of approximately 150 ppmv for IGCC system effluents has been established. Therefore, a desulphurization system capable of reducing H_2S concentration from about 5000 – 15000 ppmv to 150 ppmv or lower is required^[6]. There are a number of reasons that sulphur needs to be removed. 1) Hydrogen sulphide and other sulphur compounds can cause pipeline corrosion and thus limit plant lifetime^[7]. 2) Sulphur in fuel is a precursor to SO_2 that will

be released into the atmosphere, resulting in downstream environmental problems. 3) Hydrogen sulphide is a well-known catalysts poison.

Information on the effect of sulphur on tar reforming or steam reforming catalysts in biomass product gas environments is widely available and generally shows significant negative impacts of sulphur on catalyst performance^[7]. Hydrogen sulphide should be removed from the syngas while it is still hot so that the gas can be used directly without losing its heat. This would completely eliminate the conventional low-temperature liquid-based syngas scrubbing system that will be described in the next section. Additionally, since the volume of the syngas is considerably smaller than that of conventional flue gas streams, the removal of H₂S at higher temperature results in considerably lower hardware costs^[8].

1.3.2 Hydrogen sulphide properties

Hydrogen sulphide is a colourless, highly flammable, and extremely toxic gas with a characteristic odour of rotten eggs. The odour threshold for humans is as low as 1 ppm. It is slightly soluble in water (0.4 % w/w at 20 °C) and a H₂S-saturated aqueous solution has a pH = 4.5. Five minutes of exposure to 1000 ppm H₂S in air can be fatal to humans^[9]. If exposed to H₂S, symptoms can include headache, nausea, nervousness, cough, eye irritation, and insomnia. High doses can cause unconsciousness, respiratory paralysis, and death. H₂S in solution is corrosive and therefore damages the equipment in contact. It is poisonous to many industrial catalysts as well.

Motivations

There are many commercial treatment techniques that are used to remove H₂S including adsorption by activated carbon, condensation, chemical oxidation and dry/wet absorption. The disadvantage of these techniques is that hot coal gas, which temperature of syngas produced from coal gasification reaches 500 °C or above^[10], must be cooled down to ambient temperature or around 150 °C for desulphurization and then preheated to high temperature before being fed into gas turbine. In this way the thermal

efficiency of the system is significantly reduced. It is for this reason that high temperature desulphurization technique has attracted more and more attention due to the fact that it can reduce H_2S down to 10 ppm level and avoid heat loss^[10]. Actually, the IGCC has also disadvantages. Heat integration is the main variable that determines thermal efficiency. Increased integration means increased thermal efficiency, but also increased cost and complexity of the process.

1.3.3 Current Acid Gas Removal (AGR)

Currently, the eligible processes in commercial IGCC facilities for the acid gas removal are both the chemical solvent AGR processes based on aqueous methyldiethanolamine (MDEA) and the physical solvent-based Selexol process which uses mixtures of dimethyl ethers of polyethylene glycol^[11]. In most of the IGCC applications now, with both of these AGR processes, the AGR units are preceded by carbonyl sulphide (COS) hydrolysis units to convert most of the COS to H_2S . This then enables the AGR units to accomplish deeper total sulphur removal and lower H_2S levels. Total sulphur (COS + H_2S) levels of <20 ppmv may be required if selective catalytic reduction (SCR) is to be used with IGCC to prevent ammonium sulphate salt deposition and corrosion problems in the colder sections of the heat recovery steam generator (HRSG). While physical solvent processes are capable of meeting the stringent sulphur cleanup required for SCR, the processes themselves are more expensive than the MDEA-based amine ones. With COS hydrolysis, MDEA-based solvents can also meet a 10-20 ppmv total sulphur level in the treated gas, albeit at the expense of increased solvent circulation rates and a decrease in H_2S selectivity. The use of MDEA-based solvents will require acid gas enrichment (AGE) to give a suitable feed for the Claus plant. Commercial MDEA formulations (with proprietary additives) have been developed, which offer enhanced selectivity for H_2S , and their use is widespread in the gas treating industry. BASF Corporation has shown some success in tests of its newly formulated MDEA solvent that removes much of the COS while retaining a high degree of H_2S selectivity^[12]. However, the performance to date is not adequate for the elimination of the COS hydrolysis step. SFA Pacific believes that if SCR is to be used, COS hydrolysis will

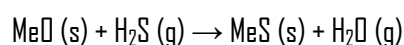
be necessary for any acid gas removal system, except possibly the Rectisol process. Although the Selexol process by itself is more expensive than an MDEA AGR process, the total AGR, sulphur recovery (SR) process, and tail gas treating (TGT) process package based on Selexol could be more cost effective than the package based on MDEA especially if the syngas pressure is high and deep sulphur removal is required. Deeper desulphurization can be accomplished by chilling the Selexol process. However, CO₂ co-absorption then also increases. For future IGCC with CO₂ removal by sequestration, a two-stage Selexol process presently appears to be the preferred AGR process as indicated by ongoing engineering studies at EPRI and various engineering firms with IGCC interests. In CO₂ removal applications, the Selexol process is chilled thus facilitating deep H₂S removal as well as CO₂ removal. The Rectisol physical solvent AGR process based on low-temperature (refrigerated) methanol is capable of deep total sulphur removal, but it is regarded as the most expensive AGR process. Therefore, its use is generally reserved for chemical synthesis gas applications in which very pure syngas is required. Its use in IGCCs with CO₂ removal has also been proposed. Further studies of the main IGCC processes with various feedstocks and all of the potentially competitive AGR options are required to quantify the relative performance and cost benefits of the various options and elucidate the ranges of conditions and cases in which they are competitive ^[13,14]. Related studies are underway at EPRI and various engineering organizations.

1.3.4 Mid-temperature gas desulphurization

A typical AGR process requires the cooling of the syngas approximately to ambient temperature. Hot syngas treatment could eliminate, or at least reduce, the need for syngas cooling; and this could improve the overall thermal efficiency of the process ^[15]. Mid-temperature desulphurization of coal derived fuel gas from the coal gasification unit is considered as one of the most promising advanced technologies to remove the sulphur components from coal ^[16]. This process takes place in a separate unit after the gasifier and utilizes regenerable sorbents, mainly oxides of transition metals ^[17, 18]. They are either pure or mixed oxides that can be deposited on an inert carrier material to increase reactivity and/or

mechanical stability. So far, a large variety of these sorbents have been tested on laboratory-, bench- as well as pilot-scale ^[19,20]. Some authors reviewed mid- to high-temperature solid sulphur sorbents ^[7], and focused on sorbents based on zinc, copper, calcium, manganese, iron, and rare earths oxides ^[21].

Hot gas desulphurization is based on the non-catalytic reaction between a metal oxide and hydrogen sulphide. This reaction is represented generically by the following equation:



The ultimate capability of removing H₂S depends on the thermodynamic properties of the metal oxide.

1.4 General basic principles of “sorbent technology”

A sorbent is usually a solid substance that adsorbs or absorbs another type of substance. It is the sorbent that makes a sorption process a unique and different separation and purification process from others ^[22]. With the rapid development in novel sorbent materials and innovative cyclic adsorption processes, sorption has become a key separation process in many process industries including chemical, petrochemical, environmental, pharmaceutical, and electronic gases ^[23]. In the case of H₂S removal, the sorbents are used as “getter” materials. So, the mechanism in chemical adsorptive separation is the “*gas-solid reaction*” where a solid reacts more or less readily with reactive gas specie with a reaction mechanism dependent both of physical diffusion (external and internal) and chemical reaction (toward the over-all mass transfer rate) ^[24].

References

- [1] U. S. Energy Information Administration, Annual Energy Outlook 2014, **2014**.
- [2] CIA World Factbook.
- [3] U. S. Department of energy, Annual Energy Outlook 2004, available at [www. Eia.doe.gov/oiaf/aeo/](http://www.Eia.doe.gov/oiaf/aeo/), January **2004**.
- [4] A. Pettinau, C. Frau and F. Ferrara, *Fuel Processing Technology*, **2011**, 92, 1946.
- [5] P. W. Sage and S. J. Mills, in *Overview of clean coal technologies and current status of the air blown gasification cycle, desulphurisation of hot coal gas with regenerable metal oxide sorbents: New developments*, NATO ASI Series, Kusadasi, July **1996**.
- [6] B. Slimane and M. T. Hepworth, *Energy Fuels*, **1995**, 9, 372.
- [7] S. Cheah, D. L. Carpenter and K.A. Magrini-Bair, *Energy Fuel*, **2009**, 23, 5291.
- [8] B. Slimane and M.T. Hepworth, *Energy Fuels*, **1994**, 8, 1184.
- [9] P. Patnaik, in *A Comprehensive Guide to the Hazardous Properties of Chemical Substances*, 2nd ed., John Wiley, New York, **1999**, pp. 505-536.
- [10] T. H. Ko, H. Chu and L. K. Chaung, *Chemosphere*, **2005**, 58, 467.
- [11] N. Korens, D. R. Simbeck and D. J. Wilhelm, SFA Pacific Inc. Mountain View California, Final Report prepared for U.S. Department of Energy , National Energy Technology Laboratory, December **2002**.
- [12] G. Vorberg, R. Notz (DASE[®] Gas Treatment Excellence BASF SE, Ludwigshafen/Germany) and K. Sugavanam (DASE[®] Gas Treatment Excellence BASF Corporation, Houston, TX), in *Selective H₂S removal: Case studies by using a new promoter system in amine units*.
- [13] *Phased Construction of Natural Gas Combined Cycle Plants with Coal Gasification and CO₂ Recovery*, a report prepared by SFA Pacific for EPRI, EPRI Interim Report No. 1004233, October **2002**.
- [14] Evaluation of Innovative Fossil Fuel Power Plants with CO₂ Removal, EPRI, Palo Alto, CA, U.S. Department of Energy Office of Fossil Energy, Germantown, MD and U.S. Department of Energy/NETL,

Pittsburgh, PA, 2000. 1000316. Prepared by Parsons Energy and Chemicals Group Inc. and Wolk Integrated Technical Services.

[15] F. Ruggeri, M. Sudiro, I. Papa, A. Gallio, A. Bertucco and M. Fontana, *Energ. Fuel.*, **2011**, 25, 5345.

[16] A. T. Atimtay, *Clean Prod. Proc.*, **2001**, 2, 197.

[17] N. Haimour, R. El-Bishtawi and A. Ail-Wahbi, *Desalination*, **2005**, 181, 145.

[18] K. Kim, S. K. Jeon, C. Vo, C. S. Park and J. M. Norbeck, *Ind. Eng. Chem. Res.*, **2007**, 46, 5848.

[19] J. Abbasian, R. P. Bachtá, J. R. Wangerow, W. Mojtahedi and K. Salo, *Ind. Eng. Chem. Res.*, **1994**, 33, 91.

[20] A. G. J. Van der Ham, A. B. M. Heesink, W. Prins and W. P. M. Van Swaaij, *Ind. Eng. Chem. Res.*, **1996**, 35, 1487.

[21] P. Mondal, G. S. Dang and M.O. Garg, *Fuel Process. Technol.*, **2011**, 92, 1395.

[22] S. Deng, in *Sorbent Technology*, Encyclopedia of Chemical Processing, Ed. by S. Lee, Marcel Dekker, Inc. New York, NY, **2006**, pp. 2825-2845.

[23] R. T. Yang, in *Adsorbents: Fundamentals and Applications*, John Wiley & Sons: Hoboken, NJ, **2003**.

[24] D. Montes, E. Tocuyo, E. González, D. Rodríguez, R. Solano, R. Atencio, M.A. Ramos and A. Moronta, *Micropor. Mesopor. Mat.*, **2013**, 168, 111.

Chapter 2

Sorbent materials

2.1 Sorbent materials

According to King, a mass separating agent is needed to facilitate separation from any separation processes ^[1]. The mass separating agent for adsorption process is the adsorbent, or the sorbent. Therefore, the characteristic of the sorbent directly affects the performance of any adsorptive separation or purification process. The basic definitions of adsorption-related terminologies are given in the following to clarify and standardize these widely used terms in this field.

- ✚ *Adsorption*. The adhesion of molecules (as of gases, solutes, or liquids) to the surfaces of solid bodies or liquids with which they are in contact.
- ✚ *Absorption*. The absorbing of molecules (as of gases, solutes, or liquids) into the solid bodies or liquids with which they are in contact.
- ✚ *Sorption*. Formation from adsorption and absorption.
- ✚ *Adsorbent*. A usually solid substance that adsorbs another substance on its surface.
- ✚ *Sorbent*. A usually solid substance that adsorbs and absorbs another substance.
- ✚ *Adsorbate*. Molecules (as of gases, solutes, or liquids) that are adsorbed on adsorbent surfaces.
- ✚ *Microporous*. Pore size smaller than 20 Å.
- ✚ *Mesoporous*. Pore size in the 20 and 500 Å range.
- ✚ *Macroporous*. Pore size larger than 500 Å.

Adsorptive separation can be achieved through one of the following mechanisms. Understanding the fundamentals of adsorptive separation mechanisms will allow to better design or modify sorbent materials to achieve their best possible separation performance^[2,3].

Adsorption equilibrium effect is due to the difference in the thermodynamic equilibria for each adsorbate/adsorbent interaction. The majority of adsorptive separation and purification processes are based on equilibrium effect.

Adsorption kinetics effect arises from the difference of rates at which different adsorbate molecules move into the internal structure of the adsorbent. There are only a few commercial successes using adsorption kinetic difference to achieve adsorptive separation of gases.

Molecular sieving effect, also called steric effect, is derived from the molecular sieving properties of some adsorbents with a microporous structure. In this case, the pore openings of the adsorbent structure are small enough to exclude large adsorbate molecules from penetrating the micropores of the adsorbent. This is the extreme case of the kinetic effect. There are several commercial applications based on this mechanism in adsorptive separation processes. One typical example is separating normal paraffin from iso-paraffin and aromatics in an adsorption process using a "5A" zeolite as adsorbent. *N*-paraffin, with a long straight chain, has a smaller effective diameter than the well-defined aperture of 5A zeolite.

2.1.1 General characteristics of sorbent materials

Commercial sorbents used in cyclic adsorption processes should ideally meet the following requirements:

- ✚ Large selectivity derived from equilibrium, kinetic, or steric effect;
- ✚ Large adsorption capacity;
- ✚ Fast adsorption kinetics;
- ✚ Easily regenerable;

- ✚ Good mechanical strength;
- ✚ Low cost.

The above adsorbent performance requirements can simply transfer to adsorbent characteristic requirements as follows:

- ✚ Large internal pore volume;
- ✚ Large internal surface area;
- ✚ Controlled surface properties through selected functional groups;
- ✚ Controlled pore size distribution, preferably in micropore range;
- ✚ Weak interactions between adsorbate and adsorbent (mostly on physical sorbents);
- ✚ Inorganic or ceramic materials to enhance chemical and mechanical stability;
- ✚ Low-cost raw materials.
- ✚

These basic requirements are usually proposed for adsorbents used in cyclic adsorption processes that are based on physical adsorption.

2.1.2 New developments in sorbent materials and applications

The past two decades have witnessed major advances in new nanostructured sorbent materials including mesoporous molecular sieves, sol-gel-derived metal oxide xerogels and aerogels, metal organic framework, composite adsorbents, new carbonaceous materials (carbon nanotubes, carbon fibers, superactivated carbons), high-temperature ceramic sorbents, and strong chemical sorbent materials. Although these new sorbent materials have demonstrated promising sorption properties for many existing and new applications, systematic studies on synthesis methods and characterization of these new materials are necessary to fully explore and realize their potential as commercial sorbents.

2.2 Description of the New Hot Gas Desulphurization technology

High- and mid-temperature desulphurization of syngas from the coal gasification is considered as the key technology, which has different benefits. The process offers potential improvements on the thermal efficiency of the systems using coal gasification, such as integrated gasification combined cycle (IGCC) power plants, hydrogen fuelled solid oxide fuel cells (SOFC) and molten carbonate fuel cells (MCFC) technologies. The development of these systems depends on the ability to remove sulphur compounds, mainly H_2S , from the coal gas.

The important factors of hot gas desulphurization sorbent are:

- ✚ The sorbent should have good sulphur removal capacity and fast adsorption kinetics;
- ✚ The sorbent should be chemically stable, *i.e.*, it should not evaporate or sinter during regeneration;
- ✚ The sorbent should be physically stable, *i.e.*, it should withstand any attrition;
- ✚ The sorbent should catalyze formation of elemental sulphur upon reductive regeneration, hydrolyze carbonyl sulphide (COS), and react with other contaminants such as tars;
- ✚ The sorbent should be regenerable and it should maintain its sulphur removal capacity for many cycles;
- ✚ The sorbent replacement cost should be affordable.

Process requirements taken as a basis for determining metal oxides suitability for high-mid-temperature desulphurization:

- ✚ Rate of desulphurization and stability of the sulphide under reducing gas conditions;
- ✚ Potential for detrimental secondary reactions on the solid under reducing coal gases (*e.g.* metal carbides, reduction to zero-oxidation state, formation of chlorides from HCl);
- ✚ Rate of regeneration and production of SO_2 or elemental sulphur under oxidizing gas conditions;

- ✚ Potential for detrimental secondary reactions on the solid under oxidizing gases (e.g. sulphates) and hydrothermal stability during regeneration.

The most important factors to be considered in process design and sorbent selection are schematically given in Figure 1^[4].

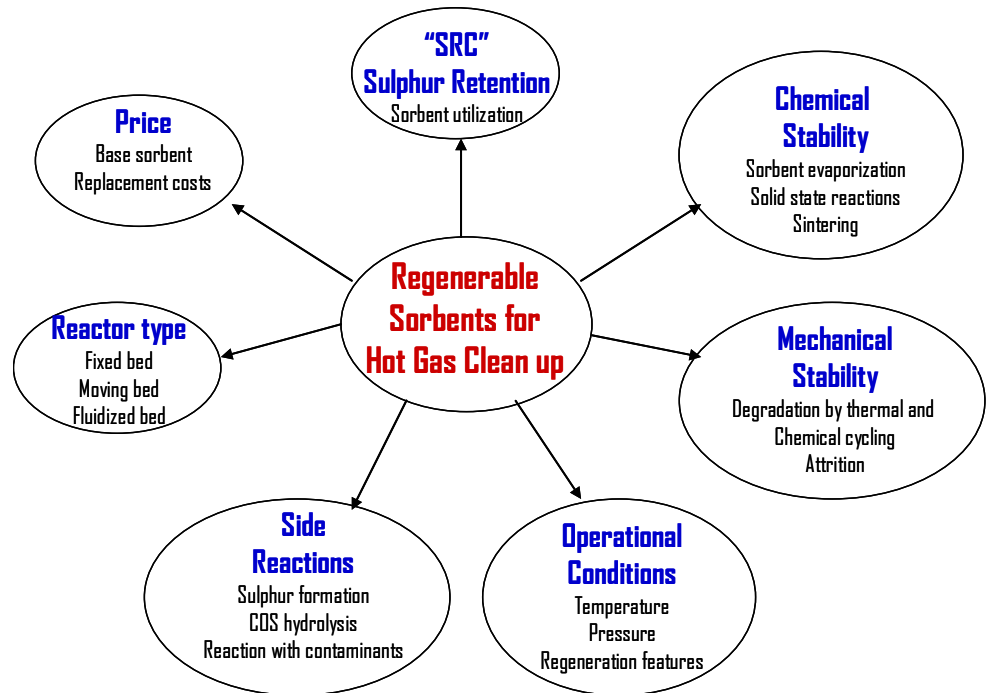
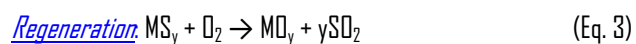
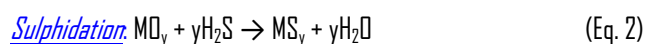
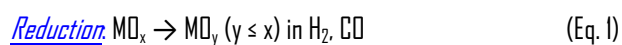


Figure 1. Important factors for regenerative high temperature desulphurization with solid sorbents^[4].

2.3 Reaction mechanism

The chemistry of a complete sulphidation-regeneration cycle may be represented by the overall reactions:



In most cases of heterogeneous reactions between H_2S and metal oxide sorbents are controlled by pore and/or lattice diffusion. In the pore diffusion, the reaction rate is controlled by diffusion rate of H_2S in the pores to the fresh oxide. H_2S molecules mainly interact with the metal sites of the oxides; the interactions of H_2S with oxygen sites of the oxide surfaces are negligible (Figure 2) ^[5].

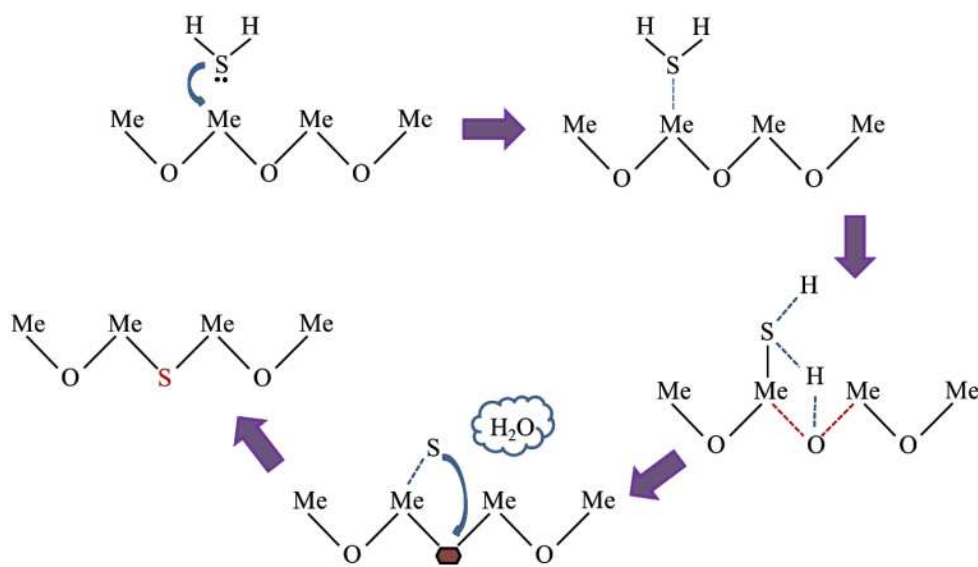


Figure 2. Mechanism of surface reaction of H_2S with metal oxide (Me).

The following steps are represented in the figure above:

1. H_2S is approaching to the surface adsorption site of the metal oxide;
2. The H_2S is chemisorbed onto the surface, followed by the formation of a chemical bonding with a metal cation;
3. One of hydrogen from H_2S is interacting with the surface oxygen atom from metal oxide;
4. Water molecules are formed with the subsequent formation of an oxygen vacant site;

5. Sulphur atom is incorporated in the previously formed oxygen vacant site to form a surface metal sulphide.

The mechanism of H_2S adsorption on an ionic solid has been suggested in previous studies starting with the dissociation of H_2S into H^+ and HS^- , followed by diffusion of HS^- into the oxide lattice and migration of oxide and water to the surface ^[6, 7]. Therefore, the diffusion of S^{2-} and HS^- ions into the metal oxide is required in order to convert MeO to MeS by proton transfers from H_2S to the chemisorbed OH groups on the Me-O surface ^[5]. The overall dissociative H_2S adsorption on MeO can be represented by the above Eq. 2.

2.3.1 Non-catalytic gas-solid reaction models

Non-catalytic gas-solid reactions represent an important category of heterogeneous reactions. A great number of models have been developed to describe the kinetics of gas-solid reactions. Some of them, such as the "*unreacted shrinking core model*" ^[8], do not require specific knowledge of the internal structure of the reacting solid. Other models, such as the "*grain model*" ^[9], require the knowledge of physical parameters characterizing the internal structure of the solid *i.e.*, the specific surface area or the average pore size. In more recent works, some models even include such considerations as pore size distribution, change of porosity during the reaction, and pore plugging in the course of the reaction ^[10, 11]. The models demand more extensive and precise experimental information about the structure of the reacting solid.

2.3.2 Unreacted shrinking core reaction model

The unreacted shrinking core reaction model was developed for the situation when the diffusivity in the core of the pellet is so much lower than that in the reacted layer that virtually no gaseous reactant

can reach the unreacted core, and a distinctive front of reaction exists as shown in Figure 3. The model gives the time necessary to reach a given conversion of the solid:

$$t = \tau_{DP}[1 - 3(1 - X)^{2/3} + 2(1 - X)] + \tau_{MT}[X] + \tau_{R,SC}[1 - (1 - X)^{1/3}]$$

Where τ_{DP} is the characteristic time for diffusion through the pellet's product layer, τ_{MP} the characteristic time for external mass transfer from the bulk gas to the surface of the pellet (film diffusion), and $\tau_{R,SC}$ the characteristic time for chemical reaction at the interface between the unreacted core of the pellet and the reacted product layer, and X is the conversion of the pellet.

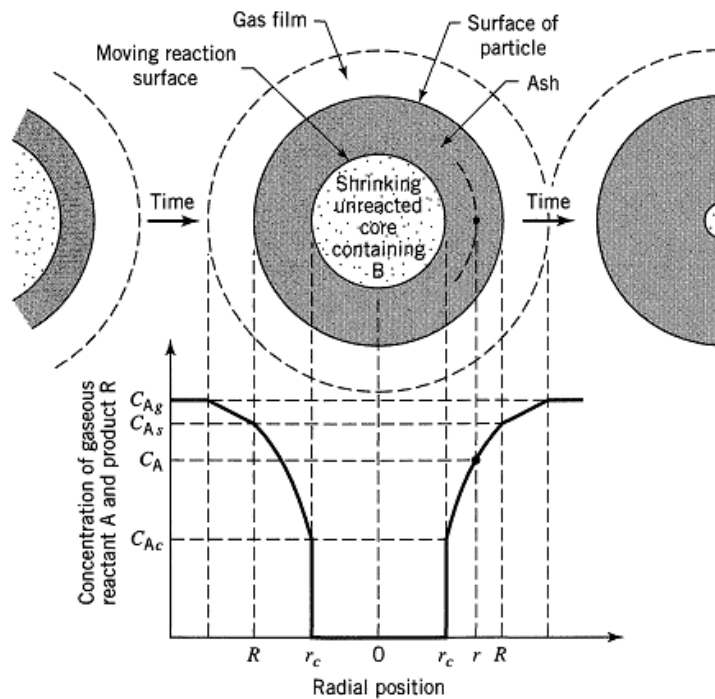


Figure 3. Schematic diagram for unreacted shrinking core model^[8].

2.3.3 Grain model

The grain model assumes that the solid structure consists of a matrix of very small grains, usually spherical in shape. The first grain model was established by who applied the grain model theory by assuming that the shrinking grains of solid reactant are surrounded by a dense layer of solid product with uniform thickness^[12]. Most early grain models assume that the overall grain size remains constant during the course of the reaction. If the diffusivity of the gaseous reactants (or products) in the core of the reacting pellet is not significantly lower than that of the completely (or partially) reacted layer, then the gases have the potential to reach the centre of the pellet even if only a thin outside layer of the pellet is reacted. This is shown in Figure 4. The dark parts of the grains represent the product layer. The relationship between reaction time and conversion is:

$$t = (\tau_{DP} + \tau_{DG})[1 - 3(1 - X)^{2/3} + 2(1 - X)] + \tau_{MT}[X] + \tau_R[1 - (1 - X)^{1/3}]$$

where τ_{DG} is the characteristic time for diffusion through the grain and τ_R is the characteristic time for chemical reaction at the interface between the unreacted core and the reacted layer of the grain. τ_{DP} and τ_{MT} are defined the same as in the unreacted shrinking-core model.

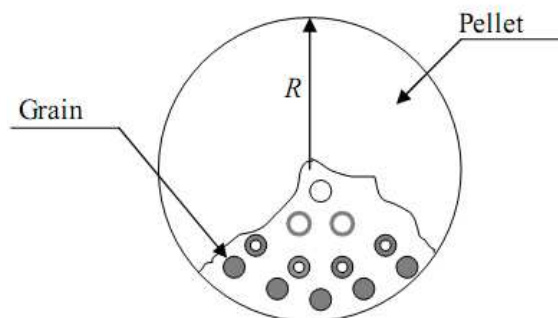


Figure 4. Schematic diagram for a grain model (dark parts of the grains represent the product layer).

2.4 Criteria for selecting sulphur sorption materials

Preliminary to the preparation of metal oxide sorbents under this study, a review of the literature was done to identify pure metal oxides and combinations of metal oxides that had been evaluated in the past for high- and mid-temperature desulphurization of coal gases.

Based on thermodynamic calculations the metal oxides of Fe, Zn, Mn, Mo, V, Ca, Sr, Ba, Co, Cu and W are feasible for hot gas desulphurization^[13]. In the temperature range 300 - 800 °C, desulphurization performance (% of sulphur adsorbed from the gas phase) of some metal oxides decreased in the order $MnO > CaO = ZnO > V_2O_3$. Fractional desulphurization results are summarized in Figure 5. From the latter, it is obvious that manganese, for example, satisfies the 95% desulphurization criterion at all temperatures below 1060 °C. Figure 6 summarizes solid stability results.

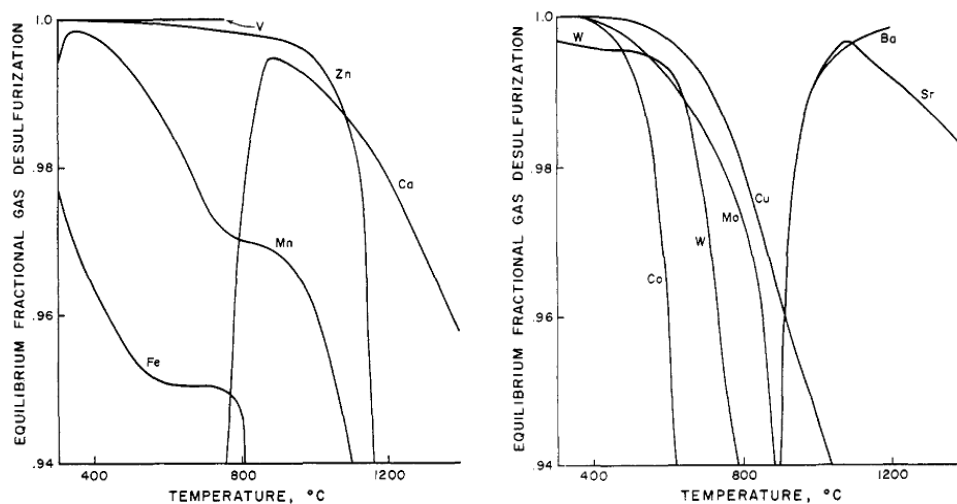


Figure 5. Desulphurization potential of candidate solids^[13].

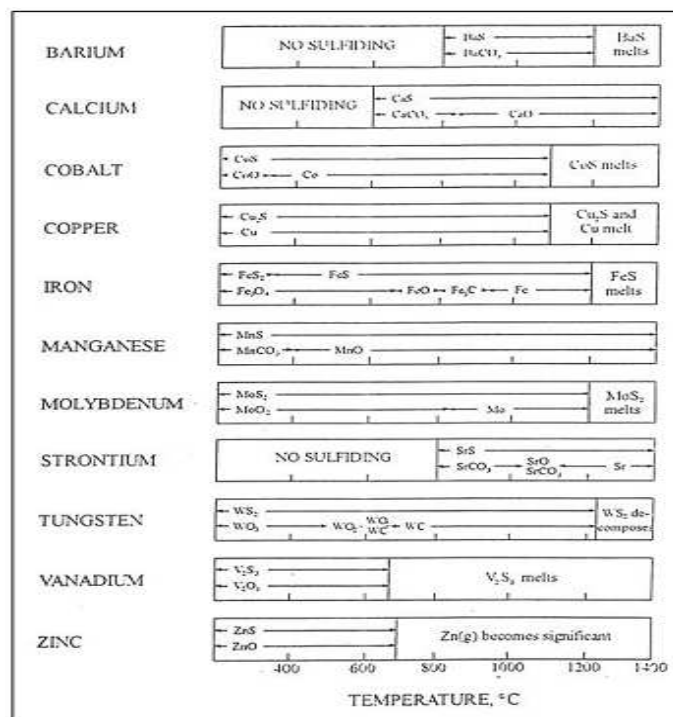


Figure 6. Stable solid phases of candidate solids^[13].

By properly combining information from Figures 5 and 6, the desulphurization potential of several candidates can be established. These results are summarized in the following paragraphs.

Cobalt: Cobalt satisfies desulphurization criterion to a maximum temperature of 600 °C with CoS the sulphided product. In the reducing atmosphere of coal gas, excess cobalt would be present as the metal at temperatures in excess of 300 °C.

Copper: The behaviour of copper and cobalt is similar, although copper maintains 95% desulphurization capability to a temperature in excess of 900 °C. In the reducing atmosphere, excess copper would be present in metallic form over the entire temperature range.

Iron: Iron is a suitable desulphurizing material at temperatures up to 700 °C. At these temperatures, Fe₃O₄ is the stable form of excess iron. The rapid decrease in fractional desulphurization near 700 °C corresponds to Fe₃O₄ reduction to FeO.

Manganese: Oxide stability and high fractional desulphurization are predicted to temperatures in excess of 1000 °C. Below 400 °C, MnO is stable. Manganese shows desulphurization potential in the temperature range of 600-700 °C where metal oxides currently known to be reactive with H₂S are unsatisfactory.

Vanadium: In the reducing atmosphere, V₂O₃ is the stable form of the excess metal. Essentially 100% desulphurization, with V₂S₃ as the sulphided product, is predicted up to the melting temperature of V₂S₃ near 650 °C.

Zinc: On the basis of fractional desulphurization, zinc is acceptable to 1150 °C with ZnS as the sulphided form and ZnO as the stable form of excess zinc. However, zinc is limited to a maximum temperature of approximately 700 °C because of the formation of zinc vapor. Experimental observations in this laboratory have confirmed the formation of zinc vapor in similar atmospheres at temperatures in excess of 700 °C.

From the initial screening of metals, the following metals should be ruled out immediately: Ba, Ca, Sr, and V. The main reason was the lack of sulphidation of their oxide forms in the desired range of 340-550 °C or incompatibility with turbine operation (*i.e.*, high-temperature corrosion by vanadium compounds).

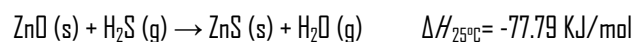
The process of selection of metal oxides for desulphurization identified the following metals as being potentially useful for desulphurization study: Zn, Cu, Co, Fe, Ce, Mo, Mn, Sn, W, Ni. It was agreed that many of these metals have weaknesses when considered as pure metal oxides, but become useful when used in combination with others (*e.g.*, Cu-Mo, and Zn-Mo systems). Zn, Cu, Fe, Ce, and Mo were ranked as being the most useful, hence worth of further evaluation. Very recently an exhaustive review on the experimental behaviour of mid- to high-temperature sorbents for the desulphurization of coal- and

biomass-derived syngas has been published ^[14]. Also in this study, Zn-, Mn-, Cu-, Fe-, rare earth- and Ca-based sorbents are considered as the most promising ^[15-17]. From an economic point of view, iron oxide sorbent is more attractive than zinc oxide; from the standpoint of desulphurization efficiency, zinc oxide is more attractive than iron oxide because of its favourable sulphidation thermodynamics.

For these reasons, in the present study, the selected sorbent materials have been zinc- and iron-oxides based sorbents. Below, a brief description of the sorbent materials proposed.

2.4.1 Zinc-oxide based sorbent

ZnO has been in use for H₂S removal for more than 30 years. Among the tested metal oxides ZnO has the highest equilibrium constant for sulphidation, yielding H₂S removal down to a fraction of 1 ppmv. Its principal limitation is that in the highly reducing atmosphere of synthesis gas it is partially reduced to elemental zinc. It is volatile above 600 °C, with consequent sorbent loss. Zinc oxide is highly efficient desulphurizer due to favourable thermodynamics in the temperature range of 350-550 °C. ZnO shows low equilibrium H₂S concentration. H₂S absorption by ZnO is considered to be controlled by the following reaction:



This is an exothermic reaction and the equilibrium H₂S concentration is determined by the temperature, the H₂S partial pressure and to a lesser extent the phase of the zinc oxide. Equilibrium H₂S concentration for ZnO with no H₂O is shown in [Figure 7](#). Thermodynamically, it is impossible to reduce the sulphur concentration to less than 100 ppbv at temperatures above 300 °C. At lower temperatures of (< 250 °C), absorption kinetics are slower but the ZnS equilibrium is more favourable. The data indicates that if the kinetics of H₂S absorption is sufficiently rapid, concentrations well below 100 ppb should be achievable.

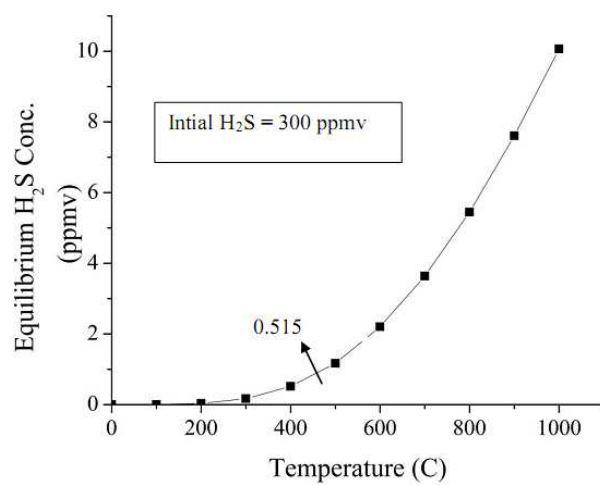


Figure 7. Equilibrium H_2S concentration (ppmv) using HSC software.

**HSC Chemistry Ver.3.0 Copyright © Outokumpu Research Oy, Finland A.Raine.*

Based on the Figure 8, there is a need of sorbents that can effectively remove sulphur in the lower temperature regime ($T < 350$ °C), high temperature regime ($T > 550$ °C), regenerable over multiple cycles, COS tolerant.

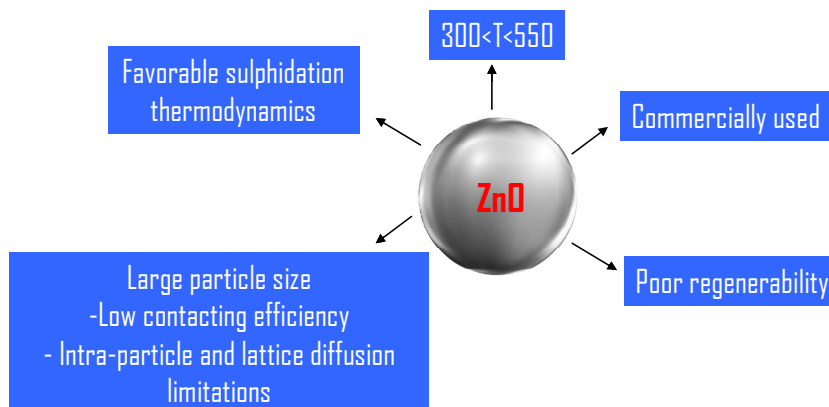


Figure 8. Background on commercial ZnO sorbent based on literature search^[18].

2.4.2 Iron-oxide based sorbent

Iron oxides, one of the best metal oxides candidates for H₂S removal, have been studied extensively in 1970s and 1980s. Compared with ZnO, iron oxides though their not favourable sulphidation thermodynamics, they get over ZnO from the cost point of view^[19]. Fe₂O₃ is not stable in reducing environments; the stable form of iron oxides in fuel gases is either FeO or Fe₃O₄, depending on the reducing power of the fuel gas and the temperatures. The desulphurization performance of FeO is shown in Figure 9. The sulphidation reaction of iron (III) is following:

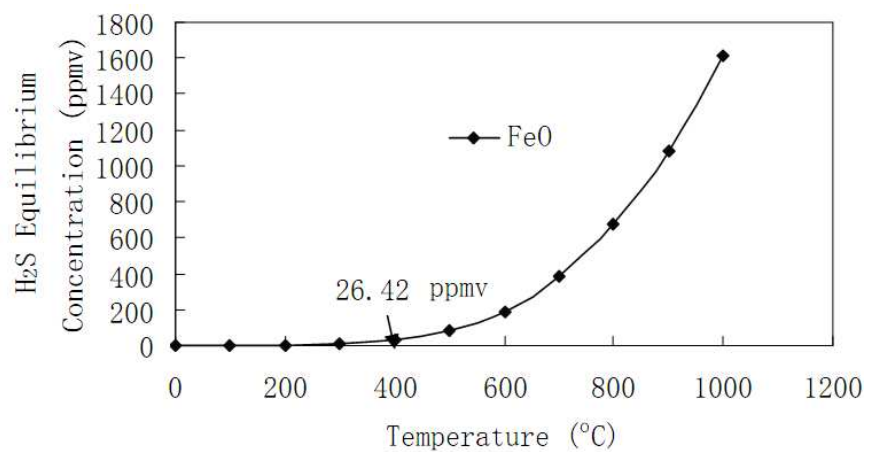
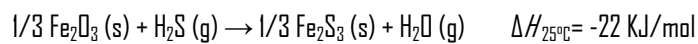


Figure 9. Equilibrium H₂S concentration (ppmv) using HSC software.

*HSC Chemistry Ver.3.0 Copyright © Outokumpu Research Oy Pori Finland A.Raine.

Iron oxide tends to be over reduced in presence of reducing agents (H₂ or CO mainly) at high temperature, which makes it unsuitable for multiple cycles of sulphidation-regeneration^[20].

2.5 Sorbent support

As announced before, the gas-solid H_2S -MeO reaction occurs first at the surface and then extends to the bulk phase: because of the influence of product-layer diffusion, pore diffusion and gas-film diffusion on the reaction kinetics, the MeO sorbent may be used only partially ^[21]. A possible way for overcoming this drawback could be the dispersing of MeO nanoparticles into a suitable, high-surface area support. Moreover, utilization of unsupported nanostructured sorbents is not useful in these cases since nanoparticles would rapidly sinter at the high temperatures used during the sorption and/or regeneration steps. One important topic of current research is the removal of H_2S by adsorption on various porous materials such as activated carbon ^[22], modified activated carbon ^[23], $\gamma\text{-Al}_2\text{O}_3$, modified clay ^[24], modified zeolites ^[25], etc. These porous materials are used extensively as adsorbents, catalyst supports and separation media. However, activated carbon suffers drawbacks of low mechanical stability which induces the formation of fines during operation, and high tortuosity with the presence of a large amount of micropores which could hinder the full accessibility of the reactants to the active site ^[26]. The main drawbacks of Al_2O_3 are the chemical interaction between the support and the active phase, leading to the decrease in catalyst performance by chemical reactions and hindering the recovery of the active phase ^[27]. Microporous materials such as (pillared) clays and zeolites present severe mass transfer limitations when large reactant molecules are involved ^[28]. Therefore, attempts to improve the diffusion of reactants into the catalytic sites have been focused on increasing the zeolite pore sizes ^[29], on decreasing zeolite crystal size, or on providing an additional mesoporous system within the microporous crystals ^[30]. A whole field of material research was opened up due to the discovery of mesoporous materials in 1992 ^[31]. Mesoporous silica with unique structural properties have demonstrated a considerable potential for the development of processes and materials designed to meet a range of environmental and technological challenges. The discovery of ordered mesoporous materials with well-defined pore sizes within the range of 2-50 nm, regular channel systems, high thermal stability and the potential for the isomorphous substitution rises up the new opportunities in material chemistry and

catalysis^[31, 32]. In view of the above, mesostructured SBA-15, an amorphous silica material with high surface area, regular channels and thick pore walls, represents a promising support candidate^[33, 34]. In comparison with classical sorbents consisting of micrometer-sized particles, nanostructured oxides dispersed into the SBA-15 channels would be sintering-resistant and would hence exhibit a higher reactivity towards H₂S. Furthermore, the oxide/SBA-15 composite would behave as an ideal reactor, with the mesopores acting as channels for the rapid transport of the reactant^[35].

This idea led the author to apply in the present thesis the unique characteristics of this kind of support for gas adsorption applications. It was expected that the SBA-15 matrix should be able to load more active and more evenly distributed metal oxides, which should improve the adsorption performance.

2.6 Introduction to porous materials

"Porous materials are like music: the gaps are as important as the filled-in bits."

Porous materials are well known since a long time and used for different applications, such as filtration, liquid adsorption and so other. During research and evolution of new porous systems, a better control of pore size, a decrease of pore diameter and a well-organized structure are necessary to increase base properties. If pore diameter have nanometric dimensions, we can speak of nanoporous materials. Nanoporous materials have unique surface, structural and bulk properties that enhance their application in various fields such as ion exchange, separation, catalysis, sensor, biological, molecular isolation and purification^[36].

The useful way to classify a nanoporous material is by the diameter size of their pores, because most of properties, interesting for applications of adsorption and diffusion, are dependent on this parameter. The prefix *nano-* means a typical dimension between 1 and 100 nm. According to IUPAC definition, nanoporous materials are classified in three main groups depending on their pore dimension (D_p):

- ✚ **Microporous materials ($D_p < 2$ nm):** These materials have very narrow pores. They can host only small molecules, such as gases or linear molecules, and generally show slow diffusion kinetics and high interaction properties. They are generally used as gas purification systems, filtering membranes or gas-storage materials.
- ✚ **Mesoporous materials ($2 < D_p < 50$ nm):** These materials have pores with diameter large enough to host some big molecules, for example aromatic systems or large polymeric monomers. Diffusion kinetic of adsorbed molecules is often due to capillarity, with a initial interaction with pore walls followed by pore filling. These systems can be used as nano-reactors for polymerization or adsorbing systems for liquids or gases.
- ✚ **Macroporous materials ($D_p > 50$ nm):** Pores of these materials could host very large molecules, such as polyaromatic systems or small biological molecules, and interactions with pore walls are often secondary respect to interactions with other molecules, mostly in case of very small guest molecules. These materials are principally used as matrices to store functional molecules, as scaffolds to graft functional groups, such as catalytic centres, and as sensing materials thanks to the quick diffusion of chemical species in the pore system.

One of the main purpose of this dissertation research is the use of ordered mesoporous silicas as supports to obtain highly efficient nanocomposite sorbents for mid-temperature H_2S removal.

2.6.1 Periodic Mesoporous Silica

Silica is perhaps the most diffused material in the world. It is the material composing crystals such as quartz or opal, large part of minerals and rocks and it is used by plants and animals to generate shells and support structures^[37]. Silica is also largely used in industrial applications, overall in the amorphous form, to produce glasses, as thermal or electrical insulator in ceramic materials or in electronic devices such as transistors. Main properties of this material are great hardness, thermal and chemical stability.

An important characteristic of the amorphous silica is the possibility to be arranged in complex structures such as monoliths, thin films and nanometric particles. A particular class of silica systems, very interesting for their large number of application fields, is that of porous silicas^[38].

Periodic mesoporous silica was discovered in 1992 by Mobil corporation^[31]. This discovery was an important news for scientific community, because, for the first time, it was possible to “escape from microporosity prison”. In fact, before this date pore diameter was limited by molecular dimension of templates and it was very difficult to obtain regular structures with pores bigger than 1-2 nm. Using supramolecular aggregates of surfactant molecules, instead, it was possible to generate regular structures still ordered in the nanometric range, but with larger pores. The same synthetic procedure was then applied to a large variety of other materials, such as aluminosilicates or metal oxides, but silica is the most versatile material and with the largest number of possible structures^[39]. Periodic mesoporous silica is a very interesting material because, as zeolites, it shows great affinity for water and other vapor species, great stability and large structural versatility. Moreover, it is easy and cheap to obtain, with synthetic procedures that are easily applicable in industrial processes.

This chapter deal with a general overview about mesoporous silica, its general properties and synthetic strategies, focusing the discussion about an hexagonal mesoporous silica similar to MCM-41, the SBA-15. This is a periodic mesoporous silica system able to self-organize itself and to grow in well defined micrometric shapes. In this PhD work such a kind of support material, as a promise candidate to confine the active metal oxide phase, has been used.

2.6.2 Structural classification

There is a large number of silica periodic mesoporous structures. They are obtained by similar procedures but, even though little differences in pore diameter size, wall thickness or condensation, the main difference is the pore organization in three-dimensional space^[40], as shown in [Figure 10](#).

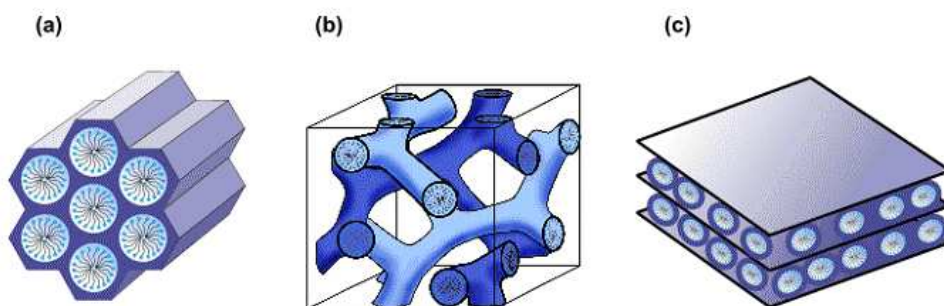


Figure 10. Examples of structural geometries of mesoporous silica structures: MCM-41 (a), MCM-48 (b) and MCM-50 (c).

Depending on synthesis conditions, it is possible to obtain:

- ✚ **Linear, parallel nanochannels structures:** in these structures pores are formed by long cylindrical channels, normally packed one close to the others in an hexagonal pattern. Nanometric channels are parallels and could be completely isolated, communicating by casual holes or connected by a secondary channel system of smaller size. Examples of this group are MCM-41, with parallel, isolated channels, and SBA-15, with channels connected by secondary pores.
- ✚ **Cubic three-dimensional structures:** in this case pores are organized in short channels interconnected in a three-dimensional structure with cubic symmetry. Typical of these systems is MCM-48 material.
- ✚ **Lamellar structures:** this case is unusual, but the same interesting. These structures are constituted by large planes with an organized pattern of holes, parallels or perpendicular to the lamella. One example of this structure is MCM-50 material.

2.6.3 Mesoporous SBA-15

Periodic mesoporous silica, which possess uniform channels with large pore size (2 – 50 nm), high surface area (up to 1500 m²/g), and tuneable structure (Figure 11), make this material very attractive for

many applications, such as catalysis, hydrogenation, desulphurization, oxidation or enzyme catalysis^[41-45]. A remarkable contribution in the synthesis of ordered mesoporous materials was made by Zhao et al. in 1998^[32], which used triblock copolymer surfactants to template the formation of ordered large-pore mesoporous silica with different structures under strongly acidic conditions. They synthesized mesoporous SBA-15 material with interesting features like large specific surface area, high porosity, controllable and narrowly distributed pore sizes, good mechanical, thermal, and chemical stability^[46].

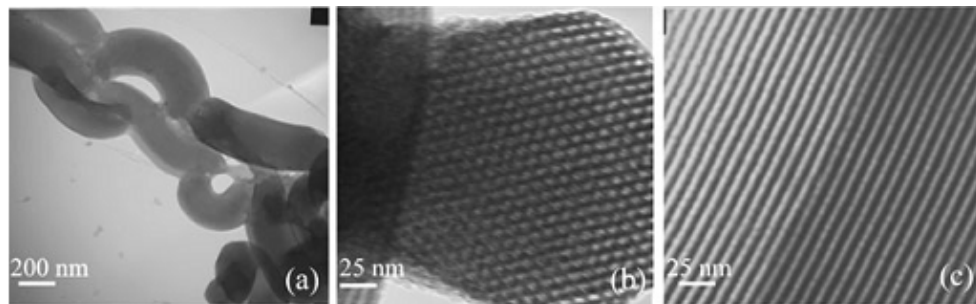


Figure 11. TEM images of mesostructured SBA-15^[47].

A large number of studies have been dedicated to SBA-15 silica after its discovery. The majority of the surface groups of dry SBA-15 are isolated silanols, and a smaller part consists of geminal and hydrogen-bonded silanols (Figure 12)^[48].

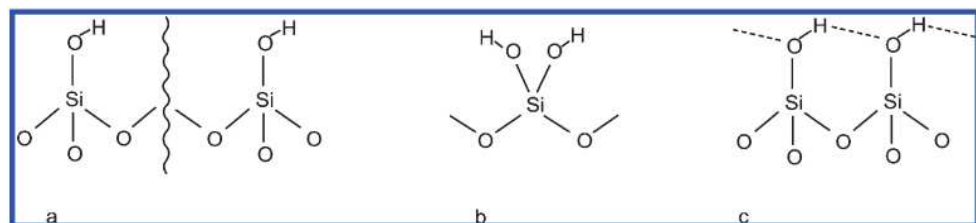


Figure 12. Proposed silanol groups at the silica surface: (a) isolated silanols, (b) geminal silanols, and (c) hydrogen-bonded silanols^[48].

The following features contributed to the high popularity of SBA-15 silica: (i) it can be easily and reproducibly prepared within a wide range of temperatures (35 – 130 °C) using tetra ethylene ortho silicate or sodium silicate; (ii) it is a hexagonally ordered silica material with tailorable uniform mesopores^[49] and micropores in the mesopore walls; (iii) it has thick pore walls (2 – 6 nm), leading to improved thermal and hydrothermal stability; and (iv) it may exhibit a large variety of morphologies depending on the synthesis conditions^[50]. The frameworks of mesoporous silica materials are neutral and, the applicability is limited. Modification of the surfaces of these materials, or introduction of nanoparticles in the SBA-15 mesochannels are ways to stabilize highly dispersed metals and oxides in uniform porous matrices. Such incorporated nanomaterials are of great interest in the nanotechnology field, gas adsorption, separation, and catalysis since they combine unique physicochemical features of nanoparticles with the well ordered structure found in mesoporous molecular sieves^[51, 52]. The introduction of precursors into the mesoporous SBA-15 is facilitated by the large amount of Si-OH groups inside the mesopores. The high surface area allows high dispersion of the precursor into the silica frameworks. Mesoporous materials present an interesting substitute for preparing nanoparticles in-situ. It is possible to control the size and the shape of the particles, and to optimize the volume fraction of nanoparticles and preserving good mechanical resistance. These materials are of fundamental interest, since they enable us to study certain metals under confinement and facilitate the synthesis of arrays with high density nanoparticles^[53]. The high hydroxyl content of SBA-15 makes it suitable support for the attachment of transition-metal species^[54].

2.6.4 Mechanism of formation of SBA-15

The syntheses of these mesoporous materials are accomplished similar to the zeolites syntheses by a structure-directed sol-gel process in a way like this: to a solution containing amphiphilic molecules as a template, a silica source (precursor), *e.g.*, tetraethylortho-silicate (TEOS), is added. During hydrolysis and condensation of the precursor a rigid composite material is formed into which the template is

incorporated. After removal of the template by calcination or solvent extraction a rigid mesoporous solid is obtained. In contrast to the structure-directed zeolites synthesis by individual molecules, the MCM- and SBA- syntheses are directed by supramolecular aggregates of amphiphilic molecules (micelles) *e.g.* long chain alkyltrialkylammonium halides or (tri)block copolymers which cause the formation of large pores. The utilization of amphiphilic molecules as structure-directing agents is often described as "soft matter-" or "endotemplating". Most of the research activity has been focused on the formation mechanism of ordered endotemplated mesoporous materials, where two different mechanisms are considered to be involved (Figure 13) [55, 56]. In case of the true liquid crystal templating (TLCT) mechanism, the concentration of the surfactant is high enough that under the prevailing conditions (temperature, pH value) a lyotropic liquid crystalline phase is formed, serving as structure-directing agent (SDA) even in the absence of a silica source. In case of the cooperative mechanism a mesostructure is formed even at lower concentration of the surfactant, when a cooperative self-assembly between surfactant molecules and already added silica precursor lead to the formation of a liquid crystalline phase [57].

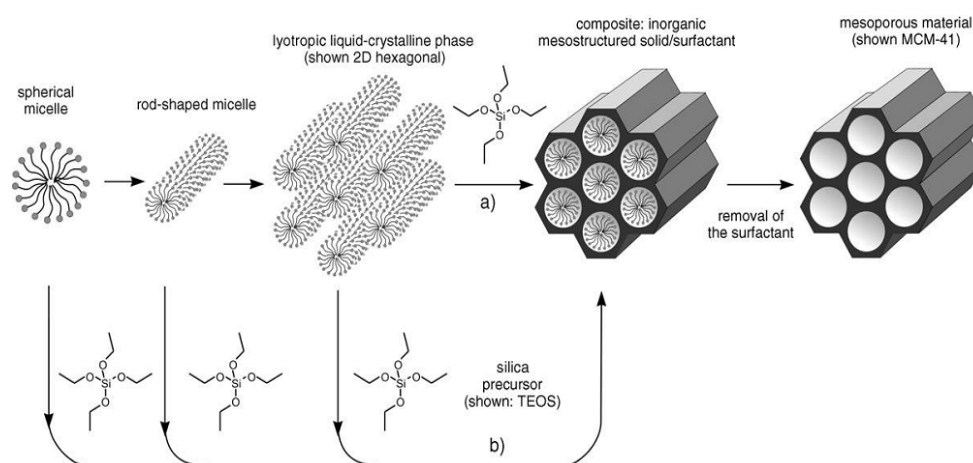


Figure 13. Formation process of the mesoporous materials by the true liquid crystalline template mechanism (a) and the cooperative liquid crystalline template mechanism (b) [55].

Tri-block copolymers (EO)_x(PO)_y(EO)_z- Pluronic

The Pluronic's consist of a propylene oxide block sandwiched between two ethylene oxide blocks. The PO-block is less polar and more hydrophobic than the EO-blocks, especially at low temperatures. Micelles are formed in aqueous solutions at concentrations above critical micelle concentration (CMC) by aggregate formation of the block copolymers, which are folded to shields the hydrophobic PO-blocks from the aqueous surrounding (Figure 14). In reversed phases the EO-blocks form the core.

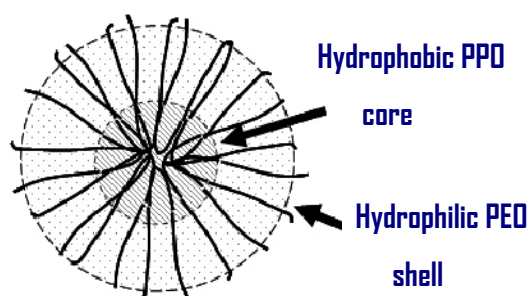
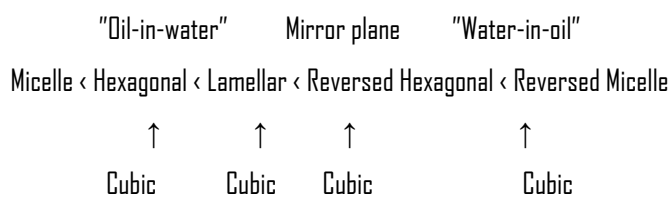


Figure 14. Schematic drawing of a micelle formed by Pluronic block copolymers.

The phase formed is dependent on temperature and concentration i.e., the Pluronic surfactants form lyotropic liquid crystalline phases. If the volume of the EO-part, which can be expanded by increasing the water content, is dominant, then phases to the left in the so called "*Fontell scheme*" are formed. On the other hand, if the PO-volume that can be swelled by addition of organic additives is high, then phases to the right are formed. At low Pluronic concentrations micellar solutions appear, and at higher concentrations they turn into different kinds of cubic, hexagonal and lamellar phases^[58].

The Fontell Scheme



2.7 Metal Oxides in the SBA-15 Pores

The existence of small complimentary pores interconnecting hexagonally ordered mesopores, high surface area, large mesopores and good hydrothermal stability, make SBA-15 a suitable sorbent or catalyst support. Using these ordered silica to grow inorganic objects of controlled dimension is known as the "*nanocasting*" strategy and has been pioneered by the Ryoo group for the preparation of ordered carbon^[59]. Nanocasting concept provides a promising strategy for the preparation of mesostructured materials. Several oxides (of indium^[60], zirconium^[61], tungsten^[62], chromium^[63], cerium, nickel, cobalt, copper, and iron^[64, 65]) and mixtures of manganese oxides (MnO_2 , Mn_2O_3 , and Mn_3O_4 ^[66]) have been patterned.

The long-standing experience of industry in catalyst manufacture, the progress of scientific understanding of the processes involved and the development of the corresponding basic sciences (chemistry of solids, colloid chemistry, etc.) mean that catalyst preparation is nowadays a science. Methods of catalyst preparation are very diverse and each catalyst may be produced via different routes. This kind of preparation routes can be extended, with some expedients, to the preparation of nanocomposite sorbents. A simple way for the patterning of metal oxide into SBA-15 matrix is either during the synthesis (*one-step* or *direct synthesis*), or by post-synthesis modification of SBA-15 (*two-steps approach*). In the "one-step" method, the metal oxide precursor is inserted already during the early stages of the SBA-15 synthesis, then it is a "direct" method, while in the "two-steps" method the silica matrix is first synthesized, and later, through different techniques, the desired oxide with the desired loading is included. The later is often preferred as incorporation of the active phase during synthesis is generally cumbersome due to the complexity of achieving simultaneous condensation of both phases and retention of the formation of an ordered pore symmetry. Furthermore, this last method allows to disperse the active phase on the support in a wide range of loading.

In the present dissertation, in view of the specific application, and with the purpose to study different metal oxide loadings on the H₂S removal performance, the post-synthesis approach has been selected as simply and easily scaled-up preparation method of the nanosorbents.

The most frequently applied preparation method is the impregnation. The major advantage of this method is its simplicity and the limited production of waste. Impregnation consists in contacting a solid with a liquid containing the components to be deposited into/over the support. During impregnation many different processes take place with different rates^[67].

- ✚ selective adsorption of species (charged or not) by coulomb force, van der Waals forces or H-bonds;
- ✚ ion exchange between the charged surface and the electrolyte;
- ✚ polymerisation/depolymerisation of the species (molecules, ions) attached to the surface;
- ✚ partial dissolution of the surface of the solid.

Usually, during impregnation a suitable support material is contacted with a solution containing a precursor of the active phase. Upon drying of the support material after impregnation solvent (usually water) is evaporated and as a result the precursor of the active phase adheres to the surface, or into the channels of the support. Generally, there are two different methods of impregnation; the "*wet impregnation*" and the "*incipient wetness impregnation*".

In "*wet*" impregnation the amount of precursor solution added to the support material exceeds the pore volume. Although this is the simplest impregnation method it can result in the deposition of a vast amount of precursor material at the exterior parts of the support bodies during drying and the resulting heterogeneous materials display an egg-shell distribution of the active component. Nevertheless such a distribution might be beneficial from an application point of view, since it alleviates the need of reactant penetration deep inside the catalyst bodies, thus improving the catalytic process. When the catalyst

bodies are subject to a lot of friction during operation, causing abrasion of the outer parts, other types of distribution of the active phase are necessary, *e.g.*, homogeneous, egg-white or egg-yolk. For this purpose the other type of impregnation is usually required, *viz.* "*incipient wetness impregnation*". This method is also referred to as "*dry*" impregnation, since during the impregnation process the amount of precursor solution added to the support material equals the pore volume. However, according to IUPAC definition reported in "*Manual of methods and procedures for catalyst characterization*"^[67], the volume of the solution is more empirically determined to correspond to that beyond which the catalyst begins to look wet. As a result the support bodies appear to be dry, even after admission of the precursor solution. After the impregnation process, is it wet or dry, the impregnated support material needs to be dried in order to allow the precursor compound to be converted into a more suitable chemical phase. Although drying of an impregnated support material appears to be very simple it should be noted that the conditions during drying can adversely influence the distribution of the precursor compound over the support material. This behaviour is caused by solvent flows inside the pores of the support material during drying. As a result of these flows the precursor material is entrained through the pores, which can lead to inhomogeneous distributions after drying. To prevent redistribution of the precursor during drying special measures have to be taken, *e.g.*, by carefully controlling the drying rate of the impregnated bodies^[68]. Another option to overcome redistribution of precursor compound during drying involves the use of chelated precursor complexes^[69]. After drying the precursor of the active phase is usually converted into a desired phase, *e.g.*, by calcination, yielding a compound in the oxidized state. A subsequent reduction treatment can be used to convert the active phase into the metallic state.

Since SBA-15 offers a relatively large pore volume, impregnation appears to be a suitable method for the application of precursors of active phase(s) inside the mesopores. However, care should be taken to avoid redistribution of precursors during drying after impregnation. In view of the above-described processes, incipient wetness impregnation is the most suitable impregnation procedure, since it offers the advantage (at least in theory) that the precursor compound is deposited completely inside the pores

of the support material. Figure 15 reports a graphical representation of the different steps involved for the confinement of the metal oxide inside the mesochannels of the SBA-15.

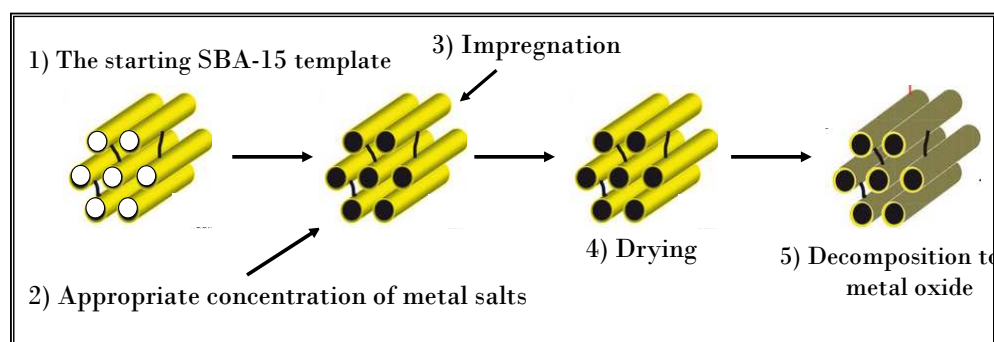


Figure 15. Schematic representation of the impregnation technique^[70].


2.7.1 Synthesis details using impregnation

Straightforward as the nanocasting concept may seem to be, research activity has to be focused on apparently small details in the synthesis process which are responsible for the success of the final nanocomposite. The optimum realization of these synthesis details is a key factor for the quality of the resulting metal oxide nanostructure; hence they have to be adapted individually for each metal oxide system. Particularly two factors are decisive for the success of the synthesis:

- ✚ *Efficient impregnation of the structure matrix*: the pore system of the matrix must be loaded efficiently with the precursor species to obtain a sufficient cross-linking of the resultant metal oxide inside the pore system. The successful impregnation depends on the consideration of mainly three factors; such as the surface polarity of the matrix, the solvent polarity, and the solubility of the precursor in the solvent. For a pore surface with a high density of polar functions, such as free silanols groups in a silica matrix, a polar solvent (ethanol or water) will be suitable in order to obtain a high degree of wettability and convenient diffusion through the

pores. Furthermore, polar solvents are needed if metal salts are used as the precursors, since these will then have a high solubility.

The final dispersion and distribution over the support of the active phase is largely affected by the type of precursor and support used, and the experimental conditions of the treatments applied during each successive step in the preparation. Upon impregnation, precursor solution is readily absorbed by the support body due to capillary forces. However, the rate at which the precursor complex is distributed throughout the support body depends on its interaction with the support ^[71-73]. When interaction is relatively weak like for instance between a silica support and $[\text{Ni}(\text{OH}_2)_6]^{2+}$ complexes in a nickel nitrate solution with a pH of ~ 2 , the complex is transported rapidly into the support body, and a homogeneous distribution is obtained. However, when nickel is introduced using a solution containing $[\text{Ni}(\text{NH}_3)_6]^{2+}$ complexes and with a pH of ~ 8 , interaction is much stronger and transport of the complex can be slowed down, resulting in a non-uniform concentration profile over the silica support body. When the system is not allowed to equilibrate completely in the later case, the inhomogeneous distribution can be retained upon drying and further treatments, resulting in a so-called egg-shell distribution of the active component over the catalyst body.

 *Evaluation of suitable conditions for the precursor conversion:* metal nitrates or chlorides are the precursor compounds of choice since they can easily be converted into the desired product by thermal treatment. The conversion temperatures of most precursors are significantly lower than the synthesis temperatures of the silica matrices, *e.g.*, temperature required for calcination. In addition, no reactions of the silica matrix and products/by-products are to be expected which might influence the template function of the matrix.

Up-to-date, several strategies have been developed to incorporate zinc oxide in the channels of mesoporous silica SBA-15 and MCM-41 and the pores of zeolites. Two examples are conventional wetness

impregnation^[74-76] and the improved method with modification of the surface walls followed by loading precursor through affinity interaction^[77, 78]. Generally, the former method seems difficult to completely avoid adsorptions of the zinc oxide precursor on the outer surface of the host template. The uncontrolled zinc oxide aggregation on the external surface of mesoporous silica will form in subsequent calcinations. The latter method involves complicated process and has low yield. So, it is necessary to develop a simple and low cost novel strategy to prepare ZnO encapsulated in SBA-15 with high thermal stability.

2.7.2 New impregnation technique: The “Two-Solvents” strategy

Recently, an original impregnation method called “two-solvents” or “double-solvent” strategy, derived from the incipient wetness impregnation technique, has attracting a considerable interest^[79-81]. This method facilitates the loading of the pores of SBA-15 with a metal oxide precursor solution and allows the preparation of highly dispersed metal oxide within silica mesopores. It is based on the suspension of dried silica inside a first hydrophobic solvent (*n*-pentane, *n*-hexane or cyclohexane) before the addition of a volume of aqueous solution containing the metal oxide precursor and set equal to the porous volume of the silica used as a support (the one determined by N₂ sorption). The surface of the SBA-15, which is in powder form, is prewetted by the hydrophobic solvent, before an aqueous solution of the desired precursor is added. It is suggested that this leads to a better wettability and therefore increases the introduction of aqueous solutions into the pores. This results in a significantly better dispersion of the metal oxide nanoparticles, obtained after drying and calcination. A study to compare the influence on the particles dispersion using different alkane solvents has been carried out^[82]. To understand the behaviour of the “mesoporous silica-solvent-water” system and what is the mechanism of the double solvent technique, an exhaustive study has been recently done by some researcher^[48]. Their proposed hypothesis is the following: when a solvent is entering the pore system, traces of water that are present are pushed against the silica wall, causing a rehydroxylation of the surface. This results in a more hydrophilic behaviour of the surface, which might favour the interaction with an aqueous

solution that is introduced afterward. In the next stage, where an aqueous solution is introduced, droplets of the solution are formed in the alkane solvent. Therefore, a slight silica surface modification has been observed when adding an alkane. The majority of the surface groups of dry SBA-15 are isolated silanols, next to a smaller part that consists of geminal and hydrogen-bonded silanols. The addition of an alkane seems to cause an increase in the number of geminal and hydrogen-bonded silanol groups, which increases the hydrophilic nature of the silica. In the drying stage, it is important to remove all traces of residual solvent. It can be hypothesized that, if some solvent molecules stay in the pores, those might hinder during the calcination step.

The two-solvents method may be employed to prepare nanocomposites of zinc- and iron-oxide supported in mesoporous silica. However, to the best of the present authors' knowledge, only a few papers dealing with the use of this innovative technique for the synthesis of zinc oxide encapsulated in mesoporous SBA-15 silica^[83] and for the Fe₂O₃ confinement within the mesochannels of SBA-15, have been published so far^[84].

References

- [1] C. J. King, in *Separation Processes*, 2nd Ed.; McGraw-Hill: New York, **1980**.
- [2] R. T. Yang, in *Adsorbents: Fundamentals and Applications*, John Wiley & Sons: Hoboken, NJ, **2003**.
- [3] W. J. Thomas and B. Crittenden, in *Adsorption Technology & Design*, Butterworth Heinemann: Oxford, **1998**, pp. 8–30.
- [4] W. J. W. Bakker, in *Structured systems in gas separation. Part 2. Manganese based sorbent for high temperature H₂S removal*, PhD thesis, Delft University of Technology, **1998**, pp. 129–303.
- [5] R. Steudel and Y. Steudel, *Chem. Eur. J.*, **2006**, 12, 8589.
- [6] A. Samokhvalov and B. J. Tatarchuk, *Phys. Chem. Chem. Phys.*, **2011**, 13, 3197.
- [7] J. A. Rodriguez, S. Chaturvedi, M. Kuhn, and J. Hrbek, *J. Phys. Chem. B*, **1998**, 102, 5511.
- [8] O. Levenspiel, in *Chemical Reaction Engineering*, Third Edition, John Wiley & Sons, **1999**.
- [9] Von J. Szekely, J. W. Evans und H. Y. Sohn, in *Gas-Solid Reactions*, Academic Press, New York **1976**.
- [10] S. K. Bhatia and D. D. Perlmutter, *AIChE Journal* **1981**, 20, 247.
- [11] G. F. Froment and K. B. Bischoff, in *Chemical Reactor Analysis and Design*, 2nd ed., John Wiley & Sons, New York, **1990**, pp. 314–327.
- [12] Von J. Szekely, J. W. Evans und H. Y. Sohn, in *Gas-Solid Reactions*, Academic Press, New York **1976**.
- [13] P. R. Westmoreland and D. P. Harrison, *Environ. Sci. Technol.*, **1976**, 10, 659.
- [14] S. Cheah, D. L. Carpenter and K. A. Magrini-Bair, *Energy Fuel*, **2009**, 23, 5291.
- [15] M. Pineda, J. M. Palacios, L. Alonso, E. Garcia and R. Moliner, *Fuel*, **2000**, 79, 885.
- [16] W. Xie, L. Chang, D. Wang, K. Xie, T. Wall and J. Yu, *Fuel*, **2010**, 89, 868.
- [17] R. A. Rodriguez and C. G. Jul, *Fuel*, **2008**, 87, 3513.
- [18] P. P. Dhage, in *Promoted ZnO Sorbents for Wide Temperature Range H₂S/COS Removal for Applications in Fuel Cells*, PhD Thesis, August 6, **2011**.
- [19] E. Sasaoka, T. Ichio and S. Kasaoka, *Energy & Fuels*, **1992**, 4, 603.
- [20] C. G. Ryu, Y. H. Wi, C. B. Lee and Y. K. Lee, *Chemical Industry and Technology*, **1998**, 16, 17.

- [21] J. B. Gibson and D. P. Harrison, *Ind. Eng. Chem. Proc. Des. Dev.*, **1980**, 19, 231.
- [22] M. A. Daley, C. L. Mangun, J. A. De Barr, S. Riha, A. Lizzio, G. Donnals and J. Economy, *Carbon*, **1997**, 35 411.
- [23] A. Bagreev, S. Katikaneni, S. Parab and T. J. Bandosz, *Catal. Today*, **2005**, 99, 329.
- [24] D. N. Thanh, K. Block and T. J. Bandosz, *Chemosphere*, **2005**, 59, 343.
- [25] M. N. Bae, M. K. Song, Y. Kim and K. Seff, *Micropor. Mesopor. Mater.*, **2003**, 63 21.
- [26] J. M. Nhut, R. Vieira, L. Pesant, J. P. Tessonnier, N. Keller, G. Ehret, P. H. Cuong and M.J. Ledoux, *Catal. Today*, **2002**, 76, 11.
- [27] J. A. Schwartz, C. Contescu and A. Contescu, *Chem. Rev.*, **1995**, 95, 475.
- [28] P. B. Venuto, *Micropor. Mater.*, **1994**, 2, 297.
- [29] M. E. Davis, C. Saldarriaga, C. Montes, J. Garces and C. Crowder, *Nature*, **1988**, 331, 698.
- [30] I. Schmidt, A. Boisen, E. Gustavsson, K. Stahl, S. Pehrson, S. Dahl, A. Carlsson and C. J. H. Jacobsen, *Chem. Mater.*, **2001**, 13, 4416.
- [31] C. T. Kresge, M. E. Leonowicz, W. J. Roth, J. C. Vartuli and J. S. Beck, *Nature*, **1992**, 359 710.
- [32] D. Zhao, J. Feng, Q. Huo, N. Melosh, G. H. Fredrickson, B. F. Chmelka and G. D. Stucky, *Science*, **1998**, 279, 548.
- [33] X. Wang, T. Sun, J. Yang, L. Zhao and J. Jia, *Chem. Eng. J.*, **2007**, 142, 48.
- [34] Y. Sun, S. Walspurger, J. P. Tessonnier, B. Louis and J. Sommer, *Appl. Catal. A*, **2006**, 300, 1.
- [35] J. A. Melero, G. Calleja, F. Martinez and R. Molina, *Catal. Commun.*, 2006, 7, 478.
- [36] G. Q. Lu and X. S. Zhao, in *Nanoporous Materials, science and engineering, Series of chemical engineering*, Vol.4, Imperial college Press, London, **2004**.
- [37] S. Weiner, L. Addadi and H. D. Wagner, *Mat. Sci. Eng. C*, **2000**, 11, 1.
- [38] R. K. Iler, in *The chemistry of Silica*, Wiley, New York, **1979**.
- [39] G. A. Ozin, A. C. Arsenault and L. Cademartiri, in *Nanochemistry: A chemical approach to nanomaterials*, **2009**, RSC Publishing.

- [40] W. Ying and D. Zhao, *Chem. Rev.*, **2007**, 107, 2821.
- [41] A. Taguchi, F. Schuth, *Micropor. Mesopor. Mat.*, **2005**, 77, 1.
- [42] S. Xiao, *Top. Catal.*, **2005**, 35, 9.
- [43] C. Li, *Catal. Rev.*, **2004**, 46, 419.
- [44] X. S. Zhao, X. Y. Bao, W. P. Guo and F. Y. Lee, *Mater. Today*, **2006**, 9, 32.
- [45] C. J. Liu, S. J. Li, W. Q. Pang and C. M. Che, *Chem. Commun.*, **1997**, 65.
- [46] L. Xiancai, H. Shaoxiang, X. Qingrong and Y. Yifeng, *Transit. Metal Chem.*, **2009**, 34, 943.
- [47] E. Rombi, M. G. Cutrufello, C. Cannas, M. Casu, D. Gazzoli, M. Occhiuzzi, R. Monaci and I. Ferino, *Phys. Chem. Chem. Phys.*, **2009**, 11, 593.
- [48] J. van der Meer, I. Bardez-Giboire, C. Mercier, B. Revel, A. Davidson and R. Denoyel, *J. Phys. Chem. C*, **2010**, 114, 3507.
- [49] A. Sayari and Y. Yang, *Chem. Mater.*, **2005**, 17 6108.
- [50] V. Meynen, P. Cool, E. F. Vansant, P. Kortunov, F. Grinberg, J. Karger, M. Mertens, O. I. Lebedev and G. Van Tendeloo, *Micropor. and Mesopor Mater.*, **2007**, 99, 14.
- [51] I. Yuranov, L. Kiwi-Minsker, P. Buffat and A. Renken, *Chem. Mater.*, **2004**, 16, 760.
- [52] W. Zhu, Y. Han and L. An, *Micropor. Mesopor. Mat.*, **2005**, 80, 221.
- [53] R. Benoit, F. Warmont, V. Meynen, K. De Witte, P. Cool, M. Treguer-Delapierre and M. L. Saboungi, *Micropor. Mesopor. Mat.*, **2009**, 120, 2.
- [54] M. Morey, A. Davidson, H. Eckert and G. Stucky, *Chem. Mater.*, **1996**, 8, 486.
- [55] F. Hoffmann, M. Cornelius, J. Morell and M. Fröba, *Angew. Chem. Int. Edit*, **2006**, 45, 3216.
- [56] G. S. Attard, J. C. Glyde and C. G. Göltner, *Nature*, **1995**, 378, 366.
- [57] A. Monnier, F. Schuth, Q. Huo, D. Kumar, D. Margolese, R. S. Maxwell, G. D. Stucky, M. Krishnamurty, P. Petroff, A. Firouzi, M. Janicke and B. F. Chmelka, *Science*, **1993**, 261, 1299.
- [58] K. Holmberg, B. Jönsson, B. Kronberg and B. Lindman, in *Surfactants and Polymers in Aqueous Solution*, John Wiley & sons, **2002**.

- [59] R. Ryoo, S. H. Joo and S. Jun, *J. Phys. Chem. B*, **1999**, 1003, 7743.
- [60] H. Yang, Q. Shi, B. Tian, Q. Lu, F. Gao, S. Xie, J. Fan, C. Yu, B. Tu and D. Zhao, *J. Am. Chem. Soc.*, **2003**, 125, 4724.
- [61] A. H. Janssen, C. M. Yang, Y. Wang, F. Schüth, A. J. Koster and K. P. de Jong, *J. Phys. Chem. B*, **2003**, 107, 10552.
- [62] K. Zhu, H. He, S. Xie, X. Zhuang, W. Zhou, S. Jin and B. Yue, *Chem. Phys. Lett.*, **2003**, 377, 317.
- [63] K. Zhu, B. Yue, W. Zhou and H. He, *Chem. Commun.*, **2003**, 98.
- [64] B. Tian, X. Liu, H. Yang, S. Xie, C. Yu, B. Tu and D. Zhao, *Adv. Chem.*, **2003**, 15, 1370.
- [65] T. A. Crowley, K. J. Ziegler, D. M. Lyons, D. Ertz, H. Olin, M. A. Morris and J. D. Holmes, *Chem. Mater.*, **2003**, 15, 3518.
- [66] B. Tian, X. Liu, H. Yang, S. Xie, C. Yu, B. Tu and D. Zhao, *Adv. Chem.*, **2003**, 15, 1370.
- [67] IUPAC, in *Pure and Applied Chemistry*, **1995**, 67, 1257.
- [68] L. M. Knijff, Ph.D. Thesis, Utrecht University, The Netherlands, **1993**, chapters 2 and 3.
- [69] A. J. van Dillen, R. J. A. M. Terörde, D. J. Lensveld, J. W. Geus and K. P. de Jong, *J. Catal.*, **2003**, 216, 257.
- [70] M. Mureddu, C. Cannas, E. Rombi, I. Ferino, M. G. Cutrufello, A. Ardu, G. Piccaluga and A. Musinu, "IX National Meeting on Materials Sciences and Technology", Bari (Italy), July **2013**, *Regenerable MeO/SBA-15 nanocomposites for mid-temperature H₂S removal from syngas coal gasification*.
- [71] O. Clause, M. Kermarec, L. Bonnevoit, F. Villain and M. Che, *J. Am. Chem. Soc.*, **1992**, 114, 4709.
- [72] T. Mang, B. Breitscheidel, P. Polanek and H. Knözinger, *Appl. Catal. A: General*, **1993**, 106, 239.
- [73] C. Galarraga, E. Peluso and H. De Lasa, *Chem. Eng. J.*, **2001**, 82, 13.
- [74] Q. Jiang, Z. Y. Wu, Y. M. Wang, Y. Cao, C. F. Zhou and J. H. Zhu, *J. Mater. Chem.*, **2006**, 16, 1536.
- [75] G. Q. Tang, Y. Xiong, L. Z. Zhang and G. L. Zhang, *Chem. Phys. Lett.*, **2004**, 395, 97.
- [76] W. Zeng, Z. Wang, X. F. Qian, J. Yin and Z. K. Zhu, *Mater. Res. Bull.*, **2006**, 41, 1155.
- [77] W. H. Zhang, J. L. Shi, L. Z. Wang and D. S. Yan, *Chem. Mater.*, **2000**, 12, 1408.

- [78] H. G. Chen, J. L. Shi, H. R. Chen, J. N. Yan, Y. S. Li, Z. L. Hua, Y. Yang and D. S. Yan, *Opt. Mater.*, **2004**, 25, 79.
- [79] M. Imperor-Clerc, D. Bazin, M. D. Appay, P. Beaunier and A. Davidson, *Chem. Mater.*, **2004**, 16, 1813.
- [80] I. Lopes, N. El Hassan, H. Guerba, G. Wallez and A. Davidson, *Chem. Mater.*, **2006**, 18, 5826.
- [81] F. Boubekr, A. Davidson, S. Casale and P. Massiani, *Micropor. Mesopor. Mat.*, **2011**, 141, 157.
- [82] J. Van der Meer, I. Bardez, F. Bart, P. A. Albouy, G. Wallez and A. Davidson, *Micropor. Mesopor. Mat.*, **2009**, 118, 183.
- [83] L. Qingshan, W. Zhongying, L. Jiangong, W. Peiyu and Y. Xialei, *Nanoscale Res. Lett.*, **2009**, 4, 646.
- [84] E. Delahaye, V. Escax, N. El Hassan, A. Davidson, R. Aquino, V. Dupuis, R. Perzynski and Y. L. Raikher, *J. Phys. Chem. B*, **2006**, 110, 26001.

3.1 Experimental Methods

This chapter describes the experimental material suppliers, set-up, procedure, and analysis of the effluent gas from the fixed-bed. The experimental parameters were chosen in terms of the operating conditions of syngas derived from coal gasification (kindly provided by [Sotacarbo S.p.A, Italy](#)) with a H₂S concentrations of 1.5 % v/v^[1].

Material suppliers

The ZnO-based commercial sorbent (Katalco_{JM} 32-5) was kindly provided by Sotacarbo S.p.A, Italy. The gas mixture, 5 % v/v H₂S and balance He, was provided by Air Liquide.

3.2 Synthesis of mesoporous SBA-15

The SBA-15 mesostructured silica was prepared by exploiting the templating effect of a neutral triblock copolymer surfactant according to the procedure reported by Zhao et al.^[2]. The equipment used in the synthesis is shown in [Figure 1](#).

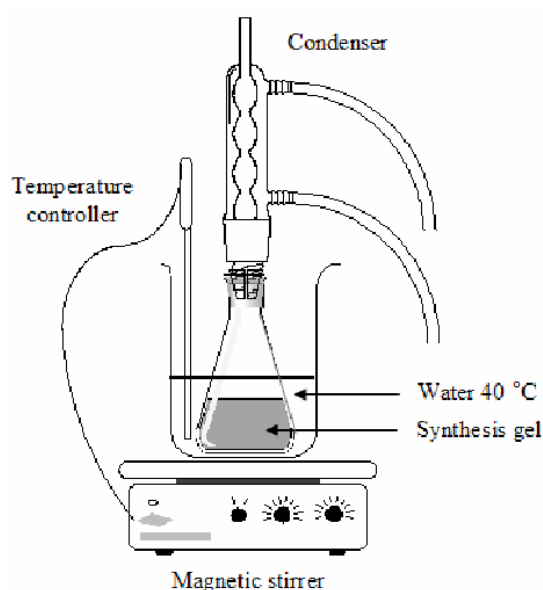
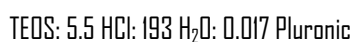


Figure 1. *Equipment setup of SBA-15 preparation.*

The chemicals used for the synthesis were poly(ethylene oxide)-poly(propylene oxide)-poly(ethylene oxide) triblock copolymer Pluronic P123 ($\text{EO}_{20}\text{PO}_{70}\text{EO}_{20}$, $M_{av}=5800$, Sigma Aldrich), TEOS (98%, Sigma Aldrich) and a 2M hydrochloric acid with the following molar ratio:



Typically, a solution of surfactant was prepared by vigorous stirring for 16h the mixture of 4.0g of Pluronic P123, 30.0g of distilled water and 120.0g of HCl (2M) in a ethylene glycol bath maintained at 36 °C until the clear solution was obtained (Figure 2, left). After that, 9.0g of tetra ethyl ortho silicate (TEOS) was added drop wise and maintained under vigorous stirring for 24h at 36 °C to allow the hydroxylation and condensation reactions (Figure 2, centre). The resulting milky white suspension (Figure 2, right) was transferred into a Teflon-lined autoclave and heated statically at 100 °C for 24 h.



Figure 2. Evolution of the SBA-15 preparation before (left), during (centre), and after (right) the addition of tetraethyl ortho silicate.

The resulting white precipitate is recovered by filtration washing with large amounts of warm distilled water and dried at 35 °C for 24 h. The final product was calcined under air atmosphere at 550 °C for 6 h (heating rate 5 °C/min) to remove the organic template and any impurity. The as-synthesized sample is labelled as "**Bare SBA-15**" and used in the next chapters as support for the confinement of different active metal oxide phases.

The synthesis of the nanocomposite sorbent materials studied in the present thesis are reported in the following chapters (4,5 and 6).

3.3 Determination of the sulphur loading and the breakthrough curve

The desulphurization activity of the sorbents was determined by studying the "breakthrough curves". A breakthrough curve gives an indication of the way in which an adsorbate (H_2S) is distributed within a fixed bed when a gaseous stream containing a fixed percentage of the adsorbate passes through a fixed-bed until the adsorbate emerges in the exit stream. [Figure 3](#) shows a typical breakthrough curve. [Figure 4](#) shows the concentration of adsorbate in the gas phase at any given point (location) in the bed as a function of time because it results from the movement of the concentration front in the bed.

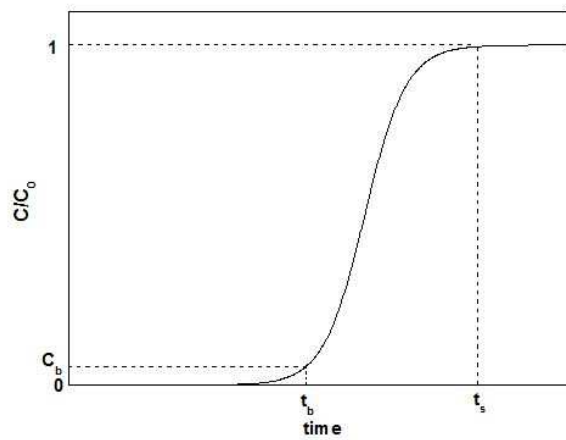


Figure 3. Profile of gas phase H_2S concentration in the adsorbent bed from the breakthrough point, t_b , to the complete saturation point t_s .

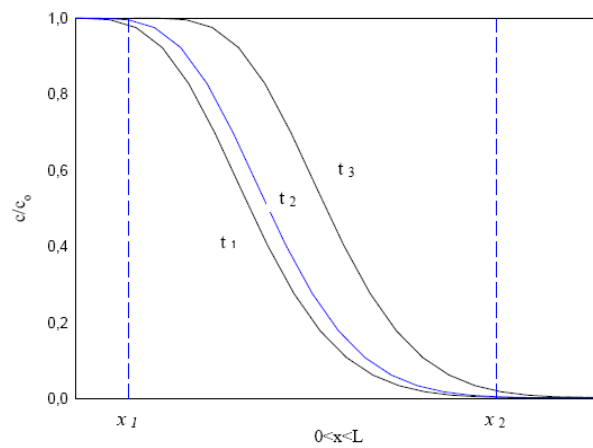


Figure 4. Profile of gas phase H_2S concentration in the adsorbent bed: development and progression of a transition zone along the bed: transition zones at different times t_1 , t_2 , and t_3 .

On first introducing the gas stream to the bed, the sorbent quickly becomes saturated at the inlet of the bed and the adsorbate concentration falls off rapidly along the bed to form a concentration profile along

the bed which is called the transition zone. As the run proceeds, if this concentration profile in the transition zone remains the same, the constant pattern is fully developed and moves in the direction of the gas stream due to the progressive saturation of the adsorption sites at the entrance of the bed. In Figure 4 t_1 shows the initial formation of the concentration profile, t_2 shows one at some intermediate time, and t_3 shows another just before breakthrough, the point at which the adsorbate H_2S is first detected in the exit stream. After breakthrough the adsorbate concentration in the effluent stream rises steeply up to the value of the inlet concentration.

The shape of the breakthrough curve represents the global adsorption kinetics, and is determined from mass and energy balances on the bed together with the intrinsic adsorption reaction. In most sorption processes, heat transfer effects within the pellet can be neglected. This is because most adsorptive gases are present in an inert carrier gas and their concentrations are small. Also when adsorbates penetrate the porous structure during adsorption and desorption, the local temperature change is negligible. It would be necessary to consider heat transfer effects if the reaction was highly exothermic.

From these latter curves, two fundamental parameters to compare the desulphurization performance of different materials synthesized in this study have been derived; they are:

- ✚ "**Breakthrough time, BT** " or "**Breakpoint time**", defined as the time between the beginning of the desulphurization activity and the moment when the H_2S concentration reaches a certain threshold value (in our case this value is taken equal to 100 ppm);
- ✚ "**Breakthrough capacity**" or "**Sulphur Retention Capacity, SRC** ", expressed in milligrams of sulphur per gram of sorbent, which provides a quantitative result on the effective capacity of H_2S removal. This has been calculated using the following expression:

$$SRC = \frac{V_{H_2S} \cdot t_b \cdot C_{A,in} \cdot MW_S}{W_{sorb.}}$$

where

V_{H_2S} is volumetric rate of feed stream (m^3/s)

t_b is breakthrough time (s)

$C_{A,in}$ is H_2S concentration (mol/m^3)

MW_S is molecular weight of elemental sulphur

$W_{sorb.}$ is adsorbent loading in the reactor (g).

3.3.1 Desulphurization setup

The desulphurization performance of the sorbents was evaluated at 300 °C and room pressure by the breakthrough curves in a vertical quartz tubular reactor (10 mm I.D. x 200 mm length), coaxially located inside an electrical furnace. Quartz wool was used to support the sorbent bed (0.05 or 0.10 g) inside the reactor. Figure 5 shows a photo of the scale-laboratory pilot plant which consists of a gas feed system, fixed-bed reactor, an on-line quadrupole mass spectrometer, a TPD/R/O instrument, and a data acquisition computer. Figure 6 shows a similar schematic diagram of the experimental setup^[3].



Figure 5. Scale-laboratory pilot plant for the desulphurization tests.

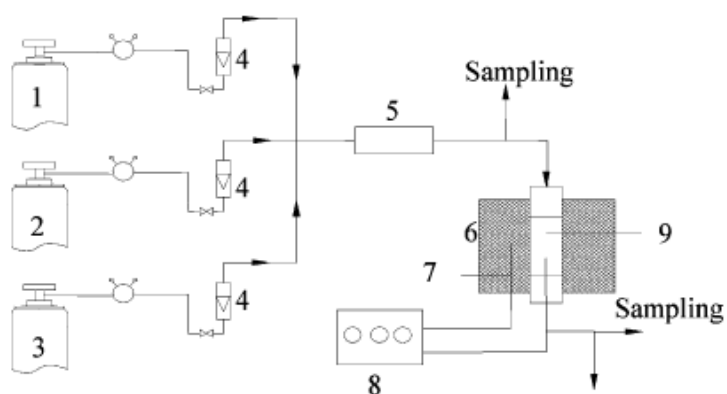


Figure 6. Schematic diagram of experimental setup: 1) Helium tank; 2) Air tank; 3) H_2S tank; 4) mass flow controllers; 5) gases mixer; 6) furnace; 7) thermocouple; 8) temperature controller; 9) fixed-bed reactor^[3].

The gas flow rates were controlled by mass flow controllers (Horiba SEC-E440). Prior to the desulphurization run, helium gas was fed into the reactor for 30 min at 300 °C in order to remove any water and/or impurities adsorbed on the sorbent surface. The H₂S-He reactant gas (1.5 % v/v H₂S, He balance) was then admitted (inlet flow rate 20 cm³/min) and the H₂S uptake during the adsorption test was monitored using a quadrupole mass spectrometer (Thermo Electron Corporation), where the detection limit of H₂S was about 50 ppm. Through the mass spectrometer (MS), the variations of the species concentration resulting from the treatment (H₂O, H₂S, SO₂) were followed, and then processed by the "Gasworks" management software. The calibration for MS detector was carried out by using known concentrations of H₂S mixture gases.

When the H₂S concentration in the outlet gas reached 15000 ppmv (saturation), the inlet stream was stopped and helium was introduced to purge the system. The breakthrough capacity or Sulphur Retention Capacity (SRC), indicating the amount of sulphur retained per unit mass of sorbent, was determined when the outlet concentration of H₂S attained to 100 ppm.

After adsorption of H₂S the samples are referred to as "sulphided" (S) samples. The breakthrough time has been assessed by subtracting the blank from the experimental profiles.

3.3.2 Multicycle Tests and Sorbent Regeneration

Commercial interest in any sorbent will be determined not only on the basis of its behaviour during sulphidation but also upon its regeneration characteristics and durability through a number of sulphidation-regeneration cycles^[4,5]. The regeneration characteristics of a sorbent are very important for its application in industry. For these reasons, to determine the sorbents regenerability synthesized and tested in the present study, four cycles of consecutive sulphidation-regeneration were performed.

The regeneration experiments were performed in the same packed-bed reactor set-up on sulphided samples. Sulphided solids were purged in nitrogen for about 30 min and then regenerated with a "Temperature/Programmed/Oxidation" TPO runs on a Thermo Electron 1100 TPD/R/O apparatus

equipped with both a thermal conductivity detector (TCD) and a quadrupole mass spectrometer (QMS). The sulphided samples were heated under flowing air (20 cm³/min) up to 500 or 700 °C (heating rate 10 °C/min) and hold for 4h or 3h, respectively. The exit gas from regeneration runs was analyzed for H₂S, SO₂, H₂O and O₂ by mass spectrometer.

The standard regeneration procedure was conducted as follows. After the sulphidation test, the reactor and all the gas line were permit to purge at 500 °C under flowing helium to desorbs any H₂S; this procedure was terminated when the H₂S concentrations in the off-gas fell to about zero. Then, the regeneration gas was switched to the air flow at 500 or 700 °C. The regeneration gas was continued until the SO₂ content of the off-gas was reduced to approximately zero.

3.4 Characterization of the sorbents

Although a variety of techniques exist for the characterization of heterogeneous catalysts and support materials, SBA-15 silica and related nanocomposites are most frequently studied with X-ray diffraction and N₂ physisorption. First of all, the application of X-ray diffraction for the characterization of a basically amorphous material appears to be rather useless, since X-ray diffraction is always used to attain information on crystalline materials. Nevertheless, the prerequisite for X-ray diffraction is that the materials studied display long-range structural ordering, and as discussed in the section of "Mesoporous SBA-15", the SBA-15 silica presents a well-ordered lattice. Moreover, because of the geometry of its lattice, SBA-15 can be indexed with a hexagonal unit cell, with $a = b$ and $c = \infty$. Because the parameters a and b are in the order of nanometers instead of tenths of nanometers, as usually encountered in crystals, X-rays are diffracted over small angles only. Therefore, characterization of SBA-15 with X-ray diffraction yields a diffractogram with a limited number of reflections, all situated at low angles. Low-angle ($2\theta = 0.8-2.5^\circ$) and wide-angle ($2\theta = 10-70^\circ$) X-ray diffraction patterns were recorded on a Philips PanAnalytical X'Pert Pro diffractometer with a θ - θ Bragg Brentano geometry with Cu K α wavelength. Low-angle diffraction patterns were recorded using a zero-background silicon sample

holder. The coherent domain (crystallite size) was obtained by Scherrer's equation using the Warren correction^[6].

Since these nanocomposite sorbents are highly porous and with high surface area, it is necessary to specify the nature of pore structure. Gas adsorption is a technique that permits to obtain a comprehensive characterization of porous materials with respect to the specific surface area, pore size distribution and porosity. Textural analysis was carried out on a Sorptomatic 1990 System (Fisons Instrument) by determining the nitrogen adsorption-desorption isotherms at $-196\text{ }^{\circ}\text{C}$. Prior to analysis, the samples were heated overnight under vacuum up to $220\text{ }^{\circ}\text{C}$ (heating rate $1\text{ }^{\circ}\text{C}/\text{min}$). The Brunauer-Emmett-Teller (BET) specific surface area and pore volume were assessed from the adsorption data. The mean pore diameter was determined by applying the Barrett-Joyner-Halenda (BJH) model to the isotherm desorption branch^[7].

The topographic information by TEM in the vicinity of atomic resolution can be used for structural characterization and identification of various phases of mesoporous materials (hexagonal, cubic or lamellar). TEM also provides real space image on the atomic distribution in the bulk and surface of a nanocrystal. Transmission Electron Microscopy (TEM) investigation was carried out using a Jeol 200CX microscope operating at an accelerating voltage of 200 kV. High resolution transmission microscope (HRTEM) images were collected using a Jeol 2010 UHR equipped with a Gatan Imaging Filter (GIF) with a 15 eV window and a 794 slow scan CCD camera. Finely ground samples were dispersed in *n*-octane and subjected to an ultrasonic bath and the suspensions were then dropped on carbon-coated copper grids for the TEM and HRTEM observations.

Infrared spectroscopy has been extensively used for identifying the various functional groups on the catalyst or sorbent itself, as well as for identifying the adsorbed or formed species. FTIR spectra were collected using a Bruker Equinox 55 spectrophotometer at room temperature in the $400\text{ to }4000\text{ cm}^{-1}$ region. The samples were analyzed dispersing the powders in KBr pellets.

X-ray Photoelectron Spectroscopy (XPS) is an analysis technique that uses X-rays in an ultra high vacuum environment to investigate the chemical compounds on a sample surface. This is a very simple

process that can supplies a vast amount of information about a sample; including composition and chemical states. X-ray Photoelectron Spectroscopy analyses were performed by using an ESCALAB200 spectrometer manufactured by Vacuum Generator Ltd., East Grinstead, U. K. A non-monochromatic Al K α X-ray source (1486.6 eV, 15 mA, 20 keV) was used and samples were analyzed as pellets. More details regarding the instrument configuration and data analysis have been reported elsewhere ^[8].

References

- [1] A. Pettinau, G. Cali, E. Loria, P. Miraglia and F. Ferrara, *Appl. Therm. Eng.*, **2015**, 74, 2.
- [2] D. Zhao, J. Feng, Q. Huo, N. Melosh, G. H. Fredrikson, B. F. Chmelka and G. D. Stucky, *Science*, **1998**, 279, 548.
- [3] R. Zhang, J. Huang, J. Zhao, Z. Sun, and Y. Wang, *Energy & Fuels*, **2007**, 21, 2682.
- [4] P. Dhage, A. Samokhvalov, D. Repala, E. C. Duin, M. Bowman and B. J. Tatarchuk, *Ind. Eng. Chem. Res.*, **2010**, 49, 8388.
- [5] B. S. Liu, Z. Y. Wan, Y. P. Zhan and C. T. Au, *Fuel*, **2012**, 98, 95.
- [6] H. P. Klug and L. E. Alexander, in *X-Ray diffraction procedures: For polycrystalline and amorphous materials*, ed. John Wiley & Sons, Inc., New York, **1954**, ch. 9, pp. 491-538.
- [7] E. P. Barret, L. G. Joyner and P. P. Halenda, *J. Am. Chem. Soc.*, **1951**, 73, 373.
- [8] M. Fantauzzi, A. Rigoldi, B. Elsener, D. Atzei and A. Rossi, *J. Electron Spectrosc. Relat. Phenom.*, **2014**, 193, 6.

4.1 Preparation of ZnO/SBA-15 nanocomposite sorbents

In the present work, to optimize and better understand the impregnation process in itself, two distinct series of samples were prepared and characterized. Both series of the zinc oxide-based sorbents were prepared by two different post-synthesis metal oxide loading techniques including the classical Incipient Wetness Impregnation (**IWI-series**) and the innovative Two-Solvents method (**TS-series**).

The efficient infiltration of the precursor in the mesochannels is a key factor for a sufficient pore filling and a complete cross-linking of the material inside the pore system. Zinc nitrate was chosen as the precursor due to its high solubility in water, low decomposition temperature (*ca.* 130 °C), and the gaseous by-products easily removable from the pores of the matrix. Before impregnation, the silica support was dried for 12 h in a drying oven at 100 °C to remove physisorbed water.

The procedure for the IWI series was as follows: 0.4 g of SBA-15 powder were put in contact under stirring at room temperature for 45 min with 2.4 cm³ of a zinc nitrate ($(\text{Zn}(\text{NO}_3)_2 \cdot 6\text{H}_2\text{O}$, Aldrich, 98%) aqueous solution containing 0.15, 0.45 or 0.90 g of salt to provide 10, 30 and 60 wt.% zinc oxide loadings, respectively (**Figure 1**). Each batch was then treated for 20 min in ultrasonic bath. The solid was then recovered by dried overnight in static air at 40 °C. Calcination treatments were carried out in a oven by heating from room temperature to 500 °C with a ramp of 2 °C/min for 2 h to quantitatively convert zinc nitrate quantitatively to zinc oxide. The fresh sorbents are labelled as IWI_10_T500, IWI_30_T500 and

IWI_60_T500, where 10, 30 and 60 represent the wt.% ZnO content. A portion of each sorbent was further calcined for 1 h at 600 °C to obtain the following samples: IWI_10_T600, IWI_30_T600 and IWI_60_T600.

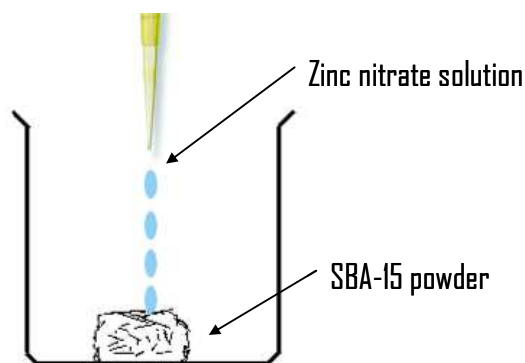


Figure 1. Graphical representation of the Incipient Wetness Impregnation technique.

The TS-series sorbents were prepared initially by suspending 0.4 g of SBA-15 powder in 12 cm³ of *n*-hexane, used as a hydrophobic solvent. After stirring for 15 min at 400 rpm, 0.48 cm³ of 0.5 or 1.5 mmol of Zn(NO₃)₂·6H₂O aqueous solutions, quantities corresponding to the pore volume of SBA-15 determined by N₂ physisorption, was added drop wise (Figure 2). Each of the resulting dispersions was vigorously stirred for 2 h at room temperature before recovering the solid, which was then dried overnight in static air at 40 °C. The resulting white powders were finally calcined at 500 °C for 2 h (heating rate 2 °C/min) to obtain the desired sorbent. The fresh sorbents are labelled as TS_10_T500 and TS_30_T500 sorbents, where 10 and 30 represent the wt.% ZnO content. A portion of each sorbent was further calcined at 600 °C for 1 h (heating rate 2 °C/min) for obtaining the TS_10_T600 and TS_30_T600 samples.

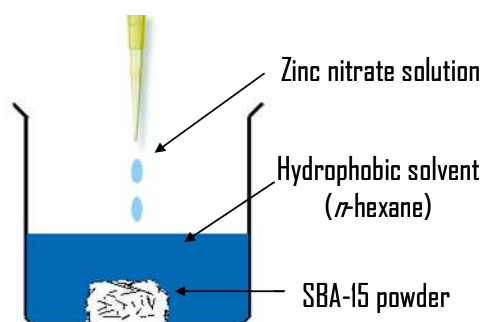


Figure 2. Graphical representation of the Two-solvents technique.

The white powders of the fresh zinc oxide-based sorbents (TS- and LWI-series) were ground in a mortar with pestle and stored in desiccators for further use. In [Figure 3](#) a photo of the final material is reported.



Figure 3. Fresh ZnO/SBA-15 sorbent.

4.2 Low- and wide-angle X-ray diffraction characterization

The results of the structural characterization are summarized in [Figure 4](#). The low-angle diffraction patterns of the bare SBA-15 and the ZnO/SBA-15 composites treated at 500 °C are shown in [Figure 4a](#). Three well-resolved diffraction peaks, which can be indexed as the (100), (110) and (200) reflections associated with a hexagonal symmetry, are present in the XRD pattern of bare SBA-15. This is in agreement with the presence of a two-dimensional hexagonal $P6mm$ structure with a large unit-cell

parameter^[1]. These peaks are clearly visible also in the diffraction patterns of all the sorbents, which indicate that the ordered mesoporous structure of SBA-15 is retained after incorporation of ZnO. A slight shift of the peaks towards higher values of 2θ seems to occur just for the IWI_60 composite, which suggests a slight shrinkage in the mesoporous framework, possibly due to a higher degree of silicate condensation after ZnO addition, in agreement with the suggestion of some authors^[2].

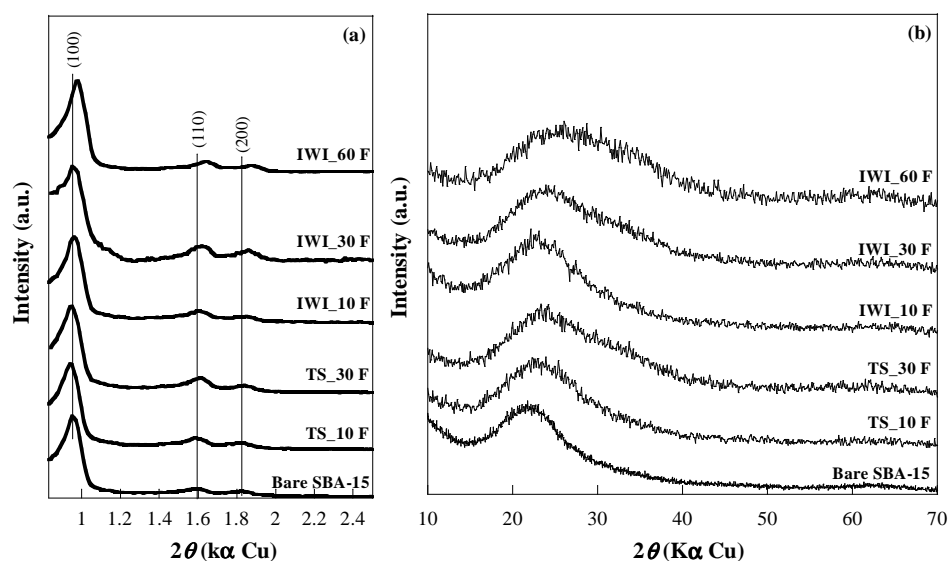


Figure 4. XRD patterns of bare SBA-15 and ZnO/SBA-15 fresh sorbents treated at 500 °C at low angle (a) and wide angle (b).

The hexagonal unit cell parameter a_H is calculated from the d -spacing (Figure 5) values starting from the experimental data using the geometrical relationship:

$$a = \frac{d}{\cos 30^\circ} = \frac{2d}{\sqrt{3}}$$

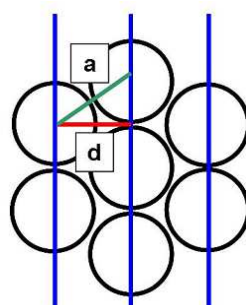


Figure 5. Scheme of hexagonal packed channels with relationship between diffraction planes (blue lines) with associate distance (d) and centre-to-centre distance (a).

The calculated d -spacing and unit cell parameters are well-matched with the hexagonal $P6mm$ space group. Table I shows the d_{00} spacing and the cell parameter obtained from the low-angle XRD patterns.

Table I. d -spacing and unit cell parameter of the fresh nanocomposite sorbents.

Sample	d_{00} (nm)	a_0 (nm)
Bare SBA-15	9.3	10.7
TS_10 F	9.4	10.8
TS_30 F	9.3	10.7
IWI_10 F	9.2	10.6
IWI_30 F	9.3	10.7
IWI_60 F	9.0	10.4

Relative Standard Deviation: %RSD (d_{00}) = 1%.

Figure 4b illustrates the wide-angle diffraction patterns for all the samples and shows the typical haloes of amorphous silica at $2\theta = ca. 23^\circ$. No evident diffractions peaks corresponding to ZnO are present in the nanocomposites treated at 500 °C. Besides the silica haloes, the patterns of the samples

with high ZnO content (TS_30, IW1_30 and IW1_60), exhibit a shoulder at $2\theta = ca. 30^\circ$ and a large band at $2\theta = ca. 60^\circ$ (IW1_60) corresponding to the region where the most intense reflections ((100), (002), (101)) of the ZnO phase occur (PDF-Card 80-0075). For these samples, the presence of shoulders and large bands instead of peaks suggests the formation of very small ZnO nanoparticles^[3]. It indicates that the crystalline size of metal oxide is below the XRD detection limit (*ca.* 2-3 nm) or an amorphous metal oxide phase is formed. On the whole the above results indicate that a good dispersion of ZnO over/into SBA-15 has been achieved and guest has been highly dispersed in the mesopores. Further treatment of the composites at 600 °C did not result in any modification of both the low and wide angle XRD patterns (not shown).

4.3 N₂ physisorption measurements: textural properties

The nitrogen adsorption-desorption isotherms of the IW1- and TS-series sorbents resulting from calcination at 500 °C are presented in [Figures 6a and 7a](#), respectively, where the isotherm for the bare SBA-15 is also reported for comparison. SBA-15 exhibits a type IV isotherm with a H1 type hysteresis loop, as defined by IUPAC^[4, 5]. Such a profile is characteristic of a mesoporous material with uniform cylindrical pores open at both ends. The shape of the isotherm is not significantly modified by the ZnO loading, which indicates that the ordered structure of SBA-15 is preserved in the sorbents. The pore size distribution plots for both IW1- and TS-series ([Figures 6b and 7b](#), respectively) show a narrow monomodal distribution. However, a progressive broadening of the pore size distribution upon increasing the ZnO loading, as well as a slight decrease of the mean pore diameter, is revealed for the IW1- and TS-series sorbents. This is consistent with the presence of a layer, clusters or small zinc oxide nanoparticles, in agreement with the XRD. The pore structure analysis further confirms the mesoporosity and that zinc oxide loading occurred inside the pore channels of the SBA-15 support. Furthermore, the BJH pore size distribution of each sample is narrow, suggesting an open mesopore

channels. It also implies that the active phase is well dispersed and accessible via the open pore channels.

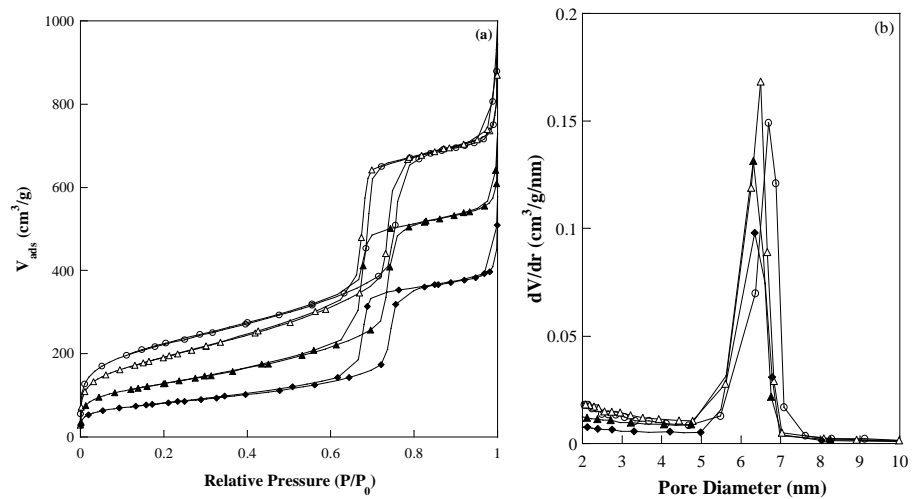


Figure 6. Nitrogen adsorption-desorption isotherms (a) and pore size distribution (b) of the bare SBA-15 and IW1_1500 fresh sorbents (empty circles bare SBA-15, empty triangles IW1_10, full triangles IW1_30, full rhombs IW1_60).

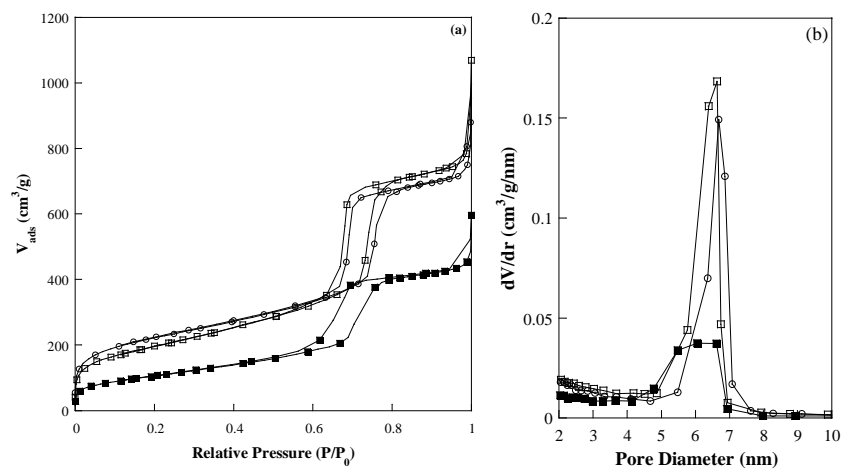
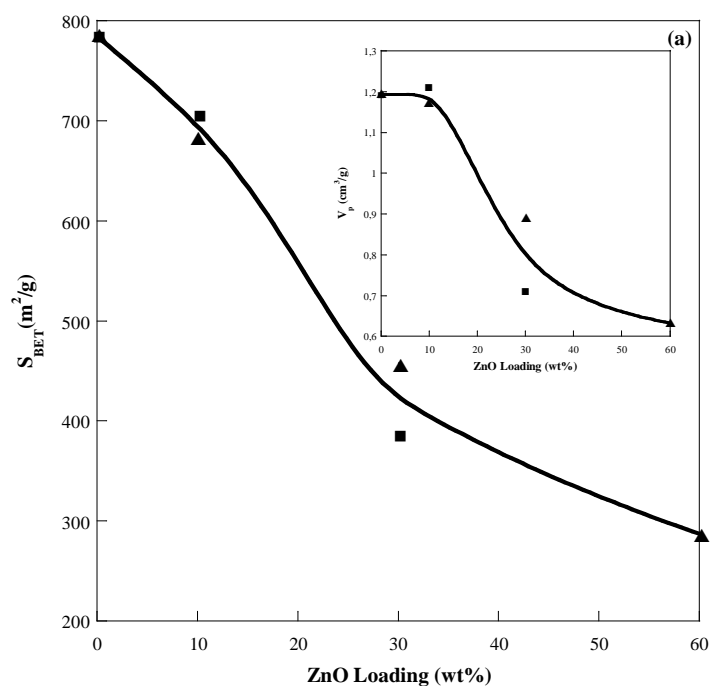


Figure 7. Nitrogen adsorption-desorption isotherms (a) and pore size distribution (b) of the bare SBA-15 and TS_1500 fresh sorbents (empty circles bare SBA-15, empty squares TS_10, full squares TS_30).

By subtracting the mean pore diameter (obtained by N_2 physisorption data) from the unit cell parameter (a_0 , calculated from low-angle XRD data), the wall thickness (T_w) values of the sorbent channels were calculated, being 4.0, 4.1-4.3 and 4.4-4.5 nm for the SBA-15 support, the IW1-series and the TS-series samples, respectively. The N_2 adsorption-desorption data for the IW1- and TS-series sorbents resulting from calcination at 500 °C followed by further treatment at 600 °C (not shown) revealed that also in this case the ordered mesoporous structure of SBA-15 is retained after loading of the active phase; upon increasing the ZnO content, an enlargement of the pore size distribution, accompanied by a slight decrease of the mean pore diameter, was observed as well.

The main textural properties of the synthesized samples resulting from calcination at 500 °C are displayed in Figure 8, including BET surface area (S_{BET}) and pore volume (V_p), and discussed below.



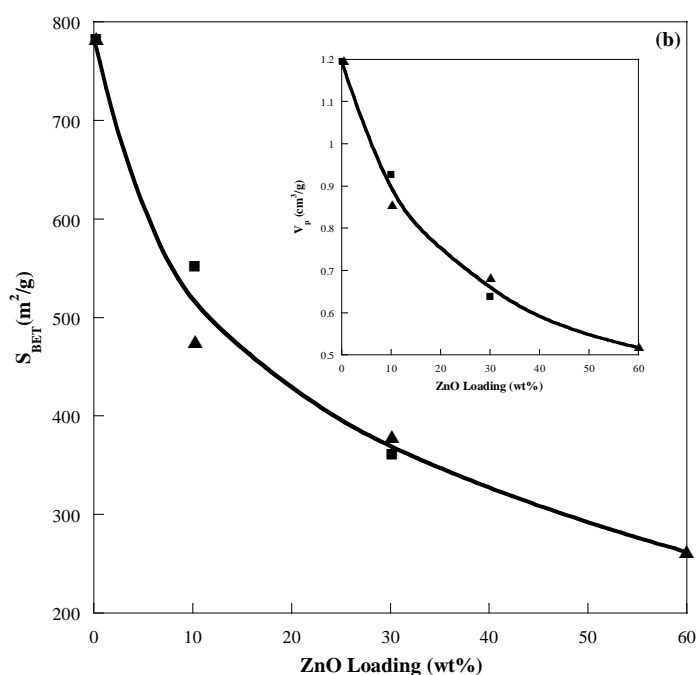


Figure 8. Surface area and pore volume (inset) versus ZnO loading for the IW- and TS-sorbents treated at 500 °C (a) and at 500 °C + 600 °C (b) (full triangles IW-series, full squares TS-series).

The values of S_{BET} and V_p both show a monotonic decrease upon increasing the ZnO loading. The data points for the IW- and TS-series sorbents are interpolated by the same decreasing curve. This also holds for the samples further calcined at 600 °C (Figure 8b), for which however a steeper decrease of S_{BET} and V_p upon increasing the ZnO loading is observed. Comparison of Figure 8b with Figure 8a reveals that this is due to a major detrimental effect of the additional calcination step on the textural features of the sorbents with a ZnO loading of 10 wt.%. Only for the highest zinc oxide loading (60 wt.%) the S_{BET} and V_p values are less than 50 % of the corresponding values for the SBA-15 host. Apparently, at least for the present sorbents, no significant effects on the textural features result from the use of the Two-Solvents method instead of the traditional Incipient Wetness Impregnation.

4.4 TEM images: morphological characterization

Morphology as well as structural ordering of bare SBA-15, IWI- and TS-series sorbents, were investigated by transmission electron microscopy studies and are shown in Figure 9. The TEM images of bare SBA-15 silica support in Figures 9a and 9b show highly ordered hexagonal arrays of mesopores with dimensional channels along two directions, parallel (Figure 9a) and perpendicular (Figure 9b) to the pore axis of which correlated to a 2D-hexagonal structure ($P6mm$). The average pore diameter is about 6-7 nm and thickness of the wall is approximately 3-4 nm, which supports the aforementioned N_2 physisorption and low-angle XRD results.

In spite of the weak difference in the electronic density contrast between silica and zinc oxide, which makes difficult their detailed investigation, the TEM images of the IWI-series samples (Figures 9c-e) reveal a good dispersion of the active phase into/over the support, in agreement with the XRD data. The micrographs of the samples with less zinc oxide content (10 and 30 wt.%) revealed that no ZnO particles have been found on the outside surface of the host. In the case of the most concentrated sample (IWI_60), zinc oxide nanoparticles with sizes (10-20 nm) larger than the pore size are also visible on the surface (Figure 9e). Dark Field image of IWI_60 (inset of Figure 9e) shows the presence of small nanoparticles outside the support; it seems reasonable to think of such particles as originally deposited on the surface, their detachment being caused by the ultrasonic treatment of the sample for TEM analysis. The micrographs in Figures 9f-h clearly indicate that a good dispersion of ZnO into/over the support is obtained also for the TS-series sorbents, no presence of aggregates or large nanocrystals of zinc oxide being revealed. Figures 9f and 9g are worthy of a further comment. The former shows two portions of the TS_10 sample: the one at the right is ZnO-free, whereas in the portion at the left the zinc oxide phase seems to fill homogeneously the cylindrical channels of the support. At the bottom of Figure 9g a portion of bare SBA-15, with neat channel contours, is visible. By converse, on the top of the same TEM image the channel contours of the solid appear rough, with a rope-like profile, suggesting a preferential zinc oxide nucleation and growth on the surface of the pore walls. These observations are

consistent with the XRD results and confirm that this preparation approach is favourable to maintain the highly ordered mesostructure.

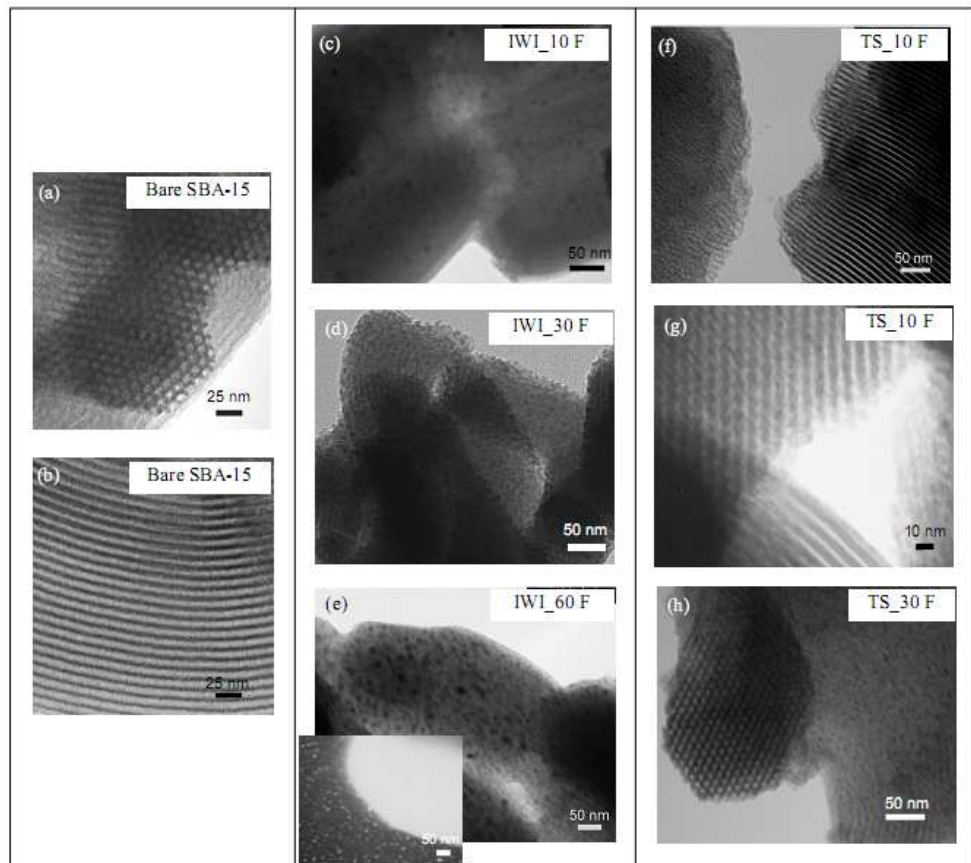


Figure 9. TEM images of mesostructured SBA-15 (a,b) and ZnO/SBA-15 sorbents prepared via conventional Incipient Wetness Impregnation (c,d,e) and Two-Solvents routes (f,g,h).




4.5 Desulphurization behaviour and post-sorption characterization of the ZnO/SBA-15 sorbents

4.5.1 Desulphurization runs

The sulphidation breakthrough curves may be divided into three sections: pre-breakthrough, active-breakthrough, and post-breakthrough. The pre-breakthrough portion is the most important section because it identifies the ultimate H₂S removal capability of the sorbent at the reaction conditions. During the pre-breakthrough portion, most of the H₂S gas reacted with zinc oxide, and the product gas contained less than 100 ppmv of H₂S. At the beginning of the active-breakthrough region, the leading edge of the sulphidation reaction front reached the exit of the sorbent bed and the product H₂S concentration began to increase with time. During post-breakthrough, the sorbent bed approached complete conversion and essentially all the H₂S in the feed gas passed through the sorbent bed without reaction. The effluent H₂S concentration in this region match the H₂S concentration in the feed gas (15000 ppmv).

To help to ensure clarity, only the pre-breakthrough and the first part of the active-breakthrough have been represent in all the figures reported in the thesis.

The aim of the first part of the desulphurization tests was to study the different effects on the breakthrough curves and sulphur retention capacity. They are:

-  Effect of the synthesis method;
-  Effect of the zinc oxide loading;
-  Effect of the calcination treatment.

4.5.2 Effect of the synthesis method

The influence of the synthesis method was studied using the two different procedures for the confinement of the active phase in the silica host, that are the classical Incipient Wetness Impregnation (IWI) and the innovative Two-solvents (TS). The study was carried out with the same ZnO loading (10 or 30 wt.%).

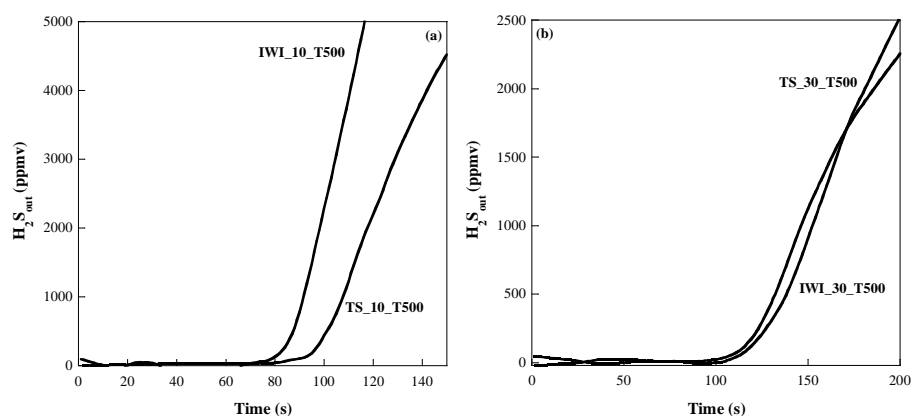


Figure 10. *H₂S breakthrough curves of ZnO/SBA-15 sorbents at 10 wt.% (a) and 30 wt.% (b) prepared through IWI and TS methods.*

All the sorbents have a very similar trend (Figure 10). The breakthrough time is higher in the sorbent synthesized with the Two-solvents method when the lowest ZnO loading (10 wt.%) is considered, therefore indicating a greater sulphur retention capacity; this could be due to the fact that the "Two-solvents" route allows to disperse more effectively the active phase inside the support. When the higher ZnO content is considered (30 wt.%), the two synthetic approach (IWI and TS) seem to produce the same result.

4.5.3 Effect of the zinc oxide loading

To study the influence of the ZnO content, the sorbents were tested at low, medium and high content of active phase (10, 30 and 60 wt.%), synthesized both with the classical and innovative impregnation techniques (IWI- and TS-series).

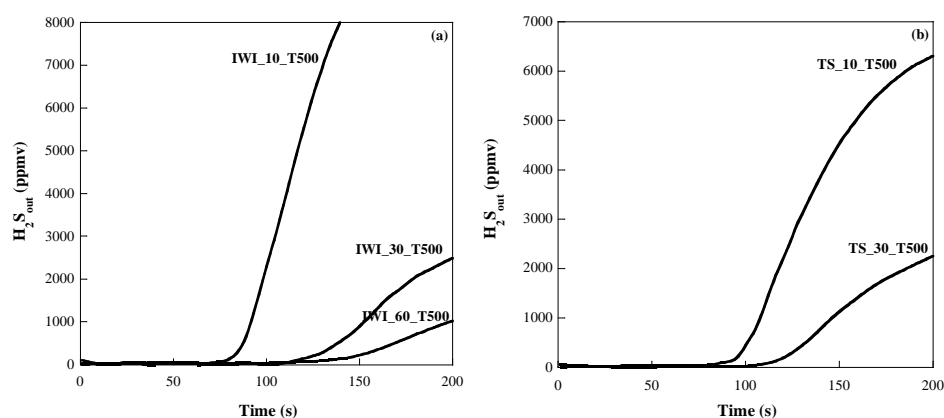


Figure 11. *H₂S breakthrough curves of ZnO/SBA-15 sorbents at 10, 30 and 60 wt.% prepared through IWI (a) and TS (b) methods.*

As expected, it can be noted that with the increase of the active phase loading from 10 to 30 wt.%, the desulphurization performance significantly improves both in the IWI- and TS-series (Figure 11). The variation of the load from 30 to 60 wt.% does not improve proportionally the H₂S removal capacity, in fact, the IWI_30 and IWI_60 curves appear almost overlapped in the first stretch. This could be due to an increase of the particle size of the active phase as the load increases resulting in: (i) exposure of a lower number of active sites and (ii) a partial blockage of the pores by both zinc oxide that product sulphidation, which would limit or prevent access to the active sites present on the particles deposited inside the channels of SBA-15.

4.5.4 Effect of the calcination treatment

Figure 12 reports the breakthrough curves comparison between the sorbents treated at 500 °C and 600 °C.

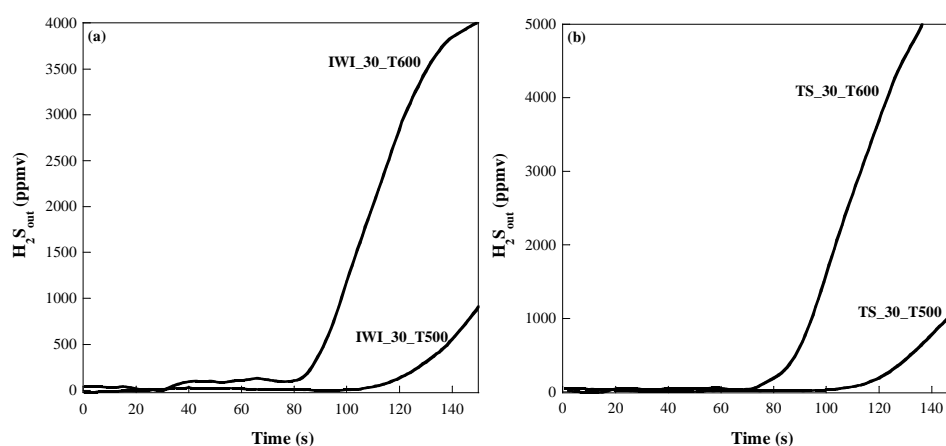


Figure 12. H_2S breakthrough curves of ZnO/SBA-15 nanocomposites at temperature of 500 and 600 °C prepared through IWI (a) and TS (b) methods.

In all cases, the calcination treatment at 600 °C seems to adversely affect the ability of H_2S removal; this fact is well visible in both the IWI- and TS-series sorbents. The decreased ability of H_2S removal could be associated to the growth of particles which hamper the active centres for the gas-solid reaction, due to the mid-percentage (30 wt.%) of the active phase.

The breakthrough time, assessed by subtracting the blank from the experimental profiles, is reported in Table 2 for all the sorbents. In the same Table 2 the sulphur retention capacity, referred to the unit mass of both the active phase and the sorbent, is also reported.

Table 2. Breakthrough time (B_t) and H_2S Sulphur Retention Capacity of the IWI- and TS- sorbents series resulting from one-step (500 °C) and two-step (500 °C + 600 °C) calcination for sorption runs at 300 °C. Data obtained on the commercial Katalco_{JM} 32-5 sorbent are also reported for comparison.

Sample	Calcination (°C)	B_t (s)	Retention Capacity (mg _S /g _{ZnO}) ± 1	Retention Capacity (mg _S /g _{sorbent}) ± 1
Katalco _{JM} 32-5	-	100	13	13
SBA-15	-	-	-	-
IWI_10	500	28	36	4
	600	14	18	2
IWI_30	500	66	29	9
	600	30	13	4
IWI_60	500	80	17	10
	600	27	6	4
TS_10	500	40	52	5
	600	10	13	1
TS_30	500	66	29	9
	600	26	11	3

The H_2S adsorption of the ZnO/SBA-15 sorbents was compared with the commercial ZnO samples obtained from Sud-Chemie (Katalco_{JM} 32-5). As expected, the maximum value for the breakthrough time (100 s) is observed for the unsupported ZnO commercial sample, and, within the series of SBA-15-supported sorbents, increases with the active phase loading, the maximum (80 s) being observed for the IWI_60 composite. It is worthy of note that the highest retention capacity per unit mass of ZnO is obtained for the TS_10_T500 sample (52 mg S/g ZnO), followed by the IWI_10_T500 sample (36 mg S/g ZnO), both being much more higher than the corresponding value for the commercial ZnO sorbent (13 mg

S/g ZnO). This suggests that the use of a high surface area support for dispersing on a nanometric scale the active phase enhances the ability of the latter to react with the pollutant gas. To check the effect of the textural features on the sulphur retention capacity, the values of the latter have been plotted *vs.* both the surface area and the pore volume for all the samples in Figure 13. The data points cannot be interpolated by the same curve. On the contrary, each set of points, homogeneous as to the preparation method (IWI or TS) or to the calcination conditions (500 °C or 500 + 600 °C), requires a specific curve. This allows one to conclude that the effectiveness of the active phase in the H₂S removal does not depend on the textural features only.

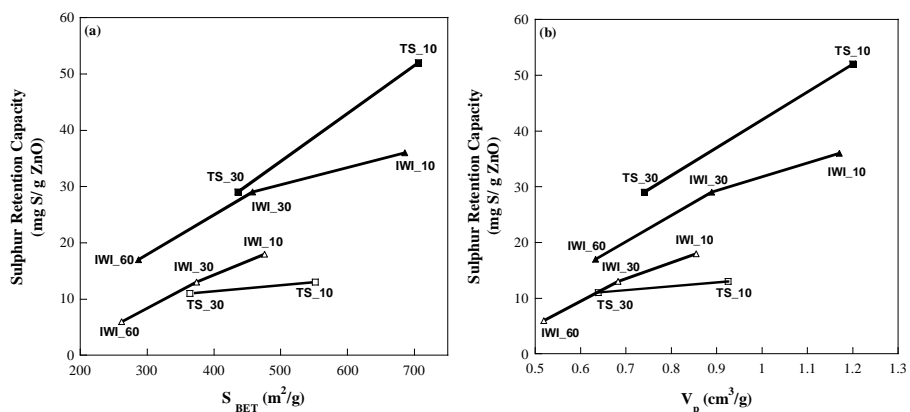


Figure 13. Sulphur retention capacity of the ZnO/SBA-15 sorbents versus S_{BET} surface area (a) and V_p pore volume (b).

It is worthy of note that the curve for the TS_T500-series samples lies above that for the IWI_T500-series, which suggests that the better way of exploiting the peculiar structure of SBA-15 is that of using the Two-Solvents methods for the confinement of the ZnO phase into its channels. Whatever the preparation method, further treatment at 600 °C after the first calcination step at 500 °C is detrimental for the performance of the active phase: for the IWI_T600-series, the curves of the sulphur retention

capacity *vs.* S_{BET} and *vs.* V_p (Figures 13a and 13b, respectively) lie below the one for the IWI_T500-series: The same holds for the TS_T600 and TS_T500-series, being the loss of sulphur retention capacity greater for the TS-series sorbents.

4.6 Characterization of the sulphided sorbents

After the sorption runs, the support mesostructure is retained (as indicated by the low-angle patterns of Figures 14a and 14b), except for the IWI_60 sorbent (which shows very large bands instead of peaks).

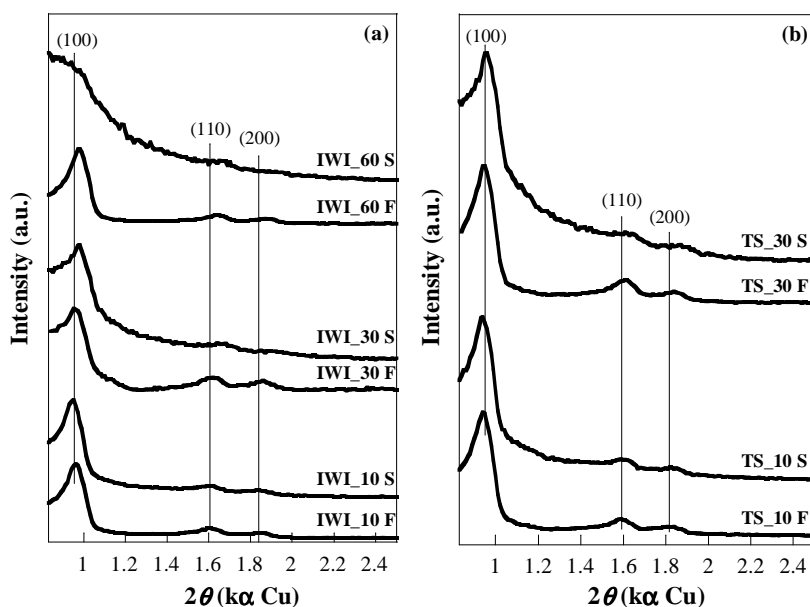


Figure 14. Low-angle XRD patterns of IWI_T500 (a) and TS_T500 (b) samples series before (F) and after sulphidation (S).

The wide-angle XRD patterns of the sorbents are presented in Figure 15, where the patterns for the corresponding fresh sorbents are also shown for comparison. In addition to the broad band attributable to amorphous silica, clear and intense reflections at 28.6° , 47.7° and 56.6° , easily assigned to hexagonal ZnS phase (PDF Card 12-688), appear in the patterns of all the samples used in the sorption experiments.

A rough estimation of the mean crystallite size of the ZnS nanoparticles by Debye-Scherrer equation gives a value in the 3-5 nm range.

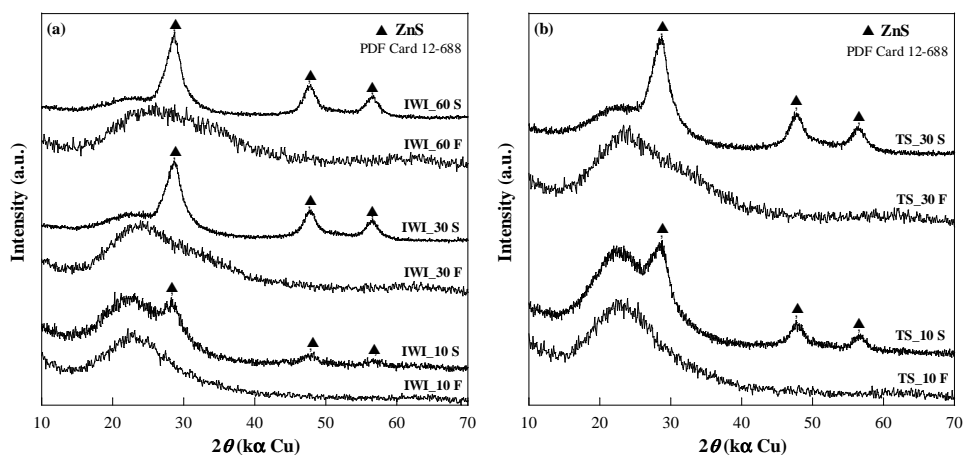


Figure 15. Wide-angle XRD patterns of fresh (F) and sulphided (S) ZnO/SBA-15 samples. IWI-series (a) and TS-series (b). The data refer to the sorbents originated by the one-step calcination at 500 °C.

HRTEM micrographs of the sulphided IWI₃₀ sorbent are presented in Figure 16. Due to the nanocrystalline nature of the ZnS phase and the increased electronic density contrast, if compared with ZnO, it is possible to evidence that the nanocrystals are mainly anchored at the channel walls. Note the rough contours of the channels, with a rope-like profile, in Figures 16a-c and the rows of small ZnS nanoparticles (3 to 4 nm wide) in the image at higher magnification (Figure 16d). The nanocrystalline nature of the ZnS particles is confirmed from *d* spacing values of 0.31 and 0.33 nm which are in agreement with the (0010) and (100) reflections of hexagonal ZnS phase (PDF Card 12-688) respectively (Figure 16e).

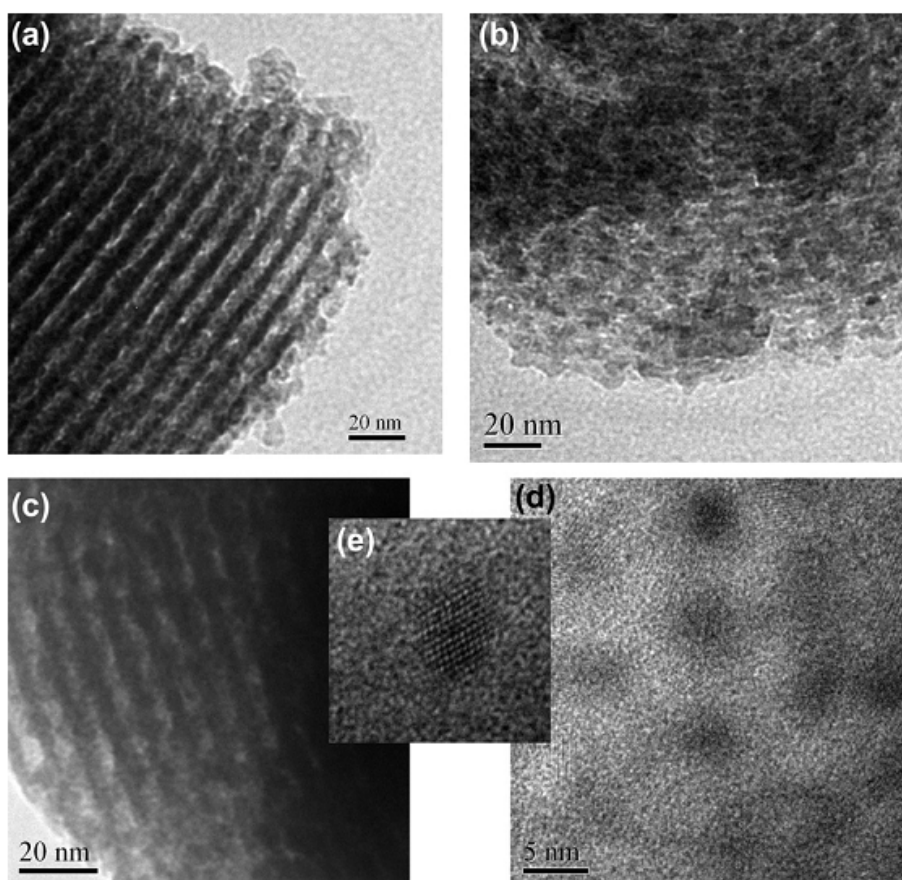


Figure 16. HRTEM images of the sulphided IWI_30_T500 sorbent.

4.7 Sorbents regeneration and desulphurization-regeneration cycles

4.7.1 Temperature-programmed oxidation of the sulphided sorbents

In order to select appropriate regeneration conditions, temperature-programmed oxidation runs in flowing air were carried out on the sulphided IWI_30_T500 sorbent, as well as on the sulphided commercial sorbent. The TPD profile (Figure 17a) obtained by heating under air the sulphided IWI_30_T500 sorbent up to 700 °C and holding for 3 h shows a large peak, centred at 590 °C, originated

by the release of SO_2 as a consequence of the ZnS oxidation. The shape of this peak indicates that the release of SO_2 is complete, *i.e.*, the whole ZnS amount present in the sulphided sorbent has been oxidised under such TPO conditions. Heating under air the sulphided IWI_30_T500 sample up to 500 °C and holding for 4 h (Figure 17a) results in a SO_2 peak of significantly lower area (67 % of the peak area at 700 °C). A further TPO run was also carried out by heating the sulphided IWI_30_T500 sample up to 500 °C, holding for 2 h (time besides which no more SO_2 is released), heating again up to 700 °C and holding for 1 h (Figure 17b). Two peaks can be observed, corresponding to two different steps of SO_2 release. The sum of the areas of the two peaks has the same value of that of the peak obtained by heating the sample up to 700 °C (Figure 17a) and the area of the first peak in Figure 17b is the same of that of the peak obtained upon heating the sample at 500 °C (Figure 17a).

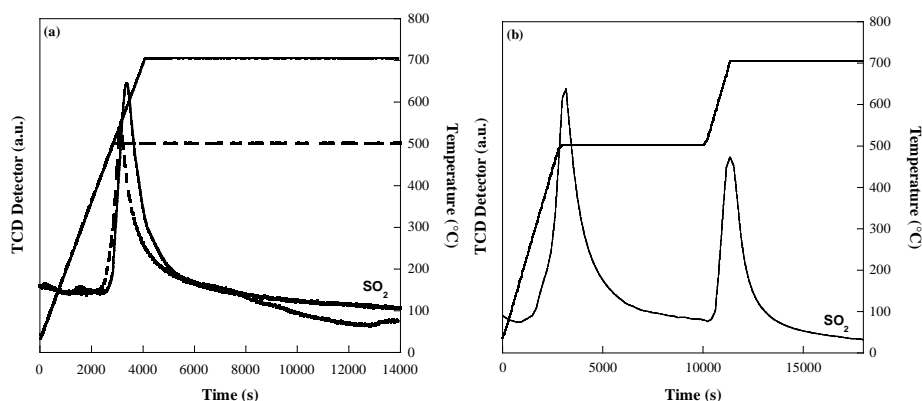


Figure 17. TPO profile of the IWI_30_T500 regenerated at 700 °C for 3 hours (a, solid line), 500 °C for 4 hours (a, dotted line) and regenerated through a two step (500 and 700 °C) treatment (b).

On the one hand, it should be concluded from the above that treating under air up to 500 °C leads to the incomplete release of sulphur from the sulphided sample. On the other hand, in view of the observed (see section 4.5.4) detrimental effect of the higher temperatures on the sulphur retention capacity, it seems safe do not exceed 500 °C in the regeneration step. Another reason for limiting the regeneration

temperature stems from previous ^{29}Si MAS NMR experiments ^[6], which revealed that in the 500-700 °C range depolymerization of the host matrix occurs. This implies the involvement of ZnO in a reaction with silica, which in turn could have, in the present case, a detrimental effect, due to the loss of ZnO active phase. Accordingly, the regeneration step of all the sulphided sorbents was carried out by heating under air flow for 4 h at 500 °C. It is worthy of note that under such conditions the sulphided commercial sorbent is far from being completely regenerated. Actually, remarkable evolution of SO_2 can be observed only upon heating up to 700 °C and holding for 3h (Figure 18).

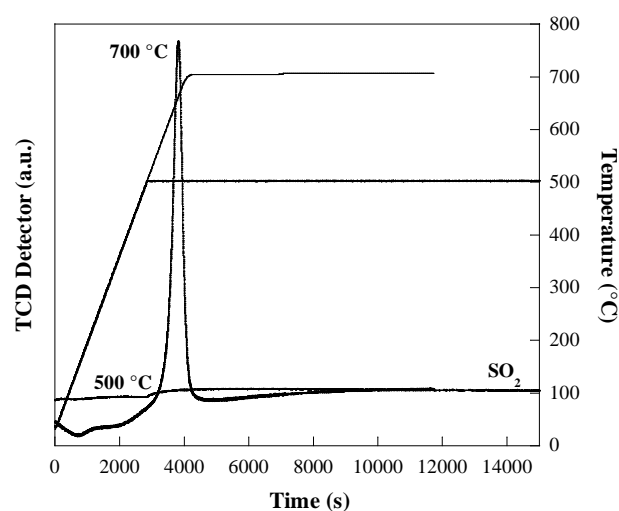


Figure 18. TPO profiles of the Katalco_{JM} 32-5_{JM} commercial sorbent at 500 and 700 °C.

4.7.2 Sorption features of the regenerated samples

Consecutive sorption-regeneration cycles were performed on the IW1_30_T500 and the TS_30_T500 nanocomposites, as well as on the commercial sorbent, and the corresponding breakthrough curves were obtained (Figure 19). The breakthrough time (assessed by subtracting the

blank from the experimental profiles) and the sulphur retention capacity (referred to the unit mass of both the active phase and the sorbent) are reported in [Table 3](#).

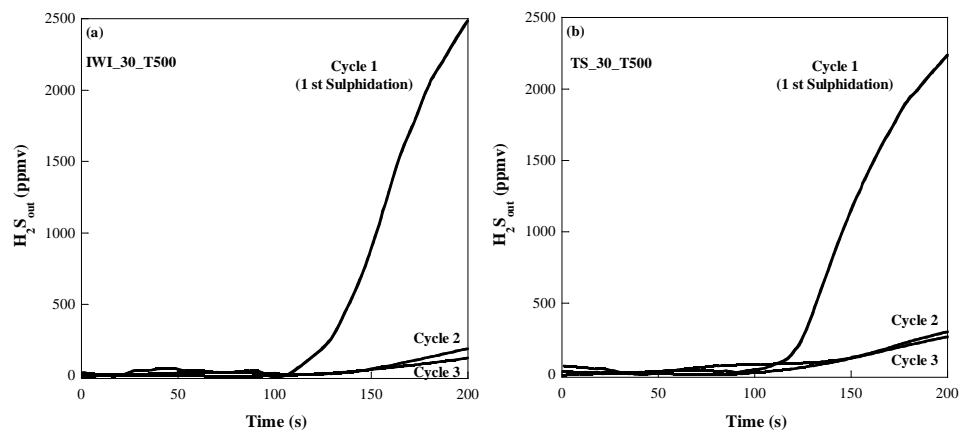


Figure 19. H_2S breakthrough curves upon three sorption-regeneration cycles for IWI_30_T500 (a) and TS_30_T500 (b).

Table 3. Breakthrough time (B_t) and Sulphur Retention Capacity of the fresh and regenerated IWI_30_T500 and TS_30_T500 sorbents during sorption-regeneration cycles. Data for the commercial Katalco_{JM} 32-5 sorbent are also reported for comparison.

Sample	Run number ^(a)	B_t (s)	Retention Capacity (mg _S /g _{ZnO}) ± 1	Retention Capacity (mg _S /g _{sorbent}) ± 1
Katalco _{JM} 32-5	1	100	13	13
	2	25	3	3
	3	25	3	3
IWI_30_T500	1	66	29	9
	2	118	51	15
	3	135	59	18
TS_30_T500	1	66	29	9
	2	92	40	12
	3	95	41	12

^(a) 1 = fresh sorbent; 2 = after 1st regeneration; 3 = after 2nd regeneration.

Expectedly, the results for the commercial sample reveal a poor sorption performance after regeneration, as a consequence of the by far incomplete conversion of the ZnS phase into the active ZnO phase. By converse, the data for the ZnO/SBA-15 sorbents clearly show that the regeneration process enhances their performance, in terms of both breakthrough time and sulphur retention capacity, and that such improvement in the sorbent features is maintained upon further cycling.

In the literature ^[7], the commonly reported feature for regenerated sorbents is a decrease in the H₂S retention capacity as the number of sorption-regeneration cycles increases. Volume expansion occurs during the sulphidation process, as the metal-oxide is converted into metal sulphide, and

subsequent contraction takes place during the regeneration process, as the sorbent returns to the original oxide phase. It is assumed that the repeated occurrence of such expansion/contraction phenomena during the sorption-regeneration cycles causes spalling or cracking of the sorbent, which in turn would lead to the loss of the sorbent performance. Furthermore, some other authors hypothesize that the performance decrease can be also due to the formation of $ZnSO_4$ phase during the regeneration process ^[8]. In this light, the enhanced performance of the present ZnO/SBA-15 sorbents in cycle operation appears somewhat puzzling, also because the complete transformation of the ZnS phase back into ZnO is not achieved during the regeneration step.

Further characterization work has hence been carried out on the regenerated sorbents. Based on FTIR analysis (not shown) on the regenerated sorbents the presence of sulphate phases, induced by the regeneration, can be ruled out. Comparison of low-angle XRD patterns (Figure 20) of the regenerated samples with the corresponding patterns for the sulphided and fresh sorbents reveals a progressive shift toward higher angles along the series: fresh > sulphided > regenerated, which suggests a progressive decrease in the pore size. Because of the volume expansion occurring during the sulphidation process, a decrease in pore size is expected when passing from the fresh to the sulphided sorbent. By converse, a further decrease in the pore size during the regeneration step (*i.e.*, when the metal sulphide phase is converted back into the original oxide phase) is unexpected. Nevertheless, evidence for pore size decrease stems also from textural data.

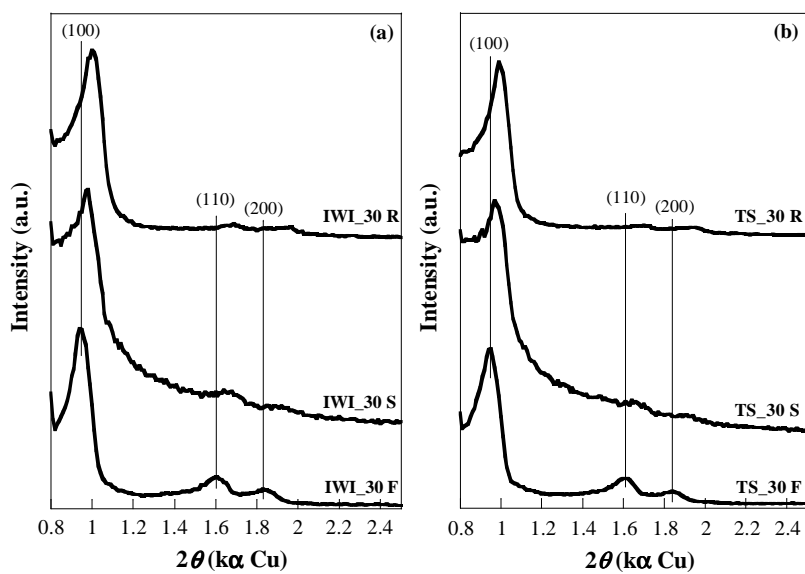


Figure 20. Low-angle XRD patterns of fresh (F), sulphided (S), regenerated (R) IWI_30_T500 (a) and TS_30_T500 (b) sorbents.

From the adsorption-desorption isotherms and the pore-size distribution plots (Figure 21), surface area values of 279 and 238 m²/g, and pore volume values of 0.61 and 0.58 cm³/g have been calculated for the IWI_30 and TS_30 regenerated samples, respectively. Comparison of such values with those for the corresponding fresh sorbents (see section 4.3) confirm that the pore size of the regenerated sorbents is slightly lower than that of the fresh ones.

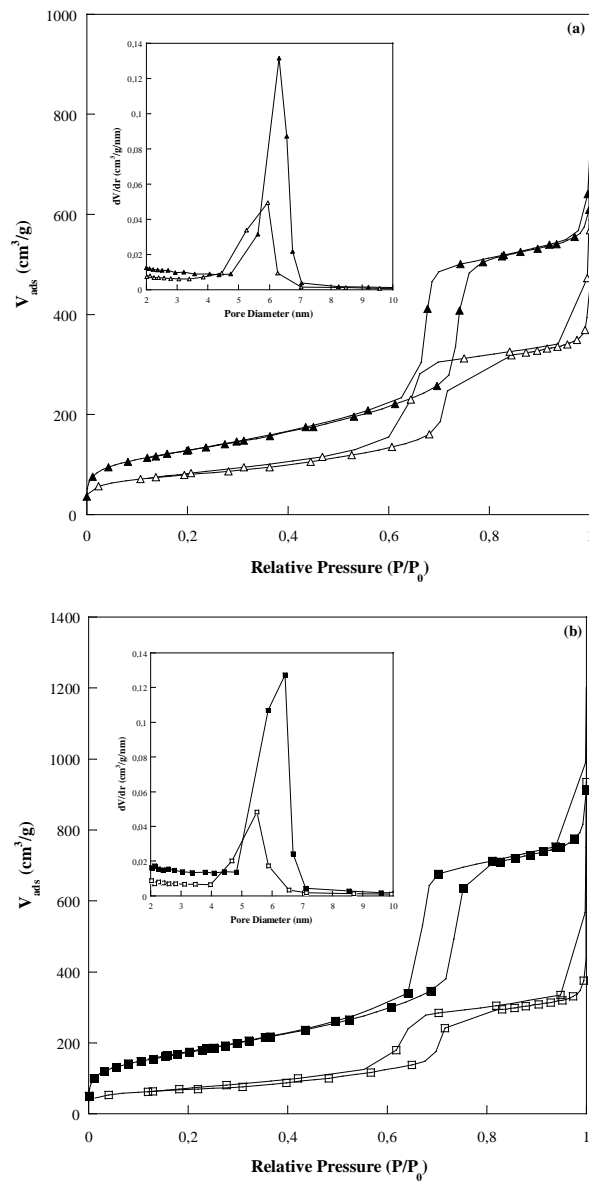


Figure 21. Nitrogen adsorption-desorption isotherms (a,b) and pore size distribution (inset) of: (a) IW1_30_T500 sorbents (full triangles IW1_30 F, empty triangles IW1_30 R) and (b) TS_30_T500 sorbents (full squares TS_30 F, empty squares TS_30 R).

These finding further supports the idea that no simple correlation exists between the accessibility parameters (S_{BET} and V_p) and the sorbent performance, which should be governed by some other features of the solid. Based on the findings of the present work, the tentative hypothesis can be advanced that the ZnO phase originating from the ZnS oxidation during the regeneration step of the sorbent is different in terms of crystallinity, particle size and texture from the one obtained directly by thermal decomposition of the zinc nitrate precursor, *i.e.*, that the regeneration process induces a reorganization of the zinc oxide nanophase. A schematic representation of the phase changes occurring during the sorption-regeneration cycle is shown in Figure 22^[9].

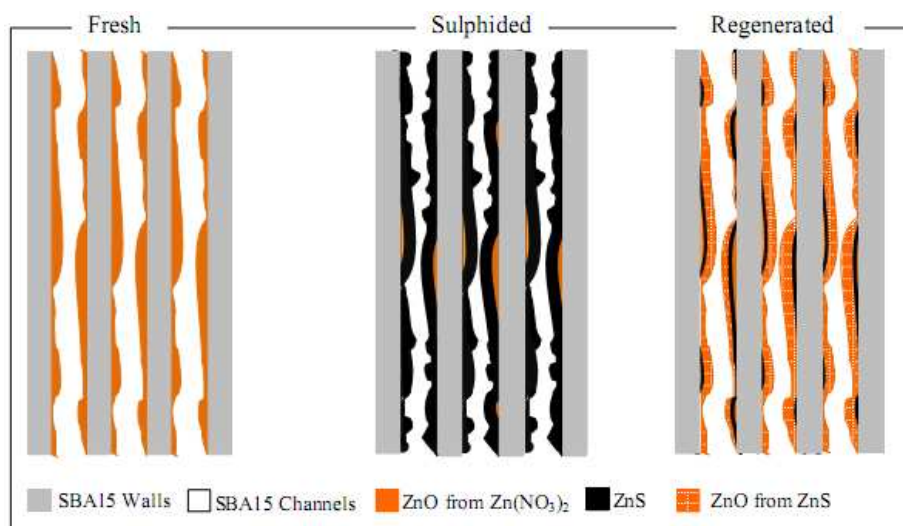


Figure 22. Schematic representation of the sulphurization and regeneration process for ZnO/SBA-15 sorbents.

To get clues to the proposed occurrence of phase reorganization, TEM analysis in the Dark Field mode was carried out on the fresh, sulphided and regenerated samples. Dark Field mode allows to evidence the coherent domain (crystallite) and therefore to discriminate among different samples in terms of

crystallite size or degree of crystallinity. In [Figure 23](#), TEM images of IW1_30_T500 are reported as an example. The fresh sample shows a low amount of small black spots (crystallites) spread into/over the grey amorphous support, indicating a low degree of ZnO crystallinity. In the sulphided sample both the number and the size of the black spots increase visibly, suggesting a higher crystallinity degree, as well as an increase in the particle size, in agreement with the wide-angle XRD patterns (*cf.* [section 4.6](#)). In the regenerated sample the number of black spots is higher than that for fresh one but lower than that for the sulphided sample; the size of the spots seems similar to that for the fresh sorbent, but smaller than that of the sulphided one. These issues can be taken as an indication of the reorganization of the zinc oxide nanophase, though the presence of residual ZnS (due to the incomplete regeneration) does not allow to give a conclusive explanation of the mechanism.

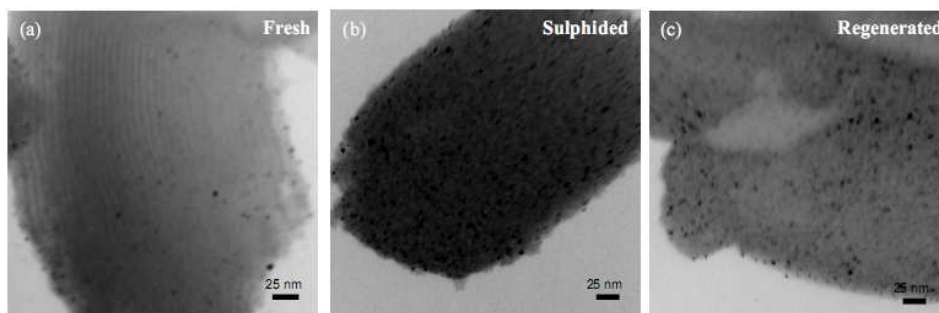


Figure 23. Dark Field TEM images of fresh (a), sulphided (b) and regenerated (c) IW1_30_T500 sorbent.

4.8 Conclusions

ZnO/SBA-15 composites with good performance for the mid-temperature H_2S removal were synthesized in a wide range of the active phase loading. Remarkable sulphur retention capacity referred to the active phase was shown by the composites if compared with a commercial sorbent. At variance with the case of the commercial product, the sorption properties are enhanced after regeneration and maintained upon repeating the sorption-regeneration cycle.

The combined use of several characterization techniques allowed to conclude that: (i) the confinement of ZnO active phase into the ordered channel system of mesostructured SBA-15 can be achieved by both Incipient Wetness and Two-Solvents impregnation strategies, even with high ZnO loadings; (ii) the sorption behaviour is not strictly dependent on the surface area and pore volume features of the composites, which are usually assumed as key parameters.

The unexpected enhancement in the sulphur retention capacity has been tentatively ascribed to a reorganization of the active phase occurring during the first regeneration step.

References

- [1] D. Zhao, J. Feng, Q. Huo, N. Melosh, G. H. Fredrikson, B. F. Chmelka and G. D. Stucky, *Science*, **1998**, 279, 548.
- [2] X. Wang, T. Sun, J. Yang, L. Zhao and J. Jia, *Chem. Eng. J.*, **2007**, 142, 48.
- [3] Q. Jiang, Z. Y. Wu, Y. M. Wang, Y. Cao, C. F. Zhou and J. H. Zhu, *J. Mater. Chem.*, **2006**, 16, 1536.
- [4] K. S. W. Sing, D. H. Everett, R. A. W. Haul, L. Moscow, R. A. Pierotti, J. Rouquerol and T. Siemieniowska, *Pure Appl. Chem.*, **1985**, 57, 603.
- [5] F. Rouquerol, J. Rouquerol and K. Sing, in *Adsorption by Powders and Porous Solids*, Academic Press, **1999**, ch. 7, pp. 191-217.
- [6] C. Cannas, M. Casu, A. Lai, A. Musinu and G. Piccaluga, *J. Mater. Chem.*, **1999**, 9, 1765.
- [7] A. Samokhvalov and B. J. Tatarchuk, *Phys. Chem. Chem. Phys.*, **2011**, 13, 3197.
- [8] K. Polychronopoulou, J. L. G. Fierro and A. M. Efstathiou, *Appl. Catal. B*, **2005**, 57, 125.
- [9] M. Mureddu, I. Ferino, E. Rombi, M.G. Cutrufello, P. Deiana, A. Ardu, A. Musinu, G. Piccaluga and C. Cannas, *Fuel*, **2012**, 102, 691.

Chapter 5

Iron oxide/SBA-15 sorbents

5 Introduction

Enhanced desulphurization activity of ZnO/SBA-15 nanocomposites prepared by different impregnation strategies, and compared with the commercial ZnO sorbent, has been demonstrated in the previous chapter. However, the slow kinetics of the reaction, limits the sulphur loading capacity of ZnO-based sorbents. Iron oxide/SBA-15 nanocomposites could represent an interesting alternative as low-cost sorbents for H₂S removal in view of the rapid kinetics of H₂S reaction with iron oxide [1-5]. Although the thermodynamics of iron oxide-hydrogen sulphide reaction at high temperature are less favourable than that of zinc oxide-hydrogen sulphide reaction, the research on iron oxide is still active because of high sulphur retention capacity, superior in regeneration performance, and lower cost in run [6-9].

A number of techniques can be employed to prepare iron-based sorbents include spray drying, crushing/screening, impregnation and granulation, and precipitation. The factors that need to be considered for sorbent production include the cost, sulphur capacity and reactivity, desulphurization efficiency, regenerability and mechanical strength (*i.e.*, resistance to attrition). These factors determine the selection of the composition, parameters of sorbent preparation and the process of desulphurization.

In view of the encouraging results obtained for the zinc oxide-based sorbents (see previous Chapter), and for the reasons reported in [section 2.4.2](#), make iron oxide/SBA-15 composites worthy of being investigated in parallel with zinc oxide/SBA-15 sorbents for the mid-temperature (300 °C) H₂S removal.

The Fe_2O_3 content was selected based on the previous results of the zinc oxide-based sorbents. From the results obtained in the previous chapter, the desulphurization activity increased when the ZnO loading goes from 10 to 30 wt.%, but when the content was 60 wt.%, the H_2S removal increase was not proportionally to the active phase content: so, the composition of 20 wt.% has been chosen as the better compromise between desulphurization activity and dispersion inside the SBA-15 support.

5.1 Preparation of iron oxide/SBA-15 nanocomposite sorbents

The SBA-15 mesostructured silica was prepared according to the procedure reported by Zhao et al.^[10] and described in detail in the Chapter 3 (see [section 3.2](#)).

The sorbent was prepared by the two-solvents hexane-water impregnation procedure^[11, 12]. Here too, iron nitrate was chosen as the precursor due to its high solubility in water, low decomposition temperature (*ca.* 130 °C), and the by-products are all gaseous and are therefore easily be removable from the pores of the matrix. Prior to impregnation, the silica support was dried for 12 h in a drying oven at 100 °C to remove physisorbed water.

The procedure for the "Two-solvents" synthetic route was as follows: 0.4 g of SBA-15 powder were put under stirring at 400 rpm for 15 min at room temperature in 12 cm³ of *n*-hexane, used as hydrophobic solvent. Then, 0.48 cm³ of an aqueous solution, quantity corresponding to the pore volume of SBA-15 determined by N_2 physisorption, containing 1 mmol of $\text{Fe}(\text{NO}_3)_3 \cdot 9\text{H}_2\text{O}$, Aldrich, 98%, was added drop wise. The resulting dispersion was vigorously stirred for 2 h at room temperature and then left to dry in air at 40 °C overnight. Finally, the hazel dried product was calcined at 500 °C for 2 h (heating rate 2 °C/min) to decompose the metal nitrate and to obtain the desired sorbent ([Figure 1](#)).

With a similar procedure, a zinc oxide-based sorbent with 20 wt.% of active phase was synthesized and tested for comparison.

The sorbent samples, with nominal content of active phase equal to 20 wt.%, are labelled as Zn_*X* and Fe_*X*, where *X* denotes the state of the sorbent, F (Fresh), S (Sulphided) and R (Regenerated). Similar notation is used also for the commercial unsupported ZnO sorbent (Katalco_{JM} 32-5).



Figure 1. Fresh Fe₂O₃/SBA-15 sorbent.

5.2 Desulphurization activity of fresh sorbents

Breakthrough curves for all the sorbents, the pure zinc oxide commercial sorbent (Katalco_{JM} 32-5) included, were recorded at 300 °C (Figure 2). No H₂S removal was detected for the bare SBA-15.

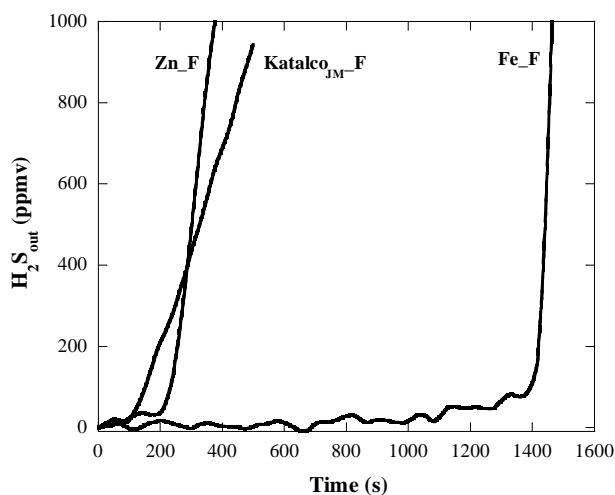


Figure 2. H_2S breakthrough curves of the ZnO commercial sorbent ($Katalco_{JM_F}$), Zn_F and Fe_F supported sorbent at the first sulphidation run.

For all the sorbents the values of breakthrough time and sulphur retention capacity (SRC), expressed relative to either the active phase content or to the total composite amount (active phase + support), are reported in [Table 1](#). The incorporation of zinc- or iron-oxide into SBA-15 induces a considerable improvement of the SRC compared to the commercial sorbent. The highest retention capacity per unit mass of active phase is obtained for Fe_F (401 mg S/g Fe_2O_3), being more than seven-time higher than that of the Zn_F (53 mg S/g ZnO), and even much more higher than the corresponding value for the commercial zinc oxide sorbent (6 mg S/g ZnO).

Table 1. Breakthrough time (B_t) and Sulphur Retention Capacity (SRC) of fresh zinc oxide- and iron oxide-based sorbents. Data for the ZnO commercial sorbent (Katalco_{JM} 32-5) are also reported for comparison.

Sample	B_t (s)	SRC (mg _S /g _{active phase}) ± 1	SRC (mg _S /g _{sorbent}) ± 1
Katalco _{JM} _F	103	6	6
Zn_F	180	53	10
Fe_F	1350	401	80

The by far superior performance of the SBA-15-supported sorbents with respect to that of the commercial sample can be reasonably ascribed to differences in the exposure of the active phase to the reactant H₂S. As reported in the following, though the surface area and the pore volume of the Fe_F are higher than that of the corresponding sorbent with zinc oxide, these textural properties cannot justify the tremendous enhancement of the SRC, since also differences in the intrinsic kinetics should be considered for explaining the sorption behaviour of Zn_F and Fe_F.

5.3 Characterization of the fresh sorbents

5.3.1 Low- and wide-angle X-ray diffraction characterization

The low-angle diffraction patterns of the bare SBA-15, zinc oxide- and iron oxide-based sorbents are shown in Figure 3. The low-angle diffraction pattern (Figure 3a) of the SBA-15 support exhibits three observable reflections, indexable as (100), (110) and (200), which are characteristic of a two-dimensional

highly ordered hexagonal arrangement of the channels (space group $P6mm$). The low-angle diffraction patterns of the sorbents also exhibit the three well-resolved diffraction peaks, which indicates that the organized pore structure is maintained despite the quite high active phase loading. A slight shift of the reflections towards higher angles can be observed for both sorbents, suggesting a small contraction of the cell parameters.

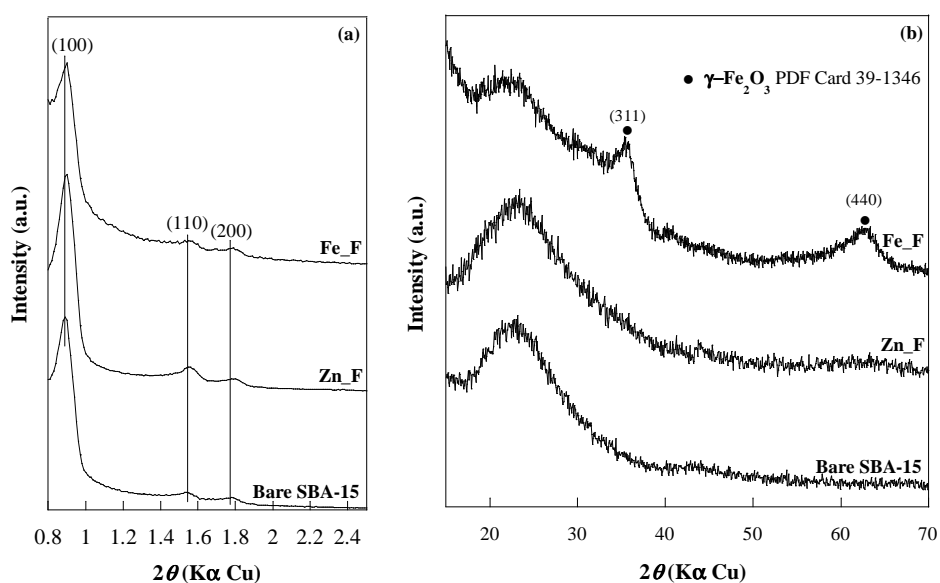


Figure 3. XRD patterns of bare SBA-15, zinc oxide- and iron oxide-based fresh sorbents at low-angle (a) and wide-angle (b). The main reflection planes are marked.

The wide-angle diffraction pattern of Zn_F (Figure 3b) shows only the typical halo of amorphous silica at $2\theta = ca. 23^\circ$. As previously found (see Chapter 2, section 4.2), no diffraction peaks corresponding to ZnO phase are observable, indicating that the active phase is well dispersed into/over the support as an amorphous phase or as nanocrystals whose size is under the XRD detection limit. The pattern of Fe_F

exhibits two further broad peaks at $2\theta = 35.5^\circ$ and 62.5° that can be attributed to the most intense reflections of maghemite- Fe_2O_3 phase (PDF Card 39-1346).

5.3.2 N_2 physisorption measurements: textural properties

Figure 4 shows the nitrogen adsorption-desorption isotherms (a) and the pore size distribution plots (b) of the fresh sorbents (Zn_F and Fe_F) in comparison with the bare SBA-15. The silica support exhibits a type IV isotherm with an H1 type hysteresis loop, characteristic of a mesoporous material with uniform cylindrical pores open at both ends^[13].

The mesoporous character of the solid is preserved after the incorporation of the active phase, as revealed by the type IV shape of the isotherm for both the sorbents. A two-step desorption branch showing two inflection points at about $P/P_0 = 0.4$ and 0.6 is observed for Fe_F, in contrast with the case of Zn_F, whose hysteresis loop is rather similar to that of the parent SBA-15.

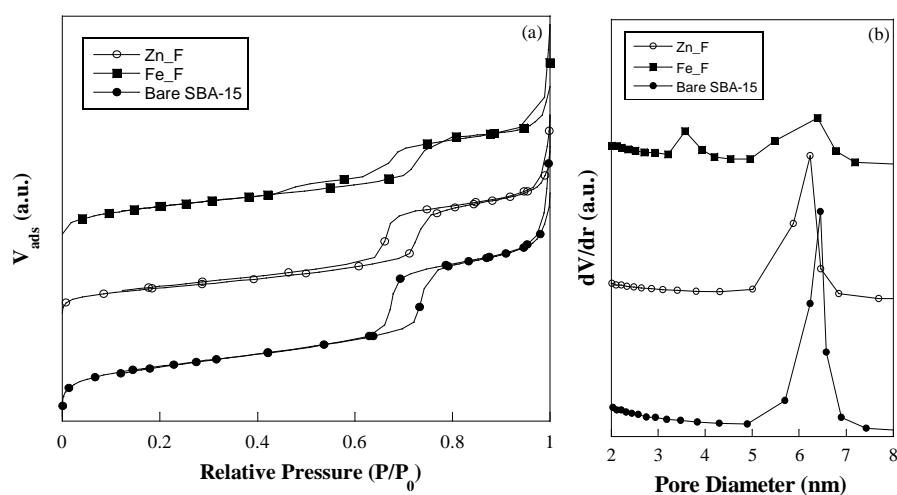


Figure 4. Nitrogen adsorption-desorption isotherms (a) and pore size distribution (b) of bare SBA-15, zinc oxide- and iron oxide-based sorbents in the fresh state (full circles bare SBA-15, empty circles Zn_F, full squares Fe_F).

The calculated values of surface area (S_{BET}) and pore volume (V_p) are reported in Table 2. For Zn_F, S_{BET} and V_p are much lower than the corresponding values of the bare support, which indicates partial filling of the mesopores by the metal oxide. Also for Fe_F the surface area and pore volume values are remarkably lower than those for the parent SBA-15.

Table 2. N_2 physisorption data of fresh zinc oxide- and iron oxide-based sorbents compared with the bare SBA-15 and the ZnO commercial sorbent (Katalco_{JM} 32-5). The thickness of the pore walls (T_w) is also reported.

Sample	S_{BET} (m^2/g)	V_p (cm^3/g)	D_p (nm)	T_w (nm)
Bare SBA-15	770	1.20	6.4	5.0
Katalco _{JM} _F	9	0.10	-	-
Zn_F	482	0.90	6.2	5.2
Fe_F	545	0.87	3.6 ; 6.4	-

S_{BET} : BET Specific Surface Area; V_p : Pore Volume; D_p : Pore Diameter; T_w : Wall Thickness = ($a_0 - D_p$); a_0 : XRD unit cell parameter. Relative Standard Deviation: %RSD (S_{BET}) = 2.1%; %RSD (V_p) = 1.1%; %RSD (D_p) = 1.8%.

The pore size distribution plot for Zn_F (Figure 4b) shows a narrow monomodal distribution centred at 6.2 nm. It is worthy of note that this value is slightly lower than that of SBA-15 (Figure 4b). By subtracting the mean pore diameter from the unit cell parameter (a_0 , calculated from low-angle XRD data), the wall thickness (T_w) values were calculated, resulting 5.0 and 5.2 nm for the bare SBA-15 and Zn_F, respectively (Table 2). Such a slight increase in the wall thickness as a consequence of ZnO deposition would be consistent with the presence of the oxide either as a layer or dispersed in clusters or very small nanoparticles. This is in agreement with the lack of ZnO reflections in the wide-angle XRD pattern

(Figure 3b). At variance with the case of the zinc oxide-containing sorbent, Fe_F shows a bimodal pore size distribution (Figure 4b) which seems related to the two-step feature observed in the desorption branch of the isotherm of this sample (Figure 4a) and indicates that two distinct families of pores contribute to the overall pore volume. The family with wider size (maximum at 6.4 nm) is responsible for the hysteresis at $P/P_0 = 0.6$, typical of open-ended cylindrical mesopores, reasonably those pores of SBA-15 in which no deposition of iron oxide has occurred. The other pore family (maximum at 3.6 nm) can be associated with the hysteresis loop closing at relative pressure of *ca.* 0.4, which is suggestive of ink-bottle type mesopores, resulting from the iron oxide deposition: in the same pore, the volume between two oxide particles would be only accessible through a small neck. Similar features were also observed by other authors in the desorption branch of zirconia- and iron oxide-containing SBA-15 [14, 15].

5.3.3 TEM images: morphological characterization

Morphology as well as structural ordering of bare SBA-15, Zn_F and Fe_F sorbents, were investigated by transmission electron microscopy studies and the images are collected in Figure 5.

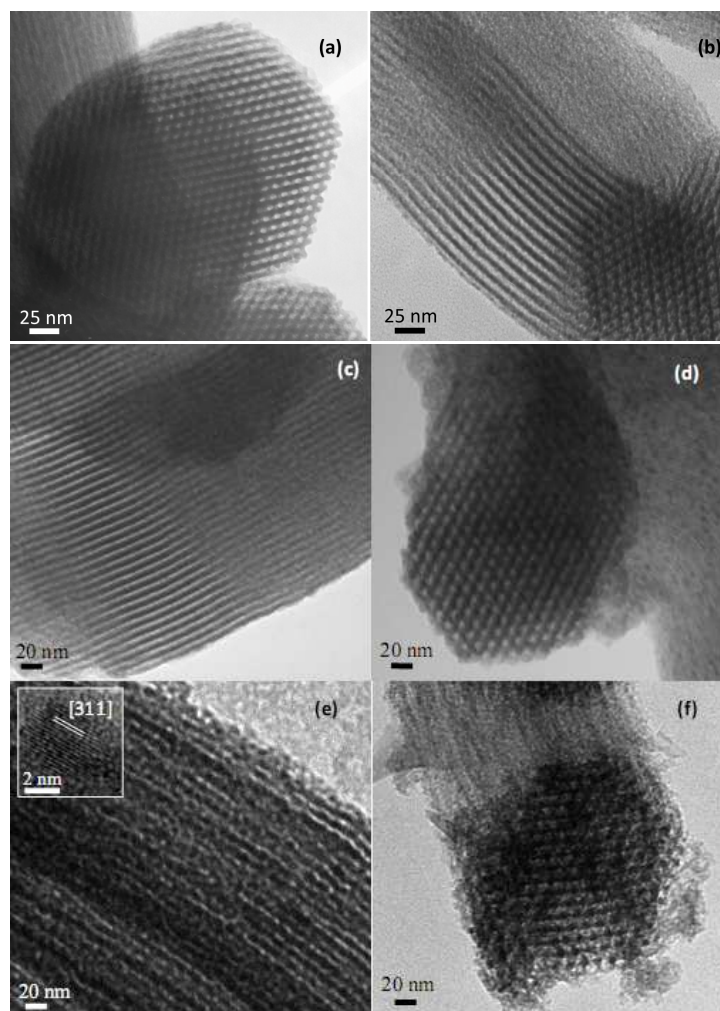


Figure 5. Representative TEM images of: bare SBA-15 viewed along (a) and perpendicular (b) to the axis of the hexagonal arranged mesopores; Zn_F (c and d); Fe_F (e and f).

The well-ordered 2D-hexagonal symmetry of SBA-15 with regular empty mesochannels of *ca.* 6–7 nm in diameter and walls thickness of about 5 nm is clearly visible in Figures 5a and 5b. The 2D-hexagonal structure of the silica template is preserved after the zinc- and iron-oxide loading. This observation is consistent with the XRD and N₂ physisorption results. However, differences in terms of both crystallinity and dispersion of the active phase are observed for the Zn_F and Fe_F sorbents. TEM images of the Zn_F sorbent (Figures 5c and 5d) do not show an evident variation if compared with bare SBA-15. No isolated ZnO particles are visible onto the external surface or inside the pores of Zn_F. This suggests that the formation of an amorphous and quite uniform thin layer of zinc oxide has occurred at the inner surface of the pore walls, in agreement with the XRD and BET data. At variance with the case of Zn_F, the Fe_F images (Figures 5e and 5f) show that iron oxide is not uniformly dispersed; note the rough contours of the channels (some of which appear completely filled) resulting by the deposition of the oxide nanoparticles. Inset of Figure 5e indicates the formation of "*pseudo-spherical*" crystallized iron oxide particles of whose size is slightly lower than that of the SBA-15 pore diameter. The crystalline nature of these nanoparticles is revealed by the high resolution micrograph in the inset of Figure 5e, where the calculate d /spacing (0.25 nm) is in agreement with the (311) reflection of maghemite (PDF Card 39-1346).

The different outcome of the oxide deposition process in the case of Zn_F and Fe_F could be justified by the different affinity of the zinc and iron cations for the silica host. According to the literature^[16-18], silica depolymerization can occur in the presence of zinc oxide phases even at low treatment temperature, due to the occurrence of silanol groups-oxide phase interaction. By converse, no interaction between silanols and the oxide phase was observed for a Fe₂O₃-SiO₂ nanocomposite^[19]. Accordingly, the formation of the homogeneous zinc oxide nanolayer at the internal surface of the pores of Zn_F would be triggered by the above-cited interactions, whereas their lack would lead to nanoparticles deposition in the case of Fe_F.

5.3.4 FT-IR and XPS characterization

In view of the possible role of the host-guest interactions in determining the final active phase dispersion, which in turn would influence the performance of the sorbents, the latter were also investigated by FTIR. The spectra of the sorbents are reported in Figure 6 and compared with the spectrum of the bare SBA-15.

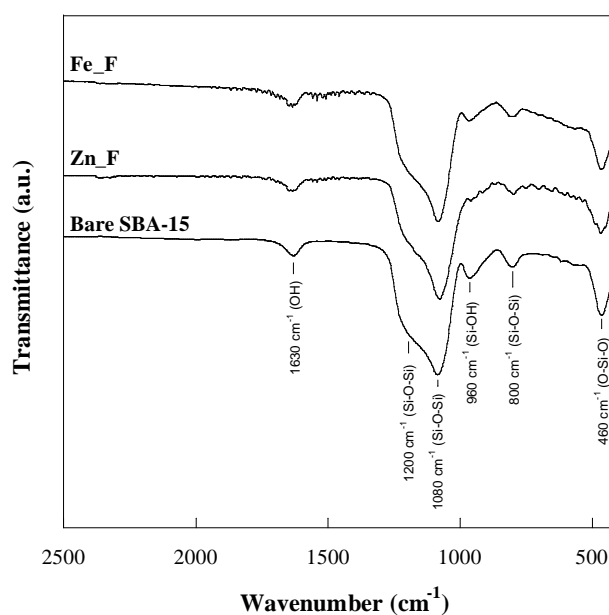


Figure 6. FTIR spectra of bare SBA-15, zinc oxide- and iron oxide-based fresh sorbents.

Most of the features are common to all the spectra: (i) the absorption bands at 1200-1080 and 800 cm⁻¹ of the asymmetric and symmetric modes of Si-O-Si groups, respectively^[20]; (ii) the absorption band at 960 cm⁻¹ of Si-OH stretching modes of the non-condensed Si-OH groups and the band at 465 cm⁻¹ due to bending of the O-Si-O groups; (iii) the absorption peak at around 1630 cm⁻¹ of the H-O-H bending vibration of H₂O adsorbed in capillary pores and on the surface. For both the sorbents, the absence of the typical

narrow signal around 1370 cm^{-1} due to the stretching vibration of the NO_3^- groups proves the complete decomposition of nitrates. Interestingly, the band at 960 cm^{-1} is still clearly visible after the incorporation of the iron oxide phase, whereas it is absent in the case of Zn_F sorbent, which provides further evidence for the occurrence of interactions between the ZnO phase and the silica matrix. Further confirmation of this interaction is obtained by XPS analyses: $\text{Zn}2p_{3/2}$ signal of Zn_F sorbent (Figure 7a) shows a single component at $1022.7 \pm 0.2\text{ eV}$ while the kinetic energy of the Auger ZnLMM peak was found to be $986.3 \pm 0.2\text{ eV}$. These values indicate the formation of Si-O-Zn bonds, in agreement with the findings of other authors^[21]. Such interactions, which are responsible for the deposition of zinc oxide as an amorphous thin layer at the surface of the SBA-15 channels, also make the zinc oxide phase differently available to react with the hydrogen sulphide, in comparison with the case of iron oxide nanoparticles not interacting with the host matrix.

As far as iron is concerned, in Fe_F sorbent XPS $\text{Fe}2p_{3/2}$ spectrum (Figure 7b) shows only the presence of two components at $710.3 \pm 0.2\text{ eV}$ and $711.6 \pm 0.2\text{ eV}$ which can be assigned to Fe (III) in Fe_2O_3 and FeOOH respectively^[22].

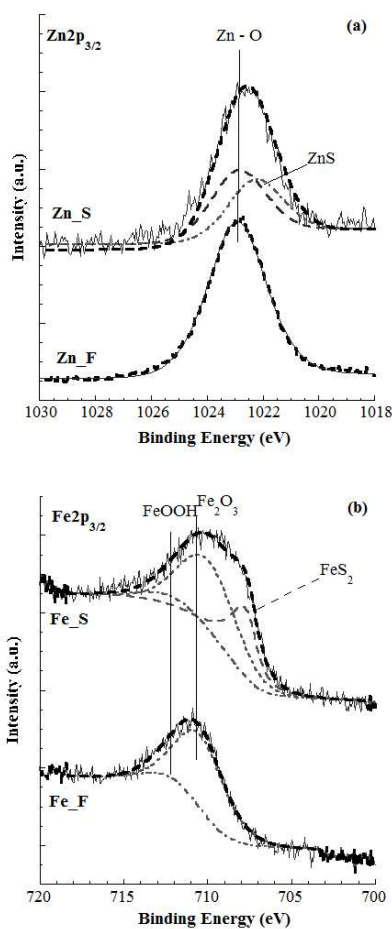


Figure 7. $Zn2p_{3/2}$ (a) and $Fe2p_{3/2}$ (b) XPS spectra of fresh and sulphided sorbents.

5.4 Characterization of the sulphided sorbents

After the sorption runs, the support mesostructure is retained (as indicated by the low-angle patterns of [Figures 8a](#)). Only in the pattern of Zn_S, the (100), (110) and (200) peaks significantly shift towards angles higher than those of the Zn_F pattern, suggesting a slight shrinkage of the mesoporous framework. The wide-angle XRD patterns of the sulphided sorbents ([Figure 8b](#)) show that for Zn_S, in

addition to the broad halo related to amorphous silica, broad and intense reflections at 28.6° , 47.7° and 56.6° are present, assigned to ZnS phase (PDF Card 12-688). The mean size of the ZnS nanocrystals can be estimated in the 3-4 nm range by Debye-Scherrer equation. The broadening of the reflections does not permit to exclude the presence of an amorphous sulphided phase. A small peak centred at about $2\theta = 33^\circ$ is observed in the pattern of Fe_S, attributed to the most intense reflection (101) of the FeS₂ pyrite phase (PDF Card 71-2219). A large band overlapping with the main reflection of pyrite phase could suggest the possible presence of an amorphous iron sulphide phase; the presence of unreacted maghemite cannot be excluded.

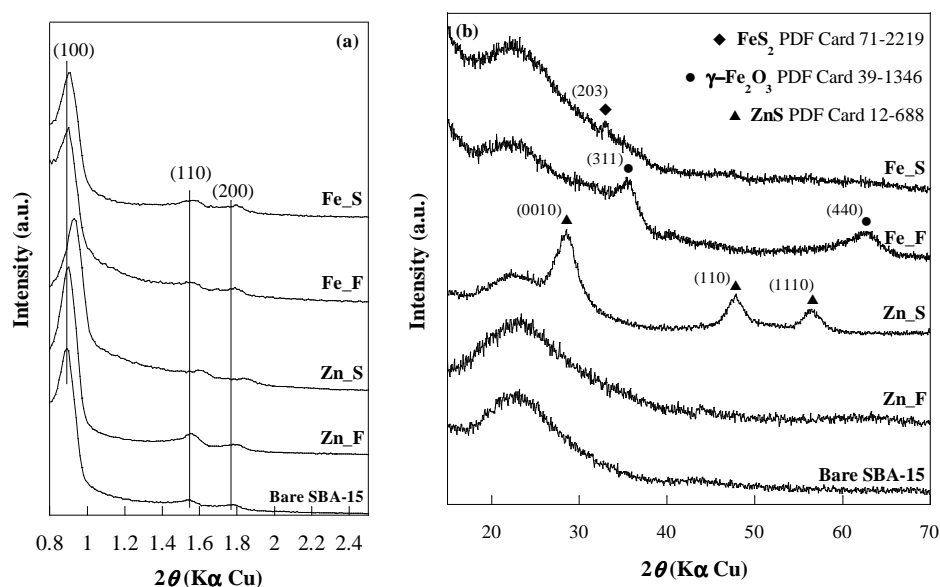


Figure 8. XRD patterns of bare SBA-15, zinc oxide- and iron oxide-based sorbents in the fresh and sulphided state at low-angle (a) and wide-angle (b). The main reflection planes are marked.

Nitrogen physisorption isotherms (Figure 9a) confirm the mesostructured character of the sulphided sorbents. As a consequence of the sulphidation process, zinc oxide is transformed into ZnS. Due to the

different molar volume values of ZnO ($15.07 \text{ cm}^3/\text{mol}$) and ZnS ($24.3 \text{ cm}^3/\text{mol}$) an expansion in the volume of the guest material as high as 38% should be expected in case of complete ZnO/ZnS conversion. Such expansion should lead to a decrease in surface area and pore volume, which is actually observed (Table 3). The occurrence of an increase in the guest phase volume is also confirmed by the monomodal pore size distribution centred at 3.8 nm observed for the sulphided sorbent (Figure 9b). Note (Table 3) that the wall thickness (T_w) value is significantly higher than the value for Zn_F.

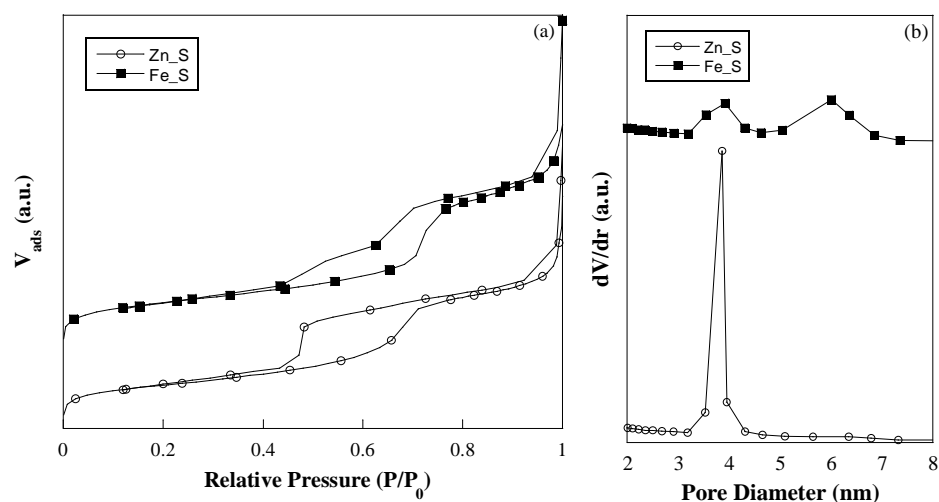


Figure 9. Nitrogen adsorption-desorption isotherms (a) and pore size distribution (b) of zinc oxide- and iron oxide-based sorbents in the sulphided state (empty circles Zn₁S, full squares Fe₁S).

Table 3. N_2 physisorption data of fresh, sulphided and regenerated zinc oxide- and iron oxide-based sorbents compared with the bare SBA-15 and the ZnO commercial sorbent (Katalco_{JM} 32-5). The thickness of the pore walls (T_w) is also reported.

Sample	S_{BET} (m^2/g)	V_p (cm^3/g)	D_p (nm)	T_w (nm)
Bare SBA-15	770	1.20	6.4	5.0
Katalco _{JM} _F	9	0.10	-	-
Zn_F	482	0.90	6.2	5.2
Zn_S	406	0.76	3.8	7.2
Zn_R	332	0.69	5.4	-
Fe_F	545	0.87	3.6 ; 6.4	-
Fe_S	525	0.84	3.9 ; 6.0	-
Fe_R	463	0.80	3.5 ; 6.0	-

S_{BET} : BET Specific Surface Area; V_p : Pore Volume; D_p : Pore Diameter; T_w : Wall Thickness = ($a_0 - D_p$); a_0 : XRD unit cell parameter.

Relative Standard Deviation: %RSD (S_{BET}) = 2.1%; %RSD (V_p) = 1.1%; %RSD (D_p) = 1.8%.

Due to the nanocrystalline nature of the ZnS phase, and the increased electronic density contrast in comparison with zinc oxide, it is possible to point out in TEM micrographs (Figure 10) that the particles are mainly anchored at the channel walls, whose contours appear rather rough, with a rope-like profile. The image at higher magnification (Figure 10, inset), shows that, in agreement with the wide-angle XRD

results, the ZnS nanoparticles are 3-4 nm wide. HRTEM image, reported as inset of Figure 10, shows two nanoparticles with d -spacing values of 0.31 and 0.33 nm which are in agreement with the (0010) and (100) reflections of hexagonal ZnS phase (PDF Card 12-688) respectively.

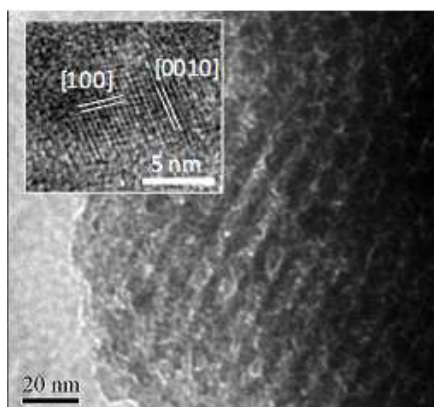


Figure 10. Representative TEM images of the sulphided Zn₂S sorbent.

Based on the sulphidation reaction stoichiometry, the conversion of Fe₂O₃ (30.71 cm³/mol) into FeS₂ (51.06 cm³/2 mol) would be accompanied by an expansion in the volume of the guest material and as a consequence in the lowering of surface area of the composite. The observed surface area and pore volume values for Fe₂S are actually slightly lower than that for Fe₂F (Table 3). The bimodal pore size distribution (Figure 9b) is maintained in the sulphided sample, and that the second peak in the pore size distribution of Fe₂S is centred at 6.0 nm, *i.e.*, slightly lower than that for Fe₂F, in agreement with the presence of iron sulphide phase occupying the pores. No significant differences between the fresh and sulphided sorbent are visible in the TEM micrographs for these samples (*cf.* Figures 5e and 11).

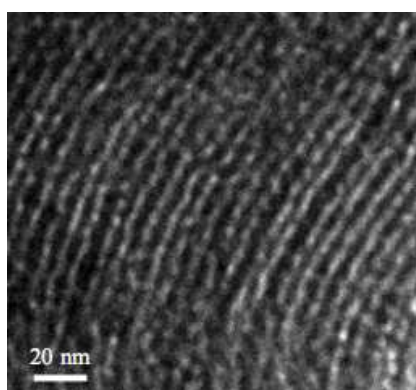


Figure 11. Representative TEM images of the sulphided Fe_S sorbent.

The FTIR spectra of the sulphided sorbents are provided in Figure 12. A comparison between the spectra for Zn_F and Zn_S reveals that in the latter the Si-OH band at 960 cm^{-1} reappears, hence suggesting that the Zn-containing phase formed upon sulphidation does not interact significantly with the silica surface. Interestingly, this occurs simultaneously with the transformation of the amorphous zinc oxide phase into a crystalline ZnS phase, evidenced by the wide-angle XRD patterns (see Figure 8b). By contrast, in Fe_S the band at 960 cm^{-1} is strongly attenuated, suggesting that interactions between the silica host and the iron sulphide guest phase take place to a remarkable extent. It is worthy of note that this is accompanied by the loss of the crystalline character of the iron oxide as a consequence of its transformation into the sulphided phase (*cf.* Figure 8b). The presence of FeS₂ phase, revealed by both the XRD pattern and the *pale brass-yellow* color of Fe_S, can be responsible for the low-intensity band at 600 cm^{-1} in agreement with Philias^[23]. The pyrite formation is also consistent with the thermodynamic stability of this phase in comparison with the other iron sulphides.

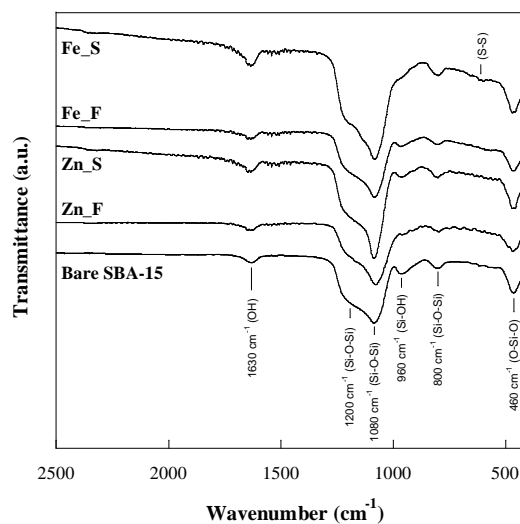


Figure 12. FTIR spectra of bare SBA-15, zinc oxide- and iron oxide-based sorbents in the fresh (F) and sulphided state (S).

The formation of both ZnS and FeS₂ is confirmed by XPS analyses. Zn2p_{3/2} signal (Figure 13a) shows, together with the component at 1022.7 eV due to Zn involved in Si-O-Zn bonds, a component at lower binding energy values (1021.9 ± 0.2 eV) which can be assigned to ZnS. In Fe2p_{3/2} signal (Figure 13b) a component at 707.2 eV ± 0.2 eV, due to pyritic iron is observed^[24] Sulphur S2p peaks of both Fe_S and Zn_S sorbents show a single component at 162.5 eV and at 162.0 eV respectively (Figure 13c) that could be assigned to sulphur in pyrite and in ZnS respectively^[25]. Further confirmation of the presence of FeS₂ and ZnS at the sorbent surfaces is obtained by stoichiometry calculated from XPS data: the ratio between pyritic iron and sulphur is found to be 0.45 while the ratio Zn/S, calculated taking into account only the lower binding energy component of the zinc signal, is 1.10. All these results are in good agreement with XRD analysis for both sorbents.

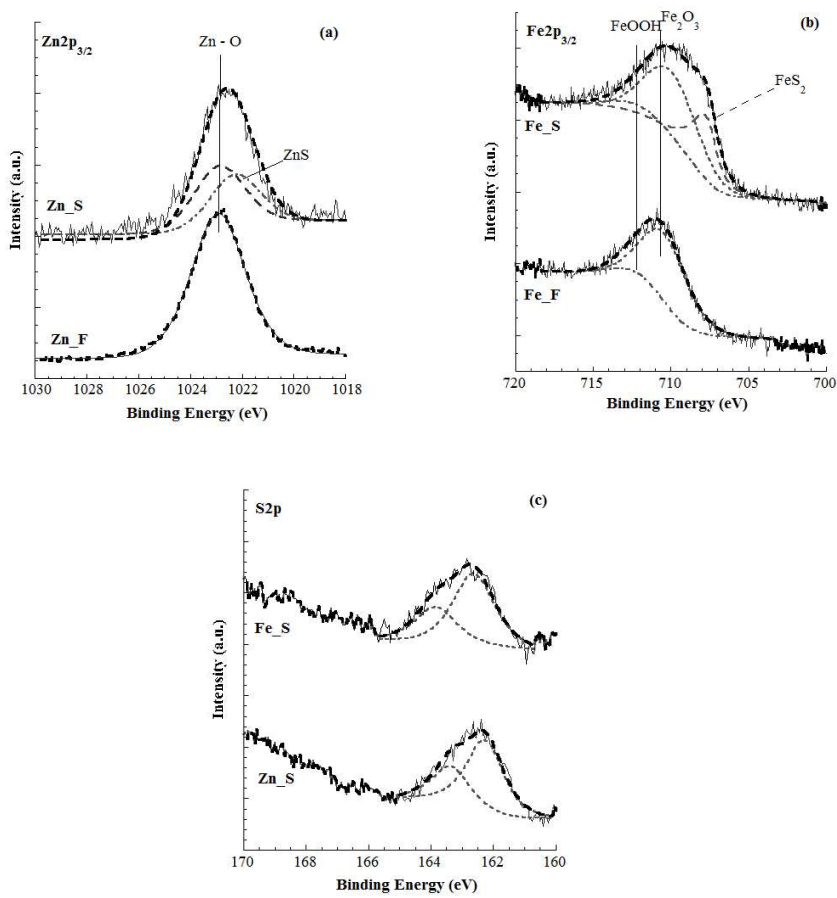


Figure 13. $Zn2p_{3/2}$ (a) and $Fe2p_{3/2}$ (b) XPS spectra of fresh and sulphided sorbents. (c) $S2p$ XPS signals of Fe_S and Zn_S sorbents.

All these findings evidence a different host-guest interactions in determining the final active phase dispersion: in the case of Zn_F , it leads to the formation of the homogeneous zinc oxide nanolayer at the internal surface of the pores, whereas in the case of Fe_F it leads to the nanoparticles deposition inside the pores.

A simple graphical representation of the reaction process, and especially about the arrangements of the active metal oxide phase (zinc or iron oxide) into the mesopore channels of the silica support is shown in Figures 14 and 15 ^[26].

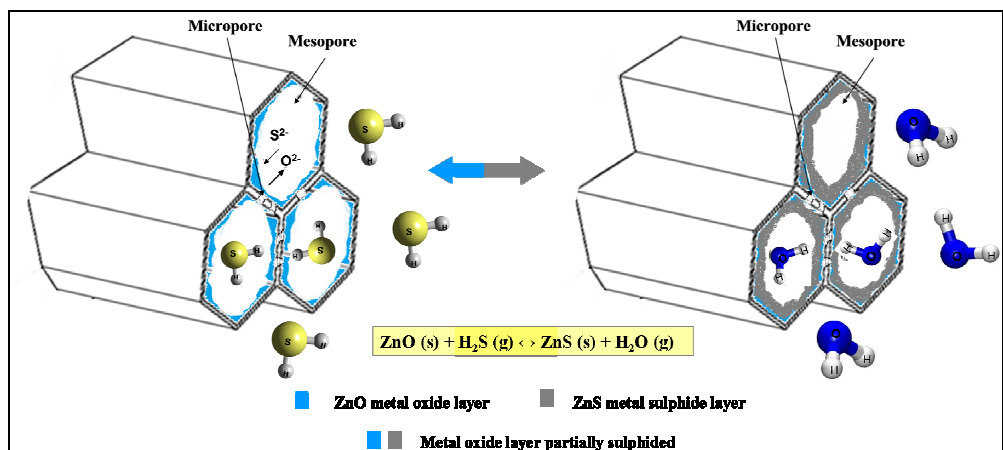


Figure 14. Graphical representation of the reaction process in the zinc oxide/SBA-15 nanosorbent.

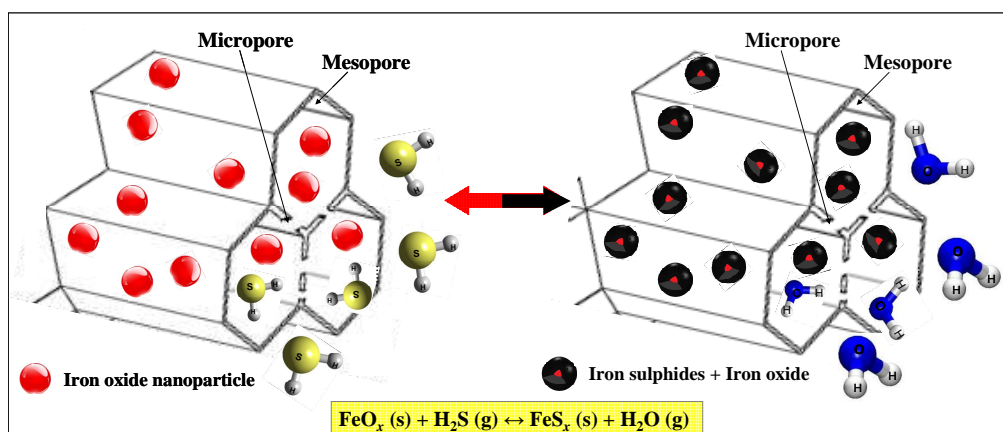


Figure 15. Graphical representation of the reaction process in the iron oxide/SBA-15 nanosorbent.

5.5 Sorbents regeneration and desulphurization-regeneration cycles

5.5.1 Temperature-programmed oxidation of the sulphided sorbents

In order to select appropriate regeneration conditions, temperature-programmed oxidation runs in flowing air were carried out on the sulphided sorbents, as well as on the sulphided commercial sorbent. The TCD profiles (Figure 16) showed for Fe₂S₃ the presence of some peaks in the temperature region not exceeding 500 °C, no further peaks being detected above such temperature. By converse, in the case of Zn₂S₃, besides a large peak at 500 °C another peak was observed at 690 °C. It is worthy of note that for temperatures ≤ 500 °C the oxidation of the sulphided commercial sample was almost negligible, only a very low, enlarged signal being detected for such temperatures in the TCD profile; heating of the sample well above 500 °C was required for the onset of oxidation to a significant extent.

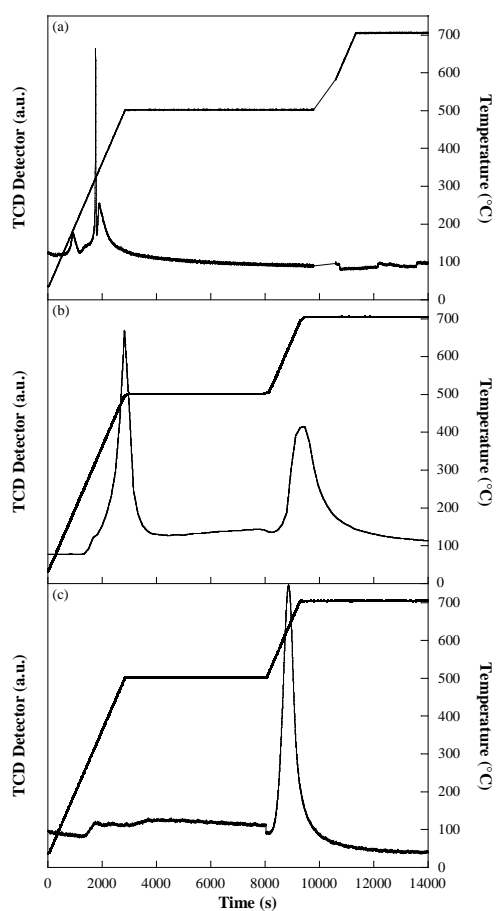


Figure 16. TCD profiles of the Fe_2S_3 (a), ZnS (b), and Katalco_{JM} S (c) sulphided sorbents, regenerated through a two-step (500 and 700 °C) treatment.

As the TCD signal does not give information about the species by which the single contributions originate, further runs were carried out in which the SO_2 and O_2 species in the outlet gas composition were simultaneously monitored by quadrupole mass spectrometer (QMS). All these runs were carried out at a

temperature not exceeding 500 °C, in view of the detrimental effect of higher temperatures on the SRC of ZnO/SBA-15 sorbents ^[27]. Another reason for such choice stems from previous ²⁹Si MAS-NMR experiments ^[6], which revealed that the thermal treatment of sol-gel ZnO-SiO₂ nanocomposites in the 500-700 °C range induces the depolymerization of the host matrix and the possible formation of zinc silicates as a consequence of its interaction with zinc oxide. [Figure 17](#) reports both the TCD and QMS signals for Fe_S. The TCD profile shows a peak at 185 °C, a broad contribution at 260 °C, as well as two well-resolved peaks at 322 °C and 345 °C. The QMS profiles for O₂ and SO₂ reveal that the peak at 185 °C and the broad contribution at 260 °C are due to O₂ consumption and SO₂ release, respectively. A second O₂ consumption step is responsible for the narrow signal at 322 °C which correlates with the successive release of a considerable SO₂ amount at 345 °C. The two different O₂ consumption steps and subsequent SO₂ formation steps are ascribable to the presence of two different sulphided species, one of which is reasonably the crystalline pyrite phase revealed by XRD.

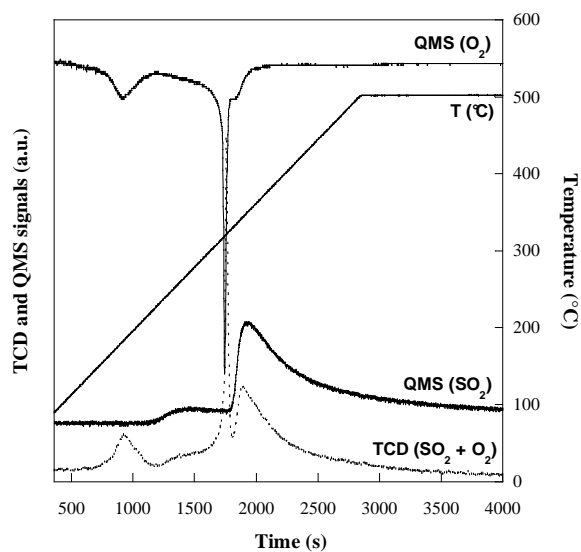


Figure 17. TPD profile and SO_2 and O_2 quadrupole mass spectrometer (QMS) signals of the Fe_xS sulphided sorbent regenerated at $500\text{ }^\circ\text{C}$.

Inspection of the TCD and QMS profiles for Zn_xS (Figure 18) shows that both the unresolved TCD peak at $322\text{ }^\circ\text{C}$ and the large peak at $500\text{ }^\circ\text{C}$ stem from an O_2 consumption and the associated SO_2 release. One of these two steps of Zn_xS oxidation corresponds to the oxidation of a crystalline ZnS phase (whose presence was revealed by XRD) while the other could be ascribed to the oxidation of a zinc sulphide amorphous phase not visible by XRD.

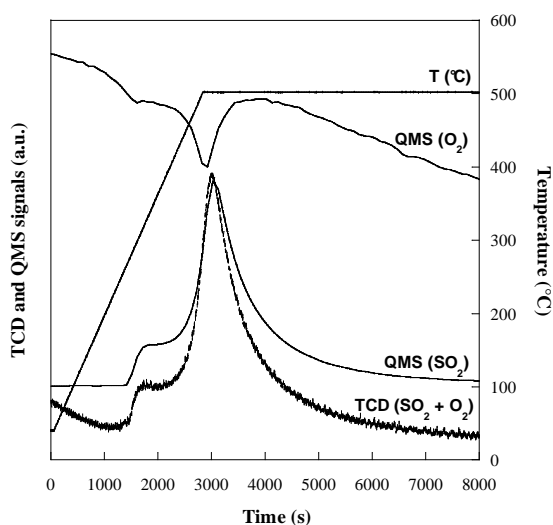


Figure 18. TPD profile and SO_2 and O_2 quadrupole mass spectrometer (QMS) signals of the Zn-S sulphided sorbent regenerated at 500 °C.

5.5.2 Sorption features of the regenerated samples

Consecutive sorption-regeneration cycles were performed on the composite sorbents, as well as on the commercial sorbent, and the corresponding breakthrough curves were obtained (Figure 19). From these, the B_t and SRC values for all the sorbents were obtained and gathered in Table 4. The regeneration process is unable to restore a significant sorption activity for the ZnO commercial sample, both the breakthrough time and the sulphur retention capacity of the regenerated sample (2 mg S/g ZnO vs. 6 mg S/g ZnO of the fresh sorbent) being dramatically lower than those of the fresh sorbent. By converse, an enhanced performance of the regenerated sample in comparison with the fresh one is observed for the ZnO-based sorbent (68 mg S/g ZnO vs. 53 mg S/g ZnO of the fresh sorbent). For the iron oxide-based sorbent the regeneration process results in the partial recovering of the original sorption activity (199 mg S/g Fe_2O_3 vs. 401 mg S/g Fe_2O_3 of the fresh sorbent), the B_t and SRC values for the regenerated sorbent being nearly halved in comparison with Fe_F. No further significantly changes in the sorption

behaviour are observed for any of the sorbents upon repeating the sorption-regeneration cycle. The superior features of the iron oxide-based sorbent are worthy of note: the breakthrough time and the sulphur retention capacity of the regenerated sample are far higher than those of the ZnO-based sorbent, both under the fresh or regenerated form.

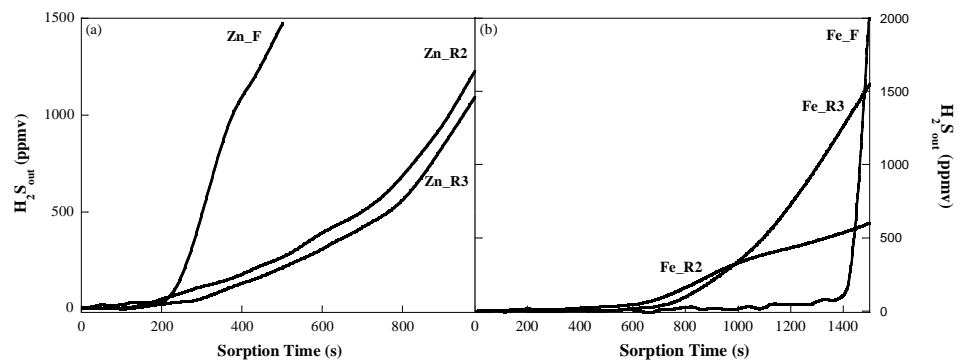


Figure 19. *H₂S* breakthrough curves upon three sorption-regeneration cycles (S1, S2, S3) for the zinc oxide-based sorbent (a) and iron oxide-based sorbent (b).

Table 4. Breakthrough time (B_t) and Sulphur Retention Capacity (SRC) of fresh and regenerated zinc oxide- and iron oxide-based sorbents during sorption-regeneration cycles. Data for the commercial Katalco_{JM} 32-5 sorbent are also reported for comparison.

Sample	Run number ^a	B_t (s)	SRC (mg _S /g _{Active phase}) ± 1	SRC (mg _S /g _{Sorbent}) ± 1
Katalco _{JM} _F	1	103	6	6
Katalco _{JM} _R	2	26	2	2
Katalco _{JM} _R	3	26	2	2
Zn_F	1	180	53	10
Zn_R	2	230	68	13
Zn_R	3	250	74	14
Fe_F	1	1350	401	80
Fe_R	2	670	199	40
Fe_R	3	710	211	42

^a 1= Fresh sorbent; 2 = after 1st regeneration; 3 = after 2nd regeneration

The poor performance of the regenerated commercial sample is not unexpected, as the TPO results showed that a thermal treatment well above 500 °C was required to convert the ZnS phase into the active oxide phase.

Concerning the regenerated zinc oxide-based sorbent, it results quite similar to the fresh one, as observed by XRD patterns (Figure 20) and the FTIR spectra (Figure 21). According to Table 3 data, the

surface area of Zn_R (332 m²/g) is significantly lower than that of Zn_F (482 m²/g). Despite this, a better performance is observed on the former. Such enhancement in the sorption activity of the zinc oxide-based composite in cycle operation is in agreement with the findings of the previous chapter on ZnO/SBA-15 sorbents (see section 4.7.2). No simple correlation exists between the accessibility parameters (S_{BET} and V_p) and the sorbent performance. Based on the evidences of the previous chapter (section 4.7.2), it can be suggested that the ZnO phase originating from the ZnS oxidation during the regeneration step of the sorbent is different in terms of crystallinity, particle size and texture from the one obtained directly by thermal decomposition of the zinc nitrate precursor, *i.e.* that the regeneration process induces a reorganization of the zinc oxide nanophase.

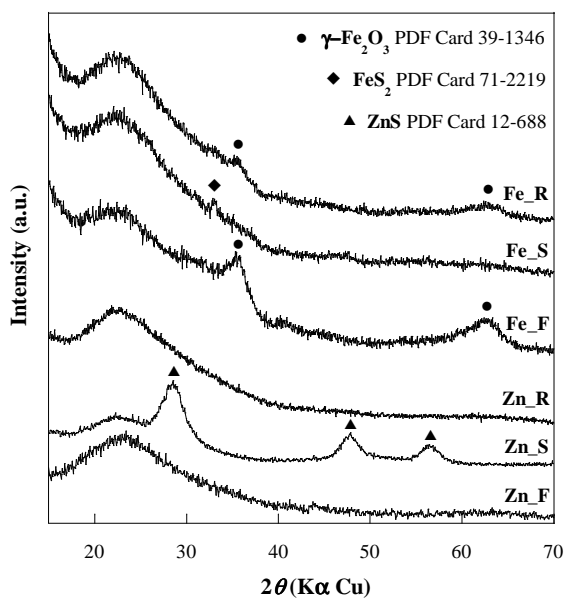


Figure 20. Wide-angle XRD patterns of the zinc oxide- and iron oxide-based sorbents in the regenerated (*R*) state compared with the fresh (*F*) and sulphided (*S*) ones. The main reflection planes are marked.

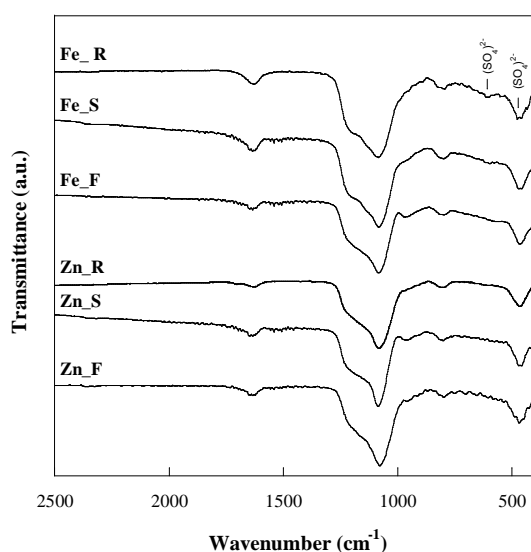


Figure 21. FTIR spectra of the zinc oxide- and iron oxide-based sorbents in the regenerated (*R*) state compared with the fresh (*F*) and sulphided (*S*) ones.

For the iron oxide-based sorbent, a decrease in surface area occurs as a consequence of the regeneration process (Table 3), but the difference (15 %) seems too slight for explaining the observed halving of the B_t and SRC values. At variance with the case of ZnO/SBA-15 sorbent, the XRD and FTIR techniques are able to reveal differences between the regenerated and fresh iron oxide/SBA-15 samples. After regeneration the XRD reflections attributable to the sulphided phases disappear and diffraction peaks ascribable to maghemite phase are observed (Figure 20), though weaker and slightly broader than for Fe_F. This can be due to either a lower amount of maghemite phase or differences in its crystallinity, owing to a decrease in the crystalline domain size and/or accumulated strain. In the FTIR spectrum of Fe_R sorbent (Figure 21), the Si-OH band at 960 cm^{-1} is less intense than that observed in the fresh sorbent, which suggests the occurrence on the former of weak interactions between the guest phase and the silica matrix. Interestingly, two low-intensity signals at about 470 cm^{-1} and 610 cm^{-1} are observable, which indicate the presence of an iron sulphate phase, not revealed in the XRD pattern.

5.6 Insight of the sulphidation-regeneration mechanism

For better understanding of the changes undergone by the sorbent during the sulphidation-regeneration cycles, the investigation was extended to a pure nanostructured maghemite phase, which was first sulphided and then regenerated. The corresponding XRD patterns (Figure 22) showed for the sulphided sample the presence of pyrrhotite (Fe_{1-x}S) and pyrite (FeS_2), as well as of a minor amount of unreacted maghemite. The absence in the sulphided composite of the pyrrhotite phase can be probably due to its metastability, enhanced by the nanodispersed nature of the sulphide. Interestingly, besides a remarkable amount of maghemite, the presence of iron sulphate ($\text{Fe}_2(\text{SO}_4)_3$) was detected by XRD after regeneration by heating at 500 °C and holding for 4 h. After heating up to 700 °C, no sulphate phase was detected in the XRD pattern where only maghemite phase was present. According to the above, the incomplete recover of the sorption activity of the iron oxide/SBA-15 composite after the sorption-regeneration cycles can be ascribed to the presence of iron sulphate, which is inert towards H_2S . Such iron sulphate phase is not visible in Figure 20 because of the overlapping of its most intense peaks with the broad silica band at $2\theta = \text{ca. } 23^\circ$.

The different behaviour of the regenerated sorbents in comparison with the fresh ones can hence be ascribed to different factors. In the case of the zinc oxide-based sorbent an increase in crystallinity of the ZnO phase originating from the ZnS oxidation during the regeneration step with respect to the crystallinity of the phase obtained directly by thermal decomposition of the zinc nitrate precursor would be responsible for the enhanced performance of the regenerated sorbent. In the case of the iron oxide-based sorbent the formation, during the regeneration step, of an iron sulphate phase unable to react with H_2S would explain the lack of complete recovery of the sorption capacity of the regenerated sorbent.

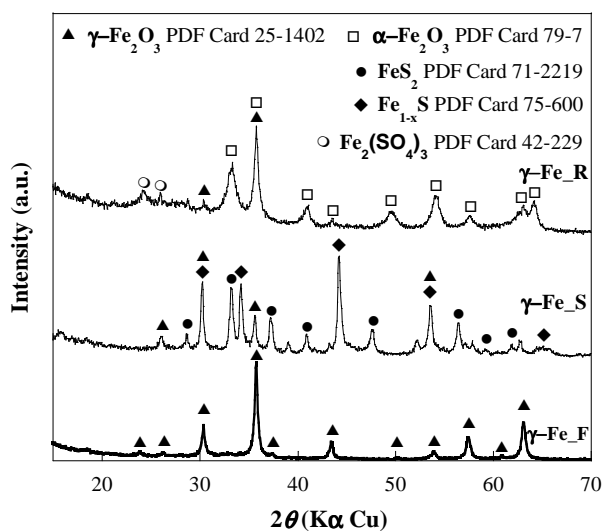


Figure 22. XRD patterns of the fresh (γ -Fe_F), sulphided (γ -Fe_S) and regenerated (γ -Fe_R) pure nanostructured maghemite sample (γ -Fe₂O₃, Aldrich commercial product).

5.7 Conclusions

A simple, reproducible and easy-to-scale-up two-solvents impregnation route has been used for dispersing zinc oxide and iron oxide inside the mesoporous channel system of SBA-15. The resulting nanocomposites have a remarkable performance for the H₂S removal from hot (300 °C) gas streams, the activity of the zinc oxide and the iron oxide systems being seven and seventy times higher than that of an unsupported zinc oxide commercial sorbent, respectively. The zinc oxide phase is incorporated as a thin amorphous homogeneous layer while the iron oxide one is dispersed in form of small maghemite crystallites. Differences in the morphology and the crystallinity of the active phase, as well as in the textural features of the composites, seem related to the lack or presence of interactions between the guest oxide phase and host silica matrix, which in turn make the iron oxide and zinc oxide phases differently prone to react with hydrogen sulphide. After regeneration of the sulphided sample, the sorption properties of the zinc oxide/SBA-15 composite appear enhanced and are maintained upon

repeating the sorption-regeneration cycle. The iron oxide/SBA-15 sorbent shows the highest sulphur retention capacity. Its performance significantly decreases at the second sorption cycle mainly due to the formation of an iron sulphate phase, but is retained at the third sorption cycle. This indicates that the amount of H₂S-inert iron sulphate does not increase further. Noteworthy, though decreased in comparison with that of the fresh sample, the performance of the regenerated iron oxide-based sorbent is still far better than that of the ZnO-based one, either fresh or regenerated. The oxidation step for obtaining the regenerated iron oxide-based sorbent can be carried out at $T \leq 350$ °C, which is considerably lower than that required in the case of the ZnO-based sample. In view of a possible application, this would be quite important for the thermal efficiency of the sorption-regeneration process.

References

- [1] P. J. H. Carnell and P. E. Starkey, *Chem. Eng.*, **1984**, 408, 30.
- [2] J. A. Rodriguez, S. Chaturvedi, M. Kuhn and J. Hrbek, *J. Phys. Chem. B*, **1998**, 102, 5511.
- [3] A. Davydov, K. T. Chuang and A. R. Sanger, *J. Phys. Chem. B*, **1998**, 102, 4745.
- [4] S. S. Tamhankar and C. Y. Wen, *Ind. Gas Sep.*, **1983**, 223, 255.
- [5] J. Deng, J. Ma, L. Mei, Y. Tang, Y. Chen, T. Lv, Z. Xu and T. Wang, *J. Mater. Chem. A*, **2013**, 1, 12400.
- [6] J. D. White, F. R. Groves Jr. and D. P. Harrison, *Catal. Today*, **1998**, 40, 47.
- [7] Y. G. Pan, J. F. Perales, E. Velo and L. Puigjaner, *Fuel*, **2005**, 84, 1105.
- [8] H. L. Fan, K. C. Xie, J. Shangquan, F. Shen and C. H. Li, *J. Nat. Gas Chem.*, **2007**, 16, 404.
- [9] S. S. Tamhankar, M. Hasatani and C. Y. Wen, *Chem. Eng. Sci.*, **1981**, 36, 1181.
- [10] D. Zhao, J. Feng, Q. Huo, N. Melosh, G. H. Fredrikson, B. F. Chmelka and G. D. Stucky, *Science*, **1998**, 279, 548.
- [11] J. van der Meer, I. Bardez-Giboire, C. Mercier, B. Revel, A. Davidson and R. Denoyel, *J. Phys. Chem. C*, **2010**, 114, 3507.
- [12] F. Boubekr, A. Davidson, S. Casale and P. Massiani, *Micropor. Mesopor. Mat.*, **2011**, 141, 157.
- [13] F. Rouquerol, J. Rouquerol and K. Sing, in *Adsorption by Powders and Porous Solids*, Academic Press, **1999**, ch. 7, pp. 191-217.
- [14] A. H. Jansen, C. M. Yang, Y. Wang, F. Schüth, A. J. Koster and K. P. de Jong, *J. Phys. Chem. B*, **2003**, 107, 10552.
- [15] E. Delahaye, V. Escax, N. El Hassan, A. Davidson, R. Aquino, V. Dupuis, R. Perzynski and Y. L. Raikher, *J. Phys. Chem. B*, **2006**, 110, 26001.
- [16] C. Cannas, M. Casu, A. Lai, A. Musinu and G. Piccaluga, *J. Mater. Chem.*, **1999**, 9, 1765.
- [17] Q. Jiang, Z. Y. Wu, Y. M. Wang, Y. Cao, C. F. Zhou and J. H. Zhu, *J. Mater. Chem.*, **2006**, 16, 1536.
- [18] R. Anedda, C. Cannas, A. Musinu, G. Pinna, G. Piccaluga and M. Casu, *J. Nanopart. Res.*, **2008**, 10, 107.

- [19] S. Bruni, F. Cariati, M. Casu, A. Lai, A. Musinu, G. Piccaluga and S. Solinas, *Nanostruct. Mater.*, **1999**, 11, 573.
- [20] A. Bertoluzza, C. Fagnano, M. A. Morelli, V. Gottardi and M. Guglielmi, *J. Non-Cryst. Solids*, **1982**, 48, 117.
- [21] Q. Jiang, Z. Y. Wu, Y. M. Wang, Y. Cao, C. F. Zhou and J. H. Zhu, *J. Mater. Chem.*, **2006**, 16, 1536.
- [22] M. Fantauzzi, A. Pacella, D. Atzei, A. Gianfagna, G. B. Andreozzi and A. Rossi, *Anal. Bioanal. Chem.*, **2010**, 396, 2889.
- [23] J. M. Philias and B. Marsan, *Electrochimica Acta*, **1999**, 44, 2351.
- [24] M. Fantauzzi, C. Licheri, D. Atzei, G. Loi, B. Elsener, G. Rossi and A. Rossi, *Anal. Bioanal. Chem.*, **2011**, 401, 2237.
- [25] M. Fantauzzi, D. Atzei, B. Elsener, P. Lattanzi and A. Rossi, *Surf. Interface Anal.*, **2006**, 38, 922.
- [26] M. Mureddu, I. Ferino, E. Rombi, M.G. Cutrufello, P. Deiana, A. Ardu, A. Musinu, G. Piccaluga, C. Cannas, *Renewable Energy Global Innovations* {ISSN 2291-2460}, **2013**, <http://reqinnovations.org/>
- [27] M. Mureddu, I. Ferino, E. Rombi, M. G. Cutrufello, P. Deiana, A. Ardu, A. Musinu, G. Piccaluga and C. Cannas, *Fuel*, **2012**, 102, 691.

Chapter 6

Zinc ferrite/SBA-15 sorbents

6 Introduction

The first metal oxide mixed with zinc oxide was iron oxide forming zinc ferrite. Zinc oxide has a very high equilibrium constant for sulphidation resulting in low equilibrium H_2S concentrations but has very slow kinetics, which limits its sulphur loading capacity. Iron oxide, on the other hand, has rapid kinetics, namely a high sulphur loading capacity, but its equilibrium constant is not high enough for the degree of H_2S removal required in IGCC systems. It is also known that iron oxide is easily regenerable^[1, 2]. The purpose for zinc ferrite formation is to combine both positive features of ZnO and Fe_2O_3 , such as high sulphur capacity, fast response, and easy regeneration.

Promising results are obtained for both the zinc oxide- and iron oxide-based sorbents (see previous chapters), on the one hand for the ability to maintain the sulphur retention capacity in several repeated sulphidation-regeneration cycles, and on the other hand for the enhancement in sulphur retention capacity during the first run and for the lower regeneration temperature, leading the research activity to investigate the synergism between the zinc and iron oxide sorbents. The $ZnFe_2O_4$ content was selected equal to 20 wt.%, the same of Fe_2O_3 /SBA-15 sorbent.

6.1 Preparation of Zinc ferrite/SBA-15 nanocomposite sorbents

Some authors have stated that prevention of redistribution during drying is the key to obtain a highly dispersed and homogeneously distributed metal (oxide) phase. These findings are mainly based on comparison of extrudates, spheres or pellets that were impregnated and dried using a metal nitrate (*e.g.*,

Ni or Fe) or citrate salt, and on the addition of polysaccharide carbohydrates (*e.g.*, hydroxyethylcellulose) to $\text{Cu}(\text{NO}_3)_2 \cdot 3\text{H}_2\text{O}$ precursor solutions^[3-6]. These studies indicated that the use of chelating salts or the addition of viscosity-increasing agents to aqueous nitrate solutions prevented the formation of egg-shell type distributions. Besides homogeneous precursor distributions, the metal dispersion of the final catalyst was also found to increase largely with these chelating precursor salts. Lensveld and others showed that these findings could be transferred to powder supports^[7]. The effectiveness of these chelating precursors is ascribed to three phenomena. Firstly, a sharp increase in viscosity due to gelation of the precursor solution upon drying inhibits migration. Secondly, the poor crystallization behaviour of these salts presumably limits redistribution due to absence of fast crystal growth, and thirdly, enhanced interaction of the covering layer with the support via hydrogen bonding.

Moving along this line, in this study $\text{ZnFe}_2\text{O}_4/\text{SBA-15}$ sorbent has been synthesized via a novel impregnation-sol-gel autocombustion combined strategy that involves a first step of impregnation of a nitrate aqueous solution containing citric acid on SBA-15 support, followed by a combustion step. In this method, precursor gels are prepared from aqueous solutions of metal nitrates and an organic complexing such as citric acid. The citrate-nitrate gels, when heated in a hot furnace, burn in a self-propagating process, rapidly converting the precursor mixtures directly into products. Due to the good capability of chelating metallic ions and to low decomposition temperatures, citric acid is suited for obtaining precursors of transition metal oxides^[8-11]. The citric acid plays two important roles: on one hand, it is the fuel for the combustion reaction; on the other hand, it forms complexes with metal ions preventing the precipitation of hydroxylated compounds; the nitrate ion is the burning oxidizer.

For comparison, the two-solvents hexane-water impregnation procedure was adopted to obtain a $\text{ZnFe}_2\text{O}_4/\text{SBA-15}$ sorbent with the same composition. For both samples the final zinc ferrite loading was chosen equal to 20 wt.% and were synthesized with Zn to Fe molar ratio of 1:2.

The SBA-15 mesostructured silica was prepared according to the procedure reported by Zhao et al.^[12] and described in detail in the Chapter 3 (see [section 3.2](#)).

Typical Two-Solvents procedure is as follows: 10 cm³ of aqueous solution of 0.33 mmol of Zn(NO₃)₂·6H₂O (Aldrich, 98%), and 0.66 mmol of Fe(NO₃)₃·9H₂O (Aldrich, 98%) was prepared as metal precursor. 0.4 g of freshly calcined silica was suspended in 12 cm³ of *n*-hexane (first non-polar solvent). After a short mixing period (15 min at 400 rpm), 0.48 cm³ of metal precursor, corresponding to the SBA-15 pore volume previously determined by physisorption analysis ($V_p = 1.2 \text{ cm}^3/\text{g}$), was then added drop-by-drop. After vigorously stirring under room temperature for 2 h, the obtained yellowish dispersion was then left to dry in air at 40 °C overnight before to be calcined at 500 °C for 2 hours (heating rate 2 °C/min) to decompose the metal nitrates.

For the innovative impregnation strategy with sol-gel autocombustion approach, zinc-, iron-nitrate, and citric acid were used respectively as sources of metal ions and chelating-fuel agent. The synthesis proceeded in three successive steps: (i) complexation of the zinc-iron nitrate precursor with citric acid; (ii) impregnation of the calcined SBA-15 silica with the complex; (iii) self-combustion of the zinc-iron(nitrate)-citrate complex. Therefore, the combustion can be considered to be a heat-induced exothermic oxidation-reduction reaction where nitrate ions act as oxidizers and the carboxyl group acts as a reducing agent. Owing to the exothermic characteristic of the reaction, high temperatures ensure the crystallization and formation of oxides in a short amount of time. The zinc and iron nitrates were dissolved in water with a 2:1 molar ratio, and citric acid (CA), was added to the solution. The molar ratio of metals (Zn(II) + Fe(III)) to CA was fixed at 1:1. The corresponding citrate-to-nitrate ratio was 0.37. 2.4 cm³ of aqueous solution containing 0.33 mmol of Zn(NO₃)₂·6H₂O (Aldrich, 98%), 0.66 mmol of Fe(NO₃)₃·9H₂O (Aldrich, 98%), and 0.99 mmol of citric acid (Aldrich, 99.5%) were put in contact with 0.4 g of freshly calcined silica under stirring at 150 °C. The orange-yellow dispersion had a spontaneous pH value ≈ 1 and was allowed to evaporate during 10 min with evolution of water. The viscous orange-yellow gel collected after evaporation, was submitted to a sudden raising of the temperature up to 250 – 300 °C activating the combustion mechanism and generating a yellow-brown dry powder. The solid was then calcined at 500 °C for 2 h (heating rate 2 °C/min) in order to eliminate the remaining carbonaceous residues.

The sorbent samples are labelled as ZF_TS_X and ZF_SC_X, where TS and SC indicate the "Two-Solvents" and "Self-Combustion" synthesis method used, and X denotes the state of the sorbent, F (Fresh), S (Sulphided) and R (Regenerated). Similar notation is used also for the commercial unsupported ZnO sorbent (Katalco_{JM} 32-5). A picture of the two synthesized samples in the fresh state is shown in [Figure 1](#).



Figure 1. Fresh $ZnFe_2O_4/SBA-15$ sorbents through two-solvents- (top) and self-combustion-impregnation (bottom).

[Figure 2](#) represents a schematic representation of the self-combustion impregnation powder preparation.

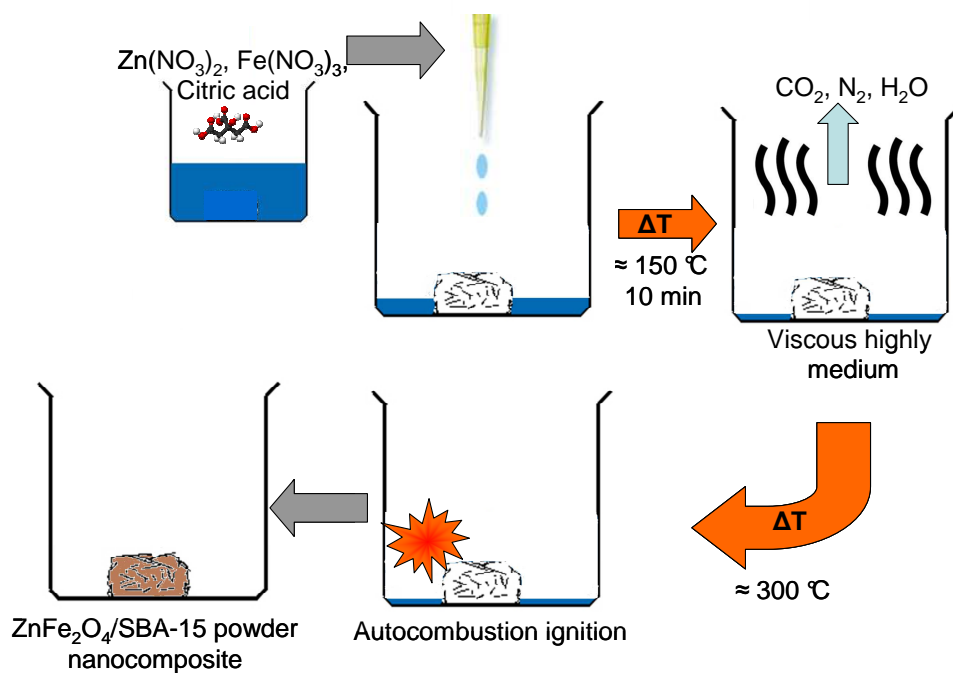


Figure 2. Graphical representation of the innovative impregnation via "Self-Combustion" approach.

6.2 Desulphurization activity of fresh sorbents

Figure 3 shows breakthrough curves for all the sorbents *vs.* the pure zinc oxide commercial sorbent (Katalco_{JM} 32-5) recorded at 300 °C. No H₂S removal was detected for the bare SBA-15.

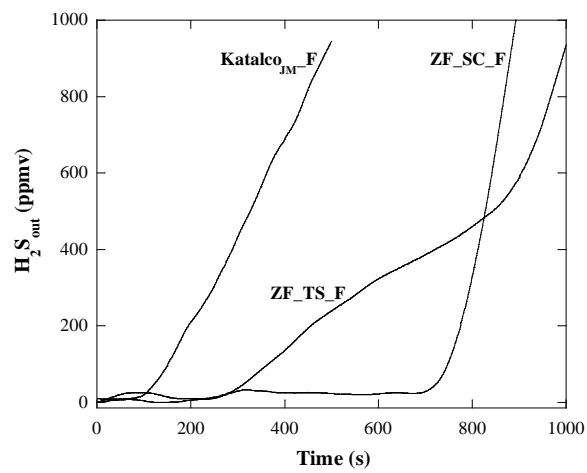


Figure 3. *H₂S* breakthrough curves of the ZnO commercial sorbent (Katalco_{JM}_F), ZF_TS_F and ZF_SC_F supported sorbent at the first sulphidation run.

Table 1. Breakthrough time (B_t) and Sulphur Retention Capacity (SRC) of fresh zinc ferrite-based sorbents. Data for the ZnO commercial sorbent (Katalco_{JM} 32-5) are also reported for comparison.

Sample	B_t (s)	SRC (mg _S /g _{active phase}) ± 1	SRC (mg _S /g _{sorbent}) ± 1
Katalco _{JM} _F	103	6	6
ZF_TS_F	317	94.4	18.9
ZF_SC_F	700	208.6	41.7

Table 1 shows the values of breakthrough time (B_t) and sulphur retention capacity (SRC), expressed relative to either the active phase content or to the total composite amount (active phase + support). Zinc ferrite-based sorbents show better performance than commercial ZnO sorbent. However, remarkable differences in sulphur retention capacity are found. ZF_SC_F, prepared through the self-combustion approach shows the highest retention capacity per unit mass of both active phase and total sorbent (208.6 mg S/g ZnFe₂O₄ and 41.7 mg S/g sorbent), despite the latter contained the same zinc ferrite loading (20 wt.%) of ZF_TS_F. These values are more than twice higher than that of the ZF_TS_F (94.4 mg S/g ZnFe₂O₄), and even much higher than the corresponding value for the commercial zinc oxide sorbent (6 mg S/g ZnO). On the basis of the observations reported in the previous chapters for zinc oxide- and iron oxide-based supported sorbents, the by far superior performance of the zinc ferrite/SBA-15 sorbents with respect to that of the commercial sample can be reasonably ascribed to differences in the exposure of the active phase to the reactant H₂S. As reported in the following, the typical properties used as key parameter to explain the differences in H₂S sorption performance (surface area and pore volume) cannot justify the great difference in SRC between ZF_TS_F and ZF_SC_F. It suggests that differences in terms of active phase crystallinity should be taken into account for explaining the sorption behaviour of these sorbents.

6.3 Characterization of the fresh sorbents

6.3.1 Low- and wide-angle X-ray diffraction characterization

Low- (a) and wide-angle (b) X-ray diffraction patterns of the fresh sorbents (ZF_TS_F and ZF_SC_F) compared with the bare SBA-15 are presented in Figure 4. The low-angle diffraction patterns of the sorbents exhibit a very intense diffraction peak indexed to the (100) reflection plane, and two well-resolved diffraction peaks, related to the (110) and (200) reflection planes corresponding to a two-dimensional highly ordered hexagonal arrangement of the channels (space group *P6mm*) with d_{100} of *ca.* 9.7 nm. Although the relative high loading of active phase (20 wt.%), the ordered mesostructure of

the SBA-15 is retained in both sorbents synthesized with different methods. Especially the self-combustion approach does not produce any significant change in the final sample pore structure due to the exothermic oxidation-reduction reaction. The same very slight shift of the reflections versus higher angles can be observed for both sorbents suggesting a very small contraction of the cell parameters.

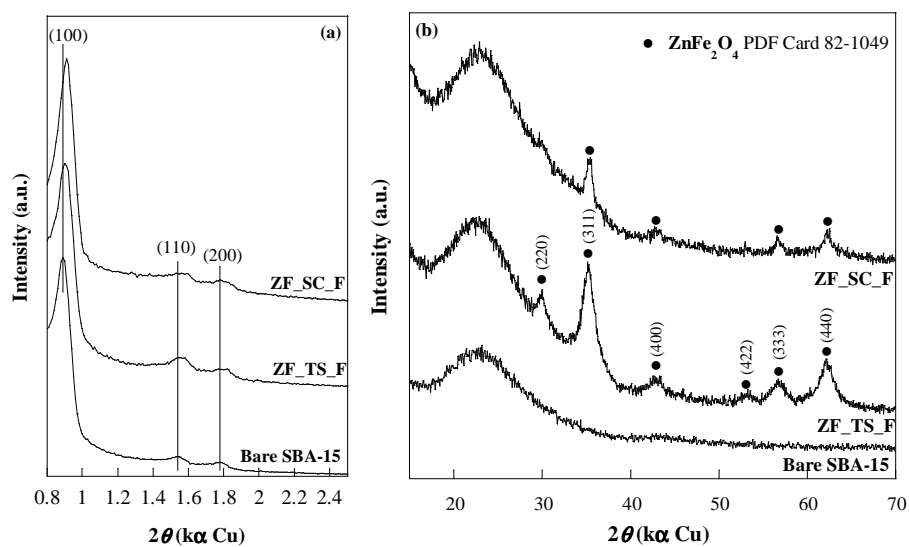


Figure 4. XRD patterns of bare SBA-15, ZF_TS_F and ZF_SC_F zinc ferrite sorbents synthesized through the two-solvents and self-combustion route at low-angle (a) and wide-angle (b). The main reflection planes are marked.

The wide-angle diffraction pattern of ZF_TS_F prepared with the "Two-Solvents" strategy is presented in Figure 4b and shows, besides the typical haloes of amorphous silica at $2\theta = ca. 23^\circ$, a series of reflections that on the basis of the 2θ values can be ascribed to the cubic $ZnFe_2O_4$ spinel structure (PDF Card 82-1049). These broad diffraction peaks (200), (311), (400), (422), (333), (440), provide a clear evidence of the formation of $ZnFe_2O_4$ as nanophase. The mean particle sizes calculated by applying the Scherrer equation to the (311), (400), (333) and (440) zinc-ferrite reflections, give a value of *ca.* 4 nm.

Slight differences are observed in the XRD pattern of ZF_SC_F prepared *via* "Self-Combustion" approach, since weaker and slightly narrower diffraction peaks than the "Two-Solvents" counterpart are visible. Again, it can be observed the typical diffraction peaks at 2θ 35°, 42.9°, 56.7° and 62.2° attributed to the most intense reflections of cubic ZnFe_2O_4 spinel structure (PDF Card 82-1049). The presence of narrower peaks suggests that the size of the particles formed are relatively larger than that of ZF_TS_F, and/or can indicate a difference in terms of the zinc ferrite crystallinity. The average size of the coherent domains obtained by applying the Scherrer equation to the (311), (333) and (440) diffraction peaks, give a result of *ca.* 7.6 nm. This result is not fully compatible with a crystallization of the particles inside the silica support because the pore size (6.4 nm) would obviously lead to a limited ZnFe_2O_4 particles size growth and consequently to weak and broad diffraction peaks as observed for the ZF_TS_F sorbent. A plausible explanation could be attributed to the formation of nanoparticles grown along the pores of the silica host, instead of spherical particles. This clearly demonstrate that the crystal size is highly affected by the impregnation method.

6.3.2 N_2 physisorption measurements: textural properties

The nitrogen adsorption/desorption isotherms (a) together with the pore size distributions (b) of the fresh sorbents compared with the bare SBA-15 support are shown in Figure 5. The silica support exhibits a type IV isotherm with an H1 type hysteresis loop, characteristic of a mesoporous material with uniform cylindrical pores open at both ends. The mesoporous character of the solid is preserved after the incorporation of the active phase, as revealed by the type IV shape of the isotherm for both the sorbents.

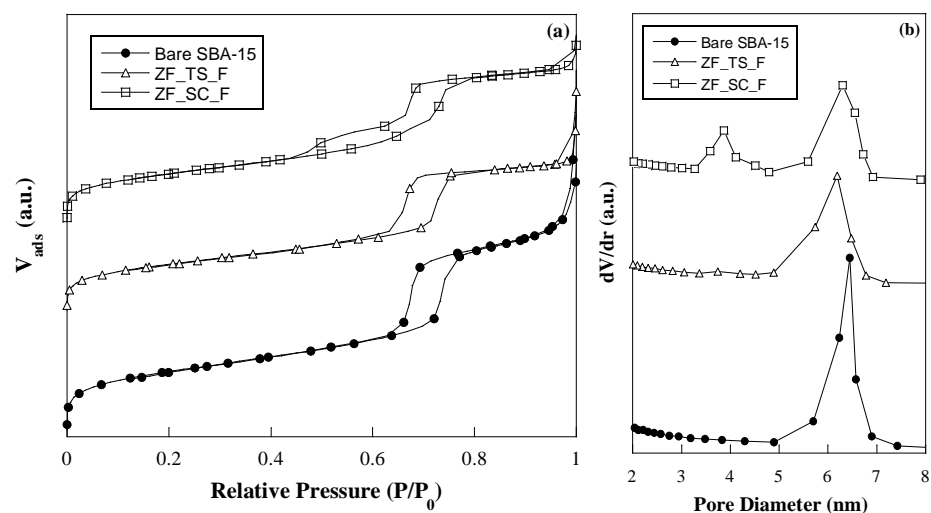


Figure 5. Nitrogen adsorption-desorption isotherms (a) and pore size distribution (b) of bare SBA-15 and zinc ferrite-based sorbents in the fresh state (full circles bare SBA-15, empty triangles ZF_TS_F, empty squares ZF_SC_F).

However, a new step is clearly observed on the desorption branch, especially in the case of ZF_SC_F sample, which generates delays in the closing of the hysteresis loop at $P/P_0 = 0.4 - 0.7$ in contrast with the case of ZF_TS_F, whose hysteresis loop is rather similar to that of the parent SBA-15. This feature could be associated with the development of a new porous system consisting of ink-bottle mesopores.

The main evolutions are concerned with the pore size distributions and the values of textural properties. As expected, a decrease in both specific surface area (S_{BET}) and pore volume (V_p), is observed due to a partial filling of the mesopores by the metal oxide loading (Table 2).

Table 2. N_2 physisorption data of fresh ZF_TS_F and ZF_SC_F zinc ferrite sorbents compared with the bare SBA-15 and the ZnO commercial sorbent (Katalco_{JM} 32-5). The thickness of the pore walls (T_w) is also reported.

Sample	S_{BET} (m^2/g)	V_p (cm^3/g)	D_p (nm)	T_w (nm)
Bare SBA-15	770	1.20	6.4	5.0
Katalco _{JM} _F	9	0.10	-	-
ZF_TS_F	614	0.83	6.2	5.1
ZF_SC_F	618	0.85	3.9 ; 6.3	-

S_{BET} : BET Specific Surface Area; V_p : Pore Volume; D_p : Pore Diameter; T_w : Wall Thickness = ($a_0 - D_p$); a_0 : XRD unit cell parameter.

Relative Standard Deviation: %RSD (S_{BET}) = 2.1%; %RSD (V_p) = 1.1%; %RSD (D_p) = 1.8%.

In any case some differences between ZF_TS_F and ZF_SC_F can be evidenced. For both ZF_TS_F and ZF_SC_F, S_{BET} and V_p are moderately lower than the corresponding values of the bare support, which indicates partial filling of the mesopores by the metal oxide. The pore size distribution plot for ZF_TS_F (Figure 5b) shows a monomodal distribution centred at 6.2 nm. This value is slightly lower than that of SBA-15 (Figure 5b). By subtracting the mean pore diameter from the unit cell parameter (a_0 , calculated from low-angle XRD data), the wall thickness (T_w) values were calculated, resulting 5.0 and 5.1 nm for the bare SBA-15 and ZF_TS_F, respectively (Table 2). Such values, together with the V_p decrease, suggest the presence of $ZnFe_2O_4$ as dispersed in very small nanoparticles. This is in agreement with the findings in the wide-angle XRD pattern. At variance with the case of the zinc ferrite/SBA-15 prepared with the two-solvents technique, ZF_SC_F sorbent prepared with the self-combustion approach, shows a clear bimodal pore size distribution (Figure 5b) which seems related to the two-step feature observed in the desorption branch of the isotherm of this sample (Figure 5a) and indicates that two distinct families of pores contribute to the overall pore volume. On one hand, the remaining empty mesopores behave as

usual and give the hysteresis loop that ends at $P/P_0 = 0.6$; on the other hand, partially blocked mesopores can be associated with the hysteresis loop at $P/P_0 = 0.4$. As indicated in the literature for zirconia- and iron oxide-containing SBA-15^[13,14], these two steps are associated with a typical ink-bottle adsorption/desorption behaviour: in the same pore, the volume between two oxide particles would be only accessible through a small neck. This peculiar behaviour can be reasonably associated with the presence of large zinc ferrite particles grown in the pores of the silica host, as detected by XRD, yielding the ink-bottle behaviour.

The textural and structural properties clearly demonstrate that the distribution of the zinc ferrite inside the SBA-15 channels is highly dependent on the impregnation technique.

6.3.3 TEM images: morphological characterization

Results of transmission electron microscopy analysis for ZF_TS_F and ZF_SC_F are shown in [Figure 6](#). Bare SBA-15 support, the same used for the preparation of iron oxide/SBA-15 in the previous chapter, exhibits a well-defined hexagonal pore structure with regular empty mesochannels of *ca.* 6–7 nm. The hexagonal arrangement is clearly visible for both ZF_TS_F and ZF_SC_F, consistent with the XRD and N_2 physisorption results that evidenced well-resolved low-angle reflections as well as typical type IV isotherm. For the samples under study, no particles at the external surface have been observed in the TEM images and this suggests that both the preparation methods are favourable to prevent the migration of oxide particles outside the pore system during the calcination step. Nevertheless, differences in zinc ferrite particles morphology and size can be observed depending on the preparation method.

TEM images of ZF_TS_F show that zinc ferrite is not uniformly dispersed. Focusing on the silica mesopores ([Figure 6b](#)) it is possible to observe the formation of "*pseudo spherical*" crystallized zinc ferrite particles which size is *ca.* 3–4 nm, fully consistent with the result of wide-angle XRD pattern. The crystalline nature of these nanoparticles (inset of [Figure 6b](#)), has enabled to calculate the d spacing (0.25 nm), in agreement with the (311) reflection of cubic $ZnFe_2O_4$ spinel structure (PDF Card 82-1049).

On ZF_SC_F, the formation of particles with well-defined morphology is more difficult to be observed and generally the guest oxide is not uniformly dispersed; the rough contours of the channels (some of which appear completely filled) are the result of the deposition of oxide nanoparticles. Figure 6c shows two different regions, *i.e.*, the one located in the inlet of the mesopores, free of oxide particles (bright zone) and the other with ZnFe₂O₄ fully infiltrated in pore channels (shrinkage dark zone). So in the same mesopore coexists both areas with or without metal oxide. This is consistent with N₂ physisorption result where a bimodal pore size distribution was observed for ZF_SC_F. In another region (Figure 6d) the zinc ferrite particles seem to fill up the SBA-15 channels with diameter close to the pore size of the support and variable length. The micrograph shows that the rod/tube-like nanoparticles have grown in adjacent mesopores.

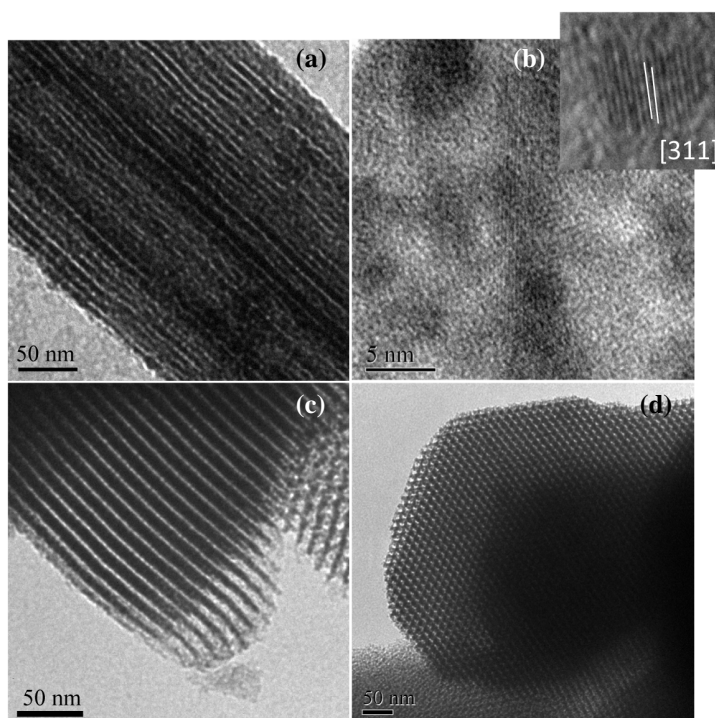


Figure 6. Representative TEM images of ZF_TS_F (a and b) and ZF_SC_F (c and d).

6.3.4 FT-IR characterization

FTIR spectra of the sorbents are reported in [Figure 7](#) and compared with the spectrum of the bare SBA-15. Most of the features are common to all the spectra: (i) the absorption bands at 1200-1080 and 800 cm^{-1} of the asymmetric and symmetric modes of Si-O-Si groups, respectively ^[15]; (ii) the absorption band at 960 cm^{-1} of Si-OH stretching modes of the non-condensed Si-OH groups and the band at 465 cm^{-1} due to bending of the O-Si-O groups; (iii) the absorption peak at around 1630 cm^{-1} of the H-O-H bending vibration of H_2O adsorbed in capillary pores and on the surface. For both the sorbents, the absence of the typical narrow signal around 1370 cm^{-1} due to the stretching vibration of the NO_3^- groups proves the complete decomposition of nitrates.

Intrinsic stretching vibrations of the metal at the tetrahedral site, $M_{tetra} \leftrightarrow \text{O}$, are generally observed in the range of 620-550 cm^{-1} . Octahedral-metal stretching vibrations, $M_{octa} \leftrightarrow \text{O}$, are generally observed in the range of 450-385 cm^{-1} ^[16, 17]. In [Figure 7](#), both ZF_TS_F and ZF_SC_F show only a broad stretching vibration band at about 560 cm^{-1} associated with the spinel structure of the zinc ferrite.

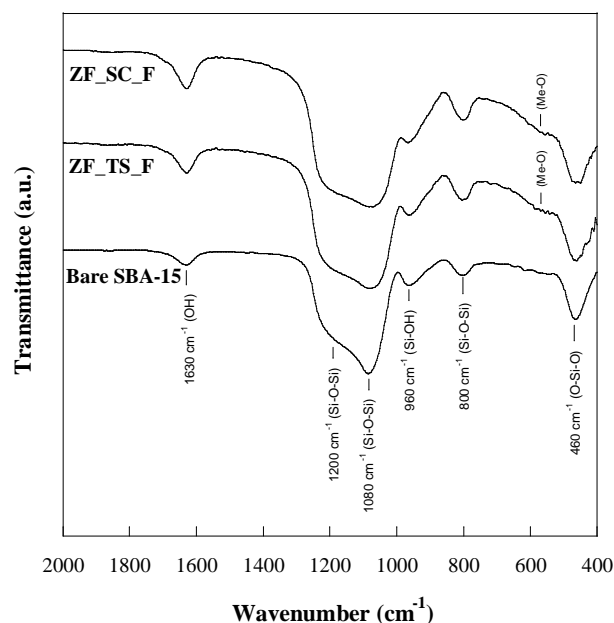


Figure 7. FTIR spectra of bare SBA-15, zinc ferrite-based sorbents in the fresh state (ZF_TS_F and ZF_SC_F).

6.4 Characterization of the sulphided sorbents

Figure 8a presents the XRD patterns in the low-angle domain for the sulphided sorbents compared with those of the fresh ones. After the sorption runs, the support mesostructure is retained in all samples. No significant shifts of the (100), (110) and (200) peaks are visible between the fresh and the sulphided materials, suggesting no shrinkage in the mesoporous framework. XRD patterns recorded at wide-angles are depicted in Figure 8b. Besides the broad halo at $2\theta = ca. 23^\circ$ typical of the amorphous silica, XRD pattern of ZF_TS_S shows diffraction peaks shifted to lower 2θ angles as compared to the fresh sorbent, which indicates that the metal oxide in the fresh sorbent is converted into metal sulphide. These peaks are associated with the most intense reflections of ZnS phase at 28.6° , 47.7° and 56.6° (PDF Card 12-688), and, although less intense, to the FeS₂ phase at 33.03° and 37.3° (PDF Card 71-2219). No remaining spinel phase from the fresh sorbent was found by XRD suggesting that the sorbent had been

completely sulphided. The mean size of the ZnS nanocrystals can be estimated in the 5-6 nm range by Debye-Scherrer equation. Nevertheless, the diffraction peaks intensity of the pyritic phase contribution remains too low to be able to estimate the size of the particles. Similarly, the XRD pattern of ZF_SC_S shows the same reflections attributed to the ZnS and FeS₂ sulphided phases, but also more resolved peaks with higher intensity appear at 40.5°, 61.4° and 64.3° (PDF Card 71-2219) ascribed to reflections of the pyrite phase. In this case it was possible to estimate the mean size of the FeS₂ nanocrystals which resulted to be *ca.* 11 nm. The average size of the ZnS resulted to be *ca.* 6.5 nm, slightly higher than that obtained for the zinc sulphide phase formed in the ZF_TS_S. These results suggest a different degree of crystallinity of the ZnS and FeS₂ sulphided phases. Furthermore, the higher intensity of the pyrite reflections in the ZF_SC_S sorbent could indicate that a greater amount of iron sulphide is formed during the sulphidation.

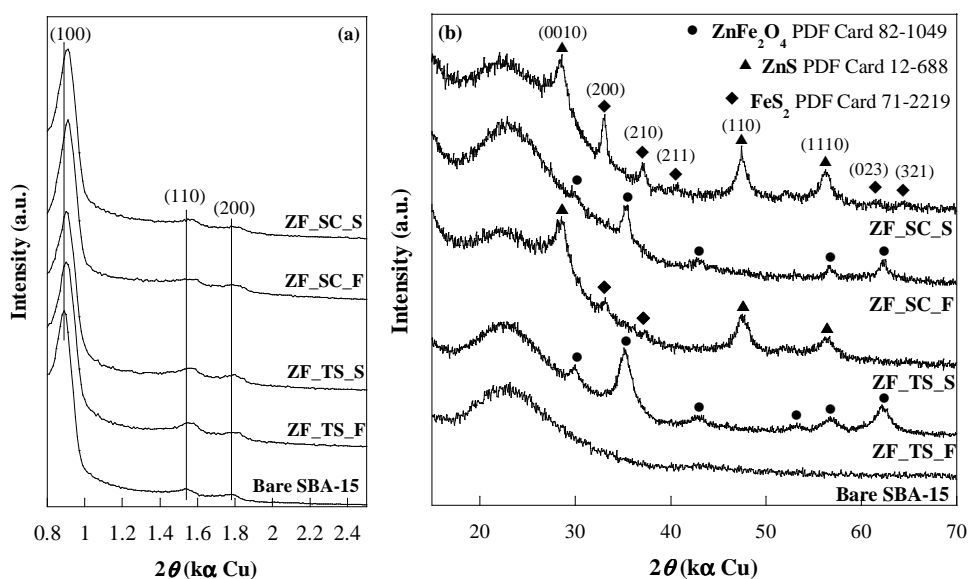


Figure 8. XRD patterns of bare SBA-15, ZF_TS and ZF_SC sorbents before (F) and after sulphidation (S) at low-angle (a) and wide-angle (b). The main reflection planes are marked.

Nitrogen physisorption isotherms of ZF_TS_S and ZF_SC_S (Figure 9a) confirm the mesostructured character of the sulphided sorbents.

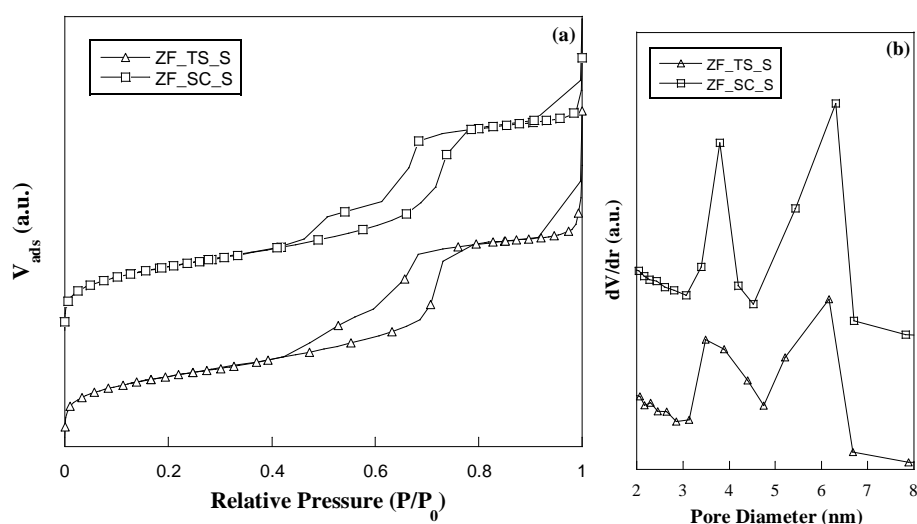


Figure 9. Nitrogen adsorption-desorption isotherms (a) and pore size distribution (b) of zinc ferrite-based sorbents in the sulphided state (empty triangles ZF_TS_S, empty squares ZF_SC_S).

As a consequence of the sulphidation process, as observed from XRD results for both ZF_TS_F and ZF_SC_F, zinc ferrite nanocrystals go towards the formation of two separate phases resulting in zinc sulphide and pyrite respectively. Due to the different molar volume values of the starting ZnFe_2O_4 phase ($47.3 \text{ cm}^3/\text{mol}$) and the resulting ZnS and FeS_2 sulphided phases (which total volume is $75.4 \text{ cm}^3/\text{mol}$), an expansion in the volume of the guest material as high as 37% should be expected in case of complete conversion. Such expansion should lead to a decrease in surface area and pore volume, which is actually observed (Table 3) for both ZF_TS_S and ZF_SC_S. The occurrence of an increase in the guest phase volume is also partially confirmed by the pore size distribution. At variance with the case of ZF_TS_F, a

bimodal pore size distribution appears with a second pore family centred at 3.5 nm for ZF_TS_S (Figure 9b). This can be reasonably attributed to the presence of the sulphided species occupying the pores.

By converse, the bimodal pore size distribution (Figure 9b) is maintained in the ZF_SC_S, even if, only a very slight reduction in D_p value is observed.

Table 3. N_2 physisorption data of fresh, sulphided and regenerated zinc ferrite-based sorbents (ZF_TS and ZF_SC) compared with the bare SBA-15 and the ZnO commercial sorbent (Katalco_{JM} 32-5). The thickness of the pore walls (T_w) is also reported.

Sample	S_{BET} (m^2/g)	V_p (cm^3/g)	D_p (nm)	T_w (nm)
Bare SBA-15	770	1.20	6.4	5.0
Katalco _{JM} _F	9	0.10	-	-
ZF_TS_F	614	0.83	6.2	5.1
ZF_TS_S	465	0.72	3.5 ; 6.1	-
ZF_TS_R	440	0.67	3.7 ; 5.9	-
ZF_SC_F	618	0.85	3.9 ; 6.3	-
ZF_SC_S	482	0.66	3.8 ; 6.3	-
ZF_SC_R	393	0.61	3.5 ; 5.9	-

S_{BET} : BET Specific Surface Area; V_p : Pore Volume; D_p : Pore Diameter; T_w : Wall Thickness = $(a_0 - D_p)$; a_0 : XRD unit cell parameter. Relative Standard Deviation: %RSD (S_{BET}) = 2.1%; %RSD (V_p) = 1.1%; %RSD (D_p) = 1.8%.

After desulphurization, the framework of ZF_TS_S still remained intact (Figure 10) despite the expansion in the volume of the guest material. The interplanar distances detected by HRTEM image (inset of Figure 10b), yield to distances (0.31 nm) consistent with the (0010) reflection of hexagonal ZnS phase (PDF Card 12-688). The main interest of these images is the possibility to observe that in the sulphided sample there is a separation phase, and nanocrystals typical of a specific phase are observable consistently with the wide-angle XRD result. The image taken along the direction parallel to the pore axis (Figure 10a) of the ZF_TS_S, compared with that of the fresh one, allows to point out (i) a remarkable reduction of the pore diameter and (ii) lots of the pores fully filled. No important difference is observed in the ZF_SC_S sorbent, identifying, once more, in the same mesopore, a completely free portion and, a partial one occupied by the sulphided product (Figure 10c and 10d), according to the bimodal distribution revealed by N₂ physisorption.

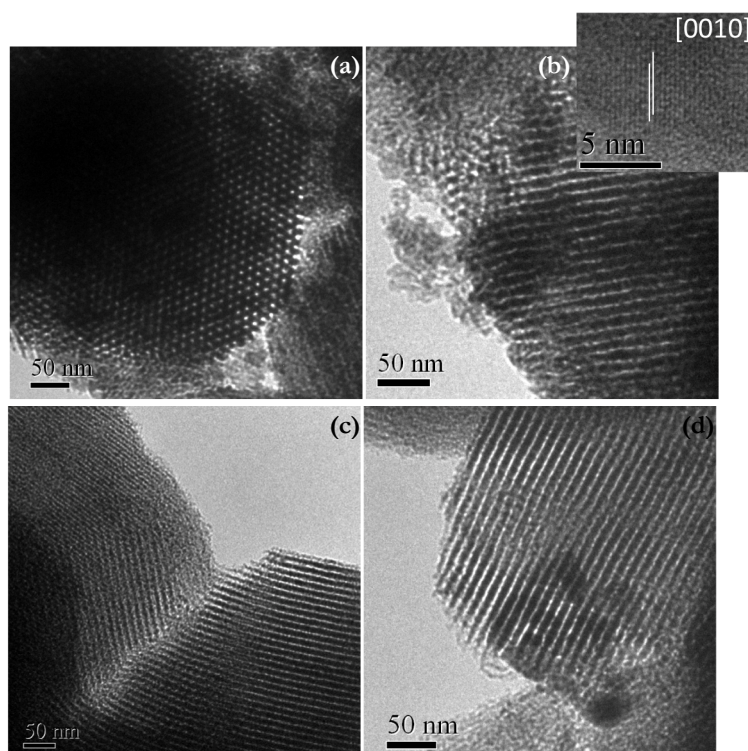


Figure 10. Representative TEM images of ZF_TS_S (a and b) and ZF_SC_S (c and d).

The FTIR spectra of the sulphided sorbents are reported in Figure 11. A very slight difference is observed for both the sulphided sorbents (ZF_TS_S and ZF_SC_S) where the Si-OH band at 960 cm^{-1} is poorly attenuated suggesting possible interactions between the silica host and the sulphide guest phases. Similar behaviour was revealed in the case of iron oxide-based sorbent (see Fe₂S₃ of Figure 12 in Chapter 5). The presence of FeS₂ phase, revealed by both the XRD pattern and the *pale brass-yellow* colour of the sulphided sorbents, can be responsible for the low-intensity band at *ca.* 600 cm^{-1} observed only in the ZF_TS_S, in agreement with Philiat^[18]. As announced in the previous chapter the pyrite formation is also consistent with the thermodynamic stability of this phase in comparison with the other iron sulphides.

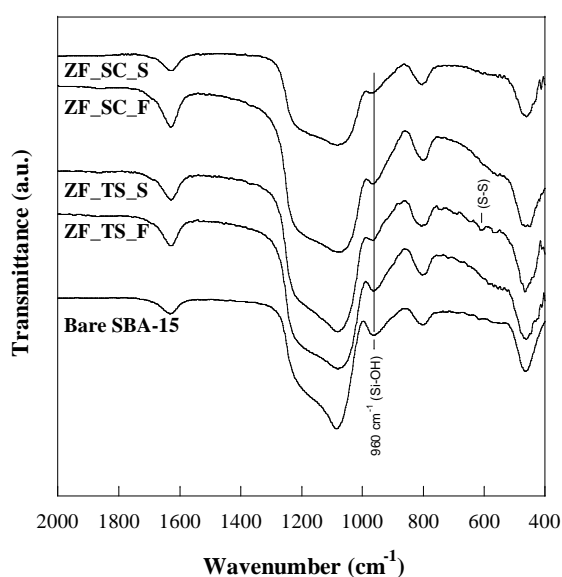


Figure 11. FTIR spectra of bare SBA-15, ZF_TS and ZF_SC in the fresh (F) and sulphided state (S).

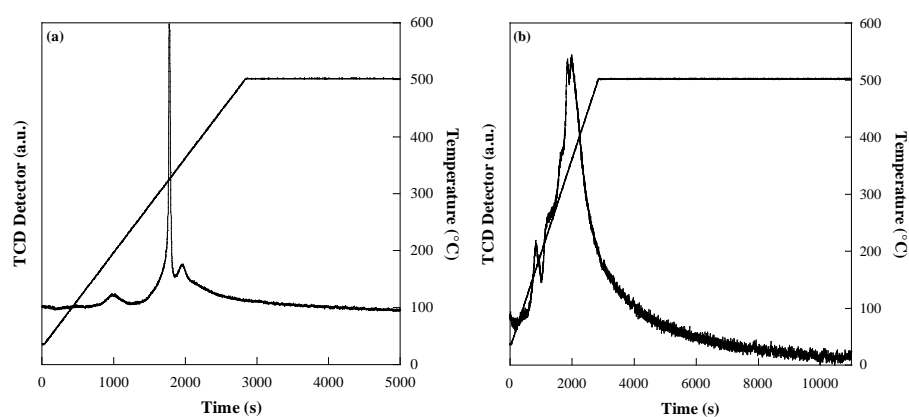
6.5 Sorbents regeneration and desulphurization-regeneration cycles

6.5.1 Temperature-programmed oxidation of the sulphided sorbents

The regeneration characteristics of a sorbent are very important for its application in industry. The main problems of the regeneration process of most desulphurization sorbent systems are associated with the regeneration at high temperatures (more than 600 °C), which, by one hand increase the cost, and by the other hand could lead to the sintering and loss of reactivity of the sorbent. More attention should be paid on how to reduce the regeneration temperatures.

To determine the suitable regeneration temperature of ZF_TS_S and ZF_SC_S, the TPO for the sulphided samples were carried out as well as on the sulphided commercial sorbent. As realized for the zinc oxide- and iron oxide-based sorbents (see section 5.5.1 of Chapter 5), the regeneration temperature has been extended up to 700 °C for both the prepared zinc ferrite-based sorbents but no peaks were

detected in the region between 500 and 700 °C (data not shown). Only for the sulphided commercial ZnO sorbent the regeneration run has been carried out through a two-step (500 and 700 °C) treatment. The resulting TPD profiles are illustrated in Figure 12. For ZF_TS_S and ZF_SC_S the shape of the curves indicate that the release of SO₂ is complete although the area subtended is higher in the case of ZF_SC_S. Another difference is that for ZF_TS_S before 500 °C, the sulphided sample is completely regenerated, whereas ZF_SC_S at 500 °C is not fully regenerated as observed from the TPD profile, which does not entirely return to the baseline. In any case, during the isotherm at 500 °C for 2h, the whole amount of sulphided phases has been oxidized. It is worthy of note that for temperatures ≤ 500 °C the oxidation of the sulphided commercial sample was almost negligible, only a very low, enlarged signal being detected for such temperatures in the TCD profile; heating the sample well above 500 °C was required for the onset of oxidation to a significant extent.



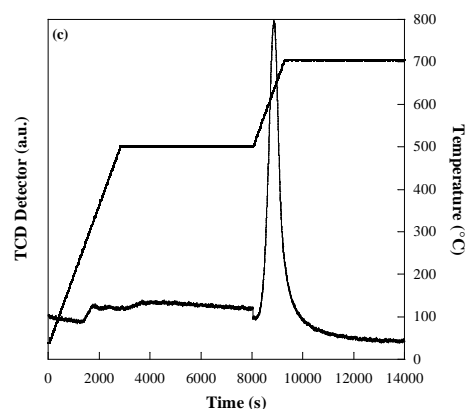


Figure 12. TCD profiles of the ZF_TS_S (a), ZF_SC_S (b) sulphided sorbents regenerated at 500 °C, and Katalco_{JM}_S (c) sulphided sorbents, regenerated through a two-step (500 and 700 °C) treatment.

Since the TCD detector is not able to discriminate among the species originated during the regeneration run, further runs were carried out in which the SO₂ and O₂ species in the outlet gas composition were simultaneously monitored by quadrupole mass spectrometer (QMS). TCD and QMS signals for both the zinc ferrite-based sulphided sorbents are reported in Figure 13a and 13b. For ZF_TS_S (Figure 13a), the TCD profile shows a peak at 194 °C, a well-resolved peak at 324 °C with a shoulder centred at 354 °C. The QMS profiles for O₂ and SO₂ reveal that the peak at 194 °C is entirely attributed to a first O₂ consumption, whereas the peak at 324 °C is formed by both a second O₂ consumption and, a small and slow SO₂ release. This second oxygen consumption is responsible for the successive large release of SO₂, that from the QMS profile is positioned at *ca.* 370 °C, slightly higher respect to the peak originated in the TCD profile. The two different O₂ consumption steps and subsequent SO₂ formation steps can be ascribable to the presence of two different sulphided species, associated with zinc sulphide iron sulphide phases revealed by XRD.

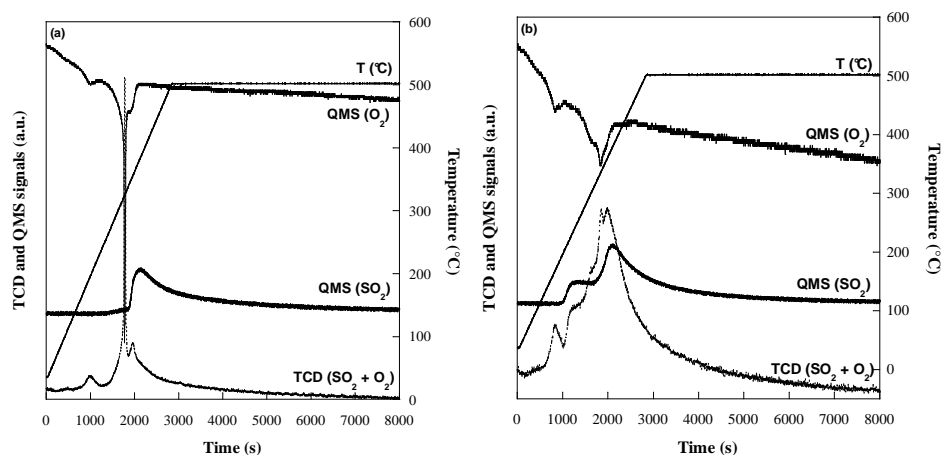


Figure 13. TPD profile and SO_2 and O_2 quadrupole mass spectrometer (QMS) signals of the ZF_TS_S (a) and ZF_SC_S (b) sulphided sorbent regenerated at 500 °C.

For ZF_SC_S (Figure 13b), the TCD profile is slightly different. The first contribution at 170 °C is due to a O_2 consumption, the shoulder at 234 °C is entirely caused by a first SO_2 release, a peak positioned on the top of the TCD curve at 337 °C corresponds to the second O_2 consumption, and finally the peak at 357 °C is attributed to the second SO_2 release that gradually returns to the baseline.

The different outcome stems from the TCD and QMS signals for ZF_TS_S and ZF_SC_S, especially in the different steps of SO_2 release, that can be related to the different amount and crystallinity of sulphided phases (ZnS and FeS_2) generated during the sulphidation cycle. According to the XRD patterns of Figure 8, the amount of ZnS in the two sulphided sorbents is quite similar, even if, differences in terms of crystallinity can be found. Conversely, the pyrite amount formed is different; it is present as a larger amount in the ZF_SC_S (which generates two different steps) respect to the ZF_TS_S. Based on a such observation, the two SO_2 step releases may be grossly associated to the oxidation of (i) FeS_2 for the peak at lower regeneration temperature (234 °C for ZF_SC_S and 324 °C for ZF_TS_S) and (ii) ZnS for the SO_2 release at higher temperature (357 °C for ZF_SC_S and 370 °C for ZF_TS_S).

6.5.2 Sorption features of the regenerated samples

Multiple sorption-regeneration cycles were performed on the composite sorbents, as well as on the commercial one, and the corresponding breakthrough curves were obtained (Figure 14). The B_t and SRC values for all the sorbents were obtained and gathered in Table 4.

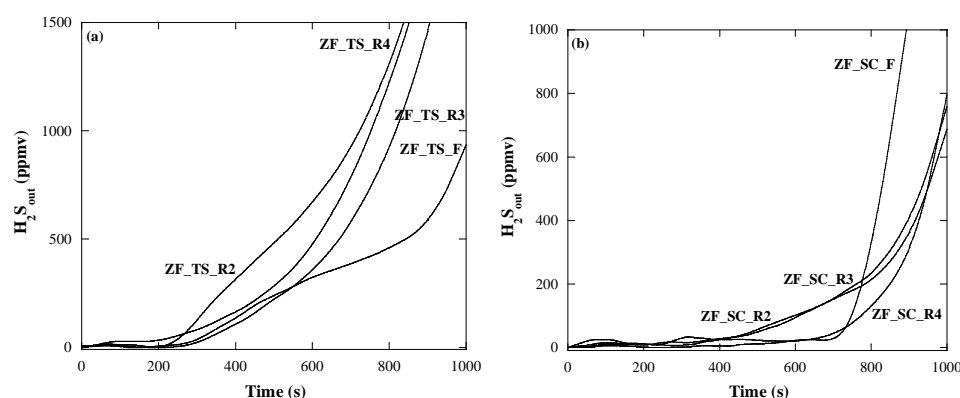


Figure 14. H_2S breakthrough curves upon four sorption-regeneration cycles (S_1 , S_2 , S_3 , S_4) for the zinc ferrite-based sorbents, ZF_TS (a) and ZF_SC (b).

From the data of Table 4, there is a significant decrease in sulphur retention capacity after the first cycle for the commercial ZnO sorbent (Katalco_{UM}). The loss of activity of the sorbents for H_2S removal upon multiple sulphidation-regeneration cycles is well known. In this particular case, the relative “low regeneration temperature” used, is unable to restore a significant sorption activity. Conversely, as shown in Figure 14a and from the data of Table 4, the desulphurization activity of the ZF_TS_R regenerated sorbent during four cycles is steady enough, although a slight reduction of 13.2% is observed going from the first to the fourth sulphidation cycle. For the ZF_SC_R sorbent, the regeneration process results in a first reduction of the sorption activity (163.6 mg S/g $ZnFe_2O_4$ vs. 208.6 mg S/g $ZnFe_2O_4$ of the fresh sorbent), the B_t and SRC values for the regenerated sorbent being decreased of 27.3% in comparison with ZF_SC_F. Surprisingly, at the fourth regeneration run, the sorption capacity is

almost identical to that of the fresh ZF_SC_F sorbent, indicating that the regeneration condition permits the full recover of the starting activity. The superior features of the ZF_SC sorbent, are worthy of note: the breakthrough time and the sulphur retention capacity of the regenerated sample are higher than those of the ZF_TS sorbent, both under the fresh or regenerated form. All these outcomes are in agreement with the previous results obtained for (i) zinc oxide-based sorbents (see Chapter 4), where the sorption features are maintained upon several sulphidation-regeneration cycles, and (ii) iron oxide-based sorbents which sulphur retention capacity of the fresh sorbent is many times higher than that of zinc oxide-based sorbent (see Chapter 5). These beneficial distinctive traits of the zinc oxide- and iron oxide-based sorbents arise as synergic effect in the zinc ferrite-based sorbent. Hence, this latter shows a sulphur retention capacity that is higher than the zinc oxide-based material (Zn_F), as observed also for the iron oxide-based material (Fe_F), and on the other hand, an activity maintained during several sulphidation-regeneration cycles, as observed for the zinc oxide-based material.

Table 4. Breakthrough time (B_t) and Sulphur Retention Capacity (SRC) of fresh and regenerated zinc ferrite-based sorbents during sorption-regeneration cycles. Data for the commercial Katalco_{JM} 32-5 sorbent are also reported for comparison.

Sample	Run number ^a	B_t (s)	SRC (mgS/g _{Active phase}) ± 1	SRC (mgS/g _{Sorbent}) ± 1
Katalco _{JM} _F	1	103	6	6
Katalco _{JM} _R	2	26	2	2
Katalco _{JM} _R	3	26	2	2
ZF_TS_F	1	317	94.4	18.9
ZF_TS_R	2	240	71.5	14.3
ZF_TS_R	3	347	103.4	20.7
ZF_TS_R	4	280	83.4	16.7
ZF_SC_F	1	700	208.6	41.7
ZF_SC_R	2	550	163.6	32.7
ZF_SC_R	3	550	163.6	32.7
ZF_SC_R	4	720	214.5	42.9

^a 1= Fresh sorbent; 2 = after 1st regeneration; 3 = after 2nd regeneration; 4 = after 4th regeneration

As observed in the previous chapter for the regenerated commercial sample, the poor performance is not unexpected, as the TPO results showed that a thermal treatment well above 500 °C was required to convert the ZnS phase into the active oxide phase.

According to the data of Table 4, the surface area of both ZF_TS_R (440 m²/g) and ZF_SC_R (393 m²/g) are considerably lower than that of fresh ones with a decreasing of 28.3% and 36.4% respectively. Such drop does not comply with the performance of both ZF_TS and ZF_SC that finally do not seem associated with the textural parameters, that normally are related to an enhancement or worsening of the sorption activity. Concerning the pore size distribution (Figure 15b) a bimodal distribution, although slightly shifted towards lower D_p values, is maintained for ZF_SC_R compared with the ZF_SC_F. At variance with the case of ZF_SC, a pseudo-bimodal pore size distribution appears with a second pore family (peak with very low intensity) centred at 3.5 nm for ZF_TS_R (Figure 15b).

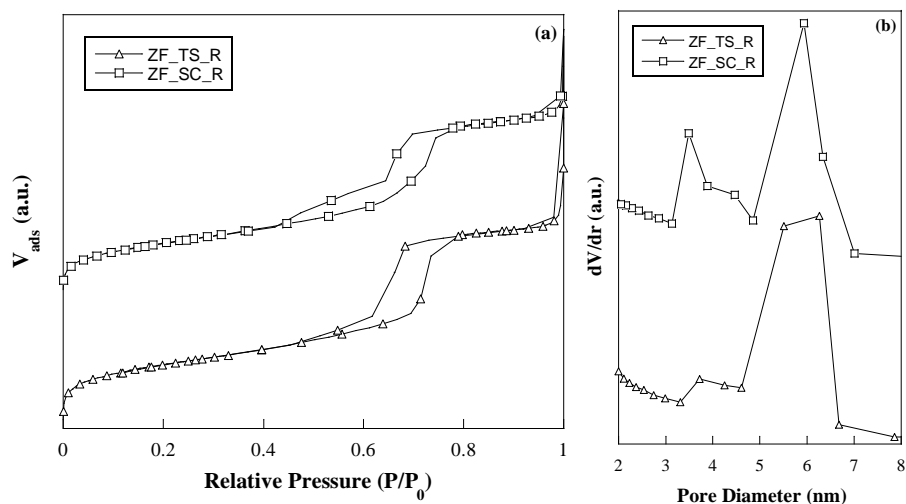
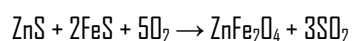


Figure 15. Nitrogen adsorption-desorption isotherms (a) and pore size distribution (b) of zinc ferrite-based sorbents in the regenerated state (empty triangles ZF_TS_R, empty squares ZF_SC_R).

The low-angle diffraction patterns of the regenerated sorbents show that the characteristic hexagonal order is preserved in all the samples (Figure 16a) and no shifts are observed for ZF_TS_R and ZF_SC_R in comparison to the fresh ones indicating that the regeneration treatment does not cause shrinkage of the mesoporous framework. For both the zinc ferrite-based sorbents, the XRD technique at wide-angle is

able to reveal important differences between the regenerated and fresh samples. After regeneration the XRD reflections attributable to the sulphided phases disappear and only a very broad diffraction peak is observed at $2\theta = ca. 35.1^\circ$ (Figure 16b). Due to the broadening of this unique diffraction peak, that may lead to a possible overlapping with the most intense reflection peaks of the maghemite phase ($\gamma\text{-Fe}_2\text{O}_3$), the only assignment of this to a ZnFe_2O_4 spinel phase cannot be appropriate. Actually, the presence of a very large band is reasonably associated with an amorphous phase. This statement is driven by the fact that during the sulphidation run, a separation phases in ZnS and FeS_2 occur. Therefore a total reconversion into zinc ferrite due to a regeneration in the state solid cannot be achievable. In the literature, there are only few papers that investigated the regeneration properties of zinc ferrite-based sorbents. Only a paper deals with the regeneration of sulphided non-supported zinc ferrite pure phase, using pure oxygen as oxidation gas in the range of 350-450 °C [19]. The main reaction occurring in this temperature range was reported as:



But also in that case the XRD technique for the regenerated sorbent revealed the presence of both ZnFe_2O_4 and Fe_2O_3 . In view of this, it is not possible totally rule out the presence of both zinc ferrite and iron oxide (Fe_2O_3), but also the presence of ZnO as an amorphous phase or as nanocrystals whose size is under the XRD detection limit in the regenerated ZF_TS_R and ZF_SC_R sorbents. A careful inspection of the XRD patterns of ZF_TS_R and ZF_SC_R reveal a slight difference in the intensity of the peak that can be associated to the amount of regenerated phase or differences in its crystallinity, owing to a decrease in the crystalline domain size and/or accumulated strain.

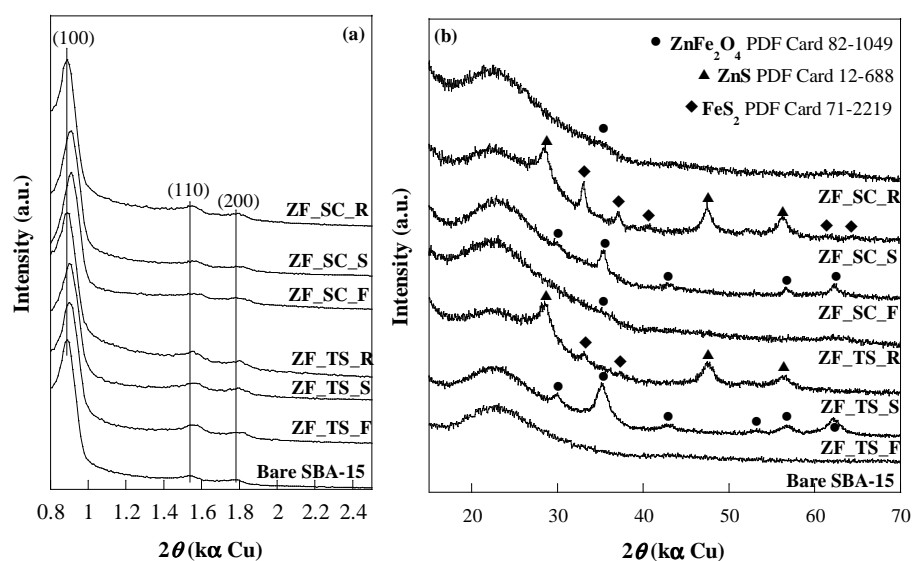


Figure 16. XRD patterns of bare SBA-15, ZF_TS and ZF_SC sorbents before (F), after sulphidation (S), and after regeneration (R) at low-angle (a) and wide-angle (b). The main reflection planes are marked.

Finally, on the basis of the experimental results, the retention of the performances during different regeneration runs for both ZF_TS and ZF_SC, but also the best performance during the fourth cycle of sulphidation of the ZF_SC_R sorbent, seem to be correlated to the structural properties, especially in terms of crystallinity, rather than to a textural properties and accessibility parameters (S_{BET} and V_p). Based on the results obtained for the zinc oxide- and iron oxide-based sorbents, it can be suggested that the phase originating from the oxidation of the sulphided product during the regeneration step is different in terms of crystallinity, particle size and texture from the one obtained directly by thermal decomposition of the nitrate precursor, *i.e.* that the regeneration process induces a reorganization of the oxide nanophase.

Interestingly, in the FTIR spectra of ZF_TS_R and ZF_SC_R (Figure 17), the Si-OH band at 960 cm^{-1} is less intense than that observed in the fresh and sulphided sorbents, which suggests the occurrence of a very weak interactions between the guest phase and the silica matrix as observed for the zinc oxide- and

iron oxide-based sorbents investigated in the previous chapter. Unexpectedly, a low-intensity signal at about 605 cm^{-1} is observable for both ZF_TS_R and ZF_SC_R, which could indicate the presence of a sulphate phase, not revealed in the XRD pattern ^[20]. However, the particles are considered not interacting with silica support, resulting in the preservation of the reactivity of zinc ferrite.

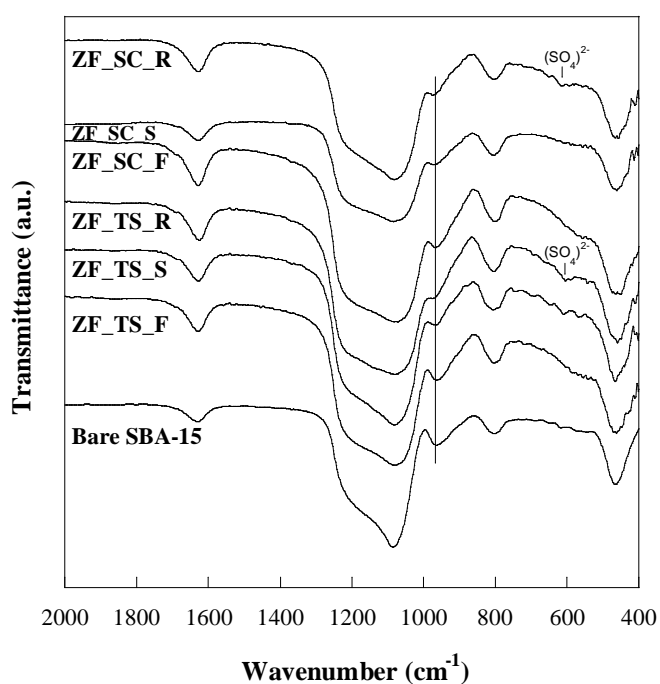


Figure 17. FTIR spectra of the ZF_TS and ZF_SC sorbents in the regenerated (R) state compared with the fresh (F) and sulphided (S) ones.

Although further study about regeneration and the understanding of the oxidation mechanism is necessary, the good stability and the low regeneration temperature prove that the zinc ferrite/SBA-15 samples hold a considerable promise as a sulphur-capturing sorbent material.

6.6 Insight of the sulphidation-regeneration mechanism

The investigation of the sulphidation mechanism was extended to a pure nanostructured zinc ferrite phase for better understanding of the changes undergone by the sorbent during the sulphidation cycles. The corresponding XRD pattern (Figure 18) shows for the sulphided sample the presence of zinc sulphide (ZnS), pyrite (FeS_2), pyrrhotite (Fe_{1-x}S) and, a certain amount of unreacted ZnFe_2O_4 fresh phase. This result supports the sulphidation reaction with a phase separation as observed in the ZF_TS_S and ZF_SC_S. The absence in the sulphided composite of the pyrrhotite phase can be probably due to its metastability, enhanced by the nanodispersed nature of the sulphide.

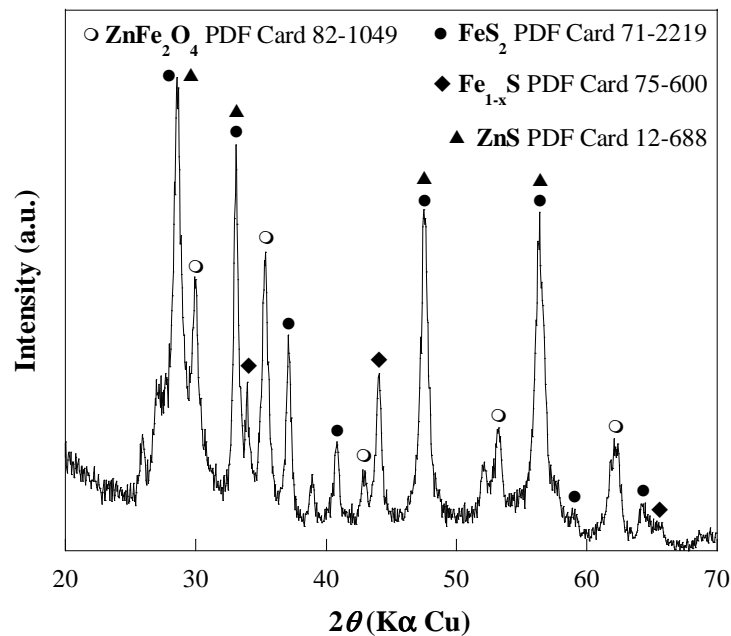


Figure 18. XRD pattern of the sulphided pure nanostructured zinc ferrite sample.

6.7 Conclusions

The preparation of zinc ferrite-based sorbent nanocomposites into SBA-15 mesochannels used as a support, has been tackled through two different synthetic strategies; a simple and reproducible two-solvents impregnation route and a novel impregnation-sol-gel autocombustion combined approach. Subsequent characterization of the nanosorbents clearly showed that the synthesis procedures are efficient to obtain nanometric crystallized particles, even if a difference in terms of zinc ferrite crystallinity was observed from XRD and HRTEM results. Compared to an unsupported zinc oxide commercial sorbent, a sulphur retention capacity six and thirteen times higher were obtained for the two composites, the highest being exhibited for the ZF_SC sorbent prepared with the sol-gel autocombustion strategy. The H₂S removal is strongly influenced by the zinc ferrite phase dispersion and its crystallinity rather than from the accessibility parameters (S_{BET} and V_p) being these latter very similar to each other both in the fresh and regenerated state. According to the TPD results, both the sorbents (ZF_TS and ZF_SC) can be regenerated completely at 500 °C, which is a much lower temperature than that reported by others. The results of four successive sulphidation-regeneration cycles revealed high performance and steady stability of these systems, especially for ZF_SC sorbent.

The following conclusions can be driven by the results of the present work: (i) the novel impregnation-sol-gel autocombustion combined method is a simple way to prepare nanocomposites and exhibited excellent sulphur retention capacity, being more than two times higher than that of the samples prepared with the two-solvents impregnation approach; (ii) the regenerated ZF_SC_R sorbent at the four cycle showed the sulphur retention capacity as high as the first cycle and two and half times greater than ZF_TS_R.

The key contribution of the current study led to, besides the preparation through this novel self-combustion approach, turn out to be more efficient for the H₂S removal compared to the two-solvents technique, a wider remarks relating to the behaviour of the zinc ferrite as sorbent if compared to the single oxides taken separately. Noteworthy is the synergetic effect between zinc and

iron when are combined in the zinc ferrite structure. The results have shown that concerning the relative high sulphidation activity and the low regeneration temperature ($< 500\text{ }^{\circ}\text{C}$), this behaviour complies with the iron oxide-based sorbent; by converse, the retention of the sorption properties upon repeating sorption-regeneration cycles seem related with the zinc oxide-based sorbent. These important properties, individually found in the single oxides of zinc and iron, and that make of a sorbent a potential candidate for the mid-temperature H_2S removal, can be get together in the zinc ferrite-based sorbents, independently from the synthetic strategies of preparation.

References

- [1] M. Flytzani-Stephanopoulos, G. R. Gavalas, S. S. Tamhankar and P. K. Sharma, in *Novel sorbents for high temperature regenerative H₂S removal*, Final report for the project DOE/MC/20417-1898 (DE86004261), October **1985**.
- [2] R. E. Ayala and D. W. Marsh, *Ind. Eng. Chem. Res.*, **1991**, 30, 55.
- [3] P. J. Van den Brink, A. Scholten, A. Van Wageningen, M. D. A. Lamers, A. J. Van Dillen and J. W. Geus, *Stud. Surf. Sci. Catal.*, **1991**, 63, 527.
- [4] D. J. Lensveld, J. G. Mesu, A. J. Van Dillen and K. P. De Jong, *Micropor. Mesopor. Mater.*, **2001**, 44-45, 401.
- [5] A. Infantes-Molina, J. Mérida-Robles, P. Braos-García, E. Rodríguez-Castellón, E. Finocchio, G. Busca, P. Maireles-Torres and A. Jiménez-López, *J. Catal.*, **2004**, 225, 479.
- [6] A. J. Van Dillen, R. J. A. M. Terörde, D. J. Lensveld, J. W. Geus and K. P. de Jong, *J. Catal.*, **2003**, 216, 257.
- [7] D. J. Lensveld, J. G. Mesu, A. J. Van Dillen and K. P. De Jong, *Micropor. Mesopor. Mater.*, **2001**, 44-45, 401.
- [8] L. R. Pederson, G. D. Maupin, W. J. Weber, D. J. McReady and R. W. Stephen, *Mater. Lett.*, **1991**, 10, 437.
- [9] A. Chakraborty, P. Sujatha Devi, S. Roy and H. S. Maiti, *J. Mater. Res.*, **1994**, 9, 986.
- [10] S. Shafer, W. Sigmund, S. Roy and F. Aldinger, *J. Mater. Res.*, **1997**, 12, 2518.
- [11] C. Cannas, A. Musinu, D. Peddis and G. Piccaluga, *J. Nanopart. Res.*, **2004**, 6, 223.
- [12] D. Zhao, J. Feng, Q. Huo, N. Melosh, G. H. Fredrikson, B. F. Chmelka and G. D. Stucky, *Science*, **1998**, 279, 548.
- [13] A. H. Jansen, C. M. Yang, Y. Wang, F. Schüth, A. J. Koster and K. P. de Jong, *J. Phys. Chem. B*, **2003**, 107, 10552.
- [14] E. Delahaye, V. Escax, N. El Hassan, A. Davidson, R. Aquino, V. Dupuis, R. Perzynski and Y. L. Raikher, *J. Phys. Chem. B*, **2006**, 110, 26001.

- [15] A. Bertoluzza, C. Fagnano, M. A. Morelli, V. Gottardi and M. Guglielmi, *J. Non-Cryst. Solids*, **1982**, 48, 117.
- [16] Y. Ahn, E. J. Choi, S. Kim and H. N. Ok, *Mater. Lett.*, **2001**, 50, 47.
- [17] H. M. Zaki and S. F. Mansour, *J. Phys. Chem. Sol.*, **2006**, 67, 1643.
- [18] J. M. Philiat and B. Marsan, *Electrochimica Acta*, **1999**, 44, 2351.
- [19] R. Zhang, J. Huang, J. Zhao, Z. Sun and Y. Wang, *Energ. Fuel*, **2007**, 21, 2682.
- [20] G. N. Krishan, G. T. Tong, R. H. Lamoreaux, R. D. Brittain and B. J. Wood, in "*A study of sulphate formation during regeneration of zinc ferrite sorbents*".

Chapter 7

Assessment of mid-temperature sorbent desulphurization technology in Puertollano IGCC process

7 Introduction

One of the fundamental parameters in a thermoelectric power plant is efficiency, which indicates the part of the fuel's energy, which is effectively transformed into electricity. The importance of developing power plants with improved levels of efficiency is founded upon:

- ✚ Reducing costs, as a result of lower specific fuel consumption;
- ✚ Reduce the environmental impact, as the emission of contaminants per kWh produced is minimised;
- ✚ Preserve resources of limited fuels (natural gas, petroleum, coal).

In thermal power plants, electricity is generated as a result of the expansion of a fluid at high pressure and high temperature in turbines, which transmit its movement to the electricity generators. In this way, efficiency is determined by the ratio between the maximum and minimum temperatures during the process or thermodynamic cycle, so that the more extreme the conditions, the greater the efficiency.

In IGCC power plants, as extensively reported in the first chapter of the thesis, Hot Gas Desulphurization (HGD) represents an attractive solution to simplify syngas treatments and to improve the global efficiency^[1]. In the Chapters 7 and 8 different alternatives of integration with a unit based on this new technology in the Puertollano IGCC process are discussed in comparison with conventional Cold

Gas Desulphurization (CGD) and the feasibility study has been carried out to understand (i) the possible application of such a kind of technology in a pre-existing IGCC plant, (ii) the real improvements that the mid-temperature H_2S removal can generate in industrial plant. Attention is paid to the potential improvements of the overall plant efficiency.

Technical literature is rich of papers dealing with HGD and investigating the process only by a chemical point of view and in particular on a laboratory scale. However, a small number of studies^[2, 3] reports a systematic analysis of the influence of hot gas clean-up on IGCC performance.

In this work, following a general assessment of the operating principle and of the mass/energy balance of a zinc-based HGD system, the performance of Puertollano IGCC power plant with CGD will be compared with the one obtained with HGD. The influence of some design variables, related to the HGD system, is also discussed, with reference to the desulphurization temperature, the oxygen concentration in the sorbent regeneration stream. The objective of this work is to conceive how conceptually incorporate the solid sorbents technology in the pre-existing plant, detailing the technical specifications, understanding how this influence the different IGCC systems and establishing the criteria for comparison of different alternatives. Zinc oxide-based sorbent has been selected as candidate for this study and represents an appropriate choice for a baseline study since it is the most mature and common sorbent for H_2S removal from coal fired power plants. The bulk of research on regenerable sorbents has been on zinc-based sorbent because this appear to have the fewest technical problems among all sorbents and represents a good compromise between thermal, mechanical, chemical stability, operational conditions (temperatures, pressures and regeneration features), and price.

7.1 ELCOGAS: Puertollano IGCC power plant

ELCOGAS S.A. is a Spanish company established in 1992 and shared by European electrical companies and equipment suppliers. It operates the Puertollano 335 MW_{ISO} IGCC (Integrated Gasification in Combined Cycle) demonstration power plant (Figure 1). This plant is the largest IGCC in the world using

solid fuel in a single pressurized entrained flow gasifier, being in commercial operation since 1998 with syngas ^[4-6].

It is located at about 10 km east/south-east the city of Puertollano, which belongs to the Ciudad Real Province. The IGCC unit is situated near an ENCASUR coal mine in an industrial area comprising a 220 MW thermal power plant and a chemical complex including a REPSOL refinery.



Figure 1. Elcogas IGCC power plant.

7.2 Overall description of the Puertollano IGCC Plant

7.2.1 IGCC power plant with CGD system

The current layout of the Puertollano IGCC power plant with conventional Cold Gas Desulphurization “CGD” system is schematized in [Figure 2](#) ^[7].

The main objective of the Puertollano IGCC is to reach a high integration level of the main units and to optimize of their operation in order to maximize the efficiency of the plant. It is useful to shortly present how the plant is designed to operate.

An entrained flow, oxygen-blown, dry-feed Prenflo-type gasifier, operating at 25 bar and 1200 – 1600 °C, is used in the plant. The gasifier is water-cooled slagging type, where the insulation granted by the slag layer minimizes heat losses and heat flux towards the membrane walls. Coal is pulverized and dried with a stream of warm air. Raw syngas composition is calculated at chemical equilibrium, a reasonable assumption because of the elevated gasification temperature. In order to assure an easy start-up and high flexibility, oxygen is produced in a stand-alone ASU, generating a 85% purity oxygen flow. Nitrogen, released at near-atmospheric pressure, is compressed and partly used in lock-hoppers for coal feeding and partly sent to the gas turbine combustor to moderate the flame temperature for NO_x emission control. The hot syngas exiting the gasifier at 1500 °C is quenched to 800 °C with low-temperature recycled syngas. The molten slag entrained by the gas stream solidifies and the syngas passes through coolers where HP (High-pressure) steam is produced. Quenched syngas is cooled down to 380 °C, so it is partly recycled back by means of a fan and partly sent to a wet scrubber for the removal of the remaining solids and soluble contaminants. Liquid water from the scrubber is clarified in a sour water stripper by means of LP (Low-pressure) steam and subsequently recycled back to the scrubber. Syngas exiting the scrubber at 126 °C is heated up to 140 °C by means of water from IP (Intermediate-pressure) drum, and sent in a catalytic bed for COS hydrolysis. After low-temperature heat recovery, syngas is further cooled with water and sent to the acid gas removal (AGR) station, after condensate separation. H₂S is removed by means of a MDEA (methyldiethanolamine) process and sent to the sulphur recovery unit. Heat duty from LP steam is also required for sour water stripper, where NH₃, SO₂ and other impurities from the scrubber are removed. After leaving the AGR unit, the syngas is heated up and humidified in a saturator. A further heating to 160 °C is obtained by using HP water as thermal medium. Before combustion, the syngas is diluted with compressed nitrogen from ASU for NO_x emissions

control. Heat recovered from gas turbine exhausts and syngas cooling is used by a two-pressure level reheat steam cycle.

The Puertollano IGCC power plant is designed to burn a mixture equally composed of coal, at least during some years, will be provided by the ENCASUR mine and petroleum coke coming from the REPSOL refinery. Analyses performed on this raw coal and on the petroleum coke give the values gathered in [Table 1](#).

Table 1. *Raw coal and petroleum coke analyses.*

	Coal	Petroleum Coke	Coal + Petroleum Coke (1:1)
Composition (wt.%)			
Moisture	11.8	7.00	9.40
Ash	41.10	0.26	20.68
Carbon	36.22	82.21	59.21
Hydrogen	2.48	3.11	2.80
Nitrogen	0.81	1.90	1.36
Oxygen	6.62	0.02	3.32
Sulphur	0.93	5.50	3.21
Chlorine	0.04	-	0.02
Phosphorus	0.01	-	0.01
Particle size of raw coal (mm)	≤ 25	-	≤ 25
Lower Heating Value (MJ/kg)	13.10	31.99	22.55
Higher Heating Value (MJ/Kg)	13.58	32.65	23.12

The process pressure is set by the gas turbine inlet pressure and the temperature is that required for the ashes to get separated, as molten slag, through the bottom of the reaction chamber ([Table 2](#)).

Table 2. *Gasifier design data.*

Chamber reaction pressure	25 bar
Chamber reaction temperature	1200 – 1600 °C
Fed fuel capacity	2600 t/d
Raw gas production capacity	180000 Nm ³ /h
Carbon conversion percentage	98 – 99%

The process of separating sulphur compounds from the raw gas consists of:

- ✚ Catalytic hydrolysis reactor, where the COS is transformed into H₂S ($\text{COS} + \text{H}_2\text{O} \rightarrow \text{H}_2\text{S} + \text{CO}_2$), and HCN in NH₃ ($\text{HCN} + 2\text{H}_2\text{O} \rightarrow \text{NH}_3 + \text{HCOOH}$);
- ✚ Absorption column using Methyl Diethanolamine (MDEA), which selectively captures the H₂S. The MDEA solution is regenerated in a second column, where the acid gas (Claus gas) is separated, and sent to the Claus sulphur recovery unit.

Table 3. *Design data for the CGO unit.*

Solvent	MDEA in water solution 50 wt.%
Absorption temperature	33 °C
Regeneration temperature	98 °C
Claus gas characteristics	Flow = 4652 Nm ³ /h, dry CO ₂ = 50.67 vol.% H ₂ S = 48.95 vol.%

Table 4. *Resulting properties of the clean gas sent to the Combined Cycle.*

Pressure	21.3 bar
Temperature	130 °C
Flow	183053 Nm ³ /h, dry
Sulphur content	< 25 mgS/Nm ³
Composition (vol.%, dry base)	CO= 60.51 H ₂ =22.08 N ₂ =12.46 CO ₂ =3.87 Ar=1.03
Lower Heating Value (LHV)	10029 KJ/Nm ³

Prior to its combustion inside the gas turbine, the clean gas is subjected to a saturation process using water, and mixed with residual nitrogen to reduce the NO_x formation during the combustion process. As a result of these processes (saturation and mixed with N₂), NO_x emission levels in IGCC mode are less than 150 mg/Nm³ at 6 % O₂.

Table 5. *Properties of clean syngas upon entering the Gas Turbine.*

Pressure	19.4 bar
Temperature	302 °C
Flow	120.2 Kg/s
Lower Heatin Value (LHV)	4242 KJ/Kg

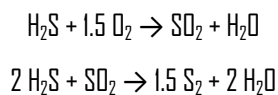
Presently the sulphur recovery unit is a system which deals with the Claus gas and the sour gas coming respectively from the sulphur removal unit and from the wet scrubbing system:

- ✚ it converts H₂S to elemental sulphur in liquid state;
- ✚ it destructs nitrogen compounds (NH₃, HCN) to give elemental nitrogen.

The sulphur recovery unit comprises the following processing steps:

- ✚ partial combustion in the Claus plant of the sour and Claus gases and of their sulphur compounds and their catalytic conversion to elemental sulphur;
- ✚ sulphur storage, liquid sulphur being collected in a sulphur pit from which it is pumped to sulphur solidification plant and then to a disposal area and transport facilities;
- ✚ hydrogenation, *i.e.*, catalytic reaction of sulphur species of the Claus tail gas with the hydrogen contained in a small flow of clean gas diverted from the main stream;
- ✚ recycling of the hydrogenated tail gas upstream from the sulphur removal unit by means of a recycle gas compressor.

In the Claus plant, the formation of sulphur already takes place partly in the Claus kiln and continues in two catalytic stages of the Claus reactor:



7.3 Basis of design of a sorbent desulphurization unit in Puertollano IGCC Plant

To make feasible the integration of solid sorbents technology in the existing Puertollano IGCC plant, a preliminary study has been necessary on different aspects currently used in the process and that are necessary for the actualization and the proper operation of the future mid-temperature desulphurization section. They mainly concern the raw gas to be treated in the desulphurization reactor (*Desulphurizer*), and the possible gas streams that can be used as regeneration gas in the regeneration reactor

(*Regenerator*). For each of them different parameters were verified, such as flow rate, temperature, pressure and composition.

The physical act of cleaning the remaining raw gas with water (180937 Nm³/h, dry basis) in a Venturi type device enables contaminant compounds (HCl, HF, NH₃, HCN and partially H₂S and CO₂), to be retained, in addition to the solid particles not extracted in the event of a ceramic filter failure.

Regarding the choice of the regeneration gas, this has to be provided, with regard to O₂ and air, from the ASU unit. The other alternative is the use of steam as regeneration gas. The Air Separation Unit (ASU) in Puertollano plant, supplied by Air Liquide, produces as a result of the distillation process and cryogenic heat exchanging, gaseous oxygen and nitrogen as well as gaseous waste nitrogen to enable the plant to comply with the overall material balance. The ASU takes 295406 Nm³/h of air from the gas turbine compressor (20% of the compressed air as a maximum) at 12.70 bar and 128 °C and performs a distillation by means of a cryogenic process.

a. Oxygen supply

70 000 Nm³/h of pure oxygen (85%) at 31.5 bar and 88 °C are sent to the gasification island to supply the PRENFLO gasifier and the Claus kilns. Moreover, there is an oxygen vaporization and storage system that helps to comply with the oxygen demand during specific operating conditions.

b. Nitrogen supply

Two flows of *gaseous nitrogen* are produced:

- ✚ 8150 Nm³/h, so called low pressure pure nitrogen (4.81 bar, oxygen content lower than 1000 ppm), goes straight on to the gasification island at 27 °C;
- ✚ The N₂ flow coming from the cryogenic heat exchanger I is pre-compressed up to 12.29 bar. A part is sent back to the cold box system to supply both the cold production unit (boosters-expanders

assembling) and the medium pressure column as reflux gas. The rest of the pre-compressed nitrogen production ($22100 \text{ Nm}^3/\text{h}$), is finally compressed and sent to the gasification island at $65 \text{ }^\circ\text{C}$. This is called medium pressure pure nitrogen (49.5 bar, oxygen content lower than 1000 ppm).

Moreover there is a nitrogen vaporization and storage system that helps to comply with the nitrogen demand during specific operating conditions.

c. Waste nitrogen supply

As it has been mentioned before, a certain flow of gaseous nitrogen with an oxygen content lower than 2% is taken away from the LP distillation column, so called waste nitrogen flow ($188025 \text{ Nm}^3/\text{h}$). This flow goes through the cryogenic heat exchanger I and is compressed up to 18.4 bar to be sent to the fuel supply system at $195 \text{ }^\circ\text{C}$.

7.4 IGCC power plant with HGD system

7.4.1 Possible HGD&R unit configurations

The layout of an IGCC power plant with HGD, as an evolution of the previous scheme, may be thought upon different layout configurations in such a way that the gasification island would result simplified: syngas exiting the high temperature cooler is partly recycled back for quenching and partly sent to the HGCU (*Hot Gas Clean-Up*) station, which is schematically represented with two blocks. In principle, in the easiest configuration (Figure 3), the latter includes two identical reactors, since when one reactor operates as adsorber (desulphurizer), the other operates as desorber (regenerator) ^[8]. In the first stage, hydrogen sulphide is absorbed by means of a circulating sorbent, which is subsequently regenerated in order to be used in several desulphurization cycles. Syngas exiting the first stage, passes through a hot gas filter (HGF) if required, and is finally ready to feed the gas turbine. Similarly to the Puertollano power plant with CGD (*Cold Gas Desulphurization*), syngas is mixed with nitrogen from ASU for NO_x emission control. However, the temperature of the final clean syngas is consistently higher than in the CGD case.

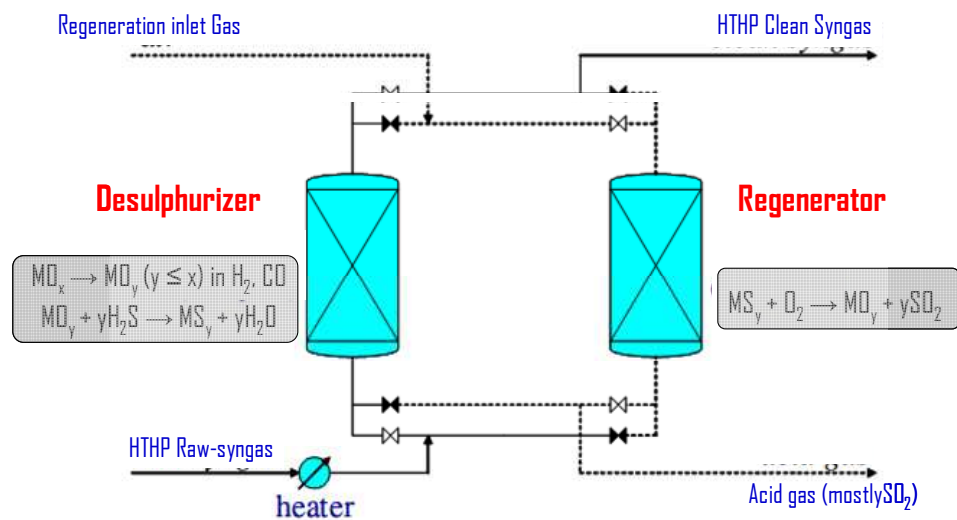


Figure 3. Simplified layout of the hot gas desulphurization and regeneration process in a fixed-bed reactor configuration^[8].

7.5 Different integration alternatives of a unit based on solid sorbents technology in IGCC Puertollano process

In Hot Gas Desulphurization, all equipments operate at elevated syngas temperatures of 200 °C to 600 °C, which eliminates the need to cool syngas to the ambient conditions required by conventional, solvent-based cleanup technologies. This cooling process results in a significant loss of thermal efficiency. The HGD is attractive since it is expected to improve the thermodynamic performance of the power plant, as well as to simplify the plant configuration, potentially reducing the investment costs. Examining and studying the block diagrams of the entire Puertollano IGCC process, how they are interfaced with each other, and especially how the thermal energy exchange take place between the various plant parts, and thinking about a future implementation in existing plant with a technology based on the use of solid sorbents for mid-temperature desulphurization, more than one alternative for such integration has been taken into consideration. Two different layout configurations have been selected for

this reason, the first one of which is quite similar to the layout existing in the gas purification section, and the second one (the most complicated, but also the most efficient way to take advantage of this technology) considers an inversion in the equipment cleaning process; they are summarized in succession:

The Alternative 1, called "**Low-temperature layout**" (Figure 4, **Layout 1**): leaves everything unchanged, including temperatures and pressures, until after the "Wet scrubbing" exit where the temperature is 130 °C. It was named as "Low-temperature layout" due to the maximum temperature of the raw gas exploitable in the Puertollano IGCC plant without any substantial change. Anyway, in order to use this technology efficiently, it is necessary to heat up the raw gas at 300 °C so that it enters within the desulphurization reactor at this temperature where, being the reaction with H₂S, in the case of zinc, exothermic ($\Delta H_r = -76.9 \text{ MJ / Kmol}$), could "self sustaining" for the entire removal. Heat of regeneration reaction ($\Delta H_r = -441.3 \text{ MJ / Kmol}$) can be used to increase the temperature of the raw gas.

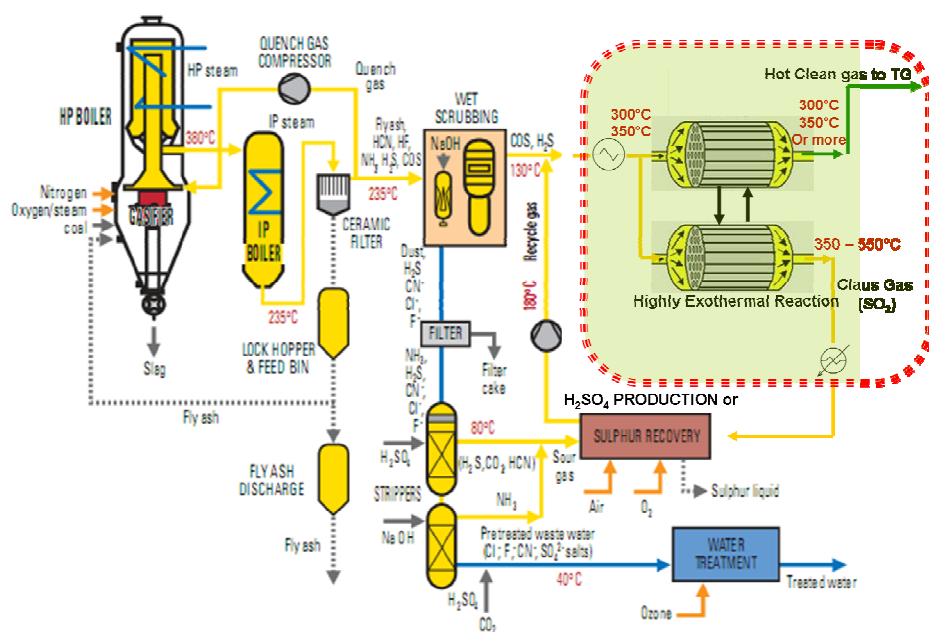


Figure 4. Schematic layout of the HGDR solid sorbents unit at mid temperature (Layout 1).

The Alternative 2, called “Mid-temperature layout” (Figure 5, Layout 2): it has been conceived at first to use all the exiting raw gas temperature equal to 380 °C, taking advantage of the sensible heat of raw gas. If this would not be possible, due to the high temperature of the raw gas in the ceramic filters, will be required a lowering down of the current 235 °C used in the process. It was designed for two reasons:

1. To get the most from this technology. For this reason it is better to have the raw gas already hot, avoiding to heat as in the first alternative.
2. To leave, or to affect the least possible the other sections of the gas cleaning (especially the Venturi scrubber). For this kind of configuration, it has been established that contaminants as HCl (in the case of the ZnO sorbent) has no complication, but rather improves the performance due to a textural modification of the sorbent by HCl.

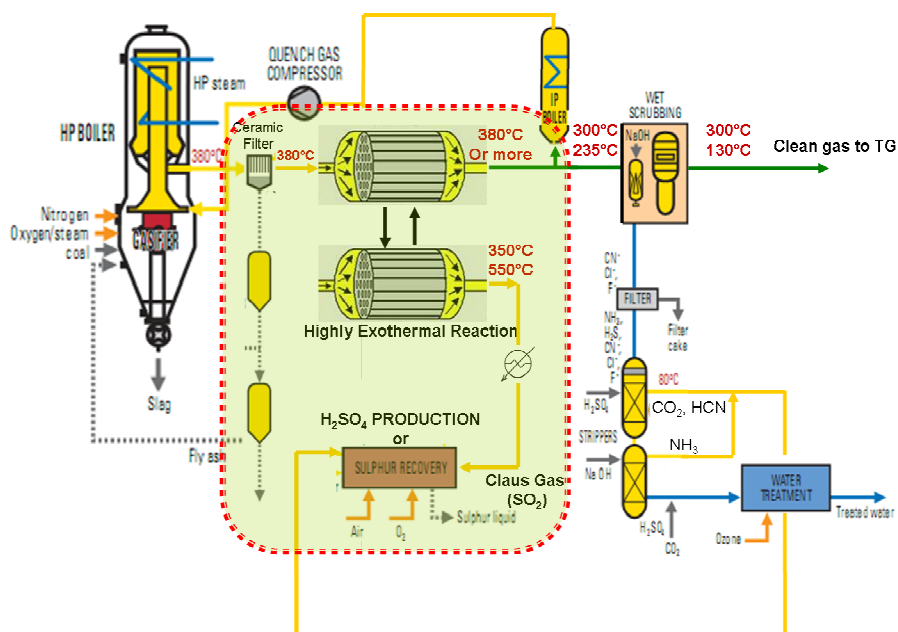


Figure 5. Schematic layout of the HGDR solid sorbents unit at mid temperature (*Layout 2*).

7.6 Discussion

These proposed integration alternatives were drawn (i) as simplest alternative and more immediate to be incorporated into the existing process without great changes (*Layout 1*), (ii) to exploit the best of this technology although with some changes (*Layout 2*). Clearly, if the clean gas exiting from the desulphurization unit is already hot, it would certainly be a much better condition than that at room temperature and must be heated (at 260 °C in the current system configuration) by means of "HP feed water". This would result in a net improvement in the saturation section of the clean gas, or even in the total elimination of this section of the plant. In any case there is the need to account for many parameters to be able to implement such a change in the system. For example, it is necessary to check the working temperature of the current gas cleaning system upstream of the MDEA unit (hot gas filter,

Venturi Scrubber), and to know the optimal temperature (minimum and maximum) of the clean gas entering in the gas turbine (TG). Actually, especially in the second alternative, different aspects in order to make plausible that option have to be carefully analyzed. First of all, if the ceramic candle filters installed in the plant, or new installed, are strong and effective in dedusting even at 380 °C, and secondarily, that the presence of NH₃, HCl and HCN does not affect the H₂S removal performance. If this happens, the latter option may be assessed with greater importance, all the heat contained in the gas could be exploited in the desulphurizer for the gas-solid reaction with the sorbent. Instead, if the temperature at the outlet from the Venturi decreases to 130 °C, the evaluation if it would be convenient to heat up again the gas has to be examined. Furthermore, if the gas turbine has a optimum temperature that is greater than that which still receives from the "clean gas" equal to 130 °C, then the thermal efficiency with the use of the desulphurization at mid-temperature downstream of the cleaning gas would surely increase. Moreover, the Alternative 2 ([Mid-temperature layout](#)) could open the way for an innovative cleaning process based on the whole use of the solid sorbents technology, without the use of any chemical solvent for the removal of all contaminants contained in the raw-gas, thus eliminating the problem considering the possible temperature drop at the exit of the Venturi in the worst case equal to 130 °C, which would not improve the downstream thermal efficiency of the process, mainly in the gas and steam turbine. Anyway, in view of the highly exothermic regeneration reaction, the heat developed can be successfully used to heat the clean syngas prior to entry in the turbine gas.

7.7 Impact on the different IGCC systems

7.7.1 Advantages and disadvantages with the use of different alternatives

Depending on the selected alternative could have some improvements both upstream and downstream of desulphurization unit. In fact, in the second configuration (Layout 2) all the hot gas at 380 °C without cooling to 235 °C could be used. In this case we should take into account how to cool the

gas to 800 °C inside the gasifier to get it out at 380 °C. A possible solution is to install an IP boiler which partially collect the syngas at 380 °C, cool down to 235 °C and recirculated it at the gasifier.

In the first layout configuration the impact in the section upstream of the desulphurization would be almost negligible. In fact the path of the raw-gas, include equipments, temperature and pressure values, are the same as in the Cold Gas Desulphurization currently used in the process. The difference is that required to heat the raw gas because the temperature of 130 °C is not enough for the gas inlet in sorbent reactor. It was thought to resolve this problem, in part to warming up with the heat generated from the exothermal regeneration reaction of the sulphided sorbent. Another solution could be to use the heat exchangers with HP or IP-saturated steam to combined cycle, or LP-steam from combined cycle.

The aim of the second configuration is to exploit all the sensible heat containing in the raw-syngas up to the sorbent desulphurization unit. All this considered, an IP-boiler downstream of the ceramic filters needs to be installed for two main reasons: (i) to cool down the temperature more or less to 250-300 °C in order to recirculated to the gasifier to obtain the desired cooling effect on the syngas, (ii) to avoid the use of very high pressure in the Venturi scrubber. Actually, in view of a possible replacement in the Venturi Scrubber equipment, commercially existing scrubbers with technical specifications more than that required in our case that operated at very high temperature and pressure (60 – 1500 °C, 30 bar).

Another important effect that might occur in both configurations, is involved with the saturator. In fact, with the production of water from the reaction of H₂S removal, and due to the higher temperature of the clean gas from the desulphurizer, in the best case this option could lead to the elimination of this part of the plant with the result of "saving" 10.88 MJ/s required from the "clean gas preheater".

Another deep impact could exhibit downstream of the desulphurization process, in the Claus plant. In fact, depending on the regeneration gas, especially when oxygen or air is used, shall not have a rich-H₂S stream, but differently, a SO₂-rich stream. So, different alternatives to conduct the SO₂ removal could be realized. Considering the latter, the simplest alternative is, substantially to leave the same process currently used in the Claus unit (see page 172), without big changes in it, but taking into account that the step of the H₂S oxidation is eliminated. It could be an advantage to avoid the use of oxygen for the oxidation reaction, making the H₂S of the sour gas derived from the wet scrubbing system to react with the SO₂ from the off-gas derived from the regeneration of the sulphided sorbent. Nevertheless, we should make sure if the concentrations of H₂S and SO₂ are close to the stoichiometric ratio, indicated by the chemical reaction.

The second option considers a new plant for the H₂SO₄ production. The industrial production of sulphuric acid involves the following steps (pass over the SO₂ production), carried out under the conditions described so as to optimise the yield:

1. Sulphur dioxide is passed over vanadium pentoxide or platinum catalyst, at 450 °C to produce sulphur trioxide. This process takes place in a catalytic converter.



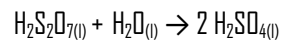
These gases pass over four catalyst beds to maximise the conversion to SO₃.

2. Sulphur trioxide is dissolved in water forming oleum (H₂S₂O_{7(l)}). This process takes place in absorption towers.



Gaseous sulphur trioxide cannot be added directly to water as the reaction is very exothermic and would cause the acid to vaporise and form a dangerous mist. To avoid this problem, the sulphur trioxide is added to a flowing solution of concentrated sulphuric acid rather than to pure water.

3. Water is added to oleum to produce concentrated sulphuric acid (typically 98% w/w). This takes place in the diluter.



Water is added in small amounts to concentrated sulphuric acid, with stirring, to form H_2SO_4 of the desired concentration.

Another important benefit with the use of this technology is that the clean syngas in outlet to the desulphurization sorbent system is still hot, with a temperature around to 300 °C. This, must be considered an advantage, in view of the lower temperature of the clean gas in outlet to the saturator (124.6 °C) in the CGD process, and considering (Table 5) the temperature of the inlet gas turbine (302 °C) upon entering the gas turbine.

References

- [1] X. Bu, Y. Ying, X. Ji, C. Zhang and W. Peng, *Fuel Process. Technol.*, **2007**, 88, 143.
- [2] G. Tsatsaronis, T. Tawfik, L. Lin and D. T. Gallaspy, *J. Eng. Gas Turb. Power*, **1994**, 116, 291.
- [3] T. Woudstra and N. Woudstra, *J. Inst. Energy*, **1995**, 68, 157.
- [4] F. Garcia Peña, *Operating Experience and Current Status of Puertollano IGCC Power Plant*, International Freiberg Conference on IGCC & Xtl Technologies, June **2005**.
- [5] P. Casero, P. Coca, F. Garcia Peña and N. Hervas, *Greenhouse Gases: Science and Technology*, **2013**, 3, 253.
- [6] P. Casero, F. Garcia Peña, P. Coca and J. Trujillo, *Fuel*, **2014**, 116, 804.
- [7] M. Treviño Coca, in *Integrated gasification combined cycle technology "IGCC": Its actual application in Spain: ELCOGAS. Puertollano*, **2010**.
- [8] G. Raggio, A. Pettinau, A. Orsini, M. Fadda, D. Cocco, P. Deiana, M. L. Pelizza and M. Marengo, *Coal gasification pilot plant for hydrogen production. Part B: Syngas conversion and hydrogen separation*, Second International Conference on Clean Coal Technologies for Our Future, Castiadas, Sardinia, Italy, May **2005**.

Chapter 8

Mass and Energy balance with the mid-temperature H₂S removal in Puertollano IGCC power plant

8 Introduction

This chapter covers an important part of the assessment of the integration of the new technology in Puertollano IGCC process, examining in more detail the layout configurations proposed. Subject of this work is to perform the mass and energy balance with the new sorbent desulphurization technology. In a particular way the attention has been focused on the desulphurization unit (HGDR, *Hot Gas Desulphurization and Regeneration*), evaluating the mass and heat balance. The latter was calculated from reaction equations and initial process data received from Puertollano IGCC process. Mass and energy balance gave useful information for becoming sorbent desulphurization testing. Quantity of reactants and products received from mass balance calculations, and the amount of heat (released or to be supplied), can be estimated from the energy balance results. An easy-to-use Excel-based mass and energy balance template which allows a user to modify the plant input before of the desulphurization unit, and automatically recalculate results, is also provided.

8.1 Hot Gas Desulphurization and Regeneration “HGDR” unit proposed

Due to lack of time, the mass and energy balance has been evaluated only in the first layout configuration proposed (Figure 4, [Layout 1](#) of Chapter 7) named “**Low-temperature layout**” where “*Low*” indicates the low raw gas temperature of 130 °C currently presents at the inlet of the desulphurization section. The latter was quite similar to the layout existing in the gas purification section with the aim to integrate the sorbent technology as seamless as possible. This proposed layout leaves

everything unchanged, including temperatures and pressures, until after the "Wet scrubbing" exit where the temperature of the raw gas is 126 °C, and takes into consideration the same boundary as with in existing MDEA desulphurization unit. For the present study the *zinc oxide (ZnO)* has been selected as sorbent material due to several reasons, first of all the "relatively" ease reactions involved in the sulphidation-regeneration cycle and being the only sorbent marketable. However, other important reasons have been considered for the selection:

- ✚ Rate of H₂S adsorption and low equilibrium achievable in the gas phase;
- ✚ Ease of regeneration of the ZnS sulphided species formed;
- ✚ Very low reduction to metal during adsorption due to highly reducing syngas (at 300 °C);
- ✚ Very low interaction between active metal oxide with other components in syngas (*e.g.* H₂, alkali metals);
- ✚ High sulphur loading;
- ✚ Cost of metal oxide.

8.1.1 Fluidized Desulphurizer

For a realistic application of this technology in a IGCC plant, the use of fluidized or transport reactors seems the most appropriate ^[1,2]. Based on several considerations, this selected configuration offers the following advantages compared to a fixed-bed process:

- ✚ Continuous syngas desulphurization and sorbent regeneration using only two reactors;
- ✚ Superior gas-solid contact, resulting in more efficient sulphur removal;
- ✚ Thermally neutral operation and regenerator temperature control by heating incoming sorbent with exothermic regeneration heat;
- ✚ Higher throughput due to high gas velocities, resulting in smaller reactor equipment for sulphur removal, and hence significantly lower capital cost.

Transport reactors have been used for several decades in the refining industry for fluid catalytic cracking. Therefore, significant design and operating experience exists for these reactors. RTI and Eastman have successfully leveraged this reactor technology for a higher-pressure operation for optimal integration within an IGCC process^[3]. Moreover this "reactor technology" is very similar to the "CLC Technology" (Chemical Looping Combustion), and that more innovative of Calcium Looping Process for CO₂ capture^[4].

The desulphurization system is comprised of two coupled circulating fluidized bed reactors: the Fluidized or Transport Desulphurizer, and the Fluidized or Transport Regenerator (Figure 1)^[5]. The circulation of the sorbent between desulphurizer and regenerator is elementary for the desulphurization process^[6]. The desulphurizer (a) is fluidized with raw-syngas, and sulphur compounds (H₂S and COS) are removed from the gas due to the chemical reaction with the sorbent. Bulk separation of the clean gas and sorbent takes place in the desulphurizer cyclone ahead of the reactor. In this way, the sulphided material leaves the reactor entering a cyclone (c) in order to separate the solids and the clean-syngas flow. Sulphided solid material is led through a standpipe and feed to the loop seal with cone valve (e). By means of the cone valve (e) the solid flux can be split and partially transferred into the regenerator (b). The main advantage using a cone valve as the split device is that the amount of circulated mass between the reactors is independent of the fluidization velocity in the reactor. The circulation rate towards the regenerator can be controlled by the opening position of the cone-valve. Both reactors are symmetric so that the regenerated sorbent material is circulated back towards the desulphurizer by means a second loop seal with cone valve (f). The SO₂- or H₂S-rich gas from regeneration (conditioned by the oxidation gas), named "*Claus-gas*", is routed to the Claus unit. A sorbent make-up system is provided to load fresh sorbent into the desulphurizer. The sorbent will be added as required to maintain sorbent inventory and reactivity.

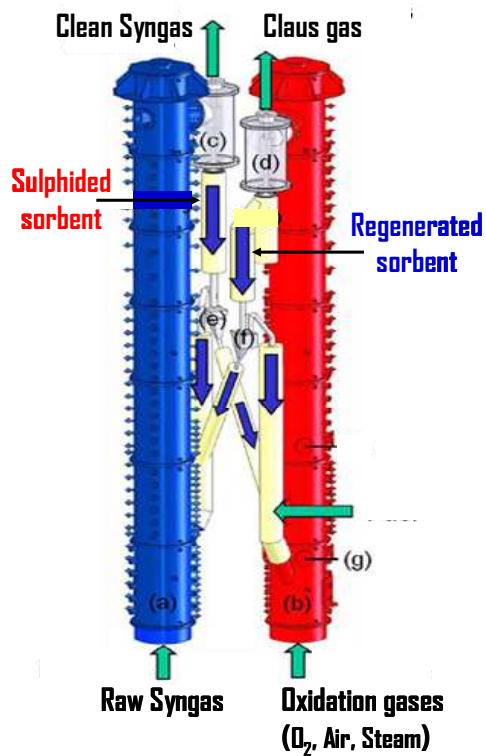


Figure 1. Coupled circulating fluidized bed reactors^[5].

8.1.2 Flow diagram for the proposed HGDSR unit

Figure 2 represents the simplified flow diagram of the desulphurization-regeneration process proposed. The global process has been denominated as *Zinc-looping process*.

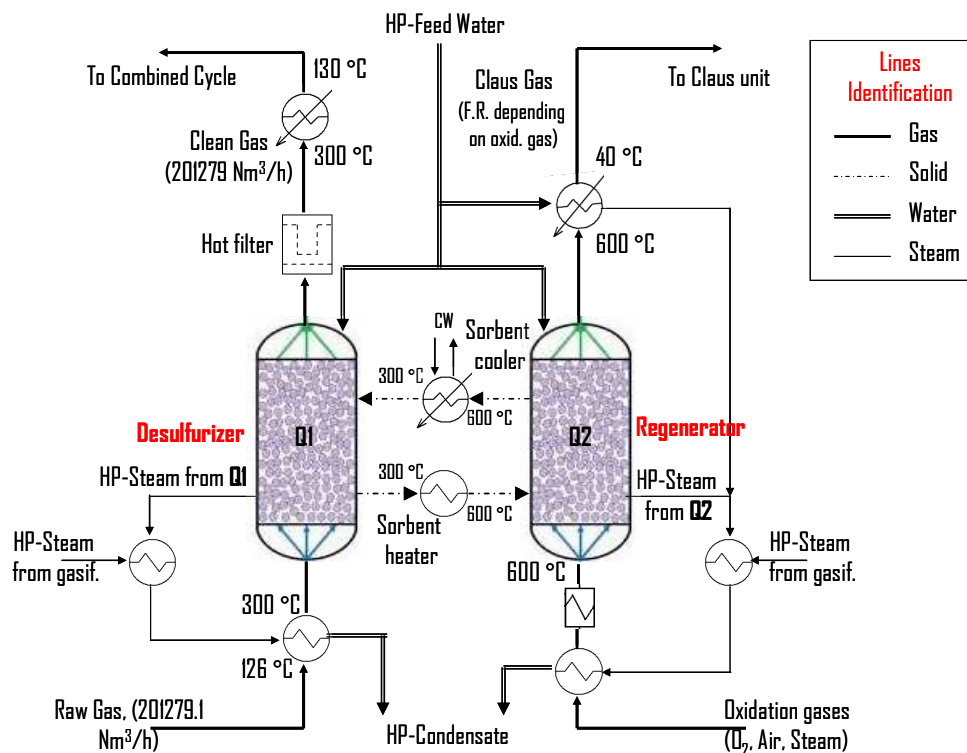


Figure 2. Simplified flow diagram of the HGDR process.

It consists of two main reactors, a desulfurizer and a regenerator. In the desulfurizer, raw gas containing H_2S and CO_2 enter the reactor, pre-emptively warmed through a first preheater (fed from both HP-steam derived from the cooling of the desulfurizer and HP-steam from gasification), where the desulphurization takes place at 300 °C at the pressure of the syngas (23.6 bar), and the exothermic reaction ($ZnO + H_2S + CO_2$) occurs. The formed sulphided sorbent (ZnS) is heated to 600 °C using the sorbent heater, and enters in the regenerator where the exothermic regeneration reaction with oxygen or air, or the endothermic regeneration reaction with steam, take place. Here, the sulphided product is converted into oxide sorbent with simultaneous SO_2 or H_2S release. The regenerated sorbent is then cooled from 600 °C to 300 °C through the "sorbent cooler" and recirculated to the desulfurizer. In the

calculation of heat balance an isotherm reactor has been considered so that the outlet temperature of the Clean and Claus gas are the same in which the reactions take place. The main advantage is the high temperature of the exit streams gas which enables additional steam generation through the heat released in the heat exchanger in outlet of the process.

8.2 Specifications of the gas streams used in the mass and energy balance

Table I presents, for a gasifier load of 100 %, the characteristics of the raw gas in outlet of the wet scrubbing system before being sent to the HGD&R unit.

Table I. Characteristics of the raw gas after the wet scrubbing system.

Gasifier Load	100 %
Pressure (bar)	23.6
Temperature (°C)	126
Flow Rate (m_n^3/h , dry)	180 937
Flow Rate (kg/h, wet)	202 527
Solids (mg/m_n^3)	1
CO ₂ * (%)	3.70
CO (%)	61.25
H ₂ (%)	22.33
N ₂ (%)	10.50
Ar (%)	1.02
H ₂ S (%)	1.01
COS (%)	0.17
CH ₄ (%)	0.01
NH ₃ (ppm)	38
HCN (%)	0.01
LHV (kJ/m_n^3)	10 429
HHV (kJ/m_n^3)	10 899

* concentrations are expressed in volume on a dry basis

A crucial point in this technology is related to the regeneration of the sulphided sorbent. So, regarding the selection of the regeneration gas, this will have to be provided, with regard to O_2 and air, from the ASU unit. The other alternative is the use of steam as regeneration gas. The Air Separation Unit (ASU) in Puertollano plant produces gaseous oxygen and nitrogen as well as gaseous waste nitrogen to enable the plant to comply with the overall material balance.

For the mass balance and energy calculation four different regenerating gas were considered: **oxygen (85%), air (21% O_2), diluted air (10% O_2), and steam.**

8.3 Material Balance Calculation

Material balances are a basis for the process design. They determine quantities of raw materials required and achieved products. For the complete process, balances of individual process units determine process stream flows and compositions. The material and heat balance of the process upstream in the desulphurization unit, up to the raw-gas exit, has been evaluated with an easy-to-use Excel-based mass balance template. All the data are referred for a gasifier load of 100 % and wet raw gas (H_2O content = 11.01 % v/v). The unit operation, may be represented diagrammatically as a box, as shown in Figure 3. The mass and energy going into the box must balance with the mass and energy coming out.

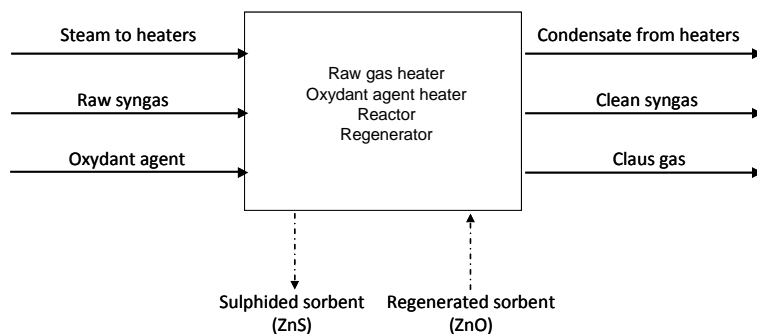


Figure 3. Simplified box for mass balance.

The conservation equation for desulphurization unit block is written as:

$$\text{Material}_{\text{out}} = \text{Material}_{\text{in}} + \text{Generation} - \text{Consumption}$$

The only reactants gas involved in the reaction (H_2S and COS), were considered in the mass balance. All the other raw gas compounds pass through the desulphurization unit unchanged, finding them in the clean gas. For the regenerator, the mass balance, and consequently the nature (composition, flow rate, etc.) of the Claus gas depends on the oxidation gas used. The material balance has been divided into two different reactions that generate two different contributes. The first one is the reaction that **occurs in the desulphurizer**:

$$m_{\text{ZnO},\text{DIN}} + m_{\text{H}_2\text{S}+\text{COS},\text{DIN}} = m_{\text{ZnS},\text{DOUT}} + m_{\text{H}_2\text{O},\text{DOUT}} + m_{\text{CO}_2,\text{DOUT}} \quad 1)$$

where

- $m_{\text{ZnO},\text{DIN}}$ ZnO sorbent mass flow into the desulphurizer
- $m_{\text{H}_2\text{S}+\text{COS},\text{DIN}}$ H_2S and COS mass flow into the desulphurizer
- $m_{\text{ZnS},\text{DOUT}}$ ZnS formed flow out of the desulphurizer
- $m_{\text{H}_2\text{O},\text{DOUT}}$ H_2O formed flow out of the desulphurizer
- $m_{\text{CO}_2,\text{DOUT}}$ CO_2 formed flow out of the desulphurizer

and the second one is that **occurs in the regenerator**:

$$m_{\text{ZnS},\text{RIN}} + m_{\text{O}_2,\text{RIN}} = m_{\text{ZnO},\text{ROUT}} + m_{\text{SO}_2,\text{ROUT}} \quad 2)$$

where

- $m_{\text{ZnS},\text{RIN}}$ ZnS sorbent mass flow into the regenerator
- $m_{\text{O}_2,\text{RIN}}$ O_2 mass flow into the regenerator

$m_{ZnO,ROUT}$ ZnO formed flow out of the regenerator

$m_{SO2,ROUT}$ SO₂ formed flow out of the regenerator

8.3.1 Mass balance in the Desulphurizer

Mass flow of H₂S and COS gases can be calculated easily from the raw gas flow rate (Nm³/h, wet).

$$m_{H2S,IN} = 2780.3 \text{ Kg/h} = 81.58 \text{ Kmol/h}$$

$$m_{COS,IN} = 824.9 \text{ Kg/h} = 13.73 \text{ Kmol/h}$$

So, the ZnO sorbent mass flow amount can be calculated from the stoichiometry of the desulphurization reaction

$$m_{ZnO,IN} = 7759 \text{ Kg/h} = 95.31 \text{ Kmol/h}$$

ZnS sulphided material is formed according to the desulphurization reaction. Mass flow of ZnS is calculated by the equation:

$$m_{ZnS,OUT} = n_{ZnS} * M_{ZnS} = 9290.2 \text{ Kg/h}$$

Mass flow of desulphurization product gases, which consists of H₂O and CO₂, are:

$$m_{H2O,OUT} = 1468.44 \text{ Kg/h} = 1827.4 \text{ Nm}^3/\text{h}$$

$$m_{CO2,OUT} = 604.1 \text{ Kg/h} = 307.5 \text{ Nm}^3/\text{h}$$

The flow rate (Nm³/h, wet) of the clean syngas after bulk separation in the desulphurizer cyclone is:

$$FR_{cleanG} = FR_{rawG} - (FR_{H2S} + FR_{COS}) + (FR_{H2O} + FR_{CO2}) = 201279 \text{ Nm}^3/\text{h}$$

with " FR ", the flow rate of the inlet and outlet gas components in the desulphurizer.

The global mass balance, referred both to the desulphurizer and regenerator can be easily realised by the gas and solid streams reported in [Figure 4](#) (enumerated streams in the rhombus).

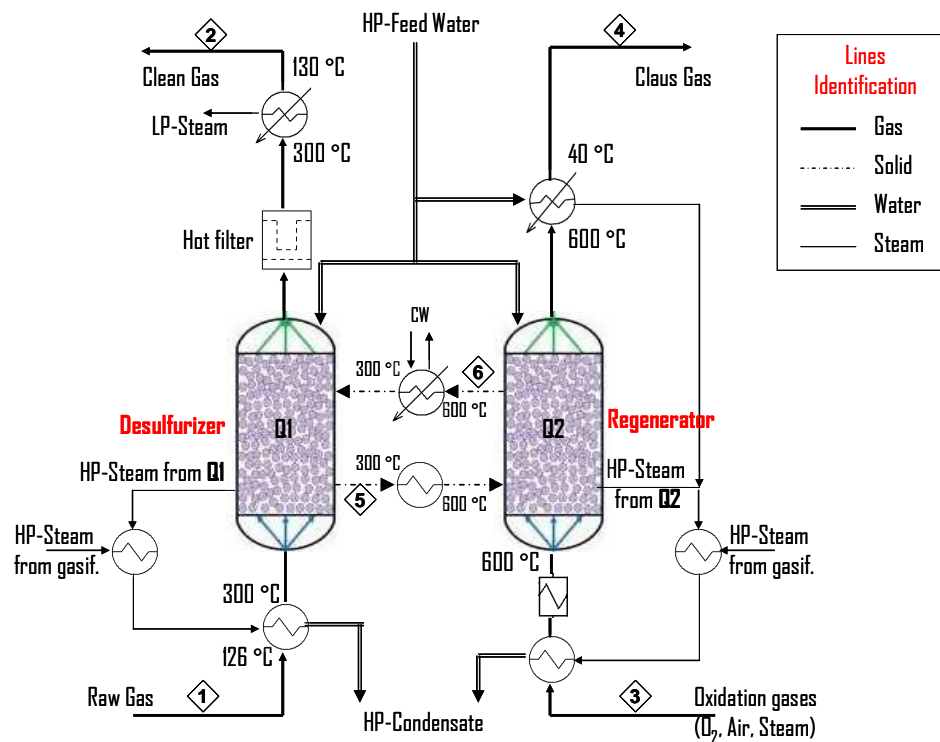


Figure 4. Gas and solid streams flow diagram.

The following [Table 2](#) details the main properties of the streams [1](#), [2](#), [5](#), [6](#), derived from the mass balance of the desulphurizer.

Table 2. Composition and mass balance in the desulphurizer of selected streams of Figure 4.

Stream	1	2	5	6
	Gas	Gas	Solid	Solid
Temperature (°C)	126	300	300	600
Mass flow (Kg/s)	56.0	55.69	2.58	2.15
Flow rate (Nm ³ /h,wet)	201279	201279	-	-
CO ₂ (%) *	3.32	3.48	-	-
CO (%)	55.06	55.06	-	-
H ₂ (%)	20.07	20.07	-	-
N ₂ (%)	9.44	9.44	-	-
Ar (%)	0.92	0.92	-	-
H ₂ S (%)	0.91	-	-	-
COS (%)	0.15	-	-	-
H ₂ O (%)	10.11	11.01	-	-
CH ₄ (%)	0.009	0.009	-	-
NH ₃ + HCN (%)	0.009	0.009	-	-

* concentrations are expressed in volume on a wet basis

8.3.2 Mass balance in the Regenerator

Oxygen regeneration case

$$m_{ZnS,RIN} + m_{O_2,RIN} = m_{ZnO,ROUT} + m_{SO_2,ROUT}$$

The oxygen stoichiometrically required to convert the ZnS sulphided product in the ZnO regenerated sorbent can be calculated with the equation:

$$m_{O_2,RIN} = 1.5 (n_{ZnS} * M_{O_2}) = 4574.9 \text{ Kg/h} = 3202.4 \text{ Nm}^3/\text{h}$$

Sulphur dioxide (**SO₂**) mass flow out of the regenerator represents the "Claus gas" that will be sent to the Claus unit.

$$FR_{ClausGas} = 2134.9 \text{ Nm}^3/\text{h}$$

Air and diluted air regeneration (21% and 10% of O₂)

Due to different reasons, it has been thought and suggested to carry out the regeneration reaction with air (21% O₂), or diluted air (10% O₂). Because, first of all, for safety reasons, due to the high exothermic regeneration reaction in presence of oxygen. According to this considerations the mass balance in the regenerator change as follows:

$$m_{ZnS,RIN} + m_{O_2,RIN} + m_{N_2,RIN} = m_{ZnO,ROUT} + m_{SO_2,ROUT} + m_{N_2,ROUT}$$

The oxygen stoichiometrically required from the regeneration reaction is unchanged. So:

$$m_{O_2,RIN} = 1.5 (n_{ZnS} * M_{O_2}) = 4574.9 \text{ Kg/h} = 3202.4 \text{ Nm}^3/\text{h}$$

and considering that the nitrogen does not react in the process, for pure air (**21% O₂**)

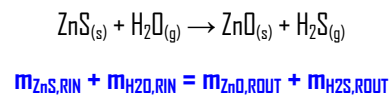
$$m_{N_2,RIN} = m_{N_2,ROUT} = 3.76 (n_{O_2} * M_{N_2}) = 15056.7 \text{ Kg/h} = 12041.1 \text{ Nm}^3/\text{h}$$

and for diluted air (**10% O₂**)

$$m_{N_2,RIN} = m_{N_2,ROUT} = [3.76 (n_{O_2} * M_{N_2})] + (n_{N_2,dil} * M_{N_2}) = 36032.1 \text{ Kg/h} = 28815.4 \text{ Nm}^3/\text{h}$$

Steam regeneration

The last regeneration gas proposed is through the use of steam. In this case, the reaction is endothermic and needed to supply heat from the outside. The most favourable reaction considered (negative Gibbs free energy of reaction) for the material balance is:



The stoichiometrically steam required to convert the ZnS sulphided product in the ZnO regenerated sorbent can be calculated:

$$m_{\text{H}_2\text{O,RIN}} = 1717.5 \text{ Kg/h} = 2134.9 \text{ Nm}^3/\text{h}$$

H₂S mass flow out of the regenerator represent the "Claus gas" that will be sent to the Claus unit.

$$FR_{\text{ClausGas}} = 2134.9 \text{ Nm}^3/\text{h}$$

The following [Table 3](#) details the main properties of the streams [3](#) and [4](#), derived from the mass balance of the regenerator taking into account different oxidation gases.

Table 3. Composition and mass balance in the regenerator of selected streams of Figure 4.

Stream	<i>O₂</i> Regeneration		Air Regeneration		Steam Regeneration	
	3	4	3	4	3	4
Temperature (°C)	88	600	127.3	600	242	600
Mass flow (Kg/s)	1.27	1.69	5.45	5.86	0.48	0.90
Flow rate (Nm ³ /h)	3202.4	2134.9	15243.5	14179	2134.9	2134.9
N ₂ (%)	15	-	79	84.94	-	-
O ₂ (%)	85	-	21	-	-	-
H ₂ O (%)	-	-	-	-	100	-
H ₂ S (%)	-	-	-	-	-	100
SO ₂ (%)	-	100	-	15.06	-	-

8.4 Energy balance calculations

In energy balance calculations, the energy considered includes the energy content of the input and of output streams. In this study, energy balances were made to determine energy requirements of the process which are the heating, cooling and power required. In particular, this calculation was performed to understand if the desulphurization unit was "self-sustaining" in terms of heat balance. A general equation can be written for the open system at steady state:

$$\begin{aligned}
 & \text{Energy Input} = \text{Energy Output} \\
 & Q = \Delta H = \sum H_{OUT} - \sum H_{IN}
 \end{aligned}$$

The energy requirement of the desulphurization unit can be calculated from two main factors. The first one and the largest, is the *heat of reaction*; indeed, the desulphurization and regeneration (with oxygen or air) reactions are exothermic. The second one is related to the *sensible heat* in the feed stream and in

the reactants and products of the desulphurization unit. *Heat of reaction* at 300 °C and 600 °C in the desulphurizer and regenerator was calculated with the application of Kirchhoff's equation:

$$(\Delta H_T - \Delta H_0) = \int_{298K}^T \Delta C_p dT$$

with

$$\Delta H_R^0 = \Delta H_{f, Products}^0 - \Delta H_{f, Reactants}^0$$

Sensible heat of the reactants and products was calculated according to the ambient conditions ($T=15^\circ\text{C}$ and $P=1.013\text{ bar}$) by the equation:

$$Q = m C_p \Delta T \quad \text{with } \Delta T = (T_f - T_i)$$

The feed stream in the first layout proposed, constituted by the raw-gas, is colder (126 °C) than the desired desulphurizer temperature (300 °C), so it has to be heated before it entries in the reactor. The flow rate, temperature, and heat capacity of the wet stream were taken into account.

The following is a list of assumptions and calculation procedures for the energy balance:

1. The zinc oxide sorbent is supposed to react completely with sulphur compounds and transforms all in zinc sulphide;
2. All the zinc sulphide products in the desulphurizer are completely regenerated in the regenerator to turn back into zinc oxide;

3. No unwanted reaction, such as the zinc sulphate formation has been considered;
4. Stationary state conditions are considered;
5. The inlet and outlet temperatures of the reactants and products are reported in [Figure 4](#).

Heat required to increase the raw-gas temperature

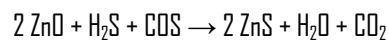
The heat to be supplied to the raw gas to increase the temperature from 126 °C, outlet temperature from the Venturi scrubber, to 300 °C, temperature required for the desulphurization reaction has been calculated.

$$Q_{126 \rightarrow 300} = 46689671 \text{ MJ} = 13 \text{ MW}$$

Below, the results of the energy balance "inside" of the two reactors, desulphurizer and regenerator will be presented.

8.4.1 Energy balance in the Desulphurizer

Considering that the H₂S and COS removal takes place in the same reactor according to the reaction:



the total generated heat in the desulphurizer considering also the heat of reaction, is

$$Q_{\text{DES}} = +0.975 \text{ MW}$$

where the "plus symbol" in this case indicates that the heat is liberates in the desulphurization process.

8.4.2 Energy balance in the Regenerator

The total generated or required heat in the regenerator, considering also the heat of reaction, is:

$$Q_{REG} = +9.173 \text{ MW} \quad (\text{with } \textit{pure oxygen})$$

$$Q_{REG} = +4.09 \text{ MW} \quad (\text{with } \textit{air, 21\% O}_2)$$

$$Q_{REG} = -2.98 \text{ MW} \quad (\text{with } \textit{diluted air, 10\% O}_2)$$

$$Q_{REG} = -2.08 \text{ MW} \quad (\text{with } \textit{IP-steam})$$

where the “plus symbol” indicates that the heat is liberates. In the regeneration with diluted air, due to the high nitrogen content to heat up, and with the use of IP-steam, being the regeneration reaction endothermic, the heat will has to be supplied from the outside.

8.4.3 Global final heat required or necessary in the Desulphurizer and Regenerator reactors

The final heat balance in the different conditions proposed are summarised below (Table 4). For each one the looping process among the desulphurization reactor (H_2S and CO_2 removal) and the four different options for the regenerator (oxygen, air, diluted air and steam) have been considered. **Here, the heat necessary to heat-up the raw-gas has not been taken into account.**

Table 4. Total energy balance in different regeneration conditions.

<i>Desulphurizer + Regenerator (D + R)</i>		
	Q (MW)	HP-Steam recovered or required (Kg/s)
D + R (O_2)	+10.15	+8.8
D + R (Air, 21% O_2)	+5.06	+4.3
D + R (Air, 10% O_2)	-2	HP not enough
D + R (Steam)	-1.1	HP not enough

+ Energy and HP steam recovered in the heat exchanger; - Energy required in the desulphurizer and regenerator

HP not enough due to the high temperature to be achieved

Also in this case, the “plus symbol” indicates that the heat is comprehensively liberates in the desulphurization-regeneration process. In the regeneration with diluted air and steam, being the heat “negative”, we will have to supply heat overall. Furthermore, as the reactor operates at regeneration temperature of 600 °C, even the use of external HP-steam is not sufficient to obtain this temperature. The conclusion is that in the latter two cases, as in the existing plant there is no source that allows to heat-up at that temperature, the installation of an equipment able to heating the reactors would be required. This result leads to consider in the next sections of the present thesis the use of oxygen and air for the comparison with the current MDEA-Solvent technology.

8.4.4 Recoverable or provided energy in the heat exchangers of the HGDSR unit

As mentioned before, it is essential to heat up the inlet streams, both of the raw gas and the oxidation gases prior to enter in the reactors. Table 5 shows the energy required for this purpose along the nature of the necessary steam.

Table 5. Energy required to heat up the raw gas and the different oxidation gases at the working temperature.

	Q (MW)	HP-Steam required (Kg/s)
Raw gas (Input)		
From 126 °C to 300 °C	13	11.3
Regeneration gas (Input)		
O ₂ Regenerat. From 88 ^(*) °C to 600 °C	0.6	0.16 + Electric preheater
Air Regenerat. From 127.3 ^(*) °C to 600 °C	2.6	0.82 + Electric preheater
Diluted air Regenerat. From ≈180 ^(*) °C to 600 °C	4.9	HP + Electric preheater
IP-Steam Regenerat. From 242 ^(*) °C to 600 °C	0.33	0.04 + Electric preheater

^(*) Starting temperature of the gas directly collected in the plant

Also in this case, the need to heat the regeneration gas at 600 °C cannot be fully realized with the high pressure steam, because this allows to heat the gas up to 300 °C. The further 300 °C must be provided through an electric heater.

Shown in Table 6 below the summarized data relative to the amount of steam (HP or LP) required or generated in the individual heat exchanger of the HGDR unit, **without considering the external supply of steam from gasification**. In Figure 5 are represented and named all the heat exchangers of the unit.

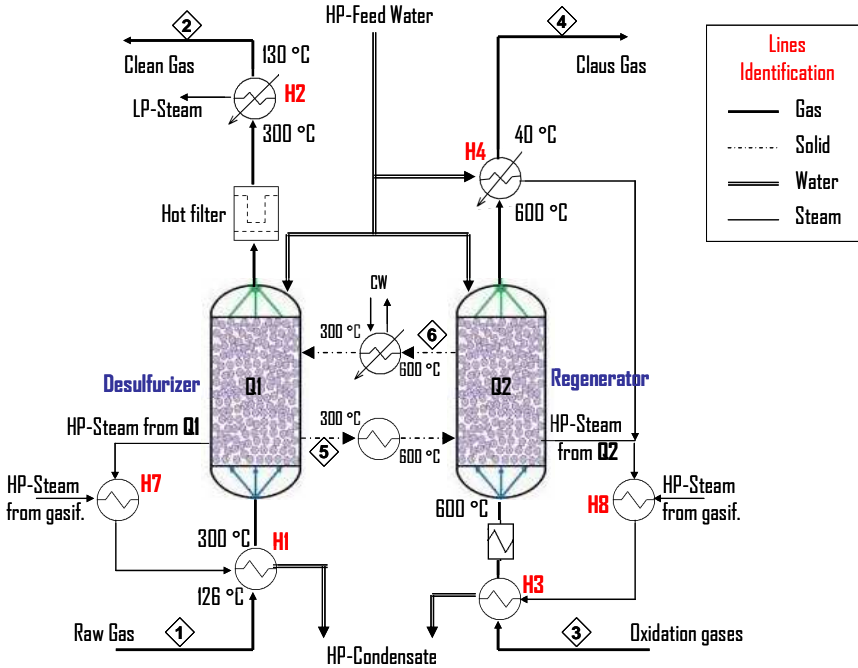


Figure 5. Flow diagram of the HGDR unit with heat exchangers identification.

Table 6. Mass flow of HP and LP steam in the heat exchangers of the HGDR unit.

Heat Exchanger	H1	H2	H3 O ₂	H3 Air	H4 O ₂	H4 Air	H7	H8 O ₂	H8 Air
HP-Mass flow (Kg/s)	-11.3	NO	-0.2	-0.8	+0.5	+2.6	+0.8	+8	+3.5
LP-Mass flow (Kg/s)	NO	+6.1	NO	NO	NO	NO	NO	NO	NO

+ Mass flow of HP or LP steam recovered - Mass flow of HP or LP steam required NO: no production of steam

From a careful analysis of Table 6, and as shown in the flow diagram of Figure 5, it can be concluded that the HGDR unit of this first proposed layout (*Low-temperature layout*) is not entirely self-consistent in terms of energy, but a certain amount of external HP-steam must be taken from the one "HP-Saturated steam from gasification".

In Table 7 below all the thermodynamic parameters at the inlet and outlet gas temperatures of the main streams involved in the process are reported.

Table 7. Energy streams data in the HGDR unit.

Stream	O ₂ Regeneration				Air Regeneration		Steam Regeneration	
	1	2	3	4	3	4	3	4
Temp. (°C)	126	300	88	600	127.3	600	242	600
Flow rate (Nm ³ /h)	201279	201279	3202.4	2134.9	15243	14179	2134.9	2134.9
LHV (KJ/Kg)	9337	9142	0	0	0	0	0	15360
Enthalpy (KJ/Kg)	346.3	605.2	523.2	425	144.7	571.3	2802	587.6
Heat flow (MW)	542.3	542.8	0.1	0.72	0.7	3.35	1.34	14.4

8.5 Cold and hot gas efficiency (CGE and HGE)

Different temperatures of the syngas at the combustor (130 °C vs. 300 °C) influence the next operations.

In fact, the cold gas efficiency of the gasification process is:

$$CGE = \frac{m_{Clean\ gas} \cdot LHV_{Clean\ gas}}{m_{Coal} \cdot LHV_{Coal}}$$

and

$$HGE = \frac{m_{Clean\ gas} \cdot (LHV_{Clean\ gas} + \Delta H_s)}{m_{Coal} \cdot LHV_{Coal}}$$

where ΔH_s is the clean syngas enthalpy minus its enthalpy at 15 °C. Reported in Table 8 the results of the cold and hot gas efficiency in the case of the conventional MDEA-Solvent and innovative ZnO-Sorbent technology.

Table 8. Cold and hot gas efficiency in MDEA-Solvent and ZnO-Sorbent technology.

	CGE (%)	HGE (%)
MDEA-Solvent technology	52	52.8
ZnO-Sorbent technology	51.85	55.3

8.6 Thermal Efficiency comparison with the conventional "MDEA-Solvent" method

To achieve a comparison in terms of efficiency, both in the currently used MDEA-Solvent technology and innovative ZnO-Sorbent technology, thermal efficiency " η_{th} " based on the heat flows incoming and outgoing from the desulphurization unit has been evaluated. To obtain a representative comparison in both cases was considered the same boundary for the efficiency calculation. Since the study carried out so far has been just limited to the unit of sulphur compounds removal and has not been extensively investigated in the Claus unit, for a "fair" comparison, even the efficiency in the current desulphurization

unit has been limited to MDEA-sorption unit. In the Figures 6 and 7 below the boundaries considered for the comparison have been reported with all the gas streams considered in the calculation.

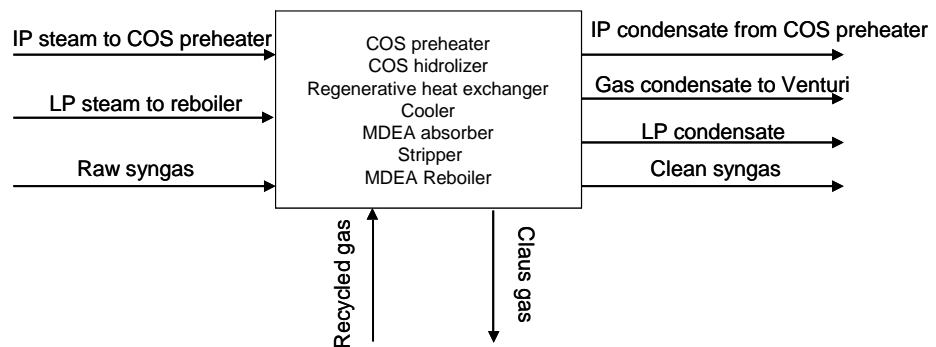


Figure 6. Schematic block diagram of the MDEA-Solvent considered in the thermal efficiency calculation.

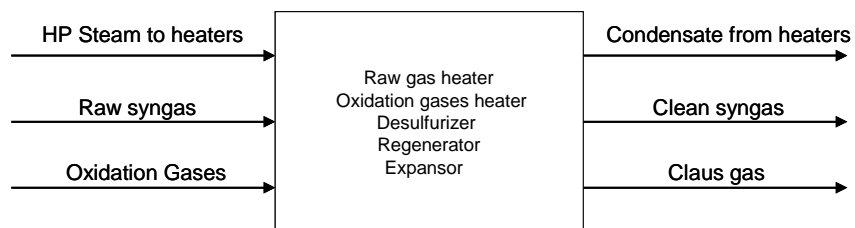


Figure 7. Schematic block diagram of the ZnO-Sorbent considered in the thermal efficiency calculation.

A difference in the "heat flow input" is that in the MDEA-solvent, in addition to the raw syngas, the recycle gas coming from the "Claus unit" is presents (7467 Nm³/h, wet). It has not been possible to evaluate this amount in the case of sorbent technology as the study in the Claus unit was not carried out.

The general formula used for this calculation was:

$$\eta_{th} = \frac{\text{Heat flow}_{out}}{\text{Heat flow}_{in}} * 100$$

where $\text{Heat flow} = \text{Mass flow (Kg / s)} \cdot [\text{LHV} + \text{Enthalpy (KJ / Kg)}]$

but the efficiency was also calculated in this different way, as $\frac{\text{MW Required}}{\text{Nm}^3 / \text{h}(\text{H}_2\text{S} + \text{COS})}$

8.6.1 Thermal efficiency in the Solvent-MDEA desulphurization

The calculation of the thermal efficiency was referred to the Raw-, Clean-, Claus- and Recycle-gas in the "wet state" where the water content was not negligible. The thermal efficiency has been calculated also considering the IP-saturated steam from gasification (0.568 Kg/s) and the LP-steam to gasification (3.663 Kg/s) necessary for the heat exchangers in the desulphurization unit. The data used for the final η_{th} determination are reported in the Excel spreadsheet and summarized in Table 9. Below all the parameters used for this calculation.

$$\eta_{th} = \frac{\text{HF Clean gas} + \text{HF Claus gas} + \text{HF IP Condens} + \text{HF LP Condens}}{\text{HF Raw gas} + \text{HF Recycle gas} + \text{HF IP Steam} + \text{HF LP Steam}} * 100$$

$$\eta_{th} = 96.4 \%$$

and

$$\eta = \frac{(\text{HF IP Steam} + \text{HF LP Steam})_{imported}}{\text{H}_2\text{S} + \text{COS} (\text{Raw gas} + \text{Recycle gas})}$$

$$\eta = 5.14 \text{ KW/Nm}^3\text{h}^{-1} (\text{H}_2\text{S} + \text{COS})$$

In this last formula, but also in the ZnO-Sorbent case, **the condensed gas has not been taken into account.**

8.6.2 Thermal efficiency in the ZnO-Sorbent desulphurization

Even in this case, the calculation of the thermal efficiency has been referred to the raw- and clean-gas in the “wet state”. The data used for the final η_{th} determination are reported in the Excel spreadsheet. Similarly to the formula used above, all the parameters employed for the ZnO-sorbent efficiency calculation are shown.

$$\eta_{th} = \frac{HF_{Clean\ gas}(300^{\circ}C) + HF_{Claus\ g}(600^{\circ}C) + HF(HP\ H.Exch\ Desulf) + HF(HP\ H.Exch\ Re\ gen) + HF_{HP\ Cond}}{HF_{Raw\ gas}(126^{\circ}C) + HF(HP\ Steam) + HF_{Oxidation\ Gas}} * 100$$

and

$$\eta = \frac{(HF_{HP\ Steam})_{imported}}{H_2S + COS (Raw\ gas)}$$

In this last case, the low-pressure steam produced has not been taken into account by the cooling of the Clean gas from 300 °C to 130 °C.

Table 9. Comparison data between MDEA-Solvent and ZnO-Sorbent technology.

	$\eta_{th}(\%)$	$\eta(KW/Nm^3/h)$	m HP-steam (Kg/s)	m IP-steam (Kg/s)	m LP-steam (Kg/s)	m HP (Kg/s)	m IP (Kg/s)	m LP (Kg/s)
	With Gas Cond.	Without Gas Cond.	Generate	Generate	Generate	Requir.	Requir.	Requir.
MDEA-Solvent	96.4	95.9	5.1	-	-	-	0.6	3.7
	$\eta_{H.E.=1}$	$\eta_{H.E.=0.3}$						
ZnO-Sorbent								
O ₂ Reg.	99.5	97.5	2.7	0.35+6.2 ^(*)	-	4.3	14.9	-
Air Reg.	98.6	96.6	6.5	1.82+3.1 ^(*)	-	4.3	15.7	-
Diluted air Reg.	97.4	95.4	9.0	3.88 ^(**)	-	4.3	14.6	-
IP-Steam	99.8	98.2	13.5	0.31 ^(**)	-	4.3	14.7	0.5

(*) HP-steam amount generated from the cooling of the Claus gas + cooling of the two reactors considering the heat exchanger efficiency $\eta_{HE}=0.3$

(**) HP-steam generated from only the cooling of the Claus gas considering the heat exchanger efficiency $\eta_{HE}=0.3$

The efficiency calculated as $\frac{MW\ Required}{Nm^3 / h(H_2S + COS)}$ in the case of the regeneration with diluted air

(10% O₂) and IP-steam was evaluated in a slightly different way compared to the other cases because as reported previously, the HP-steam from outside is not enough, but, being required to heat up the regenerator reactor at 600 °C, the MW required for this operation will be taken into account (for example through the combustion of natural gas, electrical heater or other source). So the formula has been modified as:

$$\eta = \frac{(HF\ HP\ Steam)_{imported} + (MW\ Re\ generator)_{required}}{H_2S + COS\ (Raw\ gas)}$$

Regarding these two cases, attention must be paid to the high values of " η_{th} " thermal efficiency of 97.4 and 99.8%, for diluted air and IP-steam respectively, because these values would make sense only if the plant had a source that allows to heat the regenerator at 600 °C. So, this value is not directly applicable to the currently existing Puertollano IGCC-plant. Furthermore, the value so high in the case of regeneration with IP-steam is due to the Claus gas exiting from the regenerator that is constituted by only H₂S, that in contrast with the SO₂ as obtained in the other cases of regeneration, having a higher Lower Heating Value (LHV) and consequently a higher heat flow value.

From Table 9 it is clear that the ratio (KW/Nm³ h⁻¹) compared to MDEA-solvent technology (5.1) is lower only in the case of oxygen regeneration (2.7). This is due to higher exothermicity of the regeneration reaction compared to those with air and diluted air, where the nitrogen acts as diluting gas decreasing the heat recovery and generating lower HP-steam amount. In the case of IP-steam is used as regeneration gas, the ratio (13.5 KW/Nm³ h⁻¹) is very high, caused by the endothermic regeneration reaction. So, is necessary to supply heat to the reactor, resulting in an increase of the KW required.

8.7 General impact of the use of oxygen, air and steam on the different plant sections

In this first layout configuration proposed, the impact in the section upstream of the mid-temperature desulphurization is almost negligible. The path of the raw-gas, including equipments, temperature and pressure values, are the same as in the "Cold Gas Desulphurization, CGD" process. The main objective of this layout is to integrate the new solid sorbents technology in place of the existing one, without any substantial change in the plant. Nevertheless, with this easier configuration, the raw gas is required to be heated up because the temperature of 130 °C is not enough for the gas inlet in sorbent reactor. **This is certainly a point against the first proposed layout.** However, as evidenced by the data of [Table 9](#), this heating can be avoided, mostly with the HP-steam generated from the exothermic reaction in the desulphurizer and regenerator, in the case of regeneration with oxygen, and minimally with the HP-steam generated from the exothermic reaction in the desulphurizer and regenerator, in the case of regeneration with air. On the other hand, this would be completely avoided in the second layout configuration proposed in the previous chapter, where all the sensible heat of the raw gas in outlet of the gasification island would be exploited. Keeping in mind that this layout has been conceived to be simple to be incorporated into this plant, from the data derived from the energy balance and thermal efficiency as a function of the regeneration gas used, it is possible to emphasize some important aspects. In the case of regeneration with diluted air and steam, it is necessary to provide heat to the reactor for regeneration for the reason earlier described. This heat, not being currently supplied from any source in the plant, would require the addition of a new equipment for this purpose. For the considerations previously made, the continuation of the evaluation in the combined cycle will be carried out through the use of oxygen or air as regeneration gas.

In summary, the criteria for the choice of oxygen as an oxidizing agent for the continuation of the evaluation in the combined cycle, in the first layout configuration, have been:

- ✚ Lesser general influence of the replacement of the new technology in place of the one currently used;

- ✚ Lower consumption of regenerating gas to subtract to the ASU unit;
- ✚ Lower consumption of HP-steam to be subtracted from HP-drum;
- ✚ Exothermic reaction resulting in the production of HP-steam in both reactors, desulphurizer and regenerator.

The disadvantages that there may be, are the following:

- ✚ Potential danger of the regeneration reaction;
- ✚ The need for a very careful temperature control due to the highly exothermic reaction;
- ✚ Possible unwanted formation of zinc sulphate.

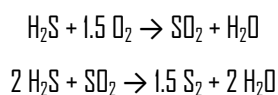
8.7.1 Impact of the use of oxygen, air and steam on the Claus unit

A deep impact downstream of the *HGDSR* process is in the Claus plant. In fact, there are two different compositions of the Claus gas, depending on the regeneration gases used. [Table 10](#) shows the off-gas in outlet of the regeneration unit.

Table 10. *Different off-gas in outlet from the regenerator.*

Regeneration Gas	O ₂	Air (21% O ₂)	Diluted air (10% O ₂)	IP-Steam
Claus Gas obtained (Nm³/h)	SO ₂ (2134.9)	SO ₂ + N ₂ (14179)	SO ₂ + N ₂ (30950)	H ₂ S (2134.9)

Keeping in mind that presently the sulphur recovery unit is a system which deals with the Claus gas and the sour gas coming respectively from the sulphur removal unit and from the wet scrubbing system and it converts H₂S to elemental sulphur in liquid state through two reactions in the Claus kiln:



The idea with this proposed layout, in the case of oxygen and air regeneration, was directly to make the H_2S of the sour gas derived from the wet scrubbing system to react with the SO_2 derived from the regeneration of the sulphided sorbent. From a material balance evaluation, the H_2S necessary for the reaction is definitely deficient respect to the theoretically amount required, so that only a low percentage of the SO_2 -Claus stream could be treated. The other alternative considered to treat the SO_2 stream, was a new plant for the H_2SO_4 production (see Chapter 7, section 7.7.1). There is a third alternative which would transform the current Claus unit: it is the "*Direct Sulphur Recovery Process (DSRP)*", a fixed-bed catalytic process that selectively reduces SO_2 from the regenerator of the *HGD&R* into elemental sulphur^[3].

On the other hand, with steam regeneration, the situation is more similar to that now used in the process: the Claus gas, made from H_2S only, will be treated in the same Claus unit currently present in Puertollano plant.

8.8 Impact of ZnO-Sorbent technology in the Puertollano IGCC efficiency

The aim of this part of the work was to evaluate the effect of the *HGD&R* unit (*Hot Gas Desulphurization and Regeneration*) in the combined cycle of the plant in terms of thermal and gross efficiency compared with the MDEA-Solvent technology. The Thermo-economic Diagnosis System "TDG" software has been used in order to perform the simulation with the new technology. The mass balance in the air separation unit (ASU) has been evaluated in view of the increased demand of oxygen or air in the sulphided sorbent regeneration of the new technology. It provided, for this purpose, an easy-to-use Excel-based mass balance template which allows a user to modify the air or oxygen taken out of the gas turbine air compressor.

8.8.1 Different impacts of the ZnO-Sorbent technology on the Combined Cycle efficiency

The impact deriving from the use of the new ZnO-Sorbent technology on the final gross efficiency in the combined cycle can be divided as:

- ✚ Impact originated from different parameters of the clean syngas (mostly mass flow and composition);
- ✚ Impact originated from the new oxygen requirement;
- ✚ Impact originated from the steam balance in the *HGDR* unit.

8.8.2 Impact of the clean syngas in the outlet of the Desulphurizer

Table II presents, for gasifier load of 100%, the main characteristics of the clean syngas, obtained with the new ZnO-Sorbent technology, sent to the saturator before being fed to the combined cycle in comparison with that obtained currently in the plant (**MC15.100 reference of Siemens design**).

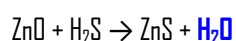
Table II. Characteristics of the clean gas after the HGD&R unit in comparison with the reference data (MC15.100).

	ZnO-Sorbent	MC15.100 Design
Gasifier load	100 %	100 %
Pressure (bar)	23.6	21
Temperature (°C)	300	129
Flow rate (Nm³/h, dry)	180937	183053
Mass flow (Kg/s)	55.687	52.371
CO₂ (%) *	3.48	3.86
CO (%)	55.06	60.35
H₂ (%)	20.07	22.02
N₂ (%)	9.44	12.46
Ar (%)	0.92	1.03
H₂S (%)	ppm level	ppm level
COS (%)	ppm level	ppm level
CH₄ (%)	0.009	0.01
NH₃ + HCN (%)	0.009	0
H₂O (%)	11.01	0.27
LHV (KJ/Kg)	9142.02	9737.5

* concentrations are expressed in volume on a wet basis

The data show the main differences in the clean gas mainly concerning temperature, mass flow and composition. The temperature of the clean gas obtained at the outlet of the desulphurizer for the ZnO-Sorbent technology is 300 °C. In view of the comparison with the current MDEA-Solvent technology it was established for the lowering of the temperature from 300 °C to 129 °C, the recovering of the LP-Steam produced. Regarding the clean gas composition (wet basis) in outlet from the desulphurization section, the H₂O content = 11.01% v/v is much higher than that in the current design. Since in the ZnO-Sorbents technology, the COS hydrolysis section is removed, the water necessary for this reaction, which in the currently technology is in part taken from that contained in the wet raw gas (H₂O content =

10.11% v/v), is found totally at the end of the sorbent desulphurization process. Additionally, in the desulphurization reaction, water is produced as a result of the H₂S removal by the following reaction:



As a result, the final water content in the clean gas is equal to **11.01 % v/v**. The flow rate in the ZnO-technology is a bit lower than that of the original design because in this last case also the recycled gas derived from the sulphur recovery is considered.

Finally, the most significant impact of the syngas produced with the new technology in the combined cycle, will be on the gas turbine, due to the different composition and mass flow of the fed gas, and in the steam turbine. Actually, the higher content of H₂O, could be a great advantage especially in view of the construction of a new plant, because as described later, the entire section of the saturator with the obvious advantages could be avoided. In effect, surprisingly, the water content in the clean gas after the saturator in the reference case (11.52%) is pretty much the same of the sorbent technology, but otherwise, before the saturator (11.01%).

8.8.3 Impact of the new oxygen amount required in the Regenerator

In view of the increased oxygen demand in the regenerator, it was necessary to evaluate a new mass balance in the ASU unit. As a consequence of the greater amount of air, having fixed the amount of pure nitrogen (99.9%) as in the original configuration, in order to match the required material balance, more “waste” nitrogen (O₂ content lower than 2%) will be available to be mixing with the clean gas before entry in the combustion chamber. In [Table 12](#) all the data relatively to the impact of the oxygen demand on the combined cycle and ASU unit are reported.

Table 12. *Impact of the new oxygen demand in the combined cycle and ASU unit.*

	ZnO-Sorbent	MC15.100 Design
Mass flow Air extracted to compressor (Kg/s)	102.96	96.996
Mass flow of O₂ produced in ASU (Kg/s)	26.70	25.348
Mass flow of LP- and IP-Nitrogen (Kg/s)	7.518	7.518
Mass flow of Waste N₂ to CC (Kg/s)	68.98	62.555

In this case, the main impact will be on the gas turbine as a greater amount of air must be extracted by the compressor to be sent to the ASU unit and hence is not used for combustion. On the other hand, consequently to the variation of the mass flow of air, more waste nitrogen is available to be mixed with the clean gas leading to an increase of the gas turbine power output.

8.8.4 Impact originated from the steam balance in the *HGD&R* unit

Last but not least, the impact concerning the steam at high-, medium- and low-pressure that is produced or must be supplied in the *HGD&R* unit, and that consequently it will, or not, be available in the "HRSG" *Heat Recovery Steam Generator* of the combined cycle. From a final steam balance in the *HGD&R* unit, shown in the [Table 13](#) the values of HP-, IP- and LP-steam mass flows imported to the HRSG.

Table 13. *Mass flow of HP-, IP-, LP-steam streams.*

	ZnO-Sorbent	MC15.100 Design
HP-Saturated steam from Gasification to the Drum (Kg/s)	61.67	63.83
IP-Saturated steam from Gasification to the Drum (Kg/s)	6.54	5.94
LP-Saturated steam from Gasification to the Drum (Kg/s)	7.577	0

8.9 Simulation tests with the Thermo-economic DiaGnosis System “TDG” software

The **Thermo-economic Diagnosis System** is a software tool integrated in the Plant Information Management System of the Puertollano IGCC power plant, that has been developed by ELCOGAS in conjunction with CIRCE ^[7, 8]. It consists of a data acquisition and reconciliation module, performance test module, state of reference simulator, cost calculation module and thermoeconomic diagnosis module. The tool is conceived to assist plant performance analysis for the steady state. TDG allows to continuously evaluate the plant thermal balances in unattended mode, electricity production cost and to allocate performance degradation at the component level by a particular diagnosis methodology. It has also been used as the reference calculation tool to carry out the acceptance test and for several studies regarding equipment performance in order to improve overall efficiency.

In all the simulations performed with the data related to the ZnO-Sorbent technology, once all the new parameters have been inserted, other parameters were necessary to be modified for different reasons:

- ✚ The flue gas temperature at the outlet of the gas turbine reached a value always higher than the predetermined threshold of 539.3 °C;
- ✚ The mass flow (kg/s) value of the clean gas was not the real output from the desulphurizer.

To modify these values, the power of the gas turbine has been slightly changed, reducing it down to a value such as the temperature and the mass flow of the clean gas were to the desired values.

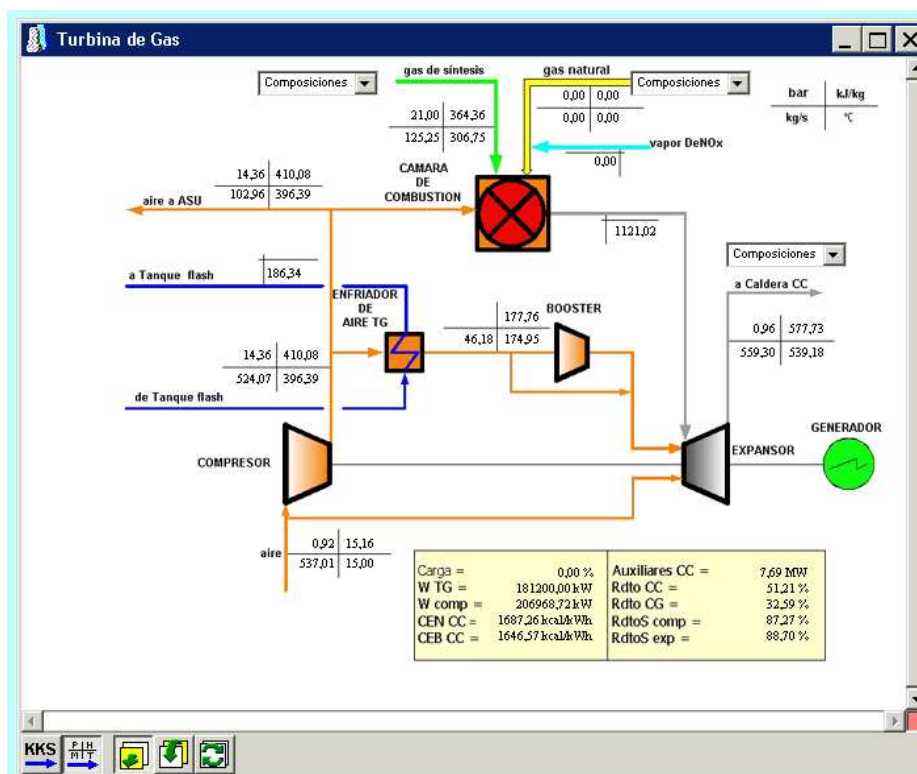


Figure 8. Example of gas turbine TGG performance results in the case of ZnO-Sorbent technology.

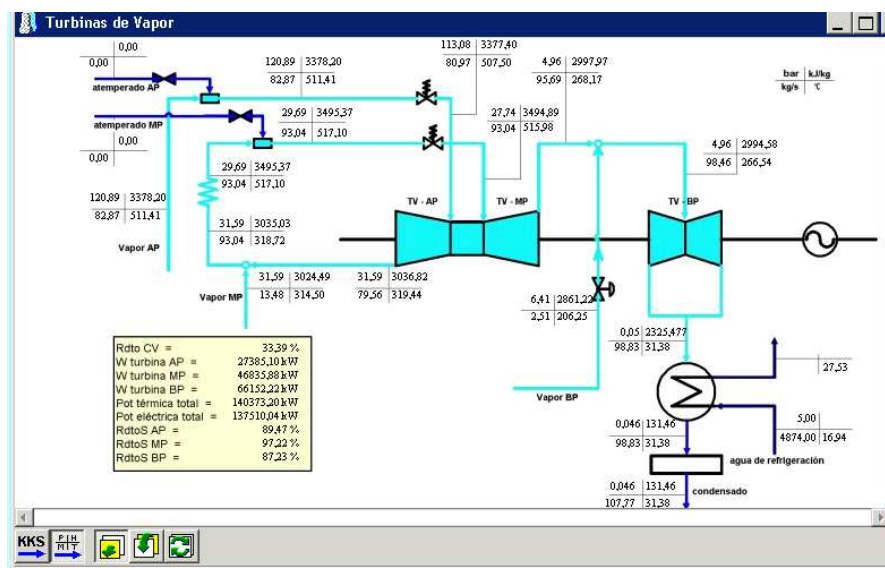


Figure 9. Example of steam turbine TDG performance results in the case of ZnO-Sorbent technology.

TDG software has limitations in the boundary conditions regarding water content of the clean syngas, so only **2.5 % v/v** was possible to be used, instead of **11.01 % v/v**, (Table 14). This is due to the fact that the software provides for the saturator section adding the water for the clean syngas, and which therefore cannot be eliminated during the simulation. This involves a negative influence on the potential of this new technology, which would allow, in principle, the removal of the entire section of the saturator, which provides in the project data a consumption of 10.88 MJ, corresponding to 14.9 KJ/s of HP-steam. The effect of water content, within the limits imposed with the maximum possible content (**2.5 % v/v**), during the simulation has been assessed on the performance of the gas- and steam-turbine, and it was found that:

- ✚ a low water content improves the performance of the gas turbine, worse rather than of the steam turbine;
- ✚ a higher water content enhanced the performance of the steam turbine, worse rather than of the gas turbine.

Table 14 shows the different parameters introduced in the TDG software in comparison with the TDG reference data.

Table 14. Different parameters introduced in the TDG software for the simulation (2.5% Water).

Parameter	Unit	ZnO-Sorbent (T _{room} = 15 °C)	TDG Design (T _{room} = 15°C)
Gas Turbine load	%	100	100
Gas turbine section			
Gross GT Power Output	MW	181.3	182.3
Waste N ₂ Mass flow	Kg/s	68.98	62.555
Waste N ₂ Temperature	°C	195	195
Air extract from ASU	Kg/s	102.96	96.996
TG Outlet Gas Temperature	°C	539.30	539.30
HRSG			
HP-Steam imported	Kg/s	61.67	63.83
IP-Steam imported	Kg/s	6.54	5.94
Saturator			
Clean Gas Temperature	°C	129	129
Clean Gas Pressure	bar	21	21
Clean Gas Mass flow	Kg/s	51.92	52.72
Ar	% v/v	1.0086	1.03
NH ₃	% v/v	0.0099	ppm
H ₂ O	% v/v	2.5	0.27
COS + H ₂ S	% v/v	0	0
H ₂	% v/v	22	22.02
CO ₂	% v/v	3.81	3.86
CO	% v/v	60.37	60.35
N ₂	% v/v	10.35	12.46
CH ₄	% v/v	0.0099	0.01

Table 15 gives the performance comparison between the ZnO-Sorbent technology and the TDG reference data.

Table 15. Performance results in different sections of the plant (2.5% Water).

Parameter	Unit	ZnO-Sorbent (T _{room} = 15 °C)	TDG Design (T _{room} = 15°C)	Difference
Gas Turbine load	%	100	100	-
Gas turbine section				
Gross GT Power Output	MW	181.3	182.3	-1
Gas Cycle Efficiency	%	32.59	32.80	-0.2
CC Efficiency	%	51.37	51.31	+0.06
Steam turbine section				
Gross ST Power Output	MW	137.89	138.37	-0.48
ST Power Output HP	MW	27.399	27.887	-0.49
ST Power Output IP	MW	46.695	47.190	-0.49
ST Power Output LP	MW	66.660	66.164	+0.496
Steam Cycle Efficiency	%	33.31	33.52	-0.20
Combined Cycle Efficiency				
Gross Efficiency	%	52.64	52.57	+0.06

8.9.1 Low pressure Steam turbine Power determination

Since the TDG software does not allow the adding of the new amount of low-pressure steam produced from the cooling of the clean gas exiting the desulphurizer, "manual" calculation of the new power of the low pressure steam turbine was performed. It can be roughly calculated by the formula:

$$W_{LP} = m_{LP} \cdot (H_{inp} - H_{out}) \cdot \eta$$

where

m_{LP} [Kg/s]	LP-steam mass flow at the inlet of the steam turbine
$H_{imp} - H_{out}$ [KJ/Kg]	Enthalpy difference
η	Steam turbine efficiency

8.10 Comparison with the Siemens MC15.100 reference data

TDG software makes use of data slightly different if compared to the MC15.100 that are the real project data. For a more accurate comparison, the final results obtained from TDG were compared with those of reference relating to the Siemens MC15.100 data. In this case the contribute relative to the LP-steam on the steam turbine previously calculated has been added. [Table 16](#) reports the data and the final results.

Table 16. Performance results comparison between *ZnO-Sorbents* and *MC15.100 Reference Case*.

Parameter	ZnO-Sorbent ($T_{room} = 15\text{ }^{\circ}\text{C}$)		MC15.100 Design ($T_{room} = 15\text{ }^{\circ}\text{C}$)		Difference
Gas Turbine load	100 %		100 %		-
Clean gas to the Saturator	Mass Flow (Kg/s)	Heat Flow (MW)	Mass Flow (Kg/s)	Heat Flow (MW)	
Mass flow	51.92	521.003	52.371	518.876	+2.13
Heat flow to the CC	Mass Flow (Kg/s)	Heat Flow (MW)	Mass Flow (Kg/s)	Heat Flow (MW)	
Waste N_2	68.98	14.17	62.555	12.855	
HP-Steam from Gasif.	61.67	164.94	63.83	170.72	
IP-Steam from Gasif.	6.54	18.32	5.94	16.649	
LP-Steam to CC	7.577	20.90	0	0	
LP-Condensate from Evap	10.265	6.394	10.265	6.394	
Make Up Water	9.258	0.778	9.258	0.778	
Total Heat Flow	225.502 MW		207.393 MW		+18.11
Heat flow extracted from CC	Mass Flow (Kg/s)	Heat Flow (MW)	Mass Flow (Kg/s)	Heat Flow (MW)	
Air to ASU	102.96	14.898	96.996	14.035	
HP-Feed Water to Gasif.	64.329	88.832	64.329	88.832	
IP-Feed Water to Gasif.	14.269	9.493	14.269	9.493	
LP-Steam to Gasif.	0	0	2.785	7.684	
LP-Feed Water to Claus	2.621	1.722	2.621	1.722	
Total Heat Flow	114.945 MW		121.766 MW		-6.82
Gas turbine section					
Gross GT Power Output	181.85 MW		182.3 MW		-0.45
Steam turbine section					
Gross ST Power Output	139.9 MW		135.4 MW		+4.5
Gross Efficiency					
CC Gross Efficiency	50.95 %		52.55 %		-1.6

IGCC Gross Efficiency	47.73 %	47.13 %	+0.6
-----------------------	----------------	----------------	------

The results show again a lowering of the gross gas turbine power output, but contrary to the previous data, an increase of the gross steam turbine power output, due to the greater amount of low pressure steam in inlet. However, there is an opposite effect on the efficiency of the combined cycle and the entire IGCC process. Indeed the latter were calculated respectively as:

$$\eta_{CC} = \frac{(W_{TG} + W_{ST})}{(HF \text{ of Clean gas to the Saturator} + HF \text{ to the CC} - HF \text{ extracted from the CC})} \cdot 100$$

$$\eta_{IGCC} = \frac{(W_{TG} + W_{ST})}{(HF \text{ of Raw Coal} + HF \text{ of Natural Gas})} \cdot 100$$

Concerning the gross efficiency of the combined cycle (η_{CC}), this is penalized by 1.6 percentage points due to the fact that both the heat flow of the clean gas to the saturator and the heat flow to the combined cycle are higher than the reference data. On the contrary, the gross IGCC efficiency (η_{IGCC}) is higher being higher the W_{ST} at the numerator.

8.11 Conclusions and future R&D overview

Based on the obtained results reported in this chapter, and from the considerations set out in the Chapter 7, some important conclusions and key points on the work done so far can be listed.

- ✚ In the first and simplest proposed layout (**Layout 1**), conceived to be a retrofitting of the existing process, the ZnO-Sorbent technology does not seem to benefit any significant improvement in terms of gross efficiency of the combined cycle. In contrast it seems to slightly benefit the whole efficiency of the IGCC process. This result is certainly greatly

underestimated as the simulation software did not allow to take into account the high percentage of water (11.01 % v/v), but only 2.5 % v/v has been considered, and that would have two positive effects, that are i) to be able to delete the entire section of the saturator and ii) the increase of the clean syngas flow rate.

- ✚ The raw gas heating requires a significant amount of high pressure steam (11.3 kg/s) that cannot be completely recovered by the heat released from the exothermic reactions in the two reactors, or by the cooling of the clean- and the off-Gas. As a consequence, a significant amount of HP-Steam (2.2 kg/s) is subtracted from the "HP-Saturated Steam from Gasification".
- ✚ The clean- and off-gas cooling, made it necessary for a direct comparison with the MDEA-Solvent technology through the TDG software, it does not positively affect the performance of the combined cycle.
- ✚ Nevertheless, this first layout is the simplest way to obtain the integration in the current Puertollano process, obtaining a greater thermal efficiency of the Hot Gas Desulphurization unit than that with the MDEA-Solvent.
- ✚ Given the high temperature of the clean gas at the exit of the desulphurizer (**300 °C**) and the high content of H₂O (**11.01%**), there may be the possibility to remove the entire Saturator section with evident saving of equipment, including the "Clean Gas Preheater" which requires 10.88 MJ/s, corresponding to 14.9 kg/s of HP-Steam.
- ✚ Given the different composition of the gas to be sent to the sulphur recovery unit, particularly with the use of oxygen or air as regeneration gas, it is necessary a new treatment plant for the SO₂ produced.

In view of the results obtained for this first layout, some considerations may be announced for the second alternative "**Mid-temperature layout**" proposed.

- ✚ Configuration more complicated than the first layout since it implies severe modifications in the raw gas cleaning process (and therefore more adequate for a new plant design), but represents the best to exploit the potential of this new technology; the objective is to use all the exiting raw gas temperature equal to 380 °C, taking advantage of the sensible heat of the raw gas.
- ✚ In this layout it is not required to heat the raw gas, leading to save 11.3 kg/s of high-pressure steam.
- ✚ Additional production of high pressure steam resulting from the cooling of the desulphurization and regeneration reactors, thus increasing the steam turbine power output.
- ✚ As in the first layout, the H₂O content in the exit gas from the desulphurizer is equal to 11.01%, very similar to the water content of the clean gas after the section of the saturator (11.5%), used in the current process. As a consequence, there may be the possibility to remove the entire Saturator section with:
 - evident saving of equipments;
 - saving of the "Clean Gas Preheater" which requires 10.88 MJ/s, corresponding to 14.9 kg/s of HP-Steam;
 - saving of a remarkable amount of water.
- ✚ Possibility of the direct mixing of the clean gas at 300 °C with the waste nitrogen, with the result of a more simple plant configuration in the section immediately upstream of the combined cycle.
- ✚ Significant amount of HP-Steam available in the combined cycle: approximately 34 kg/s more than the 64 kg/s normally imported with the original plant configuration, with a remarkable enhancement of the Combined Cycle and IGCC gross efficiency.
- ✚ Possible re-evaluation of the regeneration with IP-Steam, with which, in contrast with the use of oxygen, the reaction would be better controlled and safer, being an endothermic reaction.

- ✚ Need for further studies to test the effects of contaminants contained in the raw-gas on the desulphurization performance or the possibility to open the way for a new cleaning process generation based on the only use of solid sorbents ^[1].

References

- [1] J. T. Konttinen, A. P. Zevenhoven, K. P. Yrjas and M. M. Hupa, *Ind. Eng. Chem. Res.*, **1997**, 36, 5432.
- [2] J. T. Konttinen, A. P. Zevenhoven and M. M. Hupa, *Ind. Eng. Chem. Res.*, **1997**, 36, 5439.
- [3] RTI International, in *RTI and Eastman Chemical Demonstrate High-Temperature Syngas Cleanup Technology*, **2010**.
- [4] C. C. Cormos and L. Petrescu, *Energy Procedia*, **2014**, 51, 154.
- [5] C. Hawthorne, H. Dieter, A. Bidwe, A. Schuster, G. Scheffknecht and S. Unterberger, *Energy Procedia*, **2011**, 4, 441.
- [6] P. Cargill, G. DeJonghe, T. Howsley, B. Lawson, L. Leighton and M. Woodward, Piñon Pine IGCC project. Final technical report to the Department of Energy, DOE Award No. DE-FC21-92MC29309, Sparks, NV, USA, **2001**.
- [7] F. García Peña, A. Gálvez, L. Correas and P. Casero, *Advanced operation Diagnosis for Power Plants. Performance Monitoring and Cost Assessment in Puertollano IGCC*, Power-Gen **2000** Helsinki, Finland.
- [8] L. Correas, A. Martínez and A. Valero, *Operation Diagnosis of a Combined Cycle based on the Structural Theory of Thermoconomics*, ASME International Mechanical Engineering Congress and Exposition, November **1999**, Nashville, TE.

Overall Summary and Conclusions

This thesis deals with the development of efficient $\text{MeO}_x/\text{SBA-15}$ -based sorbents for H_2S removal in view of possible applications in hydrogen purification, air pollution control and deep desulphurization of fossil fuels. Just for this last topic has been studied and evaluated the possible application of this innovative sorbent technology in a real Integrated Gasification Combined Cycle plant. To achieve this goal has been carried out an assessment of mid-temperature sorbent desulphurization technology in Puertollano (Elcogas S. A.) IGCC process.

The thesis reports three different strategies to prepare a great variety of $\text{MeO}_x/\text{SBA-15}$ composites where the MeO_x active phase, formed inside the mesochannels, can reach the maximum size of 6-7 nm physically imposed by the pore diameter. The proposed "Two-solvents" incipient impregnation method is easily reproducible and easy to scale up. Furthermore, this method should provide, at least in principle, ideal systems to be compared, and therefore to understand how the active phase nature influence their performance. An innovative impregnation-sol-gel autocombustion combined method has been successfully proposed and developed to prepare nanocomposites that exhibited excellent sulphur retention capacity, being more than two times higher than that of the samples prepared with the two-solvents impregnation approach.

For the first time, a careful comparative study on the effect of the different nature of the nanostructured MeO_x ($\text{Me} = \text{Zn}, \text{Fe}$) dispersed into a mesostructured silica matrix (SBA-15) on the H_2S removal performance is carried out. The combined use of different techniques has allowed to evidence that, although the same SBA-15 starting material and synthetic strategy have been used, the active phases tend to disperse inside the host matrix in a different way. This is due to the different interactions between the Me^{n+} and the silanols groups at the surface of the SBA-15. Such interactions, which are responsible for the deposition of zinc oxide as an amorphous thin layer at the surface of the SBA-15 channels, also make the zinc oxide phase differently available to react with the hydrogen sulphide, in comparison with the case of iron oxide nanocrystals not interacting with the host matrix. In the light of

these results, the sorption-desorption behaviour, which is commonly justified only on the basis of the different nature of the active phase and of the textural features (surface area and pore volume), was discussed also considering the morphology and the crystallinity of the active phase.

Some of the notable achievements of this work are listed below:

- ✚ Novel zinc oxide/SBA-15, iron oxide/SBA-15, and zinc ferrite/SBA-15 mesostructured nanocomposite sorbents are developed for H₂S removal over mid-temperature (300 °C);
- ✚ The activity of the zinc oxide and the iron oxide systems are seven and seventy times higher than that of an unsupported zinc oxide commercial sorbent, respectively;
- ✚ Differences in the morphology and the crystallinity of the active phase, as well as in the textural features of the composites, seem related to the lack or presence of interactions between the guest oxide phase and host silica matrix, which in turn make the iron oxide and zinc oxide phases differently prone to react with hydrogen sulphide;
- ✚ After regeneration of the sulphided sample, the sorption properties of the zinc oxide/SBA-15 composite appear enhanced and are maintained upon repeating the sorption-regeneration cycle;
- ✚ The iron oxide/SBA-15 sorbent shows the highest sulphur retention capacity. Its performance significantly decreases at the second sorption cycle mainly due to the formation of an iron sulphate phase, but is retained at the third sorption cycle;
- ✚ The oxidation step for obtaining the regenerated iron oxide-based sorbent can be carried out at $T \leq 350$ °C, which is considerably lower than that required in the case of the ZnO-based sample;
- ✚ The synergetic effect between zinc and iron when are combined in the zinc ferrite structure. The results have shown that concerning the relative high sulphidation activity and the low regeneration temperature (< 500 °C), this behaviour complies with the iron oxide-based

sorbent; by converse, the retention of the sorption properties upon repeating sorption-regeneration cycles seem related with the zinc oxide-based sorbent.

In the literature, to our best knowledge, no one have reported similar correlations. For this reason it has believed that this thesis can give an important contribution to improve the basic knowledge in the field of sorbents for gas-removal.

Concerning a real commercial application of the sorbents, this thesis presented a performance evaluation of the Puertollano IGCC power plant with mid-temperature syngas desulphurization. In comparison with a reference power plant with conventional cold gas desulphurization, two different layout with Hot Gas Desulphurization were proposed and discussed. Particular attention was paid to the effects of: i) impact on the different IGCC systems; ii) impact of different regeneration gas on the energy balance of the Hot Gas Desulphurization section; iii) general impact of the use of oxygen, air and steam on the different plant sections (mainly ASU and Claus unit); iv) impact of ZnO-Sorbent technology in the Puertollano IGCC efficiency through several simulations performed with the Thermo Economic Diagnosis system software. The latter had some limitations, mainly because is conceived to operate with the actual process and equipments used in the plant, and manifested modest flexibility especially respect to the water content in the clean syngas. This limitation has not allowed to investigate and better take advantage of the potentiality of this technology, so that the calculated final IGCC gross efficiency turns out to be underestimated. However, not even taking advantage of the potential of this technology, has achieved an improvement of +0.6 % of the overall IGCC gross efficiency.

Of the two proposed layout, the first ([Low-temperature layout](#)) represents the simplest solution to be integrated to replace the conventional MDEA-Solvent technology, keeping unchanged all the equipment, pressures, temperatures, flow rates etc., upstream of the new desulphurization section. The first layout is also more cost effective to be installed. On the other hand, is not the best solution for an improvement of the overall efficiency of the plant, in fact, even with this proposed layout the raw syngas must necessarily be heated before to be sent to the desulphurizer.

Recommendations and future works

In a gasification plant the gas cleanup steps have a big impact on plant economics. In a conventional cold gas cleanup, the cooling equipment required and the need to reheat the syngas before its use in a gas turbine result in economic and thermodynamic penalties that decrease the efficiency of a gasification plant. Therefore gas cleanup that would operate at higher temperature while still removing multiple contaminants would provide a significant efficiency improvement.

Keeping this in mind, the second layout proposed ([mid-temperature layout](#)) that allows to fully exploit the potential of this new technology, it should fully meet the expectations. This layout that permits to remove sulphur compounds in the desulphurizer without heating of the raw syngas, eliminates the need for substantial syngas cooling and expensive heat recovery systems, which would significantly increase the thermal efficiency and reduce the capital and operating costs of new gasification-based system when compared to conventional process technologies, with up to 3% improvement in thermal efficiency. Preliminary assessment performed on the second layout suggests that it compares favourably with the first one. More detailed assessment on the second layout should be performed with the new mass and energy balance, and a new evaluation on the overall gross IGCC efficiency. Furthermore, estimates have suggested that the mid-temperature cleanup coupled with CO₂ capture might be 15-30% cheaper than conventional syngas cleanup paired with CO₂ capture.

Nomenclature

Symbol	Unit	Explanation
<i>BET</i>	-	Brunauer, Emmet, Teller: method for determination of the specific surface area
<i>BJH</i>	-	Barret, Joyner, Halenda: method for determination of the pore size distribution
<i>FTIR</i>	-	Fourier Transform Infrared Spectrometer
<i>HGD</i>	-	Hot Gas Desulphurization
<i>HRTEM</i>	-	High Resolution Transmission Electron Microscopy
<i>TCD</i>	-	Thermal Conductivity Detector
<i>TPD</i>	-	Temperature Programmed Oxidation
<i>QMS</i>	-	Quadrupole Mass Spectrometer
<i>XRD</i>	-	X-ray Diffraction
<i>XPS</i>	-	X-ray Photoelectron Spectroscopy
<i>SBA-15</i>		<i>Santa Barbara Amorphous</i>
a_0	nm	Cell parameter
S_{BET}	$m^2 g^{-1}$	Specific surface area
V_p	$cm^3 g^{-1}$	Pore volume
D_p	nm	Pore diameter
T_w	nm	Walls thickness
<i>IWI</i>	-	Incipient Wetness Impregnation
<i>TS</i>	-	Two-Solvents
<i>SC</i>	-	Self-Combustion
B_t	s	Breakthrough time
<i>SRC</i>	mgS/gSorbent	Sulphur Retention Capacity
η_{th}	%	Thermal Efficiency
ΔH_f°	$KJ mol^{-1}$	Standard Molar Enthalpy of formation at 298.15 K
ΔH_R°	$KJ mol^{-1}$	Enthalpy (Heat) of reaction
C_p	$J mol^{-1} K^{-1}$	Molar Heat Capacity

<i>FR</i>	$\text{Nm}^3 \text{h}^{-1}$	Flow Rate
<i>m</i>	Kg h^{-1}	Mass Flow
<i>M</i>	g mol^{-1}	Molar mass
<i>n</i>	Kg mol	Moles Number
<i>Q</i>	MJ or MW	Amount of Heat
<i>T</i>	$^{\circ}\text{K}$	Temperature
<i>CGD</i>	-	Cold Gas Desulphurization
<i>HGD&R</i>	-	Hot Gas Desulphurization and Regeneration

List of publications

R. Piras, M. Aresti, M. Saba, D. Marongiu, G. Mula, F. Quochi, A. Mura, C. Cannas, **M. Mureddu**, A. Ardu, G. Ennas, V. Calzia, A. Mattoni, A. Musinu and G. Bongiovanni, "Colloidal synthesis and characterization of Bi_2S_3 nanoparticles for photovoltaic applications", 5th Young Researcher Meeting, Trieste, *Journal of Physics: Conference Series 566* (2014) 012017. (<http://iopscience.iop.org/1742-6596/566/1/012017>)

M. Mureddu, I. Ferino, A. Musinu, A. Ardu, E. Rombi, M. G. Cutrufello, P. Deiana, M. Fantauzzi and C. Cannas, "MeO_x/SBA-15 (Me = Zn, Fe): highly efficient nanosorbents for mid-temperature H₂S removal", *J. Mater. Chem. A*, 2 (2014) 19396.

M. Aresti, M. Saba, R. Piras, D. Marongiu, G. Mula, F. Quochi, A. Mura, C. Cannas, **M. Mureddu**, A. Ardu, G. Ennas, V. Calzia, A. Mattoni, A. Musinu and G. Bongiovanni, "Colloidal Bi_2S_3 Nanocrystals: Quantum Size Effects and Midgap States", *Adv. Funct. Mater.*, 24 (2014) 3341.

Publication on international site of interest in the energy sector of the article: "ZnO/SBA-15 composites for mid-temperature removal of H₂S: synthesis, performance and regeneration studies" **M. Mureddu**, I. Ferino, E. Rombi, M.G. Cutrufello, P. Deiana, A. Ardu, A. Musinu, G. Piccaluga, C. Cannas, *Renewable Energy Global Innovations* {ISSN 2291-2460} (2013): <http://reginnovations.org/>

Technical report: "Sintesi e sperimentazione di materiali innovativi per il trattamento del syngas da carbone", M.G. Cutrufello, E. Rombi, R. Monaci, I. Ferino, **M. Mureddu**, C. Cannas, A. Musinu, G. Piccaluga, Report Ricerca di Sistema Elettrico Accordo di Programma Ministero dello Sviluppo Economico – ENEA Area: Produzione di energia elettrica e protezione dell'ambiente Progetto: 2.2 – Studi sull'utilizzo pulito dei combustibili fossili, la cattura ed il sequestro della CO₂ con Responsabile del Progetto: Ing. Stefano Giammartini, ENEA.

M. Mureddu, I. Ferino, E. Rombi, M.G. Cutrufello, P. Deiana, A. Ardu, A. Musinu, G. Piccaluga and C. Cannas
"ZnO/SBA-15 composites for mid-temperature removal of H_2S : synthesis, performance and regeneration studies", *Fuel*, 102 (2012) 691.